Author:
Malone, Liam Douglas

Title:
The Gap Symmetry of the Organic and Iron Based Pnictide Superconductors

The Gap Symmetry of the Organic and Iron based Pnictide Superconductors

Liam Douglas Malone

March 2009

A thesis submitted to the University of Bristol for the degree of Doctor of Philosophy in the Faculty of Science, Department of Physics

31826 words

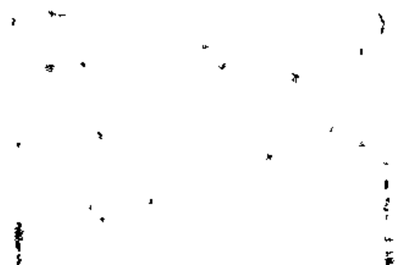

Abstract

In this thesis, a low temperature heat capacity experiment is developed for operation down to 400 mK in fields up to 14 T which is capable of measuring small single crystals (mass of around 500 μg) to an accuracy of 2 %. The calorimeter is mounted on a rotating platform and is capable of measuring the field angle dependence of the heat capacity to a precision of 0.1 %. The gap symmetry of the organic superconductors is a contentious issue with contrasting reports on the position and even presence of nodes. Angle dependent heat capacity measurements have been successful in revealing the presence of nodes in superconductors such as Sr_2RuO_4 and $CeCoIn_5$. Measurements of the angle dependant heat capacity of the organic superconductors κ-$(ET)_2Cu(NCS)_2$ and κ-$(ET)_2Cu[N(CN)_2]Br$ show a fourfold oscillation consistent with nodes along the crystal axis. The amplitude of the fourfold oscillation is in good agreement with a quasi-classical Doppler shift model. The temperature dependence of the heat capacity of κ-$(ET)_2Cu(NCS)_2$ and κ-$(ET)_2Cu[N(CN)_2]Br$ below 1 K also shows evidence of a nodal gap. These results support a nodal gap which is the same as in the cuprate superconductors and underline the similarities between these two classes of compounds.

Low temperature measurements of the magnetic penetration depth of the newly discovered pnictide superconductors $SmFeAsO_{0.8}F_{0.2}$ and $Ba(Fe_{0.93}Co_{0.07})_2As_2$ show contrasting results. The low temperature penetration depth of $SmFeAsO_{0.8}F_{0.2}$ supports a fully gapped superconducting state, however the low temperature penetration depth of $Ba(Fe_{0.93}Co_{0.07})_2As_2$ supports a nodal superconductor. This could indicate a change in gap symmetry across the pnictide family however more work is required to understand these new superconductors.

Author's declaration

I declare that the work in this thesis was carried out in accordance with the Regulations of the University of Bristol. The work is original, except where special reference is made to the work of others. No part of this work has been submitted for any other degree. The views expressed in this thesis are those of the author, and not the University of Bristol.

L. D. Malone

March 2009

Acknowledgements

The biggest thanks goes to my supervisor Tony Carrington for always being available. Secondly Jon Fletcher who was always willing to offer help and advice.

I would like to thank all the members of the low temperature group past and present for offering help and the chance to go for a drink. Specifically Owen, Matt, Rosie, Xiaofeng, Olly, Caroline, Alex, Neil and Ed.

Amalia Coldea and Luis Seabra for their advice and discussion.

Bob Wiltshire and Dick Iles for providing me with Helium.

The technicians in the workshop, especially Tim, Adrian and Richard for all their help.

Mairi Haddow in the Chemistry X-ray department.

Chris for carefully finding all the mistakes.

Finally my family and Laura for all their support.

Liam Malone

March 2009

Contents

Chapter 1

Introduction and Theoretical Background

1.1 Motivation and Outline

Superconductivity has been discovered in many elements and compounds. The elements and the majority of compounds are labelled as conventional superconductors. These conventional superconductors have transition temperatures less than 30 K (apart from MgB_2) and can be described by theories using a phonon mediated mechanism like the BCS theory and the Eliashberg theory (see section 1.3). Some of the more recently discovered superconductors are not well described by these theories and tend to display unusual physics in their phase diagram in proximity to superconductivity. These superconductors are generally labelled unconventional superconductors. The definition of unconventional superconductivity is quite loose. MgB_2 [1] is often regarded as unconventional due its' two gap nature and high T_c of 39 K but is well understood and a phonon mediated superconductor. Perhaps an appropriate definition is a superconductor which has some property which is not included in the BCS

theory (for example two gaps). A common definition is a superconductor which has a gap symmetry which breaks gauge symmetry and one additional symmetry. The gap symmetry refers to the gap which appears in the quasiparticle energy spectrum as a material enters the superconducting state. In a conventional superconductor this gap is finite in all directions (strictly speaking not true for this definition, see below) however in many unconventional superconductors the gap goes to zero along certain momenta (referred to as nodes). The BCS theory shows how the details of the gap symmetry are derived from the underlying pairing mechanism. For a phonon mediated superconductor in the BCS framework the gap is isotropic and the superconductor is called s-wave. The term s-wave derives from the angular momentum quantum number l of the superconducting state in exactly the same way as atomic orbitals are labelled (l=0 for s-wave, l=1 for p-wave and l=2 for d-wave). In most unconventional superconductors, the superconducting gap symmetry has a non-zero value of l which breaks additional symmetries (see ref [2]). The gap symmetries that are possible for a superconductor are restricted by the electronic structure. For example, in the cuprate superconductors several symmetries are allowed (see figure 1.1) for s-wave and d-wave scenarios (assuming spin singlet pairing). Note how the s^- state has nodes even though it is a conventional state using the symmetry definition, the converse is also true as some unconventional states have no nodes.

There are several classes of unconventional superconductors. The cuprate superconductors [3] which have the highest T_cs and are the subject of a large amount of research and debate. The heavy fermion superconductors [4], which were discovered before the cuprates, have very low T_cs and an unconventional pairing symmetry. Sr_2RuO_4 [5] has been shown to have spin triplet pairing with a T_c around 1 K. The organic superconductors [6], which have a lot of similarities to the cuprates as pressure is applied to a Mott insulator and superconductivity is produced with a maximum

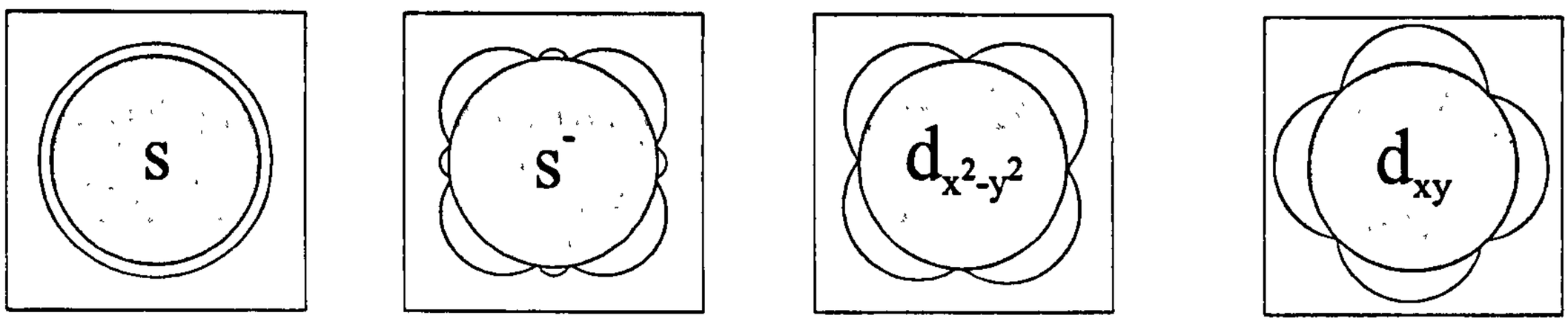

Figure 1.1: Various possible gap symmetries for the cuprate superconductors taken from [2]. The square represents the Brillouin zone, the circle the Fermi surface and the blue lines the gap.

T_c of $\sim 12\,\mathrm{K}$. The pnictides are the most recently discovered class of superconductors [7]. They exhibit the highest transition temperatures apart from the cuprates (up to $\sim 55\,\mathrm{K}$). A lot of work has been performed already on the pnictides but no consensus has been reached on the nature of their superconductivity.

The first step in producing a theory of superconductivity for a compound is determining the gap symmetry. The cuprates are d-wave superconductors [8] but no first principles theory has been shown to successfully describe all their properties. Most measurements on the organic superconductors conclude d-wave, but there is still controversy surrounding the gap symmetry of these superconductors. The pnictides are newly discovered and the gap symmetry is still under debate. Most probes show evidence of nodes and the spin fluctuations of the parent compound seem to imply an unconventional mechanism is at work.

The main part of this thesis is about measuring the gap symmetry of unconventional superconductors using precise low temperature measurements. To that end, a heat capacity experiment capable of measuring small single crystals which operates down to 400 mK in a field up to 14 T and is mounted on a rotating platform was developed and then used to measure the organic superconductors κ-$(ET)_2Cu(NCS)_2$ and κ-$(ET)_2Cu[N(CN)_2]Br$. The gap symmetry of these superconductors is still a

contentious issue and this experiment is designed to measure the gap symmetry using angle dependent heat capacity measurements. Angle dependent heat capacity measurements have been used in Sr_2RuO_4 [9], $CeCoIn_5$ [10] and $CeIrIn_5$ [11] to determine nodal directions. Recently there has been controversy in temperature dependent heat capacity measurements on the organic superconductors [12], [13] and measurements to a lower temperature coupled with angle dependent information should resolve the issue. Precise low temperature measurements of the magnetic penetration depth were performed on the newly discovered pnictide superconductors $SmFeAsO_{0.8}F_{0.2}$ and $Ba_2(Fe_{0.93}Co_{0.07})_2As_2$. The low temperature behaviour of the penetration depth is sensitive to the presence of nodes in the gap symmetry of a superconductor. As mentioned above the presence of nodes does not prove unconventional superconductivity but does constrain the gap symmetry.

The final chapter of this thesis is about a different project to measure the heat capacity of the frustrated antiferromagnet $AgNiO_2$. Measurements were performed in high magnetic fields up to 33 T and were used to determine the phase diagram of this newly synthesised material. Torque and transport measurements on this material reveal a rich phase diagram in high fields and measurements of the specific heat can provide more information on the underlying physics.

1.2 Determining the Gap Symmetry of a Superconductor

As described below, determining the gap symmetry of a superconductor is of fundamental importance to producing a theory to describe the superconductivity. There are many experimental techniques used to measure the gap symmetry, generally several are employed before a consensus is reached on the gap symmetry of a particular

superconductor.

1.2.1 Low Temperature Dependence of DOS

The most widely used method is to measure the low temperature dependence of the density of states. Any experimental quantity which is sensitive to the density of states can be used in this method. Heat capacity [12], penetration depth measurements [14], Nuclear Magnetic Resonance (NMR) [15] and thermal conductivity [16] are all used as probes of the density of states. NMR is actually sensitive to the electron electron correlation function which includes the density of states and other information. The density of states mainly provides information on the presence of nodes in the gap. In an isotropic superconductor, there is no density of states below the energy gap Δ and therefore experimental quantities are exponentially activated. In a superconductor with nodes, there is a finite density of states in the nodes and experimental quantities generally follow a power law. A highly accurate experiment is often required to be able to determine the difference between a superconductor with nodes and a superconductor without nodes. Good quality samples are also required as impurities can effect the results.

1.2.2 Field Angle Dependent DOS

In a nodal superconductor the density of states depends on the angle of magnetic field to the nodes. This can be used to determine nodal directions. This effect was first theorised by Volovik[17], who showed that in a d-wave superconductor the low energy density of states is dominated by normal state quasiparticles along the nodal directions. Since then a lot of theoretical work has been performed to quantify this effect [18], [19], [20], [21]. Recently, several experiments have measured the direction

of nodes in superconductors using angle dependent heat capacity measurements [22], [9], [23], [24] and angle dependent thermal conductivity measurements [25], [26].

1.2.3 Tunnelling Measurements

Scanning Tunnelling Microscopy (STM) measurements have been used to determine the gap symmetry of superconductors [27] and more generally tunnelling measurements have been instrumental in confirming the theory of conventional superconductors [28]. In STM, the differential tunnelling spectra from the tip to sample is measured and the gap value can be extracted. Rotating the sample relative to the tip can give nodal directions. The tunnelling spectrum of a superconductor can be calculated using the density of states and compared to experimental data. Tunnelling measurements are surface sensitive and this often leads to debate about the accuracy of the results.

1.3 The BCS Theory

The first microscopic theory of superconductivity to successfully explain the experimental data was published by Bardeen, Cooper and Schrieffer in 1957 [29]. It is generally referred to as the BCS theory. Cooper [30] showed that an electron gas is unstable to any attractive interaction between electrons. If there is an attractive interaction between electrons then these electrons pair up in a 'Cooper pair'. The BCS theory shows that this attractive interaction can be explained by electron phonon interactions, which had also been suggested by Frohlich [31]. The BCS theory creates a ground state of quasiparticle pairs with a singlet wavefunction (see for example ref [32] for a derivation). The electrons pair in states with momentum $-\mathbf{k}$ and $\mathbf{k}$ with opposite spins. An isotropic pairing potential $-V$ is assumed up to some cut-off fre-

quency $\hbar\omega_c$, where ω_c is related to the Debye frequency in the material. This is now a solvable problem and results in excitations with energy E given by

$$E = \sqrt{(\epsilon^2 + |\Delta|^2)}, \tag{1.1}$$

where ϵ is the normal state energy of the quasiparticles without superconducting interactions and Δ is the energy gap. The gap can be solved self-consistently from

$$\Delta_k = -\frac{1}{2}\sum_{k'} \frac{\Delta_{k'}}{(|\Delta_{k'}|^2 + \epsilon_{k'}^2)^{\frac{1}{2}}} V_{kk'}. \tag{1.2}$$

In this equation the k-dependence of each quantity is included to illustrate the more general form. The BCS theory assumes no that there is no k-dependence of V and therefore there is no k-dependence of Δ. In general the k-dependence of V defines the k-dependence of Δ. In a conventional superconductor, the pairing potential originates from phonons and can be reasonably well described by the BCS theory. In unconventional superconductors, Δ can be anisotropic and the k-dependence of V must be included in any theory. The BCS theory is a weak coupling theory, which is the same as saying $N(\epsilon_f)V \ll 1$ (where $N(\epsilon_f)$ is the normal state density of states at the Fermi level). Using the BCS form of the pairing potential, then equation 1.2 can be used to derive

$$\frac{1}{N(\epsilon_f)V} = \int_0^{\hbar\omega_c} \frac{d\epsilon}{(|\Delta|^2 + \epsilon^2)^{\frac{1}{2}}}. \tag{1.3}$$

This can be solved in the weak coupling limit to give

$$\Delta \simeq 2\hbar\omega_c e^{-\frac{1}{N(\epsilon_f)V}}. \tag{1.4}$$

Including the effect of temperature in equation 1.2 leads to an equation for T_c (defined as the temperature when Δ goes to 0)

$$\frac{1}{N(\epsilon_f)V} = \int_0^{\hbar\omega_c} \frac{\tanh\left(\frac{\epsilon}{2k_BT_c}\right)}{\epsilon} d\epsilon. \tag{1.5}$$

This can be solved to give

$$k_BT_c = 1.13\hbar\omega_c e^{\frac{-1}{N(\epsilon_f)V}}. \tag{1.6}$$

Combining equations 1.4 and 1.6 leads to

$$\Delta(0) = 1.764k_BT_c. \tag{1.7}$$

This equation relates the gap at zero temperature to the transition temperature of the superconductor in an isotropic, weak coupling superconductor. Some modifications can be made which make this more applicable to a general superconductor and these are discussed in the next section.

Although there are few superconductors which are completely described by the BCS theory, it lays the foundations for analysis of experimental results. It is clear from the preceding discussion that it is important to know the gap symmetry of a superconductor as it is intimately related to the pairing potential.

1.4 The Eliashberg Theory

It became apparent that a more detailed theory was required for some superconductors. The BCS assumption of a simple paring potential and weak coupling was not good enough to describe some strong coupled superconductors e.g lead. Giaever [33] noticed additional structure in tunnelling in lead junctions. Schrieffer [34] realised that

the simple BCS Δ used to find the density of states of a superconductor is actually $\Re(\Delta(\omega))$ which contains information on the coupling between electrons. Eliashberg [35] had formulated a theory which used the electron coupling to the phonon density of states $F(\omega)$ as a basis to calculate the properties of a superconductor. This quantity is labelled $\alpha^2F(\omega)$ and is the phonon density of states multiplied by the coupling to the electrons. In Eliashberg theory $\lambda = N(\epsilon_f)V$, which is assumed to be very small in BCS theory, is given by

$$\lambda = 2\int_0^\infty \frac{\alpha^2 F(\omega)}{\omega} d\omega, \tag{1.8}$$

λ also represents the mass renormalization $m^* = m(1+\lambda)$ of the electrons due to the phonons. In the strong coupling limit McMillan extended equation 1.6 by fitting numerical results of the Eliashberg equations and found that

$$T_c = \frac{\Theta_D}{1.45} \exp\left(-\frac{1.04(1+\lambda)}{\lambda - \mu^*(1+0.62\lambda)}\right), \tag{1.9}$$

where Θ_D is the Debye temperature of the phonon frequency and μ^* is Coulomb pseudo-potential. The Eliashberg formulas have proved very successful in describing the features of lead and other conventional superconductors. Analysis of the second derivative of the tunnelling curves in lead reveals $\alpha^2F(\omega)$ and comparison of this to the phonon density of states measurements using neutron scattering shows a clear correlation as shown Figure 1.2. The deviation from the BCS prediction of the density of states is up to 5% in lead which has the strongest coupling of the conventional superconductors. The excellent agreement between the tunnelling data and the phonon data offered further proof that the superconductivity in conventional superconductors is phonon mediated. It should be noted that in general $\alpha^2F(\omega)$ is not proportional to $F(\omega)$ although it is in lead.

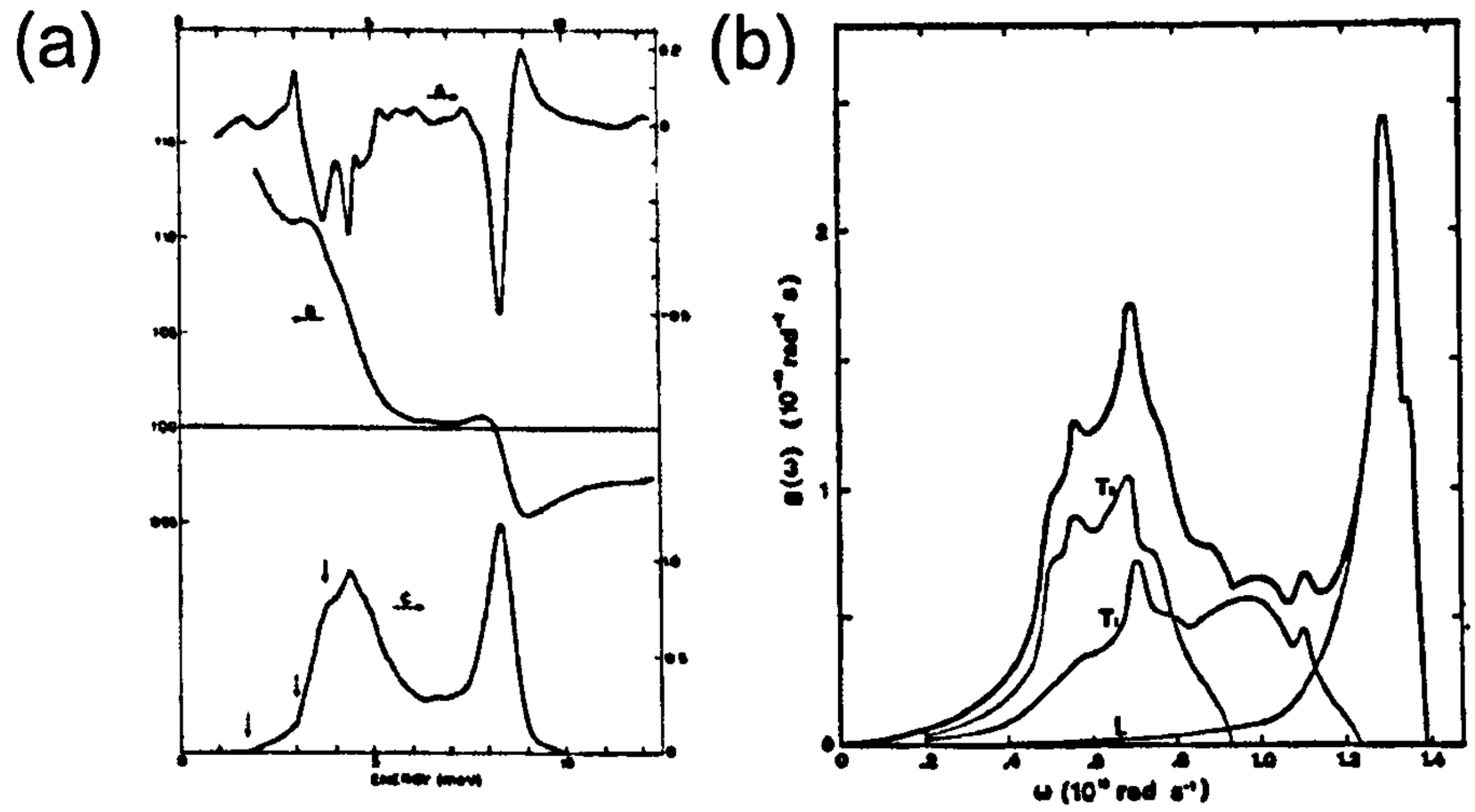

Figure 1.2: (a) Tunnelling data taken on lead from [36]. Curve A is dI^2/d^2V, curve B is the density of states in the superconducting state and curve C is $\alpha^2F(\omega)$. (b) Phonon density of states in lead measured by neutron scattering taken from [37].

1.5 Unconventional and High T_c Superconductivity

The highest T_c to date for a proven phonon mediated superconductor is 39 K in MgB_2 [1]. In 1986, Bednorz and Müller [3] discovered superconductivity in doped lanthanum cuprate with a maximum T_c of 35 K. More cuprates were discovered with transitions of 100 K and upwards [38]. The phase diagram of the cuprate superconductors shows a Mott insulator being doped into a high temperature superconductor. It has been shown that the cuprates have an $d_{x^2-y^2}$ superconducting gap symmetry (for a review see [8]). As well as the cuprates other superconductors have been shown to have nodes in the superconducting gap, most pertinently the organic superconductors (discussed in Chapter 3) but also some heavy fermion superconductors [24] and strontium ruthanate [9]. All these compounds exhibit strongly correlated physics in the vicinity of superconductivity. This has lead to much speculation that these are non-phonon mediated superconductors. This is most evident in the cuprate superconductors, where there are anti-ferromagnetic spin fluctuations along the direction of the nodes. The spin fluctuation pairing function is repulsive in some directions

and attractive in others and solutions to equation 1.2 using spin fluctuations have nodes along some directions. It should be noted that no consensus on the pairing mechanism behind superconductivity in the cuprates has yet been reached and there are some theories which explain the experimental data using phonons [39]. As unconventional superconductivity refers to a superconductor which breaks gauge symmetry and one additional symmetry there is also the possibility of a spin-triplet superconducting wavefunction which breaks time reversal symmetry. In the rest of the thesis, the experimental results are analysed using a simple BCS-like framework as described below.

1.6 Solving the BCS Gap Equation

The following discussion deals with the difference between an isotropic s-wave superconductor and a d-wave superconductor with a gap of $\Delta(\theta) = \Delta_0 \cos(2\theta)$ on a cylindrical Fermi surface as these illustrate the arguments simply and are relevant in the organic superconductors and possibly the pnictides. There are many other gap symmetries, for example the extended s-wave state discussed in chapter 4.

1.6.1 s-wave Superconductor

To find the low temperature density of states the temperature dependence of the gap must be taken into account. Equation 1.5 is for a superconductor at T_c, at temperatures in the superconducting state it is modified to

$$\frac{1}{N(\epsilon_f)V} = \int_0^{\hbar\omega_c} \frac{\tanh\left(\frac{1}{2k_BT}\left(\epsilon^2 + \Delta(T)^2\right)^{\frac{1}{2}}\right)}{\left(\epsilon^2 + \Delta(T)^2\right)^{\frac{1}{2}}} d\epsilon. \tag{1.10}$$

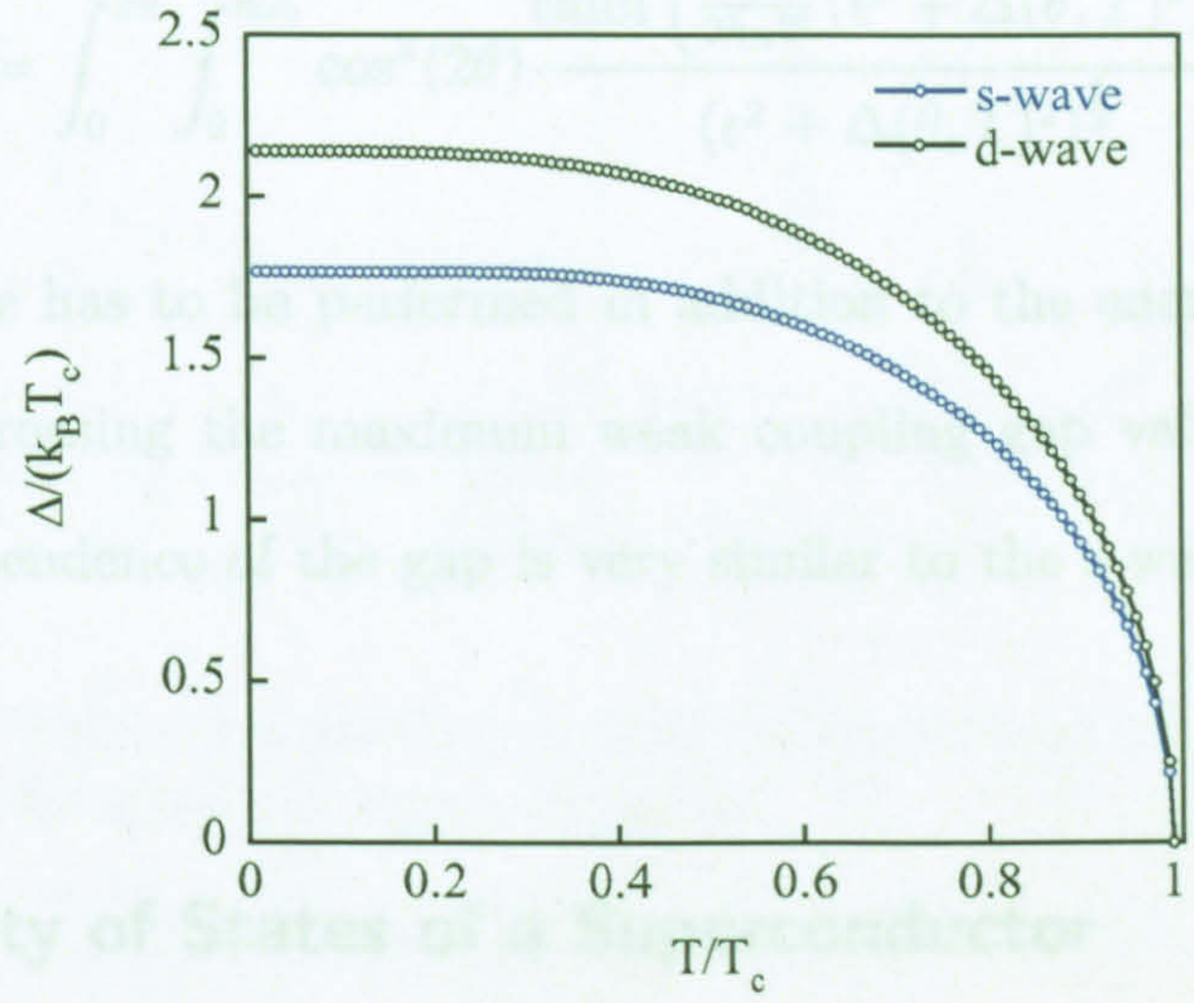

Figure 1.3: Temperature dependence of the gap for both s-wave and d-wave superconductors.

This can be solved numerically when combined with equation 1.5 to give the temperature dependence of the gap in the superconducting state. The temperature dependence of an s-wave superconductor is shown in Figure 1.3 The maximum gap value is $1.764\,k_BT_c$ as shown in equation 1.7. The temperature dependence of the gap is very shallow close to zero temperature as not many quasiparticles are thermally excited but close to T_c the gap changes very quickly.

1.6.2 d-wave Superconductor

In this thesis a d-wave superconductor refers to a superconductor with a gap function of the form $\Delta(\theta)=\Delta_0\cos(2\theta)$. This gap function is for a d-wave scenario on a quasi-2D surface, which is the case for the cuprates and most likely for the organic

superconductors. This gap function modifies equation 1.10 in the following way

$$\frac{1}{N(\epsilon_f)V} = \int_0^{2\pi}\int_0^{\hbar\omega_c} \cos^2(2\theta)\frac{\tanh\left(\frac{1}{2k_BT}\left(\epsilon^2+\Delta(\theta,T)^2\right)^{\frac{1}{2}}\right)}{\left(\epsilon^2+\Delta(\theta,T)^2\right)^{\frac{1}{2}}}d\epsilon d\theta. \tag{1.11}$$

An angle average has to be performed in addition to the energy integral. This has the effect of increasing the maximum weak coupling gap value to $2.14\,k_BT_c$. The temperature dependence of the gap is very similar to the s-wave case as is shown in Figure 1.3.

1.6.3 Density of States of a Superconductor

As there is a one to one correspondence between quasiparticles in the superconducting state and quasiparticles in the normal state, the superconducting density of states is related to the normal density of states by

$$N_s(E)dE = N(\epsilon)d\epsilon, \tag{1.12}$$

where E is the superconducting quasiparticle energy and is given by equation 1.1, $N_s(E)$ is the superconducting density of states, $N(\epsilon)$ is the normal state density of states and ϵ is the normal state quasiparticle energy. The normal state density of states can be assumed to be constant close to the Fermi energy ϵ_f. Therefore for an s-wave superconductor, the superconducting density of states is given by

$$N_s(E) = N(\epsilon_f)\frac{d\epsilon}{dE} = N(\epsilon_f)\frac{E}{\left(E^2-\Delta^2\right)^{\frac{1}{2}}} \tag{1.13}$$

for energies above Δ and zero below. This is shown in Figure 1.4.

For a d-wave superconductor, equation 1.12 still applies but an angle average is

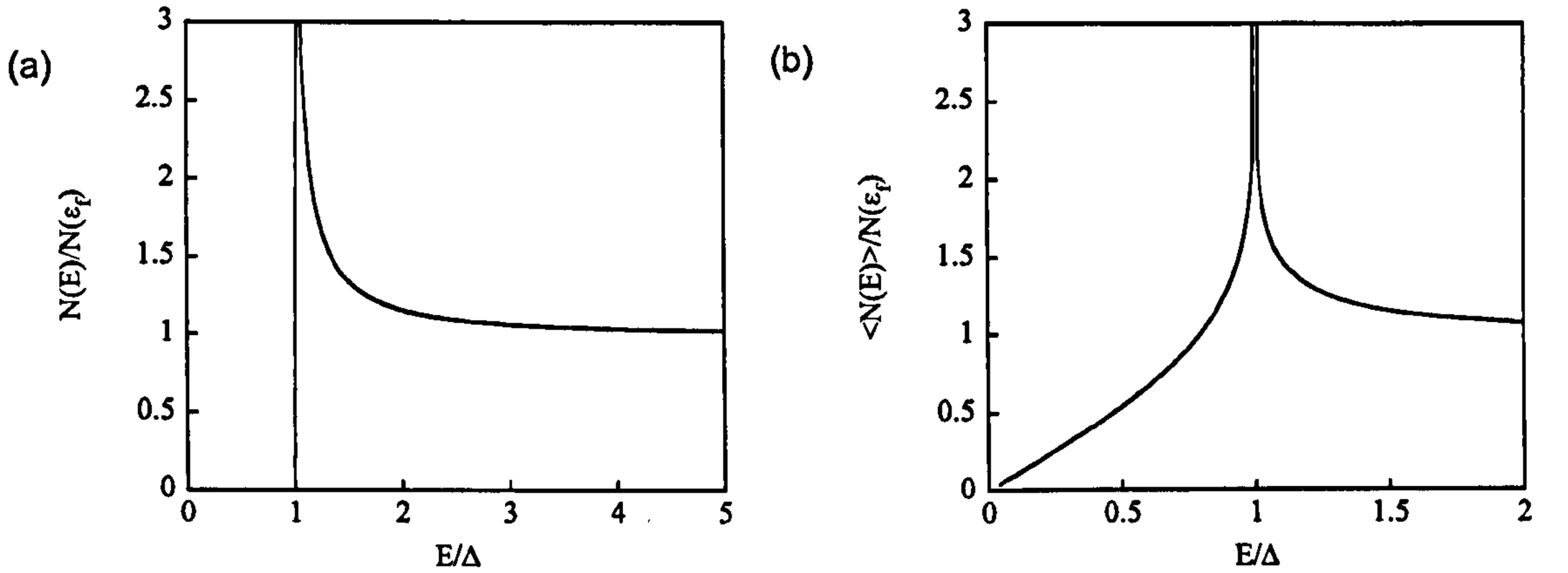

Figure 1.4: (a) Density of states for an isotropic superconductor. (b) Angle averaged density of states for a d-wave superconductor.

required:

$$\frac{< N_s(E) >}{N(\epsilon_f)} = \frac{1}{2\pi} \int_0^{2\pi} \frac{E}{(E^2 - \Delta(\theta)^2)^{\frac{1}{2}}} d\theta \tag{1.14}$$

This integral can be solved using elliptical functions. At low energies $E \ll \Delta_0$, the density of states can be expanded as

$$\frac{< N_s(E) >}{N(\epsilon_f)} \simeq \frac{E}{\Delta} + \frac{1}{4}\left(\frac{E}{\Delta}\right)^3 + \ldots . \tag{1.15}$$

The density of states is linear at low energies in a d-wave superconductor and is shown in Figure 1.4.

1.6.4 Alpha Model

Strong coupling superconductors are not taken into account in the BCS theory, and the Eliashberg theory is quite involved. The alpha model is a useful approximation in dealing with a strong coupling superconductor [40]. The alpha model assumes a BCS temperature dependence of the gap with a modified value at zero temperature.

Therefore

$$\Delta^{s,d}(T) = \frac{\alpha^{s,d}}{\Delta^{s,d}_{BCS}(0)} \Delta^{s,d}_{BCS}(T). \tag{1.16}$$

The superscripts s and d indicate that this applicable to s-wave or d-wave models. The subscript BCS indicates the weak coupling BCS gap. A value for α of 1 indicates a BCS weak coupling superconductor. This approximation can be used to interpret results on strong coupling superconductors without knowledge of the detailed microscopic situation.

1.7 Heat Capacity of Superconductors

1.7.1 Heat Capacity in the Normal State

The heat capacity of a simple metal consists of a phonon term and an electronic term. The electronic term can be derived from a simple free electron model. The electronic heat capacity is related to the density of states at the Fermi level $N(\epsilon_f)$ by

$$C_e = \frac{\pi^2}{3} k_B^2 N(\epsilon) T = \gamma T, \tag{1.17}$$

γ is called the Sommerfeld coefficient and in a real metal is related to the effective mass of the electrons through the density of states at the Fermi level. The phonon term is more complicated to calculate as in principle it would require an accurate knowledge of the phonon structure of the material. Debye assumed a simple model with a characteristic temperature Θ_D (the Debye Temperature) at which all phonon modes are excited and below which some fraction are frozen out. The phonon specific

heat at low temperatures is then given by

$$C_{ph} = 234\left(\frac{T}{\Theta_D}\right)^3 nk_B = \beta T^3, \tag{1.18}$$

where n is a number density of phonons. Combining the two contributions leads to

$$C = C_e + C_{Ph} = \gamma T + \beta T^3. \tag{1.19}$$

Therefore a plot of C/T versus T^2 at low temperatures produces a straight line with intercept γ and gradient β. This is the standard method used to determine γ for a metal.

1.7.2 Heat Capacity in the Superconducting State

The heat capacity in the superconducting state can be calculated in two different ways. The first method calculates the entropy in the superconducting state, this method is followed in [32]. The superconducting transition is a second order transition. The entropy of a fermion gas is

$$S = -2k_B \sum_{\mathbf{k}} [1-f]\ln(1-f) + f\ln f, \tag{1.20}$$

where f is the fermi function,

$$f = \frac{1}{1+e^{\frac{E-\epsilon_f}{k_b T}}}, \tag{1.21}$$

E is the quasiparticle energy in the superconducting state (equation 1.1) and ϵ_f is the Fermi level. This equation is a sum over all k states. The heat capacity can now be

calculated as

$$\begin{aligned} C &= T\frac{dS}{dT} \\ &= -2k_BT\sum_{\mathbf{k}}\frac{df}{dT}\ln\left(\frac{f}{1-f}\right) \\ &= 2\sum_{\mathbf{k}}E\frac{df}{dT} \\ &= 2\sum_{\mathbf{k}}E\frac{e^{\frac{E}{k_BT}}}{\left(1+e^{\frac{E}{k_BT}}\right)^2}\left(\frac{-2E}{kT^2}+\frac{1}{k_BT}\frac{dE}{dT}\right) \\ &= -\frac{2}{T}\sum_{\mathbf{k}}\frac{df}{dE}\left(E^2-\frac{T}{2}\frac{d\Delta^2}{dT}\right). \end{aligned} \tag{1.22}$$

These two terms can then be used to consider the difference in heat capacity between the normal and superconducting states. In the normal state, Δ is zero and the second term in equation 1.22 is zero. The remaining term is simply the normal state electronic heat capacity which can be derived by converting the $\mathbf{k}$ sum into an integral over energies.

$$\begin{aligned} C_{\Delta=0} &\simeq -\frac{2}{T}\sum_{\mathbf{k}}\frac{df}{d\epsilon}\epsilon^2 \\ &= \frac{2}{kT^2}\int_0^\infty\frac{\epsilon^2e^{\frac{\epsilon}{k_BT}}}{\left(1+e^{\frac{\epsilon}{k_BT}}\right)^2}N(\epsilon_f)d\epsilon \\ &= 2N(\epsilon_f)k^2T\int_0^\infty\frac{e^x}{\left(1+e^x\right)^2}x^2dx \\ &= C_e=\frac{\pi^2}{3}k_B^2N(\epsilon_f)T=\gamma T. \end{aligned} \tag{1.23}$$

This is because the first term is due to thermal population of energy levels. At T_c, the difference between the normal state and the superconducting state is entirely due to the second term. Just above T_c the second term is zero and at T_c the second term has a value associated with $d\Delta^2/dT$. If the weak coupling gap form for the gap is

assumed (as shown in Figure 1.3) then this jump is

$$\frac{\Delta C}{\gamma T_c} = 1.43\ . \tag{1.24}$$

If the superconductor is not in the weak coupling limit, then $d\Delta^2/dT$ is larger and the jump is larger. Therefore the jump in specific heat at the transition temperature can be used to measure the coupling strength.

In order to analyse the low temperature behaviour of the superconductor another way of writing the heat capacity is to use the internal energy. The internal energy represents all the energy contained within the system as the kinetic and potential energies of the particles. The internal energy can be calculated by summing over all particle states and associated energies which for fermions can be written as an integral over all energies. This integral could be obtained from equation 1.20,

$$\begin{aligned} U &= \int_{\infty}^{\infty} Ef(E)N(E)dE \\ &= 2N(\epsilon_f)\int_{\Delta}^{\infty} \frac{E^2 dE}{\sqrt{(E^2-\Delta^2)}(e^{\frac{E}{k_BT}}+1)}. \end{aligned} \tag{1.25}$$

At low temperatures, T$\ll \Delta$ then f(E)$\sim$e$^{-\frac{E}{k_BT}}$ and assuming the majority contribution to the integral is at energies around Δ where the density of states is peaked then the integral can be written

$$\begin{aligned} U &= \frac{2N(\epsilon_f)}{\sqrt{2\Delta}}\int_{\Delta}^{\infty} \frac{E^2 e^{-\frac{E}{k_BT}}dE}{\sqrt{(E-\Delta)}} \\ &= \sqrt{2}N(\epsilon_f)\Delta^2\int_{1}^{\infty} \frac{x^2 e^{-\frac{\Delta x}{k_BT}}dx}{\sqrt{(x-1)}} \\ &= \sqrt{2}N(\epsilon_f)\Delta^2\sqrt{\pi}\left(\frac{\Delta}{k_BT}\right)^{\frac{-5}{2}}\left(\left(\frac{\Delta}{k_BT}\right)^2+\left(\frac{\Delta}{k_BT}\right)+\frac{3}{4}\right)e^{-\frac{\Delta}{k_BT}}. \end{aligned} \tag{1.26}$$

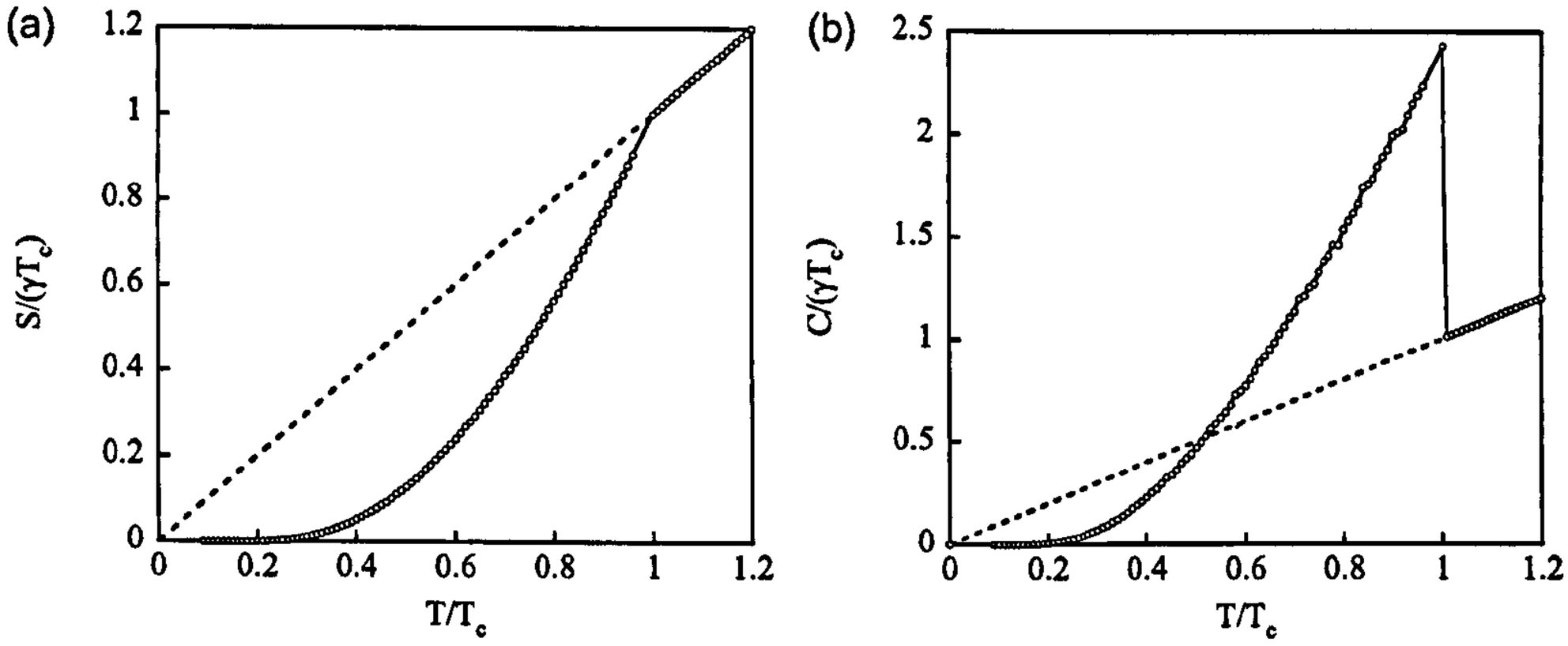

Figure 1.5: (a) Entropy versus temperature for an s-wave superconductor, normalised to the normal state value and T_c. (b) Heat Capacity versus temperature for an s-wave superconductor, normalised to the normal state value and T_c.

The heat capacity is related to the internal energy by

$$C = \frac{dU}{dT}. \tag{1.27}$$

Combining equations 1.26 and 1.27 and taking only the highest order terms gives

$$\frac{C}{\gamma T_c} \simeq \frac{3}{\pi^2 k_B T_c}\sqrt{\frac{2\pi\Delta^5}{(k_B T)^3}}e^{-\frac{\Delta}{k_B T}}. \tag{1.28}$$

The low temperature behaviour of the heat capacity in an s-wave superconductor is exponentially activated. This equation is only a low temperature approximation. To obtain the whole heat capacity curve, numerical calculations are required. In the calculation the heat capacity is found by numerically differentiating the entropy at each temperature The result of this calculation is shown in Figure 1.5. The entropy in the superconducting state is equal to the entropy in the normal state at T_c as is expected from a second order phase transition. The jump at T_c is the same as given in equation 1.24.

For a d-wave superconductor, the low temperature behaviour can be found using the low energy approximation for the density of states (equation 1.15) and the equation for internal energy (equation 1.25),

$$\begin{aligned} U &\simeq \frac{2N(\epsilon_f)}{\Delta_0}\int_0^\infty \frac{E^2 dE}{e^{\frac{E}{k_B T}}+1} \\ &= \frac{2N(\epsilon_f)}{\Delta_0}(k_B T^3)\int_0^\infty \frac{x^2 dx}{e^x+1} \\ &= \frac{3\zeta(3)N(\epsilon_f)(k_B T^3)}{\Delta_0}, \end{aligned} \tag{1.29}$$

where $\zeta(3)$ is the Riemann zeta function derived from the integral and equal to 1.202. The low temperature heat capacity for a d-wave superconductor is then

$$\frac{C}{\gamma T_c} = \frac{27\zeta(3)}{\pi^2}\frac{k_B T_c}{\Delta_0}\left(\frac{T}{T_c}\right)^2. \tag{1.30}$$

The heat capacity of a d-wave superconductor follows a quadratic temperature dependence at low temperature. Numerical calculations were performed using the entropy of a d-wave superconductor. The results of these calculations are shown in Figure 1.6.

Examining the whole heat capacity curve of a real superconductor does not make differentiating between gap symmetries easy. In a real superconductor, fluctuations broaden the transition and this can make the difference at higher temperatures difficult to observe. Figure 1.7 shows the whole curves obtained from the numerical calculations for the s-wave case and the d-wave case. The low temperature data are expanded and plotted as C/T. Looking at the data in this way makes it much easier to differentiate between s-wave and d-wave models.

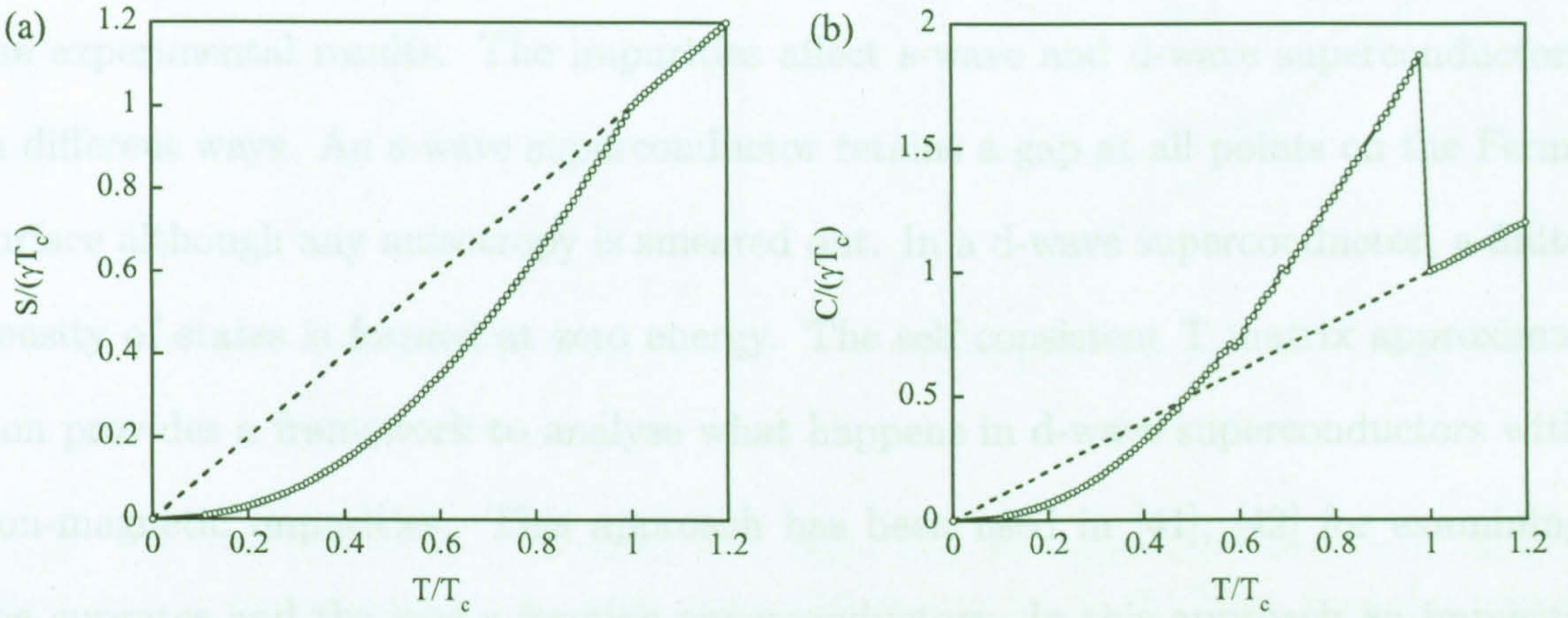

Figure 1.6: (a) Entropy versus temperature for a d-wave superconductor, normalised to the normal state value and T_c. (b) Heat Capacity versus temperature for a d-wave superconductor, normalised to the normal state value and T_c.

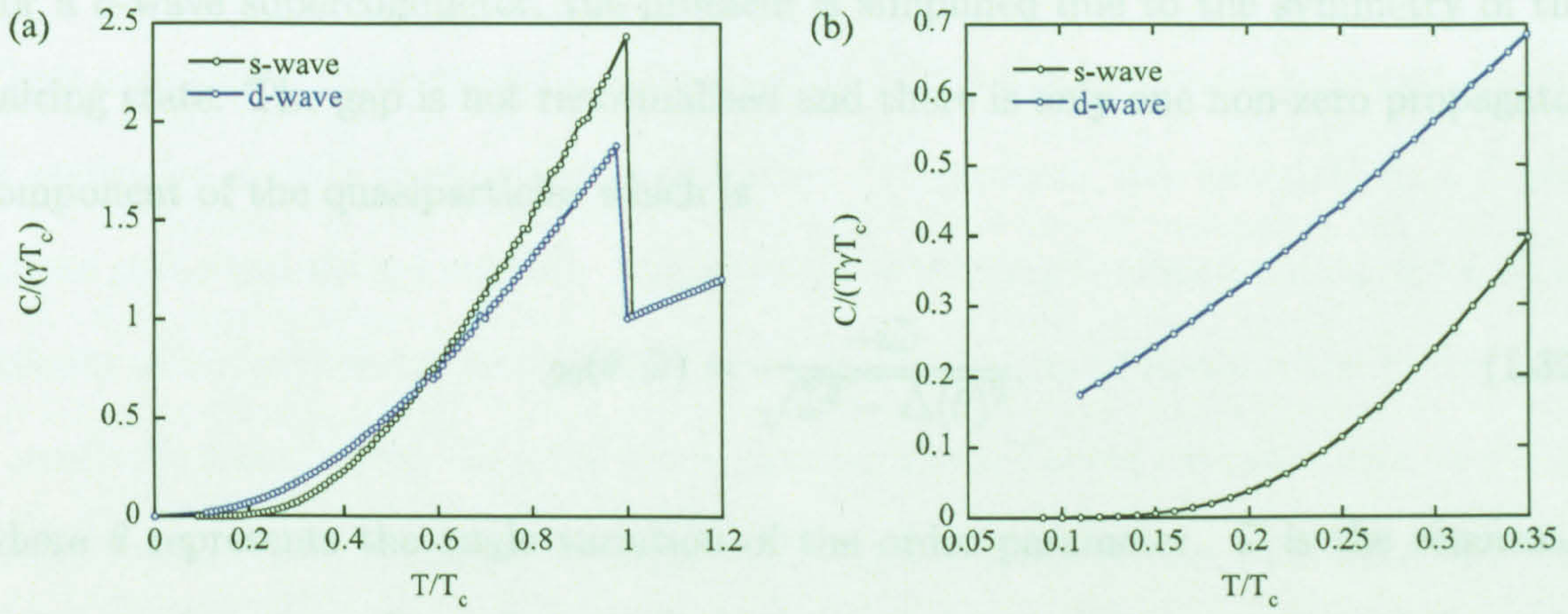

Figure 1.7: (a) The s-wave and d-wave heat capacity curves over the whole temperature range. (b) The s-wave and d-wave heat capacities plotted as C/T versus T.

1.7.3 Impurity Effects

There are often impurities present in samples of superconductors and these can affect the experimental results. The impurities affect s-wave and d-wave superconductors in different ways. An s-wave superconductor retains a gap at all points on the Fermi surface although any anisotropy is smeared out. In a d-wave superconductor, a finite density of states is formed at zero energy. The self consistent T matrix approximation provides a framework to analyse what happens in d-wave superconductors with non-magnetic impurities. This approach has been used in [41], [42] for examining the cuprates and the heavy fermion superconductors. In this approach an impurity concentration n_i is assumed and related to Γ a scattering rate parameter by

$$\Gamma = \frac{n_i n}{\pi N(\epsilon_f)}, \tag{1.31}$$

where n is the electron density and $N(\epsilon_f)$ is the density of states at the Fermi level. The full treatment of the T matrix approximation is complex and explained in [42]. For a d-wave superconductor, the problem is simplified due to the symmetry of the pairing state. The gap is not renormalised and there is only one non-zero propagator component of the quasiparticles which is

$$g_0(\theta, \tilde{\omega}) = \frac{-i\tilde{\omega}}{\sqrt{\tilde{\omega}^2 - \Delta(\theta)^2}}, \tag{1.32}$$

where θ represents the angle variation of the order parameter. $\tilde{\omega}$ is the renormalized particle energy, $\tilde{\omega}$=ω-Σ_0, and Σ_0 is the associated self energy derived from the scattering rate Γ and the scattering phase shift,

$$\Sigma_0(\tilde{\omega}) = \frac{\Gamma g_0(\tilde{\omega})}{c^2 - g_0(\tilde{\omega})^2} \tag{1.33}$$

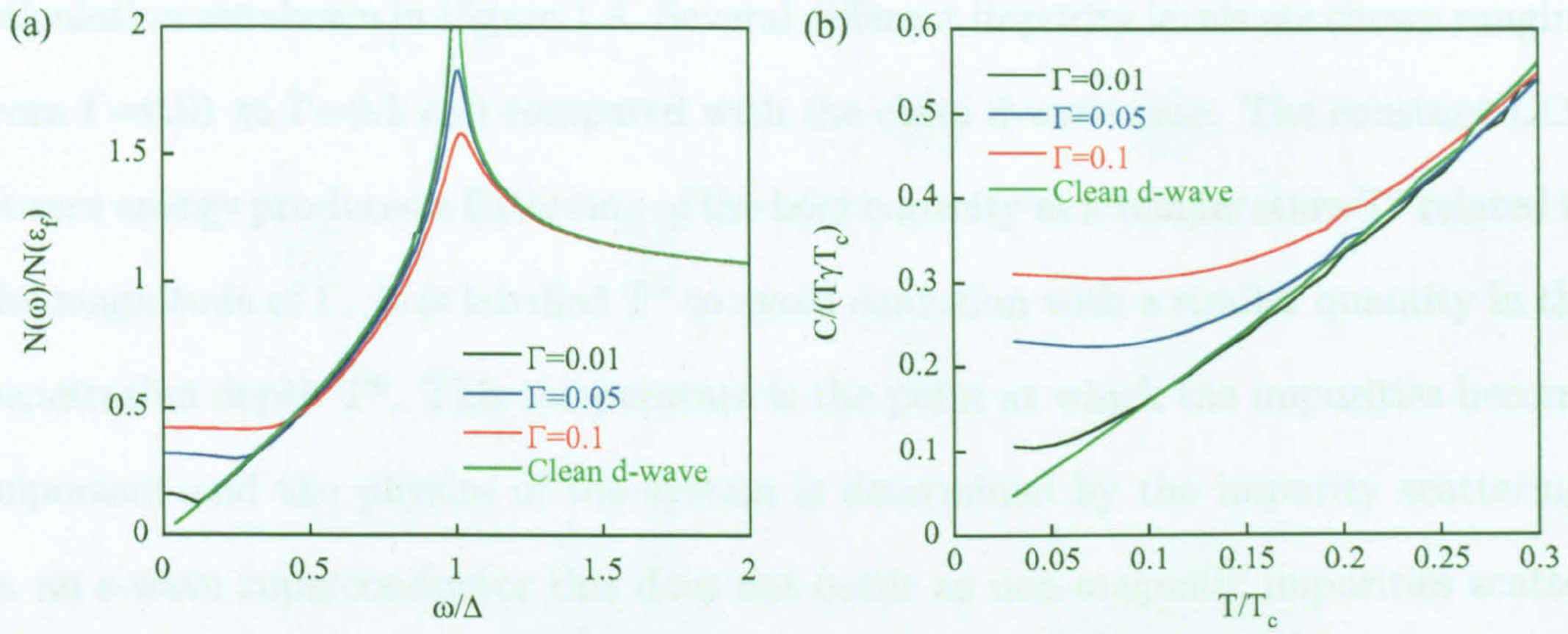

Figure 1.8: (a) The density of states of a dirty d-wave superconductor with various amounts of impurities, these results are consistent with [41] (b) Heat capacity versus temperature for a dirty d-wave superconductor with various amounts of impurities.

where c is a parameter which represents the scattering phase shift. If $c \ll 1$ then the scattering is strong (unitary limit) and if $c \gg 1$ then the scattering is weak (Born approximation). The density of states is simply

$$N(E) = -\Im(g_0(\widetilde{\omega})) \tag{1.34}$$

These equations can be solved self consistently to calculate an angle averaged density of states for a dirty d-wave superconductor. To perform this calculation, a Γ was chosen and c was always set to 0. Therefore the scattering is always strong and a small amount of impurities can have a large effect on the density of states while having only a small effect on T_c [43]. To solve the equations, the self energy is calculated and then used to renormalise the particle energy. The angle averaged Green's function can then be used to find the self energy which is then checked for consistency (see appendix for detailed description of the calculation). Once the calculation has converged, then the density of states can be calculated. The effect of impurities on the heat capacity can also be calculated using the entropy method described above. The results of the

calculation are shown in Figure 1.8. Several different impurity levels are shown ranging from Γ=0.01 to Γ=0.1 and compared with the clean d-wave case. The constant DOS at zero energy produces a flattening of the heat capacity at a temperature T° related to the magnitude of Γ. It is labelled T° to avoid confusion with a similar quantity in the penetration depth T*. This temperature is the point at which the impurities become important and the physics of the system is determined by the impurity scattering. In an s-wave superconductor this does not occur as non-magnetic impurities scatter electrons onto portions of the Fermi surface with the same phase conserving the pairs. The T* measured by the penetration depth is related to T° as discussed below.

1.8 Angle Dependent Heat Capacity

1.8.1 Doppler Shift Method

The variation of the density of states with applied field angle in a nodal superconductor was first proposed by Volovik [17]. Volovik realised that in a fully gapped superconductor the low temperature specific heat in the vortex state is mostly determined by the normal state quasi-particles in the vortex cores. In a simple picture the heat capacity is linear in field as it is proportional to the number of vortices. For a nodal superconductor, Volovik showed that the normal state quasi-particles in the vortex core are dominated by the normal state quasi-particles in the nodes. This leads to a $H^{\frac{1}{2}}$ field dependence in a d-wave superconductor and field angle dependence of the density of states. Vekhter [18] expanded these arguments for the case of a d-wave, quasi-2D superconductor. Vekhter uses an argument which shows there is an energy shift of normal state nodal quasiparticles due to the moving supercurrent. This is referred to as the Doppler shift method as the energy shift is derived from moving frames compared to a stationary frame of reference. When the field is aligned along

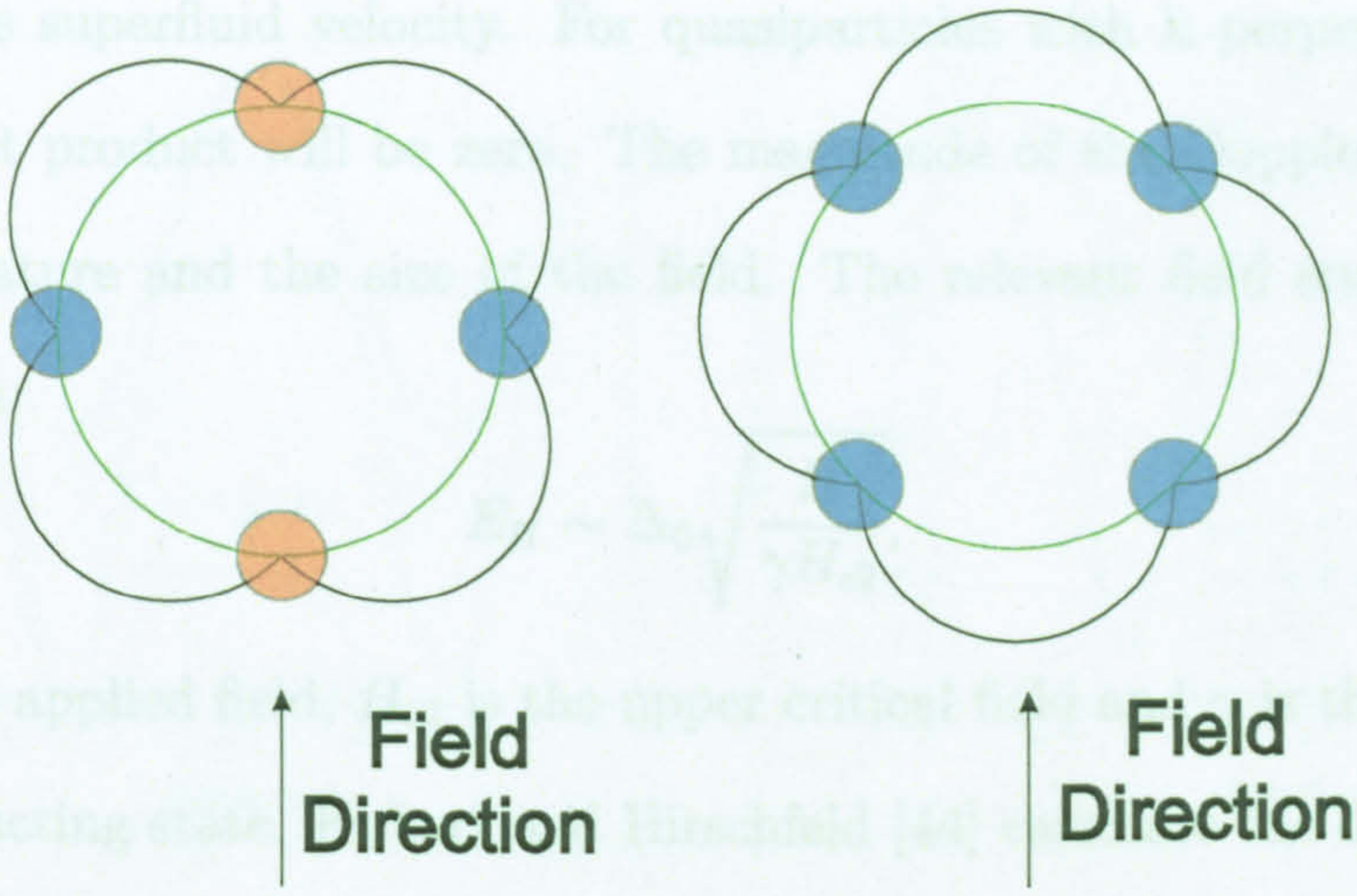

Figure 1.9: Diagram illustrating the contributions to Doppler energy shift from the different nodes. The green circle represents the Fermi surface, the black line represents the order parameter. Nodes in blue represent contributions to the energy shift, while nodes in orange represent nodes that do not contribute to the energy shift.

two nodes then the normal state quasi-particles associated with those nodes do not contribute to this effect as the field is parallel to the velocity of these quasiparticles, in contrast when the field is applied along the antinode all four nodes contribute. Therefore there is a maximum in the density of states when the field is applied along an antinode. This is illustrated in Figure 1.9. This can also be seen when quantifying the energy shift. Considering a constant magnetic field acting on a normal state particle the kinetic energy operator can be expanded as

$$\frac{1}{2m}\left(-i\hbar\nabla - 2e\mathbf{A}\right)^2 = \frac{\hbar^2}{2m}\nabla^2 + 2\frac{ie\hbar}{m}\mathbf{A}\cdot\nabla + \frac{2e^2}{m}\mathbf{A}\cdot\mathbf{A}. \tag{1.35}$$

Using the London equations the energy shift from the supercurrent can be obtained from the second term as $\mathbf{v_s} = \frac{\mathbf{A}e}{m}$ and $p = \hbar\mathbf{k}$, therefore the energy shift $\delta\omega$ is

$$\delta\omega \sim \mathbf{v_s}\cdot\hbar\mathbf{k}, \tag{1.36}$$

where $\mathbf{v_s}$ is the superfluid velocity. For quasiparticles with $\mathbf{k}$ perpendicular to the velocity the dot product will be zero. The magnitude of the Doppler shift depends on the temperature and the size of the field. The relevant field energy E_H [21] is calculated from

$$E_H \sim \Delta_0 \sqrt{\frac{H}{\gamma H_{c2}}}, \tag{1.37}$$

where H is the applied field, H_{c2} is the upper critical field and γ is the anisotropy of the superconducting state. Kubert and Hirschfeld [44] calculate the density of states based only on the quasi-particles in the nodal directions. They obtain

$$N(\omega) = \begin{cases} \frac{\omega}{\Delta_0}\left(1+\frac{1}{2x^2}\right), x > 1 \\ \frac{E_i}{\pi\Delta_0 x}\left[(1+2x^2)\arcsin(x) + 3x\sqrt{1-x^2}\right], x \leq 1. \end{cases} \tag{1.38}$$

E_i represents the energy shift associated with each pair of vortices ($E_1 = E_H|\sin(\pi/4-\theta)|$, $E_2 = E_H|\cos(\pi/4-\theta)|$) and x is ω/E_i. This simple formula has been shown to give reasonable agreement at low temperatures and fields with full numerical calculations of the Doppler energy shift [18]. Once the density of states is known then the heat capacity can be calculated as described in the previous section. Figure 1.10 shows the results of numerical calculations for parameters appropriate to the organic superconductors ($\Delta_0 \sim 3.06\, k_B T_c$, γ=18, H_{c2}=30T) at a field of 3 T. The size of the oscillation escalates rapidly below $0.1\, T_c$. These calculations offer an approximate magnitude of the oscillation but are subject to a lot of assumptions. They are only valid in the low field, low temperature regime as the vortex cores are assumed to be sufficiently far apart that no overlap occurs. The superconductor is assumed to be perfectly clean with no impurity bandwidth which would reduce the oscillation amplitude. No effects from the Fermi surface are included in this theory.

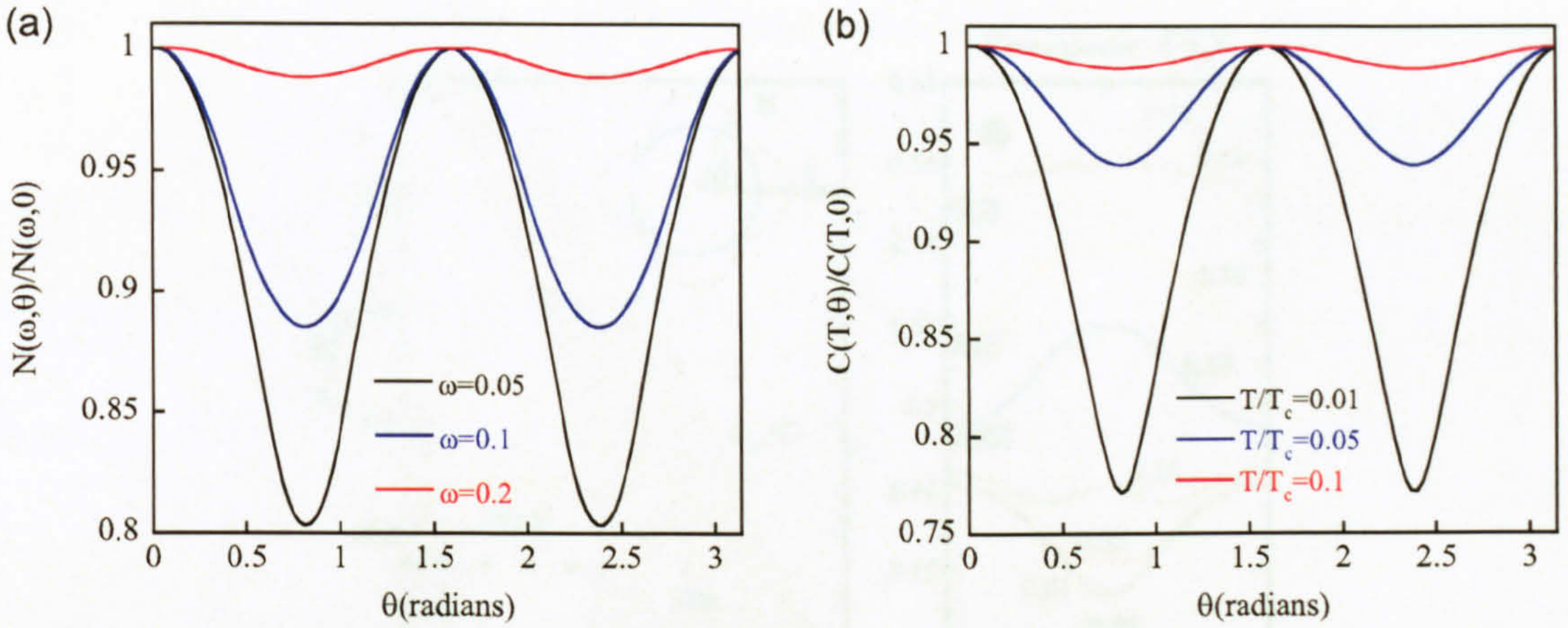

Figure 1.10: (a) The density of states of a d-wave superconductor as a function of in plane angle θ (b) Heat capacity as a function of in plane angle θ. Both calculated for the organic superconductors in this work in a field of 3 T. The values are normalised to the antinode value and θ is measured from the antinode.

1.8.2 More Sophisticated Theories

The Doppler shift method makes a lot of assumptions but is useful for simple calculations. Vorontsov [20], [45], [46] has used a full microscopic calculation over the whole field and temperature range. The effects of Fermi surface, impurities and quasiparticle scattering off vortices are included. The angle dependent heat capacity and thermal conductivity are calculated. The results show that at moderate fields the four-fold oscillation can change sign. There is a maximum in the heat capacity when the field is applied along the node. This could potentially lead to misinterpreted experimental results, however no clear evidence of this has been observed. Figure 1.11 shows the phase diagram for a superconductor with a cylindrical Fermi surface with a small quantity of impurities. At temperatures above $0.1\,T_c$ there is a sign change in the angle variation of the superconductor. However at low temperatures and fields the results are similar to the Doppler shift method with a reduced amplitude due to the impurities. The most recent theory by Nagai *et al* [47] does not make use of the Doppler shift approximation and takes into account Fermi surface geometry

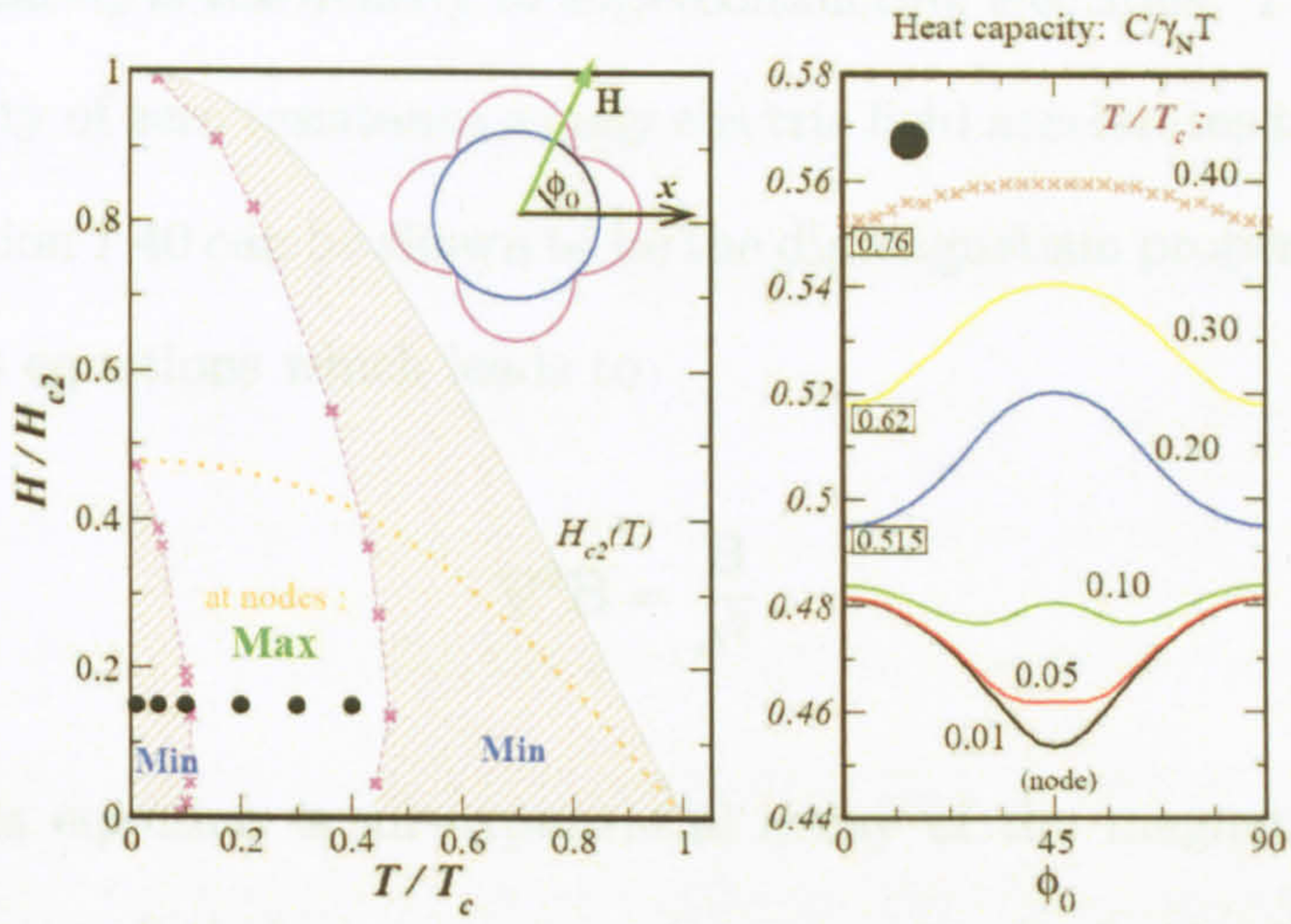

Figure 1.11: Phase diagram of the fourfold oscillation for a cylindrical Fermi surface in the presence of a small amount of impurities taken from [45].

and impurity scattering using other approximations. Qualitatively similar results are obtained for line nodes in a cylindrical Fermi surface.

1.9 Magnetic Properties of Superconductors

Meissner and Ochsenfeld [48] observed that a superconductor excludes all magnetic field, therefore a perfect superconductor has susceptibility χ of -1 and could be considered a perfect diamagnet. Superconductors in this state are described as being in the Meissner state. The description of the electrodynamics of a superconductor was produced by the London brothers [49]. They developed two equations which describe the supercurrent response (i.e the current of superconducting electrons) $\mathbf{J}_s$ to the electric field $\mathbf{E}$ and the magnetic field $\mathbf{B}$.

$$\mathbf{E} = \frac{\delta}{\delta t}(\Lambda \mathbf{J_s}) \tag{1.39}$$

$$\mathbf{B} = -\nabla \times (\Lambda \mathbf{J_s}), \tag{1.40}$$

where $\Lambda = \frac{m}{n_s e^2}$ and n_s is the density of superconducting electrons. The first equation 1.39 is the property of zero resistance as any electric field accelerates the supercurrent. The second equation 1.40 can be shown to be the diamagnetism property by combining it with Maxwell's equations which leads to

$$\nabla^2 \mathbf{B} = \frac{\mathbf{B}}{\lambda^2}. \tag{1.41}$$

A solution of this equation is an exponential decay of the magnetic field over the length scale λ. λ is called the magnetic penetration depth. In the London theory it is argued that λ changes with temperature settling on an absolute zero temperature value $\lambda(0)$, known as the absolute penetration depth,

$$\lambda(0) = \left(\frac{m}{\mu_0 n e^2}\right)^{\frac{1}{2}}. \tag{1.42}$$

Here n is the total density of electrons as at zero temperature all electrons are superconducting. This value of $\lambda(0)$ is a theoretical ideal and in practice impurities and non-local effects make this length longer. The penetration depth can change the measured susceptibility if it is long compared to the dimensions of the sample and consequently large parts of the sample are in the normal state. The measured susceptibility can also be modified by demagnetizing factors. When a field is expelled from a sample the field lines must redistribute (as $\nabla \cdot \mathbf{B} = 0$), this redistribution depends on sample geometry. For a long thin sample (e.g thin film) with the field applied along the long axis, there is essentially no change in the field lines and the demagnetising factor is zero. For a sphere the field lines are altered and there is a maximum field around the equator of the sphere, the demagnetising factor is 1/3 and the susceptibility is modified.

1.9.1 The Penetration Depth

The absolute length of the penetration depth is complicated to calculate as it depends on the exact Fermi surface topology and impurity effects. However the temperature dependence is set by the BCS gap equation in a similar manner to the heat capacity. The absolute penetration depth in the London picture is defined by equation 1.42. This equation involves m^*, the effective mass, and n_s the density of superconducting electrons (superfluid density). In a free electron model the values of m^* and n_s are trivial to calculate. In a real metal, these values are dependent on contributions from the Fermi surface. A semi-classical argument is invoked in [50], similar to the semi-classical transport model in metals. A more general form for the London penetration depth is found to be

$$\rho_{ij} = \frac{\mu_0 e^2}{4\pi^3\hbar}\oint dS_f \frac{\mathbf{v_i v_j}}{|v_f|} + 2\frac{\mu_0 e^2}{4\pi^3\hbar}\oint dS_f \frac{\mathbf{v_i v_j}}{|v_f|}\int_{-\infty}^{\infty}\frac{df}{dE}N(E)dE, \qquad (1.43)$$

where $\mathbf{v_f}$ is the Fermi velocity and the integral dS_F is over the Fermi surface. This equation is for the London penetration depth which does not include non-local effects or impurities. The first term is temperature independent and the second term contains the temperature dependence. This equation is useful for illustrating the factors which affect the penetration depth. However for examining the gap symmetry dependence of the penetration depth, it is easier to think of the isotropic case with all the details included in the absolute penetration depth.

1.9.2 Temperature Dependence of the Penetration Depth

To find the temperature dependence of the penetration depth and the superfluid density, the approach in [32] is followed. The equation for the penetration depth

assuming an isotropic Fermi surface is

$$\rho = \frac{\lambda(0)^2}{\lambda(T)^2} = 1 + 2\left(\int_{-\infty}^{\infty} N(E)\frac{df}{dE}dE\right), \tag{1.44}$$

where ρ is the superfluid density and $\lambda(0)$ is the absolute penetration depth. For an s-wave superconductor at low temperature $T \ll \Delta$ the penetration depth becomes

$$\frac{\Delta\lambda(T)}{\lambda(0)} = \sqrt{\frac{\pi\Delta}{2k_BT}}e^{\frac{-\Delta}{k_BT}}, \tag{1.45}$$

where $\Delta\lambda(T)$ is the change in penetration depth with temperature. The actual integral determines the superfluid density which is related to the penetration depth. The change in penetration depth is the experimentally accessible quantity as described in more detail in Chapter 4. For a d-wave superconductor, the low temperature limiting behaviour is

$$\frac{\Delta\lambda(T)}{\lambda(0)} = \frac{\ln(2)T}{\Delta}. \tag{1.46}$$

Using equation 1.45 for a d-wave superconductor is a simplification as the anisotropy of the gap and Fermi surface need to be taken into account together. The difference between d-wave superconductors and s-wave superconductors is shown in Figure 1.12 for the weak coupling limit. The low temperature dependence of the penetration depth and the superfluid density over the whole temperature range are shown.

1.9.3 Impurity Effects

As mentioned above the experimentally accessible quantity is $\Delta\lambda(T)$ rather than $\lambda(T)$. To find the superfluid density from $\Delta\lambda(T)$, $\lambda(0)$ must be known. The absolute penetration depth depends on the Fermi surface topology as described above and on impurities. Tinkham [32] uses a phenomenological approach based on the coherence

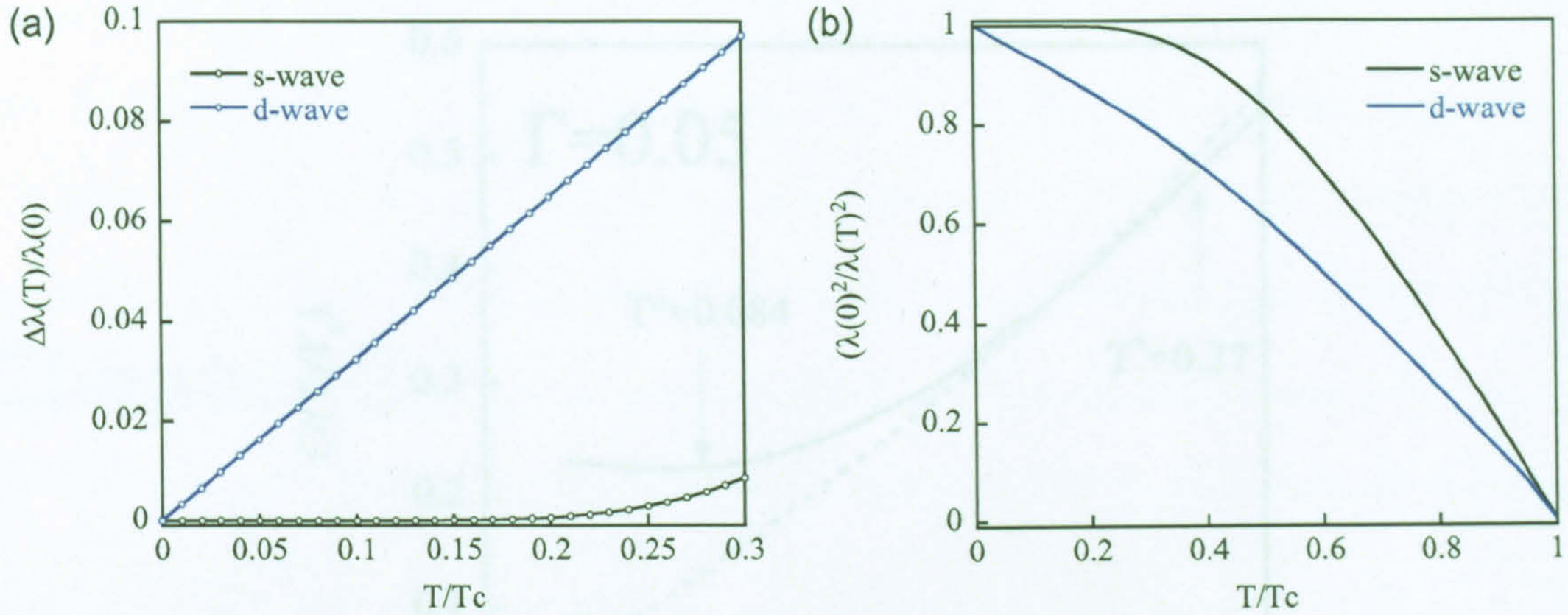

Figure 1.12: (a) The low temperature penetration depth for s-wave and d-wave superconductors calculated from the low temperature limiting behaviour. (b) Superfluid density over the whole temperature range calculated for s-wave and d-wave superconductors.

length ξ and the mean free path l of the superconductor. The effective penetration depth $\lambda_{eff}(T)$ is then

$$\lambda_{eff}(T) = \lambda(T)\left(1 + \frac{\xi}{l}\right)^{\frac{1}{2}}. \tag{1.47}$$

The coherence length in this equation has also been modified by impurities. The effect of impurities always makes $\lambda(T)$ longer. Measurements to determine $\lambda(0)$ are described in Chapter 4.

As well as modifying the length scale of λ, impurities can have an effect on the temperature dependence of λ [43]. The same theoretical framework as described in section 1.7.3 is used to determine the low temperature penetration depth of a d-wave superconductor. The density of states is the same as shown in Figure 1.8. The low temperature penetration is then modified and is approximately described by

$$\Delta\lambda(T) = \frac{aT^2}{T + T^*}, \tag{1.48}$$

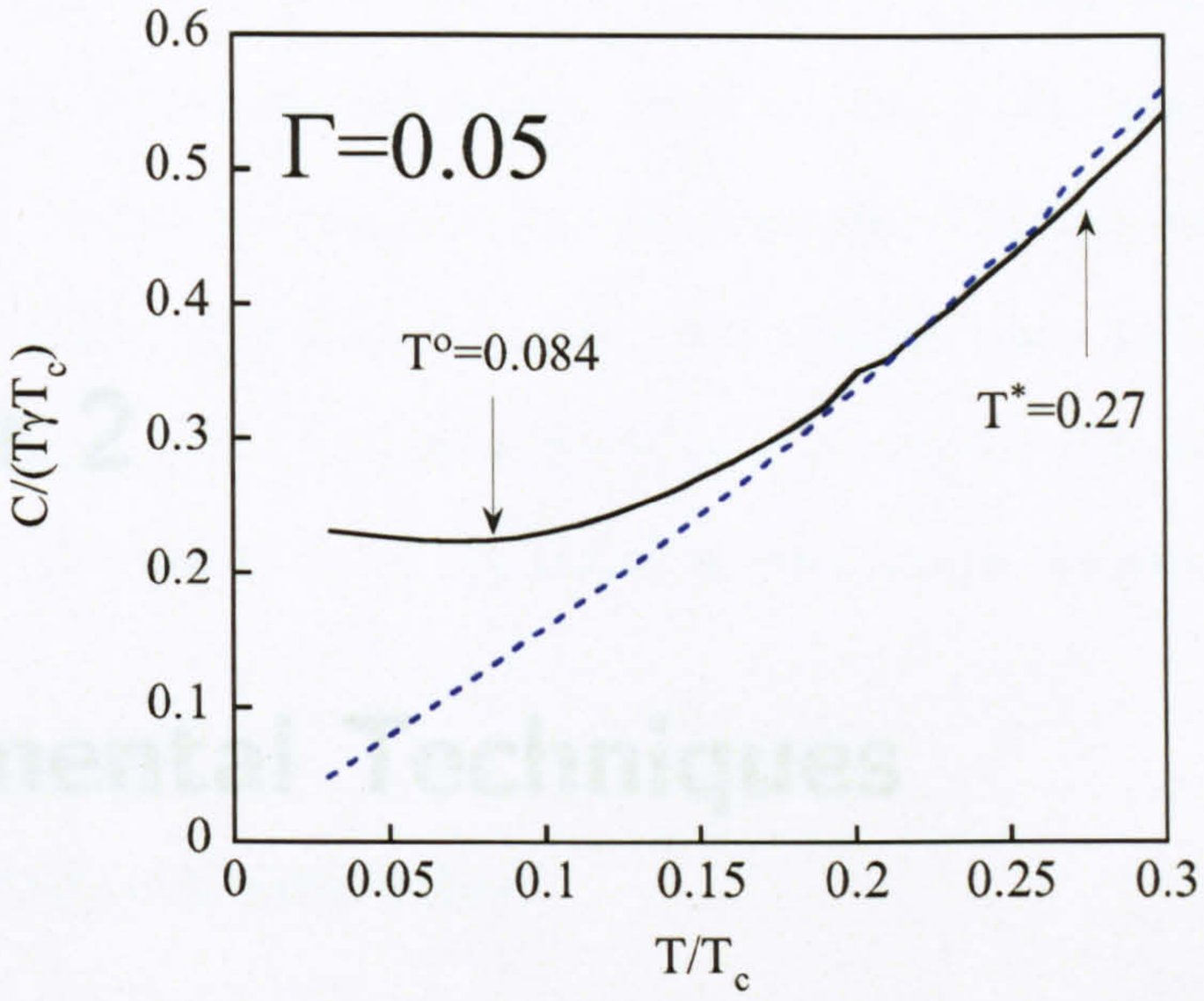

Figure 1.13: Figure showing the heat capacity of a dirty d-wave superconductor with Γ=0.05. T° and T^{*} are shown by the arrows, the dashed line is the clean d-wave case and T^{*} occurs when the dirty heat capacity has not begun to deviate from the clean case.

where T^{*} is the crossover temperature due to the impurities. T^{*} is found to be [43]

$$T^{*} \sim 0.83\,(\Gamma\Delta_0)^{\frac{1}{2}}\,. \tag{1.49}$$

Examining the heat capacity calculations from section 1.7.3 shows that the point at which C/T versus T goes flat T° is approximately 4 times smaller than the calculated T^{*} from the penetration depth. This is shown in Figure 1.13. Measurements on a dirty d-wave superconductor may observe the impurity effect in the penetration depth but not the heat capacity.

Chapter 2

Experimental Techniques

2.1 Heat Capacity Techniques

Measurements of heat capacity can be difficult to perform accurately, especially when measuring small samples. High quality single crystal samples of superconductors are often small $\sim 100\,\mu$g and consequently care must be taken to minimise the stage heat capacity (called the addenda) and the thermal link to the bath.

2.1.1 Adiabatic Calorimetry

Continuous heating techniques are a common way to measure the heat capacity. The sample is placed on a stage which is very well thermally isolated from the thermal bath. A constant power P is applied to the stage and the rate of heating is related to the heat capacity by equation 2.1.

$$, \frac{dT}{dt} = \frac{P}{C}. \tag{2.1}$$

Where C is the heat capacity of the stage and the sample. The addenda must be carefully measured in order to subtract from the measured sample plus stage heat

capacity. Care must be taken to minimise the addenda. There must be essentially zero thermal contact between the sample stage and the bath, however this can be a problem when cooling the setup to low temperature. This can be overcome with exchange gas, but then this must be thoroughly pumped away to keep the thermal conduction due to gas low. A radiation shield must be employed to stop heat transfer by radiation and this has to be at the same temperature as the sample in order not to cause errors.

2.1.2 Relaxation Calorimetry

Relaxation calorimetry is a common technique at low temperatures. The sample and stage are thermally isolated from the bath. A set power P is applied to the sample and it reaches equilibrium at some temperature T_0 which is ΔT_0 above the bath temperature T_b. The power is then switched off and the sample exponentially relaxes to the bath temperature,

$$\Delta T = \Delta T_0 e^{\frac{-t}{\tau}}, \tag{2.2}$$

where τ is the thermal time constant and is equal to C/κ_b, C is the heat capacity of the sample and κ_b is the thermal conductivity between the sample and the bath. Once again the addenda must be accurately measured and subtracted from the measured total heat capacity. An accurate knowledge of κ_b is also required to calculate the heat capacity. The time constant of the setup can be tuned by changing the thermal conductivity between the stage and bath, making this technique appropriate for a large range of sample sizes. The internal time constants of the calorimeter must all be smaller than the measured τ otherwise a 'tau-2 effect' will occur where the sample temperature is decoupled from the thermometer temperature. In the limit that τ becomes very long, then this technique becomes the adiabatic technique described

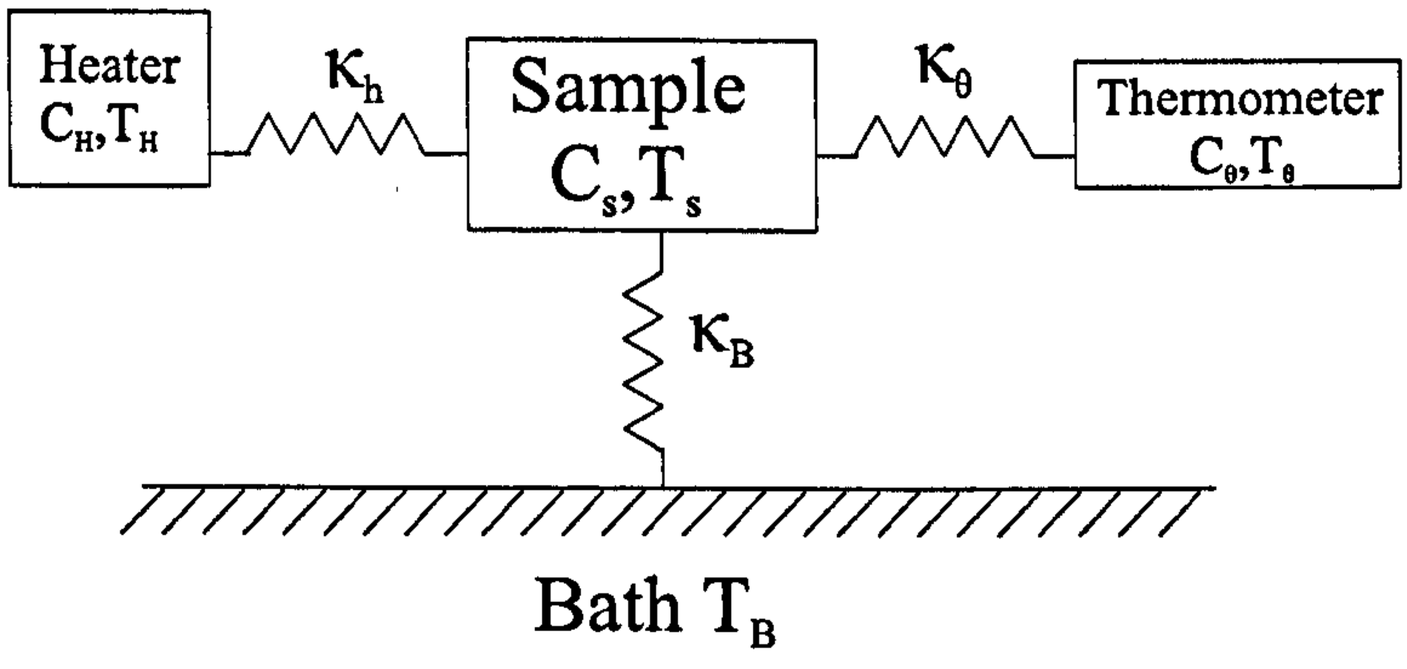

Figure 2.1: Diagram of the thermal model used by Sullivan and Seidal. The sample with heat capacity C_s and temperature T_s is thermally connected to the bath κ_B, the heater κ_h and the thermometer κ_θ. The heater and thermometer have their own heat capacities C_h and C_θ and their own temperatures T_h and T_θ.

above.

2.1.3 AC Calorimetry

Sullivan and Seidel developed a theory to describe a modulation technique to measure the heat capacity using the thermal diagram shown in 2.1. A heating ac power P with frequency ω is applied to the sample which is thermally isolated from the bath. This causes the sample to heat up by a constant temperature T_{dc} plus an oscillating temperature T_{ac}. The heat capacity is related to T_{ac} by

$$T_{ac} = \frac{P}{2\omega C}\cos(\omega t + \delta) f(\omega), \tag{2.3}$$

where C is the heat capacity of the sample and the addenda. $f(\omega)$ is a function which can be tuned to be $\sim$1 with an appropriate choice of frequency and depends on the internal time constants of the system. The phase shift δ depends on the details of the system but in an ideal system is π. The thermal model used by Sullivan and Seidel is shown in Figure 2.1.

2.2 Bare Chip Calorimeter

2.2.1 Construction

In this thesis a bare chip calorimeter was used to measure the heat capacity at low temperatures. This design was developed by Owen Taylor [51] (includes the manufacturing process). The calorimeter has been used to make accurate measurements of small samples ($\sim$100 μg) down to temperatures of 1.3 K. The angular dependence of the heat capacity due to the gap is an effect which is largest at low temperature and consequently this work extended the operating temperature of the calorimeter down to 0.3 K. The bare chip calorimeter consists of a bare chip Cernox thermometer suspended on a copper ring by silver coated glass fibres. The silver provides electrical contact to the Cernox which is used as a heater and a thermometer. The glass provides good mechanical support with a low thermal conductivity. The glass fibres have a diameter of $\sim$25 μm and the silver has a thickness of $\sim$ 0.1 μm. Using the Cernox film as a thermometer and a heater reduces the addenda enabling small samples to be measured. The low thermal conductivity of the glass fibres ensures the time constant of the system is the correct length. The sample is connected to the bare chip using Apiezon N type grease which has good thermal conductivity at low temperature. The bare chip can be used to measure heat capacity by two methods: long relaxation calorimetry and AC calorimetry.

2.2.2 Long Relaxation Calorimetry

Long Relaxation Calorimetry is a variation on the conventional relaxation technique developed by Junod and Wang [52], [53]. A large DC power $P^{\uparrow}$ is applied to the chip, causing the temperature to rise by between 20 % and 40 % of the bath temperature. A smaller power $P^{\downarrow}$ is then applied and the sample relaxes to close to the bath

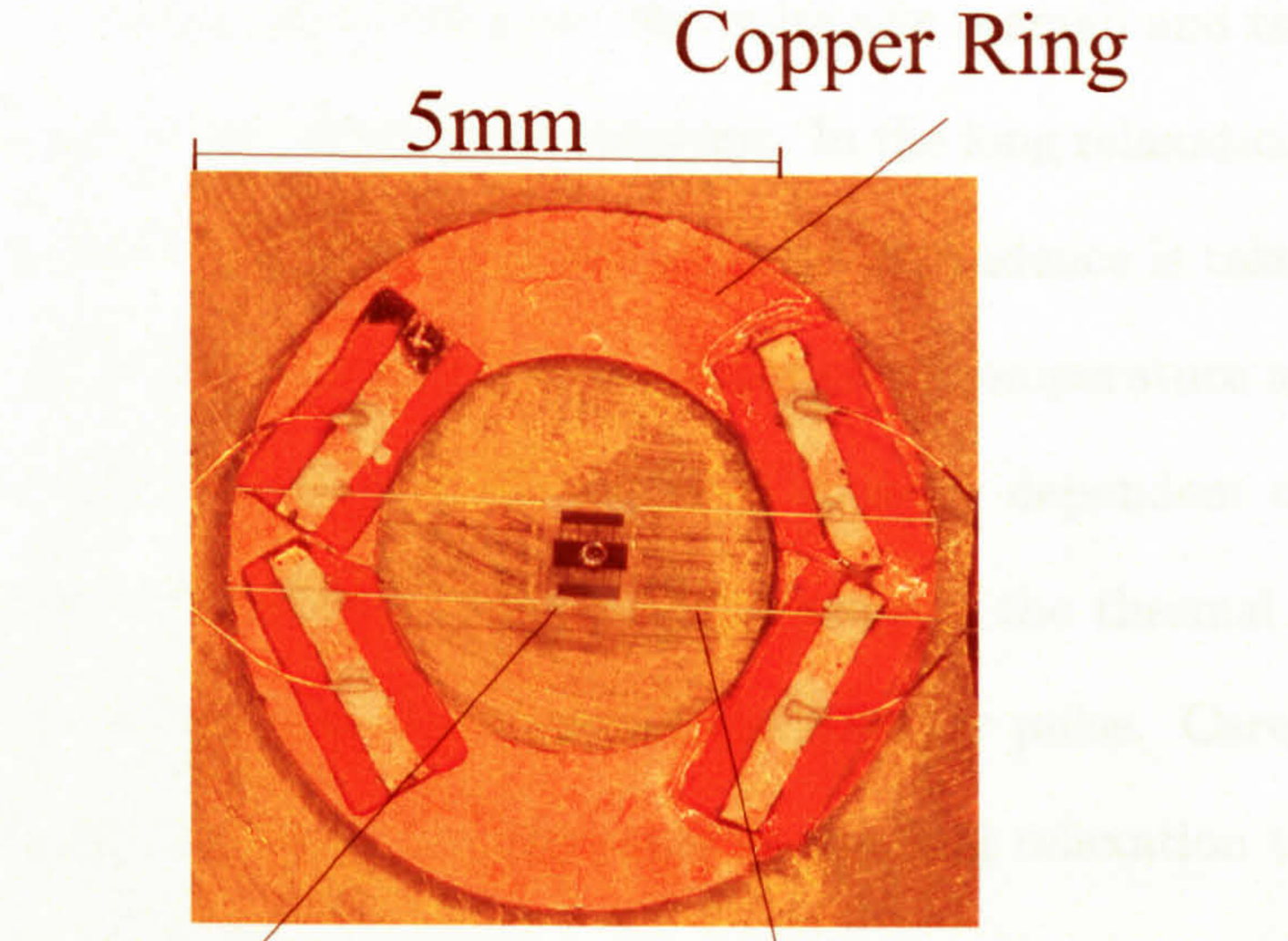

Figure 2.2: Picture of the Bare Chip Calorimeter.

temperature. The equation which relates the temperature of sample $T^{\uparrow}$, the power $P^{\uparrow}$ applied, the heat capacity C and the thermal conductivity to the bath is

$$C(T)\frac{dT^{\uparrow}}{dt}(T) = P^{\uparrow}(T) - \int_{T_B}^{T} \kappa_B(T')dT'. \tag{2.4}$$

A similar equation describes the temperature as the smaller power is applied,

$$C(T)\frac{dT^{\downarrow}}{dt}(T) = P^{\downarrow}(T) - \int_{T_B}^{T} \kappa_B(T')dT'. \tag{2.5}$$

These two equation can be combined to give,

$$C(T) = \frac{P^{\uparrow} - P^{\downarrow}}{\frac{dT^{\uparrow}}{dt} - \frac{dT^{\downarrow}}{dt}}. \tag{2.6}$$

In the conventional relaxation technique, the pulse size is small and the heat capacity and thermal time constant are taken as constant. In the long relaxation technique, the pulse size is large and each quantity's temperature dependence is taken into account. Using the bare chip calorimeter, power is a function of temperature as the resistance of the thermometer used to apply the power is strongly dependent on temperature. The long relaxation technique requires no knowledge of the thermal conductivity of the setup and produces several heat capacity points per pulse. Care must be taken to thermally connect the sample to the stage as the long relaxation technique is still vulnerable to the tau-2 effect.

2.2.3 AC Calorimetry

AC calorimetry using the bare chip is different to the Sullivan and Seidel analysis due to the heater and thermometer being the same in the bare chip experiment and the fact that the power applied depends on the temperature. The analysis of this arrangement is conducted in [51]. In brief, an AC current I_0 is applied to the bare chip with a frequency ω. The resistance of the bare chip depends on the temperature and for small temperature excursions about the bath temperature can be written $R = R_0 + \alpha T$ where α is the sensitivity of the Cernox ($\frac{dR}{dT}$) and R_0 is the resistance of the bare chip at the bath temperature. Using T_{ac} as described above then the power applied P is

$$\begin{aligned} P &= I^2 R \\ &= I_0^2 \cos^2(\omega t)\,(R_0 + \alpha T_{ac}) \\ &= P_0 + P_{2\omega} + P_{4\omega}. \end{aligned} \tag{2.7}$$

The resulting power can be separated into components where P_0 a constant power and $P_{n\omega}$ is the power associated with a frequency $n\omega$. The biggest component of P will be

$$P_{2\omega} = \frac{I_0^2 R_0}{2} + \frac{\alpha I_0^4 R_0}{4\omega C}\left(\cos(\delta) - \sin(\delta)\right). \tag{2.8}$$

Then the voltage on the lock in amplifier corresponding to $P_{2\omega}$ will be

$$\begin{aligned} V &= I_0 R \\ &= I_0 \cos(\omega t)\left(R_0 + \alpha T_{ac}\right) \\ &= I_0 \cos(\omega t)\left(R_0 + \frac{\alpha P_{2\omega}}{2\omega C}\cos(2\omega t + \delta)\right) \\ &= I_0 \cos(\omega t)\left(R_0 + \left(\frac{\alpha I_0^2 R_0}{2\omega C} + \frac{\alpha^2 I_0^4 R_0}{4\omega^2 C^2}[\cos(\delta) - \sin(\delta)]\right)\cos(2\omega t + \delta)\right) \end{aligned} \tag{2.9}$$

The biggest component to this equation will be the third harmonic and the size of this voltage $V_{3\omega}$ is

$$V_{3\omega} = \left(\frac{\alpha I_0^3 R_0}{4\omega C}\right)\cos(3\omega t+\delta)+\left(\frac{\alpha^2 I_0^5 R_0}{16\omega^2 C^2}\right)[\cos(3\omega t)+\cos(3\omega t+2\delta)-\sin(3\omega t+2\delta)+\sin(3\omega t)]. \tag{2.10}$$

If the phase shift δ is assumed to be 90°, which is the case for the ideal frequency, then the size of $V_{3\omega}$ is

$$|V_{3\omega}| = \frac{\alpha I_0^3 R_0}{4\omega C} + \frac{\alpha^2 I_0^5 R_0}{8\omega^2 C^2}. \tag{2.11}$$

This can be arranged to give the heat capacity as

$$C = \frac{2\omega I^3 R\alpha + 2\sqrt{\omega^2 I^6 R^2 \alpha^2 + 8\omega^2 |V_{3\omega}| I^5 R\alpha^2}}{16\omega^2 |V_{3\omega}|}. \tag{2.12}$$

Therefore, measuring the voltage of the bare chip on the 3rd harmonic with a 90° phase shift of the excitation frequency enables the heat capacity to be calculated.

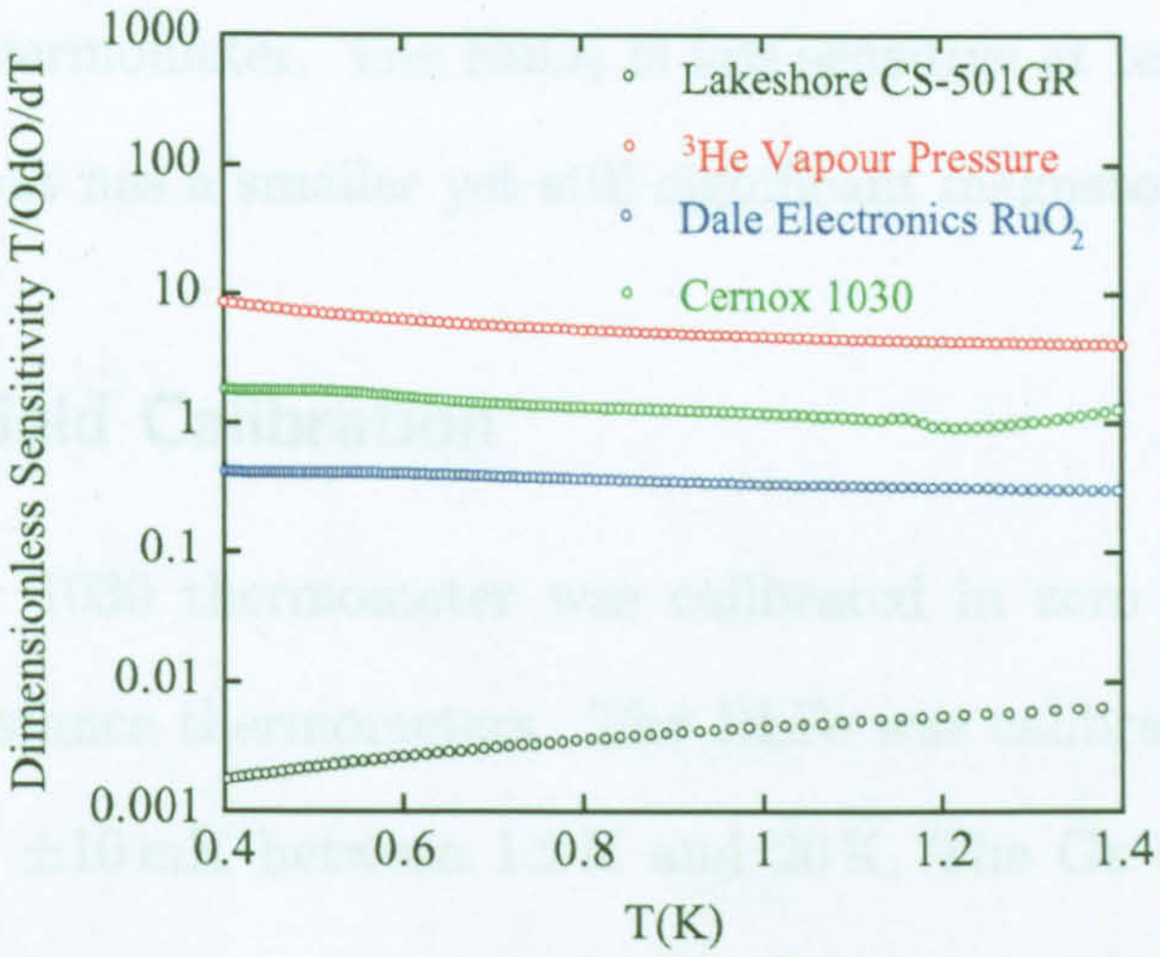

Figure 2.3: Dimensionless Sensitivity ($\frac{T}{O}\frac{dO}{dT}$, $O = R, P, C$) of several types of thermometer below 1 K.

2.3 Thermometry Calibration

2.3.1 Thermometry Between 0.3 K and 2 K in a Magnetic Field

In a heat capacity experiment very precise thermometry is required. Typically millikelvin accuracy is needed to obtain an acceptable error in heat capacity. This can be difficult to achieve, especially when using a magnetic field. Figure 2.3 shows the dimensionless sensitivities of several types of thermometer commonly used at low temperatures. Of these the vapour pressure of ^{3}He is the most sensitive. Resistance thermometers are the most widely used thermometers in cryogenic experiments due to their ease of use and high sensitivity. Many different materials are used as resistance thermometers, the requirement being a strong temperature dependence of resistivity and reproducibility on repeated cooling. The most sensitive resistance thermometers are the Cernox range [54]. The Cernox range are thin film semiconductor sensors and come in three types 1010,1030 and 1050. The major drawback to the Cernox

thermometer is the very high magneto-resistance of the thermometer. This effect is biggest at high fields and low temperatures. An alternative to the Cernox is to use a RuO_2 thick film thermometer. The RuO_2 is less sensitive at temperatures above 1 K than the Cernox but has a smaller yet still significant magnetoresistance.

2.3.2 Zero Field Calibration

Initially a Cernox 1030 thermometer was calibrated in zero field using calibrated Ge and RhFe resistance thermometers. The RhFe was calibrated by Lakeshore [54] to an accuracy of ±10 mK between 1.2 K and 20 K. The Ge thermometer was also calibrated by Lakeshore to an accuracy of ±10 mK between 2 K and 90 mK. Above 1 K measurements were performed using a Lakeshore 340 temperature controller. When using a Cernox with the Lakeshore 340 the standard excitation is 1 mV, at base temperature this voltage causes self heating of the thermometer. For measurements below 1 K a Stanford SIMS AC resistance bridge was used to measure the sensors. The excitation was limited to 100 μV to prevent self heating of the sensors. The zero field calibration of the Cernox between 0.3 K and 5 K is shown in Figure 2.4. The calibrations are in agreement but there is a slight disparity of 10 mK at 1.2 K which could be expected from the quoted accuracy of both thermometers.

2.3.3 Field Calibration

To counter the magnetoresistance of the Cernox, Taylor [51] calibrated the stage Cernox in field using a Lakeshore cryogenics CS-501GR Capacitance thermometer [54]. This uses strontium titanate as a dielectric. The Lakeshore specification quotes a minimum operating temperature of 1.5 K as below this temperature sensitivity becomes very low. To counter the magnetoresistance of the Cernox in this study, a capacitance

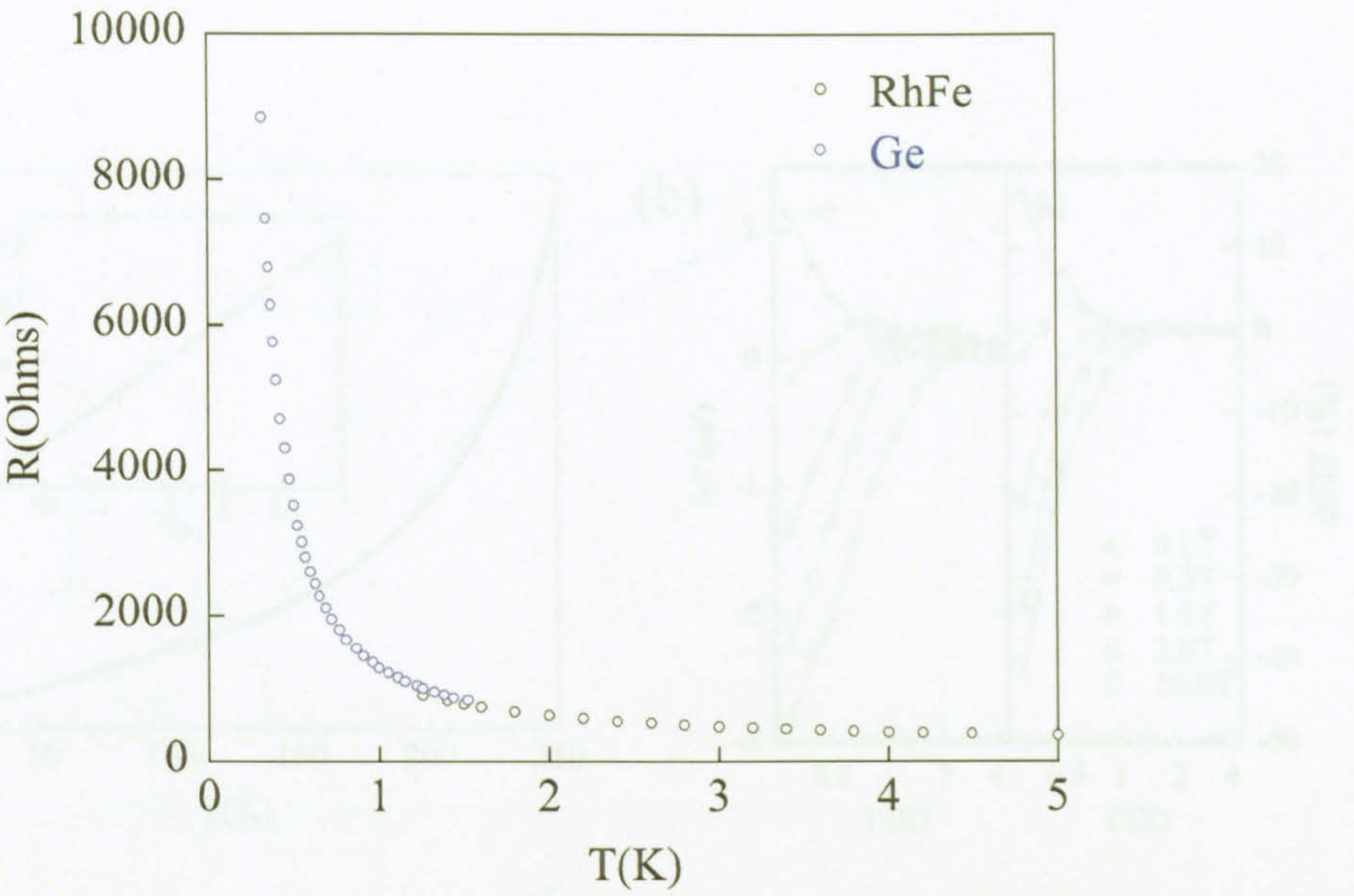

Figure 2.4: The calibration of the Cernox using the RhFe and Ge thermometers.

thermometer was first used in the same way as in ref [51]. The temperature was stabilised in zero field using the Cernox resistance thermometer and then the field ramped while holding the capacitance thermometer constant. Up and down sweeps were performed to correct for the drift of the capacitance thermometer. The field dependence of the magnetoresistance could then be found.

It became apparent that the capacitance thermometer is significantly field dependent (see section 2.3.8) at low temperatures as the magnetoresistance of the Cernox seemed very large (at worst 70 %). Using the calibration obtained from the capacitance thermometer resulted in large errors when measuring the heat capacity. This was confirmed in a recent paper which concluded that below $\simeq$2 K the Lakeshore capacitance thermometer becomes significantly field dependent [55] (Figure 2.5).

To overcome this setback a different method of calibrating the Cernox in a magnetic field had to be developed. The international temperature scale is defined by the vapour pressure of helium between 0.6 K and 4.2 K and measurements of the vapour pressure can be used to determine the temperature. The vapour pressure is essen-

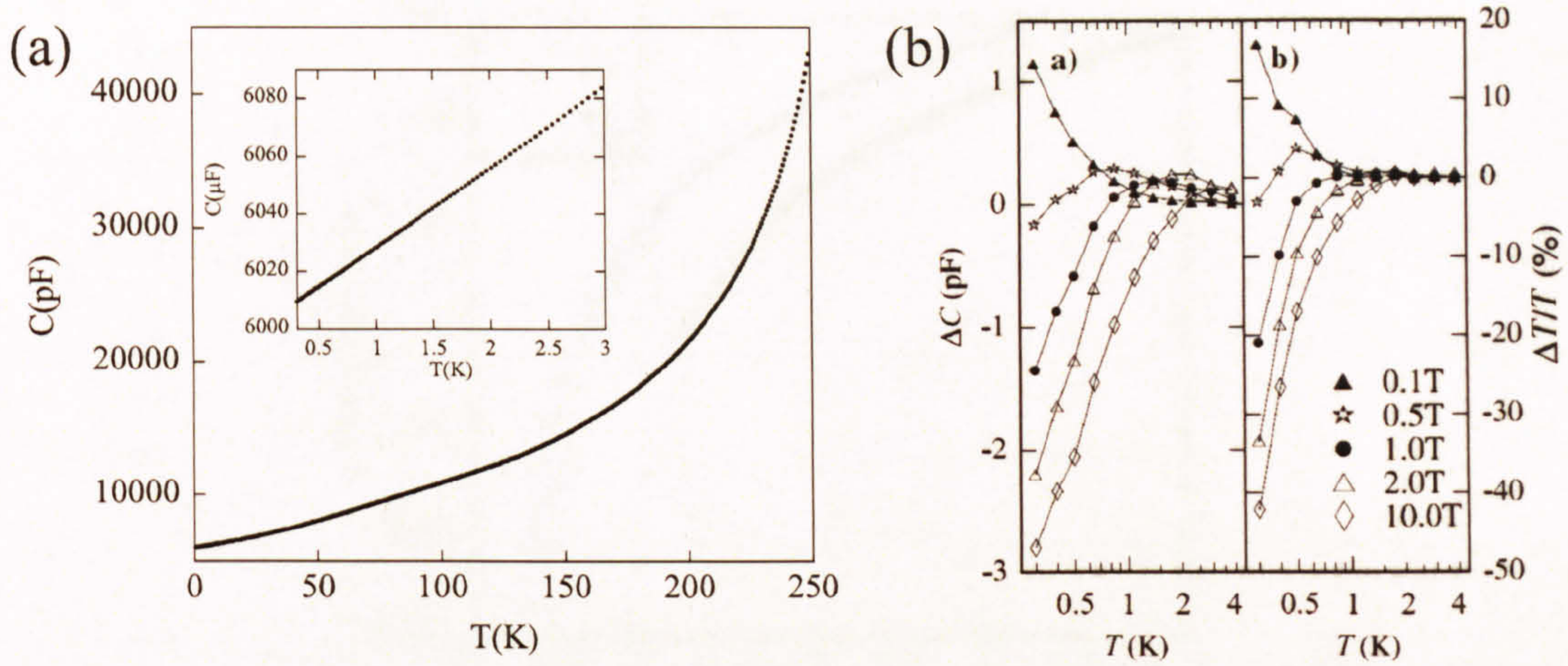

Figure 2.5: (a) Temperature dependence of Capacitance for a Lakeshore Cryogenics Capacitor and (b) magnetic field corrections taken from [55]for the thermometer below 2 K.

tially field independent and sensitive to temperature. However, a slow response time, the thermomolecular effect (see section 2.3.7) and general difficulties in handling ^{3}He make it impractical for use as the main thermometer. Vapour pressure measurements also have the advantage of being able to improve the zero field calibration.

2.3.4 Vapour Pressure of Helium

Vapour pressure thermometry was used to calibrate a Cernox 1030 thermometer for use as the main stage thermometer in the heat capacity experiment. The vapour pressures of ^{3}He and ^{4}He are part of the latest International Temperature Scale (ITS90) devised in 1990 [56]. Precise measurements are made of the pressure P just above liquid helium held at temperature T. The temperature is related to the pressure by equation 2.13,

$$T = \sum_{i=0}^{9} A_i \left(\frac{\ln(P) - B}{C} \right)^i , \tag{2.13}$$

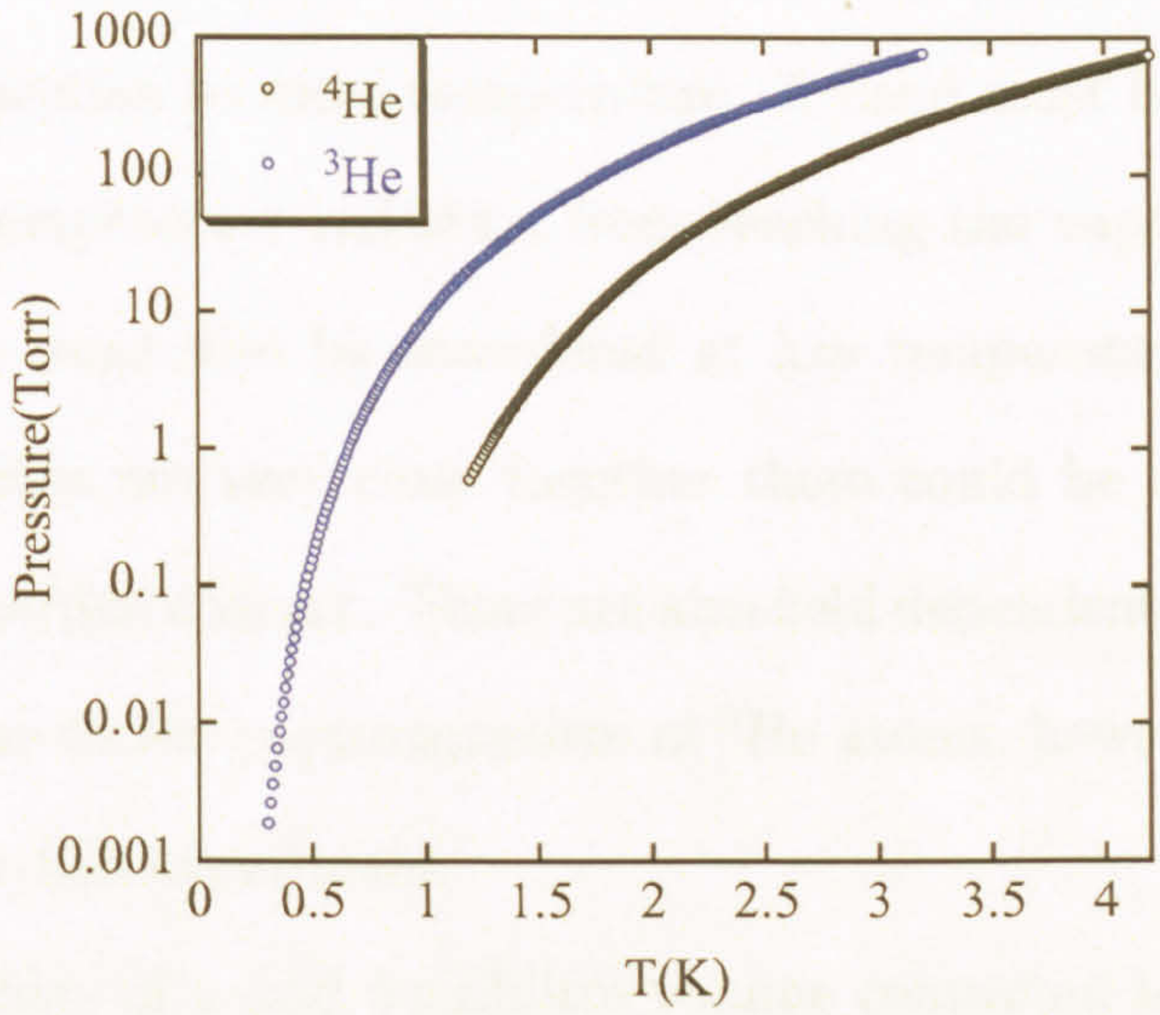

Figure 2.6: Vapour Pressures of ^{3}He and ^{4}He.

where A_i, B and C are constants defined in the ITS90 for both ^{3}He and ^{4}He. The vapour pressures of ^{3}He and ^{4}He are shown in Fig 2.6. At temperatures close to the boiling point of the liquid, 4.2 K for ^{4}He and 3.2 K for ^{3}He, the vapour pressure is less sensitive to the temperature and an accurate pressure sensor is required. However at base temperature 0.3 K the vapour pressure is much more sensitive to changes in temperature. The pressure gauge used in this experiment is accurate to 0.15% of the pressure reading. This corresponds to a temperature accuracy of 1.2 mK at 3.2 K and 0.1 mK at 0.5 K for ^{3}He vapour pressure measurements which is a greater accuracy than that quoted for the Ge and RhFe thermometers.

2.3.5 Experimental Setup

There are several factors which must be considered when designing a vapour pressure thermometer which are described in [57], [58]. The thermomolecular effect is biggest when the pipe carrying the helium gas to room temperature has a narrow diameter.

Therefore a large diameter pipe is best to reduce this effect. However a large pipe can be unfeasible due to space restrictions and if the diameter is large this can create a large thermal connection to room temperature. A bend must be included in the pipe to prevent room temperature radiation from reaching the vapour pressure pot. The Kapitza resistance must also be considered at low temperatures, even if the liquid and the thermometer are very close together there could be a boundary resistance preventing good thermal contact. There are also field dependent changes to the vapour pressure of ^{3}He due to the paramagnetism of ^{3}He atoms, however this effect is small and is neglected in this experiment.

The setup consists of a cold 5 millilitre volume connected to a room temperature 6 litre volume and pressure gauge. The 6 litre volume is filled with helium to 500 mbar. The resulting 3 litre of gas is then condensed into the cold volume over the course of 2 hours. With all the helium condensed the valve to the 6 litre volume is shut enabling pressure measurements to be made with only a small dead volume. A safety valve has been inserted between the pressure gauge and the 6 litre volume in the event of a large over pressure. The pressure gauge is a MKS Baratron 120A with 1000 Torr range. It has an accuracy of 0.1% of the reading and a resolution of 10^{-5}. The lowest operating pressure is 10^{-5} of full scale. This corresponds to temperatures around 0.4 K when using ^{3}He. For ^{4}He measurements, recovery grade ^{4}He is passed through a liquid nitrogen cold trap and then allowed to bleed into the 6 litre volume until it is at 500 mbar. For He^3 measurements, the whole system is warmed to room temperature and pumped out for 12 hours. This prevents He^4 contamination of the He^3. A 15 litre volume containing 10 litre of ^{3}He and a sorb pump are attached to the 6 litre volume. All the lines are pumped down and then the ^{3}He is allowed to expand into the whole system. This fills the whole system to 500 mbar with the remainder of the ^{3}He stored in the large 15 litre volume. At low temperature the pot is well connected to the ^{3}He

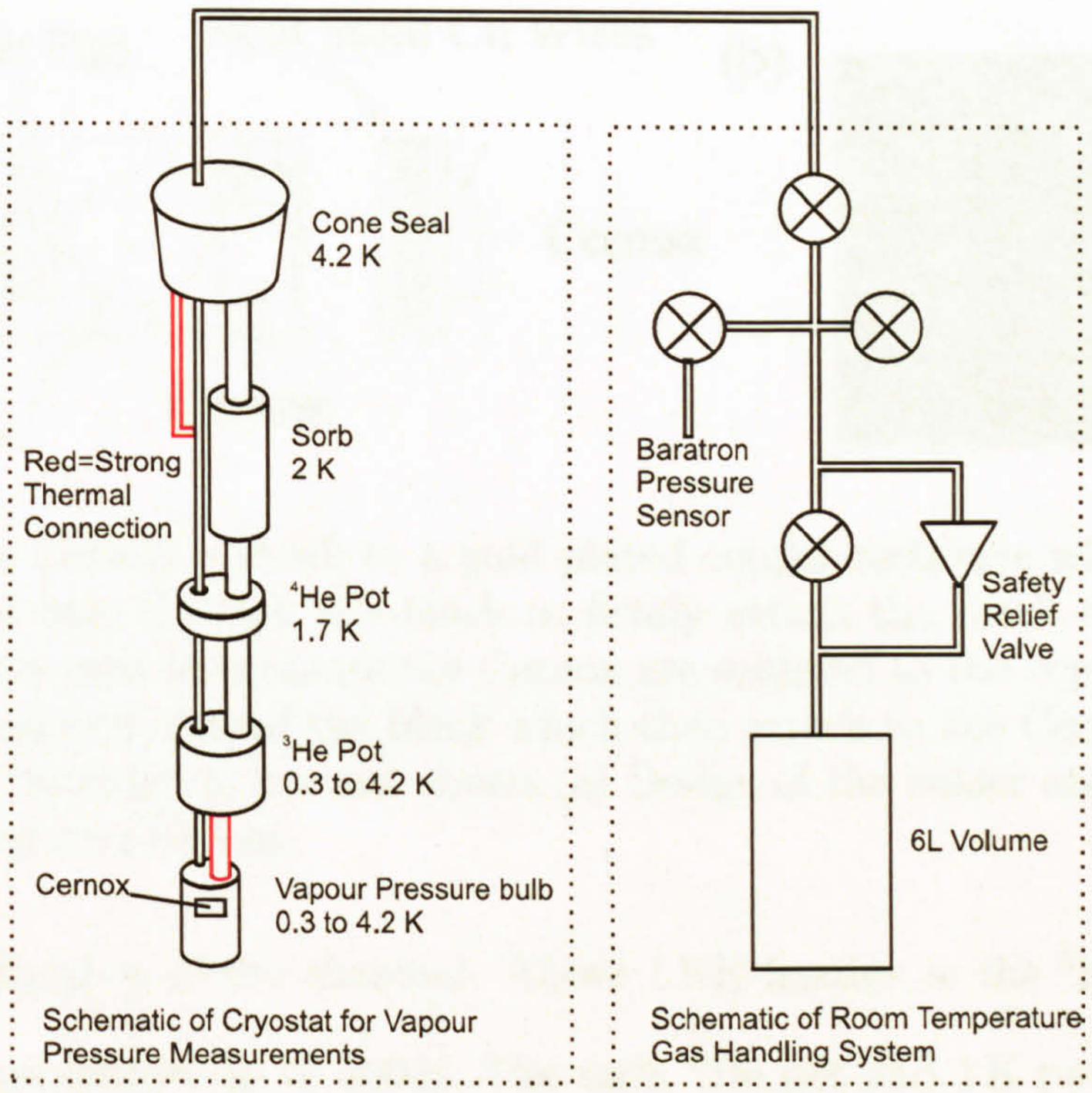

Figure 2.7: Diagram of gas handling system for vapour pressure thermometry and low temperature setup.

pot of a sorb pumped ^{3}He system with a base temperature of 0.3 K. It is vital that the tube leaving the pot is not thermally connected to any part of the experiment which is colder than the pot as this will result in liquid forming at this point and producing an incorrect vapour pressure. The tube has a copper section which is connected by a 1mm silver wire to the 4 K flange. The Cernox thermometer is mounted on a 3 mm by 5 mm by 1 mm gold plated copper rectangle which is bolted onto the vapour pressure pot. This copper rectangle is used in order to prevent repeated soldering to the Cernox which can change the calibration. The Cernox resistance is measured using a Stanford Research Systems SIMS AC resistance bridge. Below 1 K the excitation voltage of the bridge is limited to 100 μV and above 1 K it is limited to 300 μV. The Cernox is measured at 33 Hz with a time constant of 1 s. Temperature control below 1.6 K is achieved by altering the temperature of the He^3 sorb pump which changes

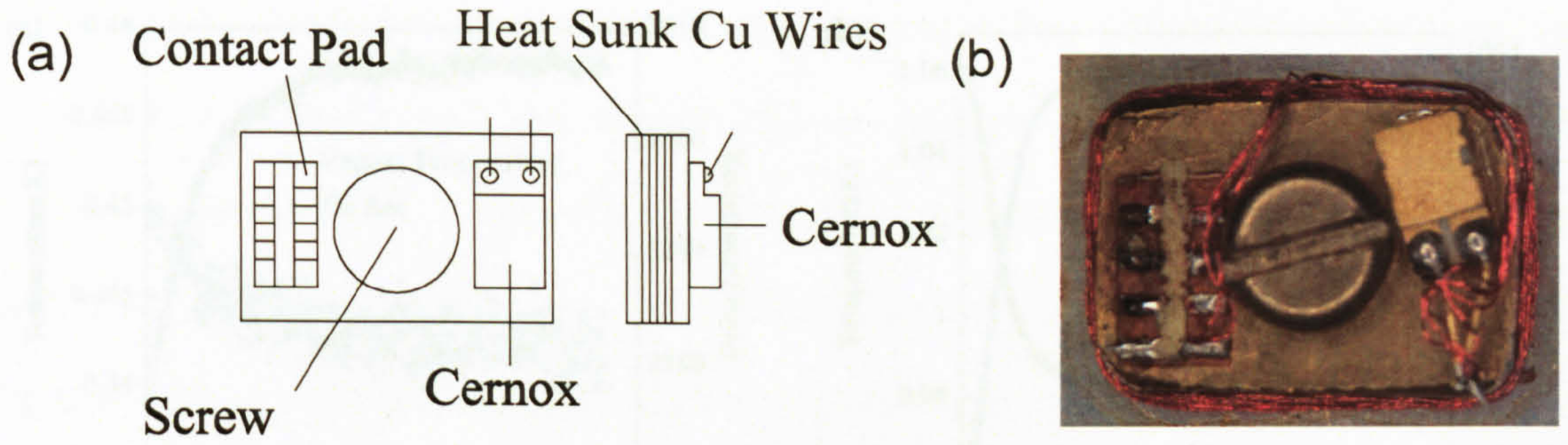

Figure 2.8: The Cernox is stuck to a gold plated copper rectangle with GE varnish. There is an M2 hole through the block to firmly attach the block to the cryostat. Constantan wires used to measure the Cernox are soldered to the copper block, then copper wires wrapped around the block which then attach to the Cernox. The edges of the block are rounded to prevent shorts.(a) Design of the holder and (b) picture of completed holder and Cernox.

the pumping efficiency of the charcoal. Above 1.6 K heaters in the ^{3}He pot are used to produce temperatures up to 100 K. The sorb, ^{3}He pot and 1 K pot thermometers are all monitored by a Lakeshore 340 temperature controller which also controls the sorb heater and ^{3}He pot heater.

2.3.6 Vapour Pressure Measurements

To condense the helium to use for vapour pressure thermometry the Sorb was held at 30 K which condensed the cryogenic ^{3}He and the ^{3}He pot settled to 1.8 K. The helium used for vapour pressure measurements was then introduced slowly in order to limit the heating caused by the warm gas. Once the helium was condensed in the vapour pressure pot fixed temperature points were used to calibrate the Cernox. These temperature points were achieved by setting the ^{3}He pot temperature and waiting for the vapour pressure to come to equilibrium. Typically this took about 5 minutes (see figure 2.9). The calibration point was taken as an average over 30 data points with a standard deviation of less than 1.5 mK. Figure 2.9 shows the vapour temperature settling over time at two temperatures 0.42 K and 1.06 K. At 0.42 K the noise level

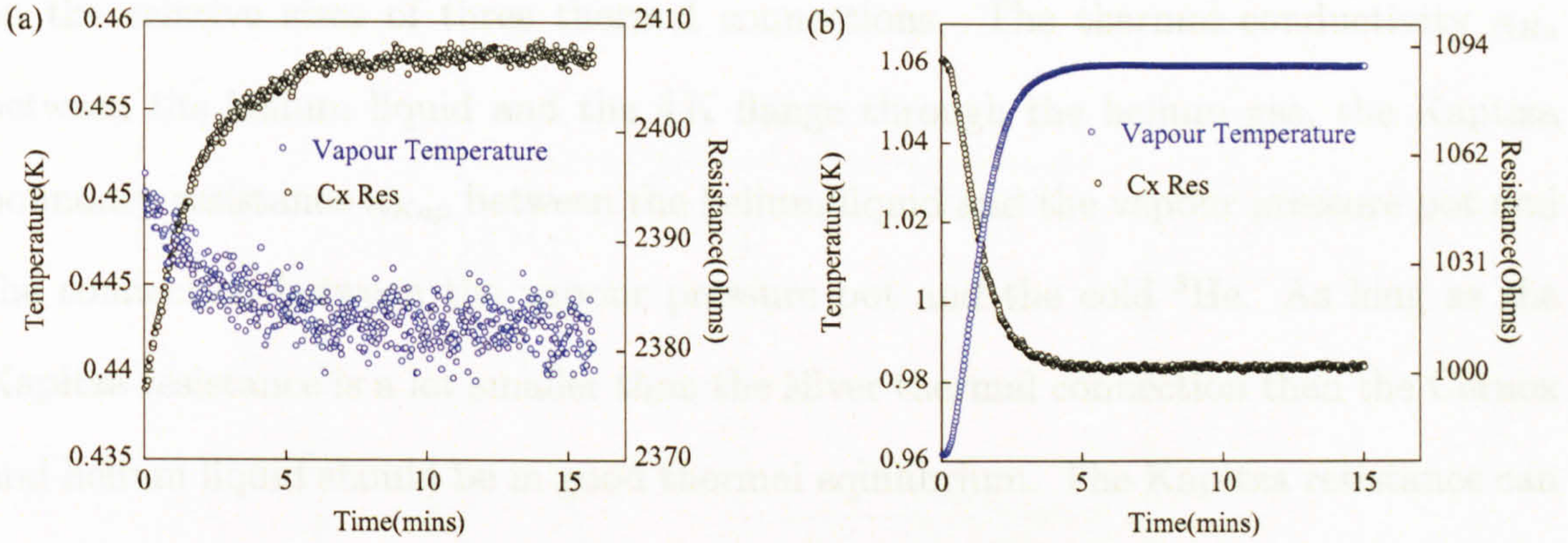

Figure 2.9: Raw data for the vapour pressure thermometer for (a) 0.42 K and (b) 1.06 K in 14 T. The vapour temperature is calculated from vapour pressure using the coefficients in [58].

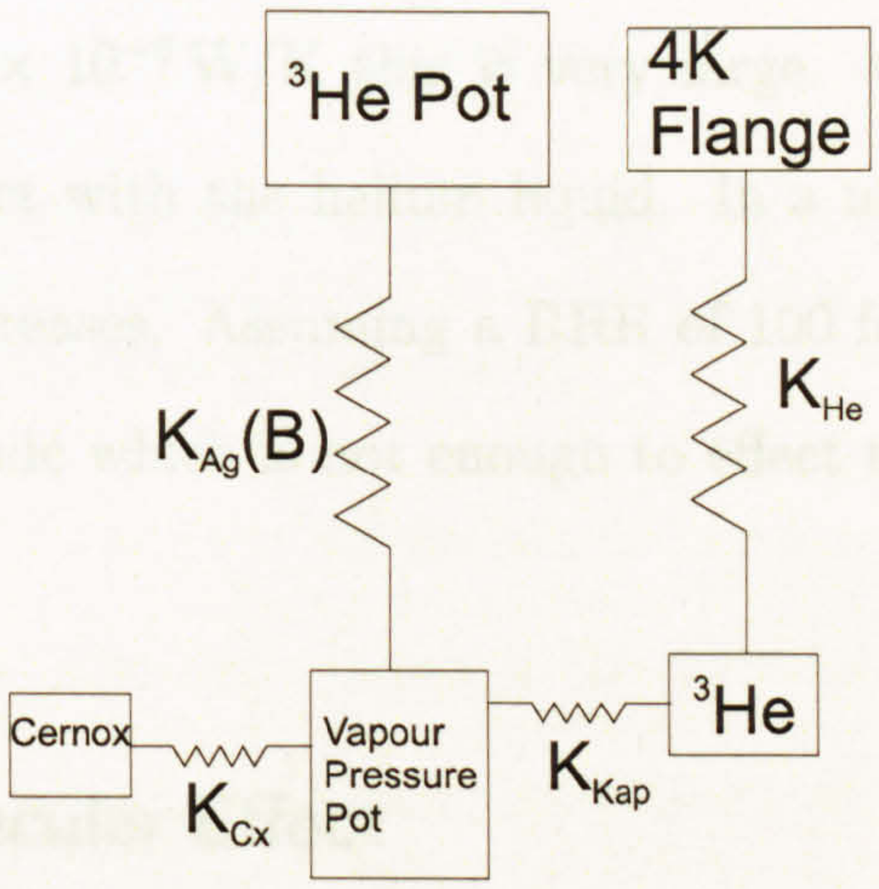

Figure 2.10: Diagram of the thermal connections in the vapour pressure thermometer.

is about 1 mK, however at 1 K the noise level is 0.01 mK. This is due to the pressure sensor. Below 0.38 K the pressure sensor no longer has the sensitivity to measure the changes in pressure and the calibration is not performed below this temperature. In a magnetic field, the same method was used as the ^{3}He pot thermometer was sufficiently out of the magnetic field to reduce the magnetoresistance of the sensor to a few percent. The thermal connections of the vapour pressure thermometer are shown in Figure 2.10. The thermal conductivity of the Cernox to the vapour pressure block κ_{Cx} is assumed to be very big. The vapour pressure thermometer then relies

on the relative sizes of three thermal connections. The thermal conductivity κ_{He} between the helium liquid and the 4 K flange through the helium gas, the Kaptiza boundary resistance κ_{Kap} between the helium liquid and the vapour pressure pot and the connection between the vapour pressure pot and the cold ^{3}He. As long as the Kapitza resistance is a lot smaller than the silver thermal connection then the Cernox and helium liquid should be in good thermal equilibrium. The Kapitza resistance can be calculated using the graph in [59]. In the present setup, with a contact area of $2.5 \times 10^{-3}\,\mathrm{m}^2$ between the helium and the copper and at a temperature of 0.4 K the thermal boundary conductance is 0.053 W/K. Compared to the thermal conductivity of the silver wire of 5.6×10^{-6} W/K this is very large. Consequently the Cernox is in good thermal contact with the helium liquid. In a magnetic field the thermal conductivity of silver decreases. Assuming a RRR of 100 for the silver this decrease is by an order of magnitude which is not enough to effect the working of the vapour pressure thermometer.

2.3.7 Thermomolecular Effect

If a very low pressure gas is in two volumes at different temperatures separated by a thin tube then a pressure difference can develop if the mean free path of the gas is of the order of the radius of the tube. In this situation, collisions between the tube wall and the gas particles become more frequent than collisions between gas particles. This creates a pressure difference. Weber [60] first derived an equation for this pressure difference in ^{4}He called the Weber-Schmidt equation,

$$\begin{aligned}\log\left(\frac{p_w}{p_c}\right) &= \frac{1}{2}\log\left(\frac{T_w}{T_c}\right) + 0.18131\log\left(\frac{y_w+0.1878}{y_c+0.1878}\right)\\ &+ 0.41284\log\left(\frac{y_w+1.8311}{y_c+1.8311}\right) - 0.15823\log\left(\frac{y_w+4.9930}{y_c+4.9930}\right), \quad (2.14)\end{aligned}$$

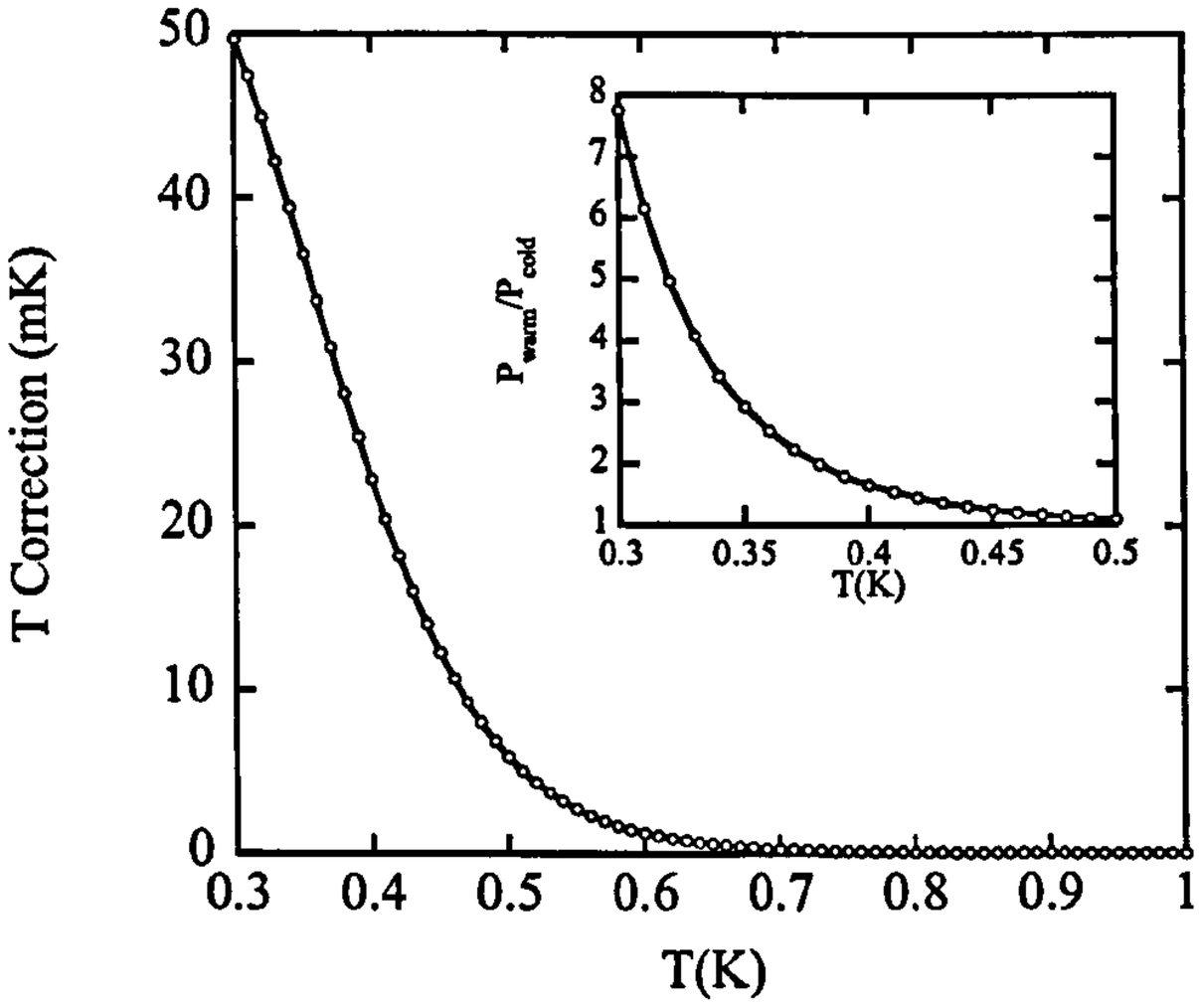

Figure 2.11: Corrections to be made to the measured temperature calculated from the Weber-Schmidt equation with a tube radius of 3.06 mm and room temperature of 300 K. Inset: Corresponding pressure difference.

where $y = (\frac{rp}{13.42})(\frac{273.15}{T})^{1.147}$ and the subscripts w and c refer to the warm and cold regions. This equation has also been shown to be correct for ^{3}He [61]. The equation works on the assumption that gas-surface interactions are diffuse and consequently the surface of the pipe can play a role [62]. The majority of work done in stainless tubes [63], [64] show good agreement with the theory. Watkins [65] used a differential measurement in stainless tubes and sees good agreement for ^{3}He but poor agreement for ^{4}He. The reason for this is cited as superfluid film flow up the pipe walls. The superfluid reaches a warmer part of the apparatus and evaporates going back down into the pot of liquid. This creates a pressure difference from the point of evaporation to the liquid level. The latest work by Bernat [64] shows excellent agreement between experiment and theory in two different stainless steel tubes using ^{3}He. The average deviation from the Weber-Schmidt equation is 0.68 %. Using the Weber-Schmidt equation the pressure difference was calculated for He^3 and ^{4}He over the full tempera-

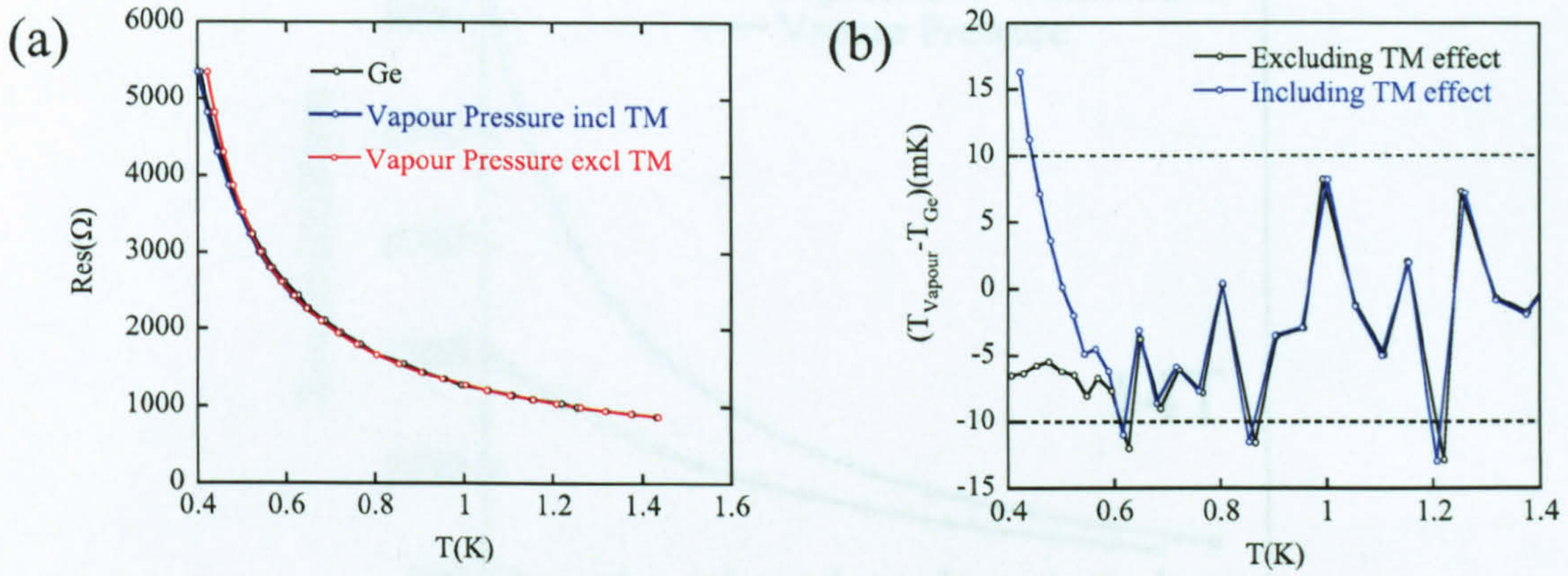

Figure 2.12: (a) Resistance versus temperature of Cernox using vapour pressure thermometry and calibrating against an externally calibrated Ge thermometer. The effect of including the thermomolecular effect is also shown. (b) Differences in the two calibrations when the thermomolecular effect is included and when it is excluded. Dashed lines represent the quoted accuracy of the Ge thermometer.

ture range of each liquid. A room temperature of 300 K and a pipe radius of 3.06 mm were used in the calculation. This ignores the thin capillary going from the pot to the 4 K flange but including this gives an additional correction of $\ll 1$ mK at base temperature. A room temperature change of 2 K will result in a 0.15 mK change in the correction.

2.3.8 Final Thermometer Calibration

The final vapour pressure calibration is shown in Figure 2.12 with and without the thermomolecular corrections compared with the calibration obtained from the Lakeshore calibrated Ge and RhFe thermometers. Including the thermomolecular correction gives an agreement within the quoted accuracy of the Ge thermometer over the entire range. It is difficult to place an absolute accuracy on the vapour pressure calibration. The accuracy of the pressure sensor in principle gives a temperature

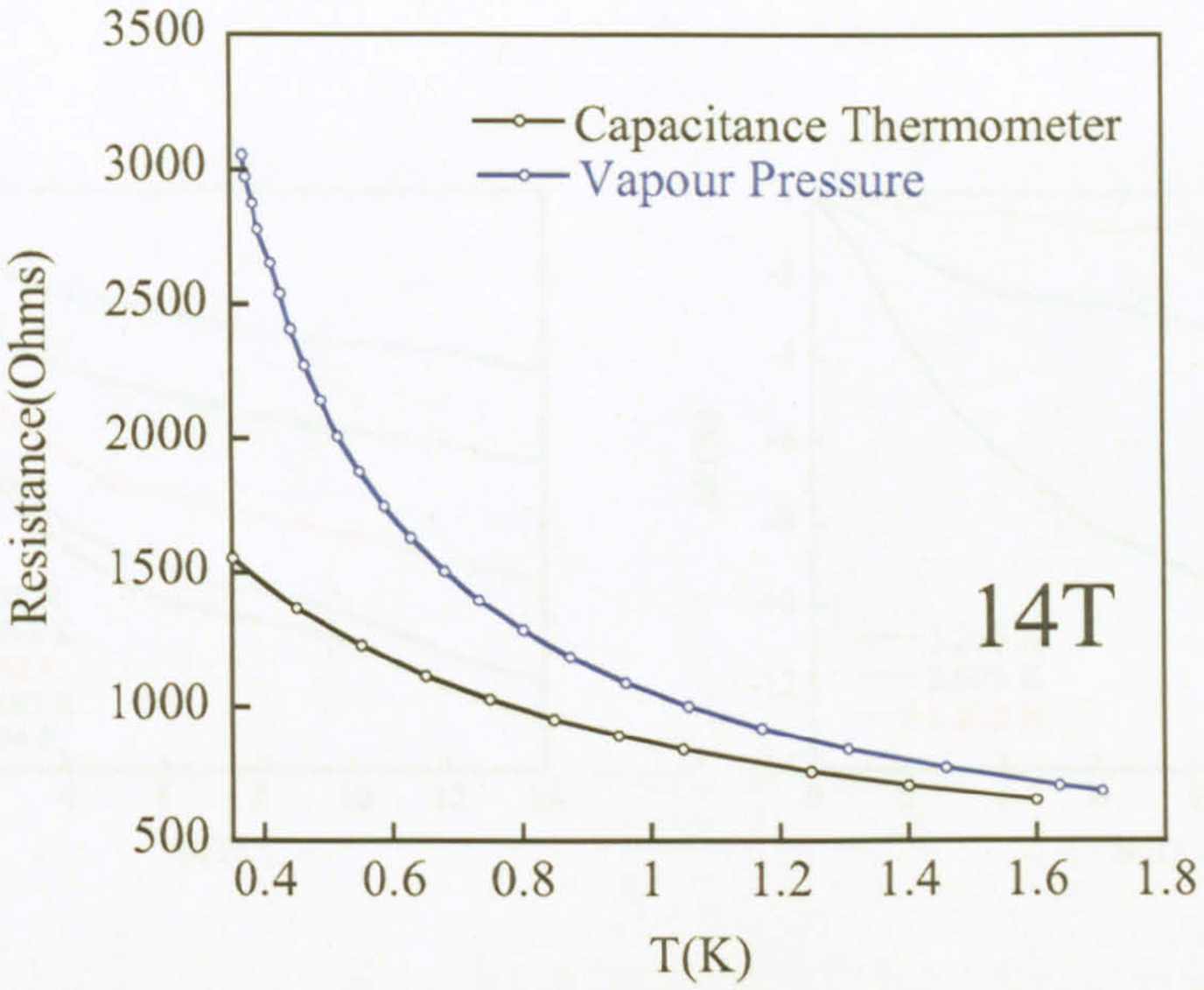

Figure 2.13: 14 T Cernox calibration using the capacitance method and the vapour pressure method.

accuracy of better than 1 mK. However the thermomolecular effect and the proximity of the pressure sensor's minimum pressure at low temperatures mean that a more realistic error is around 4 mK.

In a magnetic field the calibration obtained using the capacitance thermometer is confirmed to be very inaccurate. Figure 2.13 shows the 14 T calibration of the Cernox using the capacitance method and the vapour pressure method. There is a large difference between them, at 0.45 K the capacitance thermometer has changed by about 50 % in temperature. This is consistent with what is seen in [55]. The magnetoresistance of Cernox measured using vapour pressure thermometry is shown in Figure 2.14. The magnetoresistance of a Cernox thermometer is very large, in 14 T the resistance change is about -55 % at 0.38 K. This corresponds to a temperature change of 50 % from the 0 T calibration. The magnitude of the magnetoresistance is consistent with a study performed on ten Cernox thermometers in high fields [66]. The typical error at 2 K in 14 T is -7.61 % which is of the order of what is observed

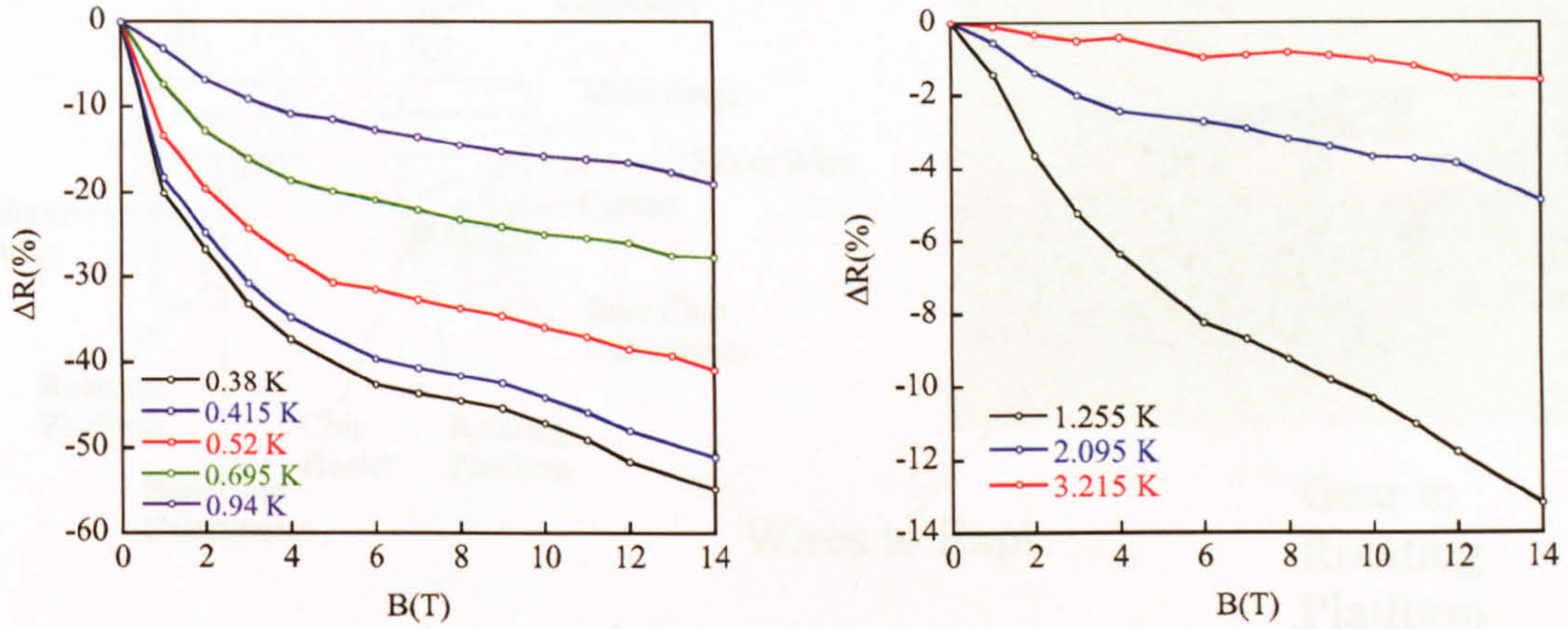

Figure 2.14: Cernox Magneto-Resistance between 0.4 K and 3.2 K.

in the current work.

2.4 Heat Capacity Measurements

2.4.1 Experimental Setup

The bare chip calorimeter was mounted on a rotating platform which is mounted on the pumped ^{3}He system with a base temperature of 0.3 K. The rotating platform was originally designed by Owen Taylor [51] to be mounted on a 1 K cryostat. A worm drive with a 20 to 1 gearing ratio is used at low temperature. Several modifications have been made in order to fit to the ^{3}He system. The gear used to couple the shaft to the platform has been removed and the shaft now connects directly to the platform through a screwdriver connection. This results in more reliable rotation at the cost of larger heating as the shaft is directly connected to room temperature and the sample stage. The screwdriver connection is used to lower the thermal connection between the stage and the shaft. Heat sinking of the shaft is achieved using copper washers

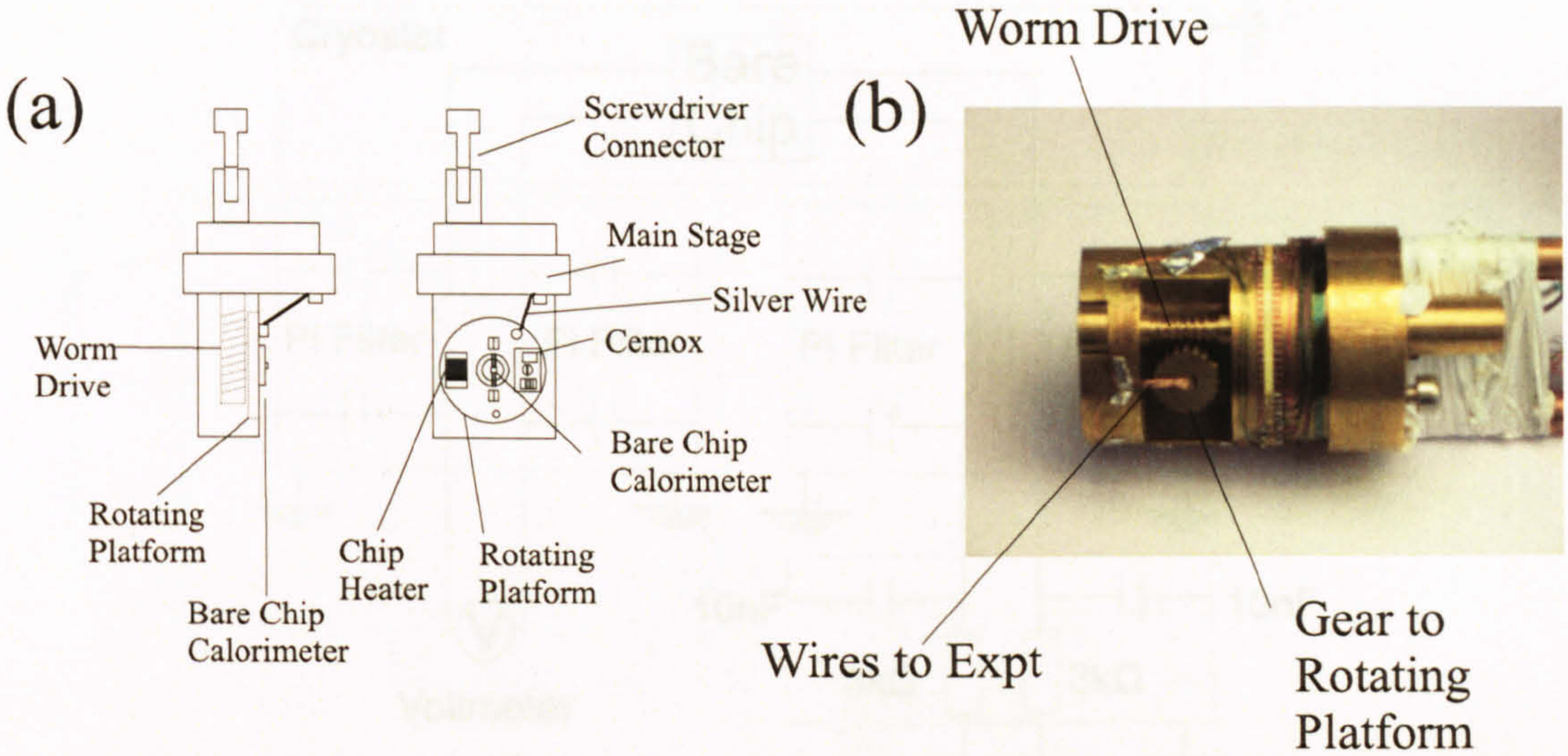

Figure 2.15: (a) Schematic of the Rotating platform. (b). Picture of the back of the rotator showing the worm gear.

attached to the 4 K flange and the 1 K pot. These washers have a knife edge on the inside and a slit enabling an adjustable thermal connection. The rotator is turned by a computer controlled stepper motor. The rotator turns reliably and has a backlash of 1° of the rotation angle. When the experiment is at base temperature a rotation of 2° causes the stage to heat up by ~1 K, with a cooling time to base temperature of around 5 minutes.

The rotating platform is thermally coupled to the main stage by 0.25 mm silver wire. The main stage houses the worm gear and is connected to a brass stage on copper rods. This brass stage is then connected to the ^{3}He pot with copper rods. Even though the stages are bolted together using copper, to ensure a very good thermal connection between the ^{3}He pot and the main stage a length of 1 mm silver wire is securely bolted between the rotator and the ^{3}He pot. On the rotating stage the bare chip calorimeter is mounted in the centre and the Cernox mounted on the copper block is bolted to the stage next to it. A 1 kΩ chip resistor is also attached to the stage as a heater. Coarse temperature control is achieved by controlling the sorb heater which

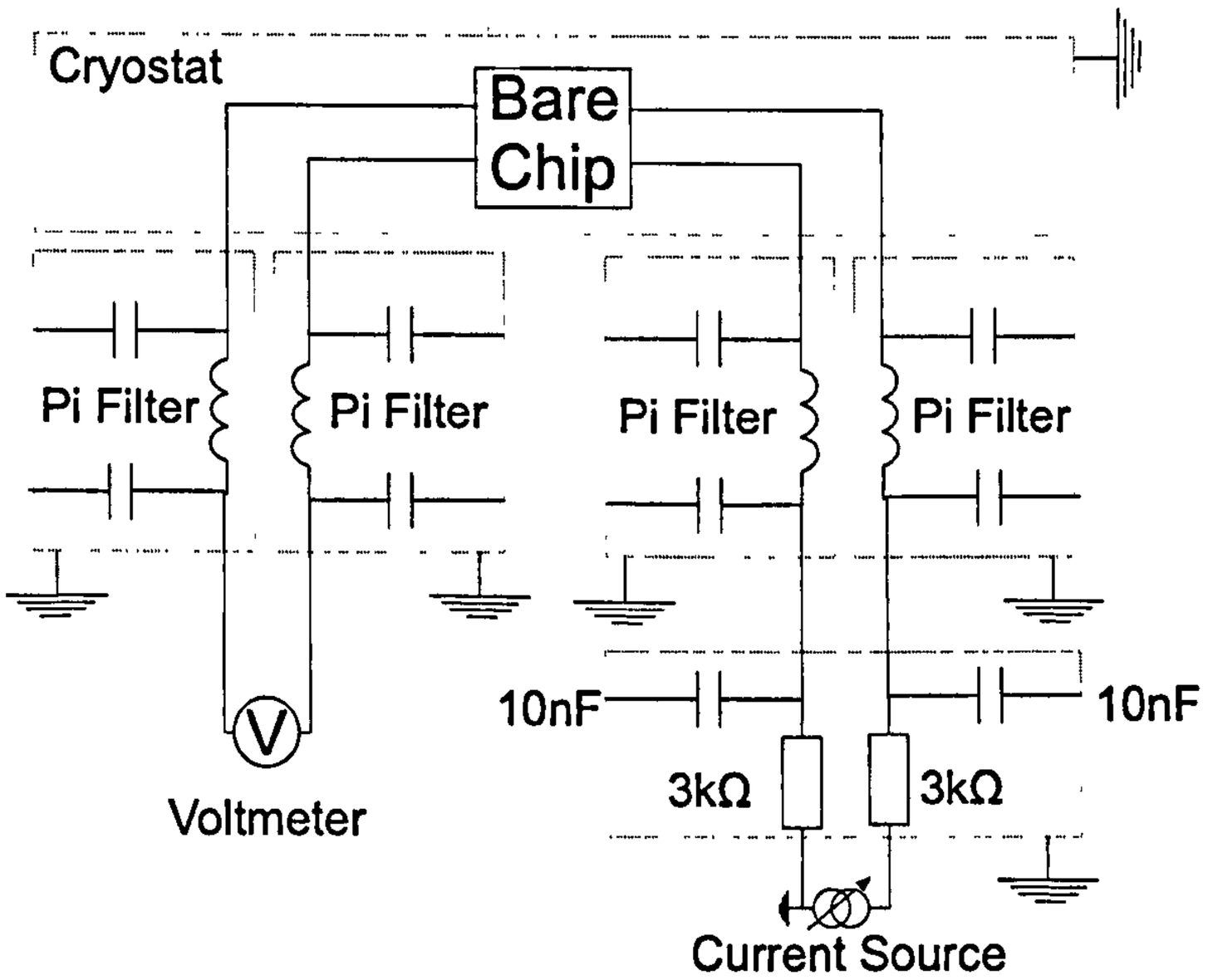

Figure 2.16: Circuit used to measure the Bare Chip Calorimeter.

sets the ^{3}He pot temperature 0.1 K below the desired temperature using a Lakeshore 340 temperature controller. Fine control is achieved by controlling the chip resistor using a Stanford Research Systems SIMS PID controller. With this method typical temperature stability is better than 0.05 mK at base temperature (standard deviation of 30 temperature points over 30 seconds).

The bare chip calorimeter is measured using a Keithley 6221 current source and Hewlett Packard voltmeter. Noise heating can be a problem on the calorimeter as it is thermally isolated from the bath. The wires to the bare chip are kept away from other wires as much as possible. Although this is not possible through the centre of the rotator, the wires are kept in separate pipes up to room temperature to minimise interference. The electrical circuit is shown in Figure 2.16. In addition to Pi filters there are low pass RC filters (R=3 $k\Omega$ and C=10 nF) which filter frequencies above ~23 kHz. These filters were investigated in [51] and found to be optimal as a large noise signal was observed at 60 kHz. This frequency is also present in the current setup and consequently the same filters are needed. The RMS noise is approximately

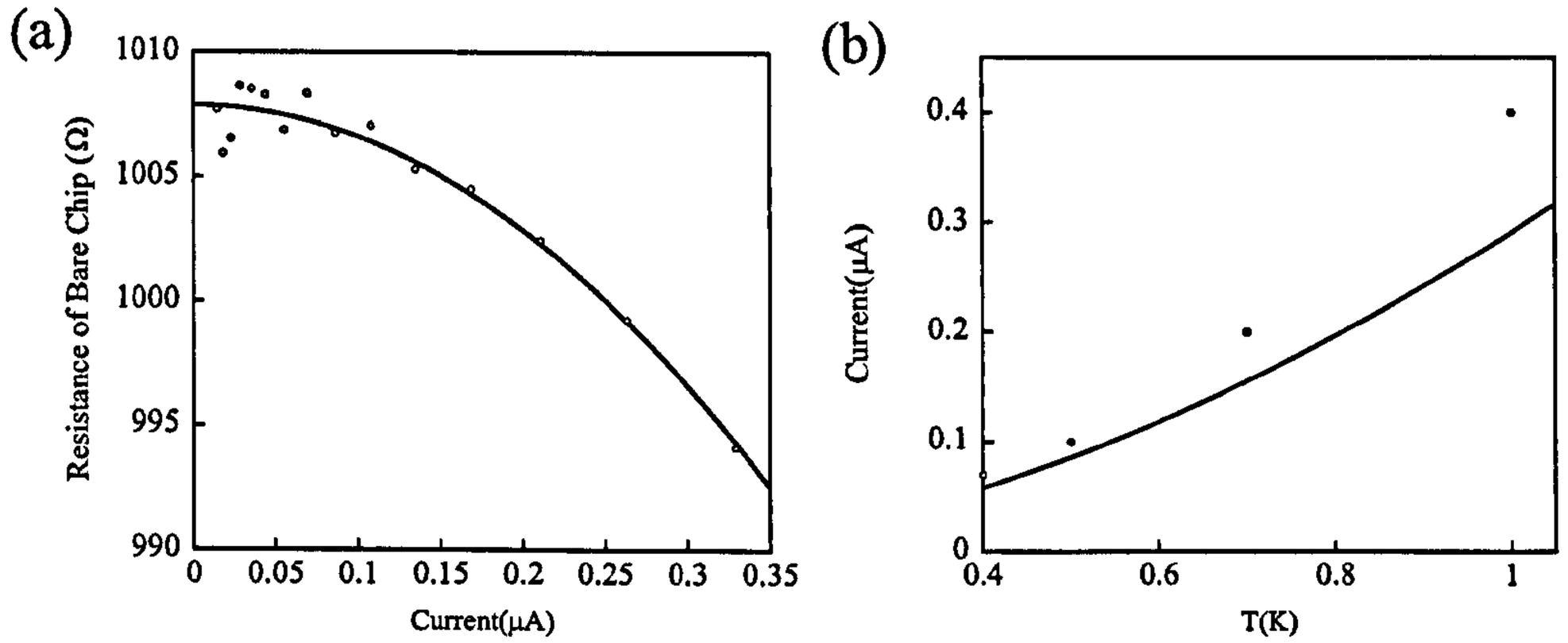

Figure 2.17: (a) Current versus resistance of the bare chip, fitted to $R = R_0 - \alpha I^2$ at 400 mK. (b) Maximum current used at each temperature, points are experiment points and line is the equation used to find the maximum current at each temperature.

20 nV/$\sqrt{Hz}$.

2.4.2 Bare Chip Calibration

The maximum non-heating current and thermal conductivity of the bare chip need to be measured. The maximum non-heating current is used to calibrate the bare chip Cernox and the thermal conductivity is used to calculate the pulse length. The maximum non-heating current is shown Figure 2.17. To find the maximum non-heating current the resistance versus current curve is fitted to $R = R_0 - \alpha I^2$. The maximum non-heating current is taken when R has changed by 0.1% of R_0. Once these points have been found over the whole temperature range, they are fitted to a polynomial. The actual equation used to find the maximum non-heating current at each temperature is the polynomial fit to the points divided by two to ensure absolutely no heating occurs. Once the maximum non-heating current has been found the bare chip can be calibrated against the main stage Cernox. The temperature of the stage is stabilised and 50 measurements of the Cernox resistance and bare chip resistance are averaged

to obtain the calibration. The Cernox resistance is then converted to a temperature using a Chebyshev polynomial fit to ln(R(T)). The final piece of calibration is to measure the thermal conductivity of the glass fibres. This is done by incrementing the power applied to the chip and then measuring the temperature rise. The thermal conductivity κ is then $\frac{dP}{dT_{BC}}$.

2.4.3 Long Relaxation Pulses

In long relaxation calorimetry care must be taken in selecting the correct pulses. A pulse consists of four parts $+I_H$, $+I_L$, $-I_H$ and $-I_L$. Where I_H and I_L are the high and low currents, the positive and negative are measured and averaged together to eliminate any thermoelectric voltages. This process of selecting the currents and the frequency of data collection is described in [51] for measurements down to 1.2 K. Below 1 K the same process is used but some parameters are changed to be more appropriate for the system at lower temperature. When taking the measurements the input parameters are high current, low current, number of data points, delay between points and number of pulses. These parameters must be calculated based on the heat capacity of the sample, the thermal conductivity and the acceptable noise level. An up pulse size is selected, typically 10% to 30% of the base temperature, and the size of the relaxation, typically 80% of the up pulse. From the integrated thermal conductivity κ, the heat capacity of the sample C and the resistance of the bare chip R the high current $I^{\uparrow}$ of the required size can be calculated,

$$P^{\uparrow} = \int_{T_L}^{T_H} \kappa(T) \tag{2.15}$$

$$I^{\uparrow} = \left(\frac{P^{\uparrow}}{R(T_H)}\right)^{\frac{1}{2}}. \tag{2.16}$$

In equation 2.15, T_H is the temperature after the up pulse, T_L is the temperature at the end of the down pulse and $P^{\uparrow}$ is the power applied to the chip on the up pulse. A similar equation can be used to find the low current $I^{\downarrow}$. Once the size of the pulse is determined the length of time τ required for the pulse is $\frac{3C}{2\kappa}$. Consideration must then be given to the systematic error arising from a curve being represented by a set of points. The derivative of the curve is required and if a set of points is used then a linear fit between points only represents the curve within a certain error. The relative systematic error in $\frac{dT}{dt}$ for a pulse of size ΔT is approximately [51]

$$\Delta \left(\frac{dT}{dt}\right)_{t\to 0} \sim \frac{1}{6}\left(\frac{\delta T}{\Delta T}\right)^2, \tag{2.17}$$

where δt is the delay between points. This equation is derived assuming an exponential temperature dependence in the relaxation pulse. An acceptable fractional error in $\frac{dT}{dt}$ is found to be 2×10^{-4} and from this the delay between points δt can be found. The smaller the delay between points δt the larger the frequency, which results in greater random noise introduced into the measurement. The random error can be reduced by repeating the same pulse several times and averaging. The number of repeats needed is calculated using the $20\,\mathrm{nV}/\sqrt{Hz}$ value of RMS noise and the need for 1 % accuracy in heat capacity. Once the delay between points is found then the number of points needed is calculated based on the length of the pulse. Finally care is taken to ensure enough points are taken to fit the 50 Hz noise for subtractions. This can be done by taking twice as many points as required and then averaging consecutive points.

2.4.4 Long Relaxation Analysis

Once the data has been taken, all the pulses taken at one temperature are averaged together. The data is then fourier transformed and any peaks due to noise are found.

A sine wave of the noise frequency is fitted and subtracted from the data. The resulting voltage vs time curves are converted into resistance and power curves. The resistances are then converted into temperatures using a Chebyshev polynomial fit to the bare chip ln(R) vs T curve. To calculate $\frac{dT}{dt}$, a local quadratic fit around the temperature point is performed and then differentiated. Finally the heat capacity can be calculated using equation 2.6. All pulses across the entire temperature range are analysed in this way and the resulting points are then averaged together in 10 mK bins. A schematic of this process is shown in Figure 2.18 for a typical pulse.

2.4.5 Heat Capacity of Silver and Copper

Measurements of silver have been used by several groups to test the method used for measuring heat capacity. Silver is used as it is constant in field, has a very small nuclear magnetic spin and is well documented in the literature. The addenda is measured before every measurement and subtracted. The mass of the silver sample measured was 1433 μg which has a heat capacity similar to the organic superconductor crystals. The measured heat capacity using the vapour pressure calibration produces a heat capacity which is correct to 1 % over most of the temperature range but deviates below 0.5 K as shown in Figure 2.19. This deviation is partly due to the Chebyshev polynomial not reproducing the calibration well at the lowest temperatures and partly due to error in the calibration. The Chebyshev is reproducing R(T) well as the points have a random error of less than 2 mK below 1 K. The ~6 % error produced in the heat capacity is most likely down to the Chebyshev fit not reproducing $\frac{dR}{dT}$ well over small temperature ranges. This is shown in Figure 2.19. The original and adjusted calibration $\frac{dR}{dT}$, compared to the points used to generate the polynomial, are shown and it is clear the Chebyshev polynomial has to oscillate on the scale of 5 %. The adjustments made are all $\leq$ 3 mK which is consistent with the error on the vapour

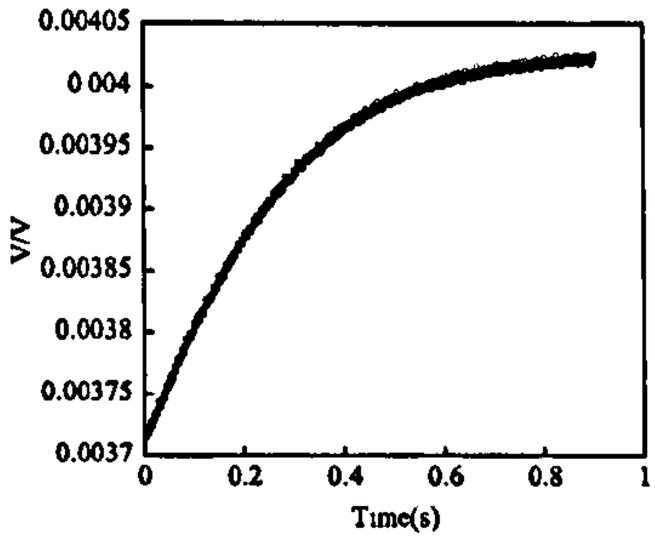

Raw Voltage data

All pulses are averaged together, typically at base temperature several hundred are taken

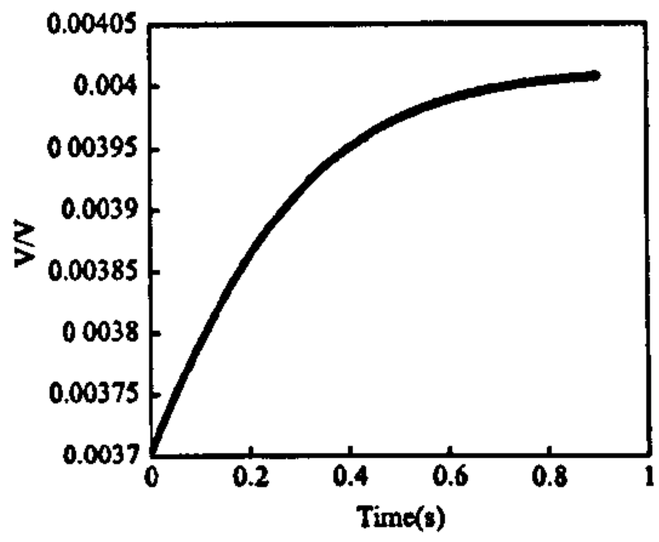

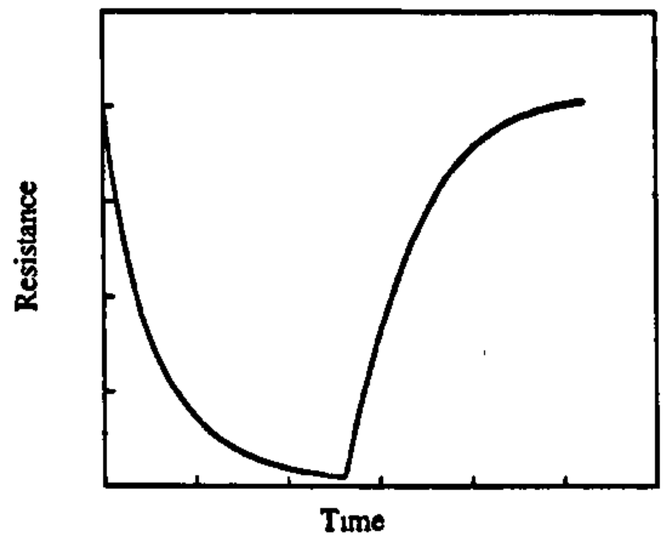

Any noise signals are filtered from the averaged pulse, the positive and negative pulses are averaged together and then converted into resistance.

Resistance is converted into temperature using a Chebyshev fit to ln(R(T)).

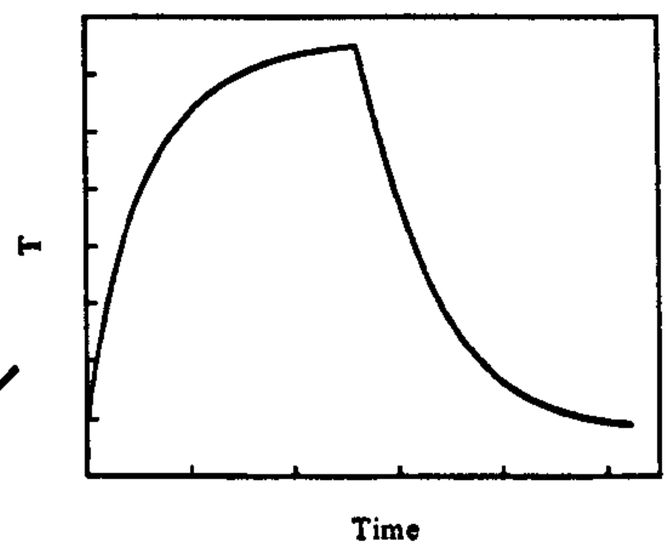

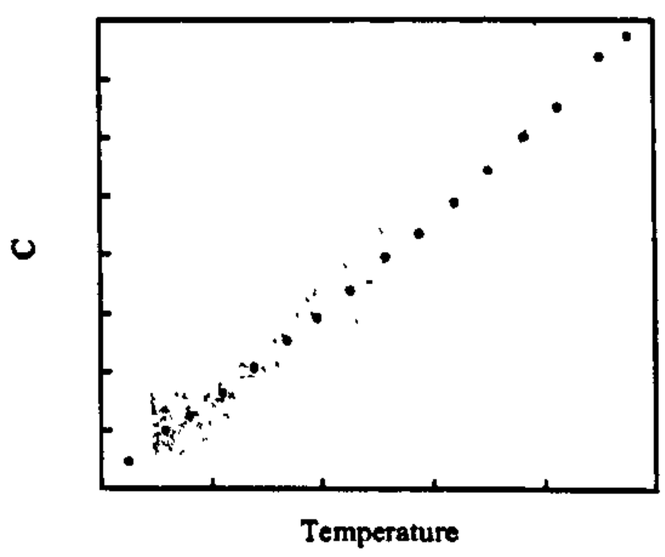

Heat capacity can then be calculated using a local quadratic fit around each point to get dT/dt.

Finally heat capacity is averaged in 10mK bins (large points).

Heat Capacity

Figure 2.18: Schematic showing steps to taken to calculate Heat Capacity from raw voltage signal for a typical pulse.

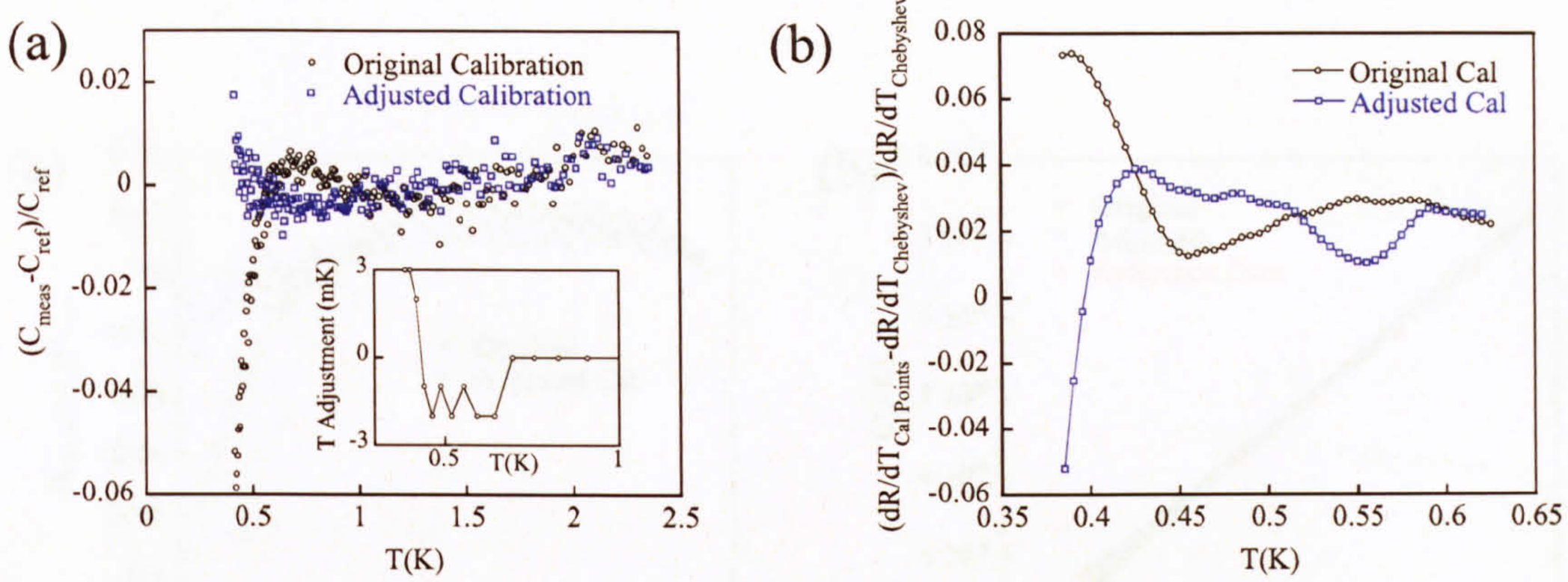

Figure 2.19: (a) Error in measured silver heat capacity C, for original calibration and adjusted calibration. Inset: Adjustments that were made to the original calibration (all $\leq$3 mK). (b) Deviations from the calibration points $\frac{dR}{dT}$ compared to the Chebyshev polynomial.

pressure calibration. To check that the adjusted calibration measured the correct heat capacity consistently, a large sample of copper was prepared. The sample of copper had a heat capacity approximately ten times that of the silver sample measured previously and a different temperature dependence. Good agreement was found again between the reference data and the measured heat capacity, as shown in Figure 2.20. It should be noted that although the Chebyshev polynomial is not a perfect reproduction of R(T), it is the best that has been found. Other methods to reproduce R(T), for example a quadratic fit to ln(R) vs $T^{-0.5}$ which approximates a linear relation, have not been as effective.

2.4.6 Heat Capacity of Silver and Copper in Field

In 14 T, the highest field, the measured heat capacity of silver is compared to the zero field measurement. Silver has a constant heat capacity in field and the addenda is assumed to be constant. The 14 T measurement of silver is shown in Figure 2.21, the error on the original calibration is larger than in zero field, up to 10 % and over a

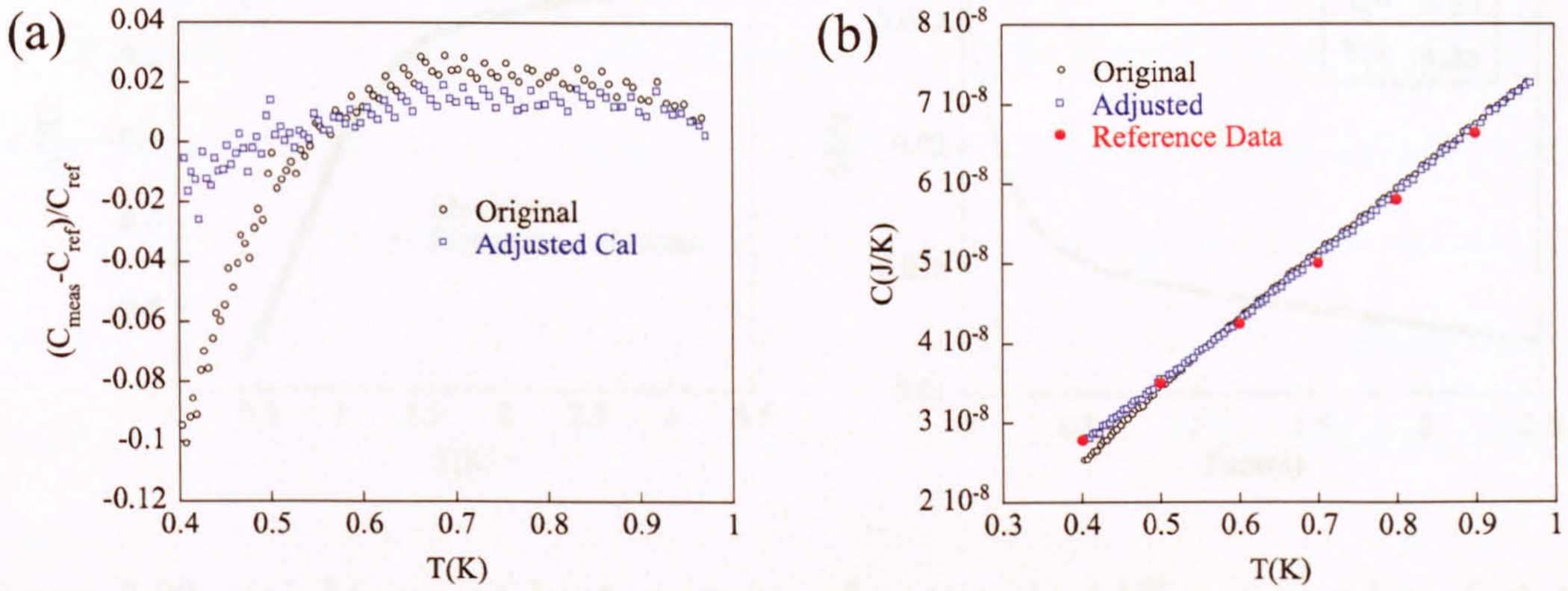

Figure 2.20: (a) Error in measured copper heat capacity C, for original calibration and adjusted calibration. (b) Measured Heat Capacity compared to reference data.

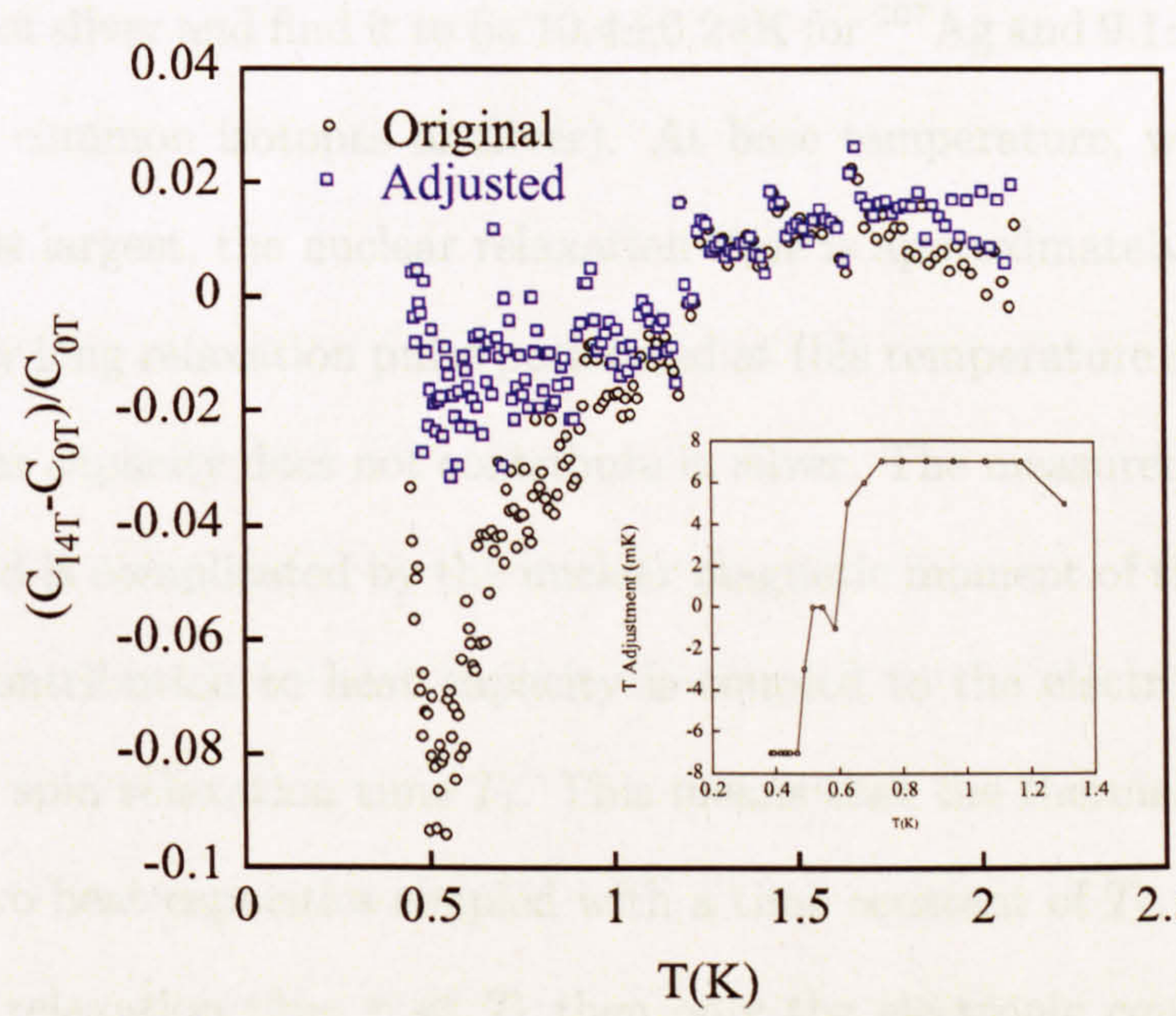

Figure 2.21: The measured heat capacity of silver in 14 T plotted as deviations from the measured zero field data. For silver, the total measured heat capacity should be the same in 14 T and 0 T.

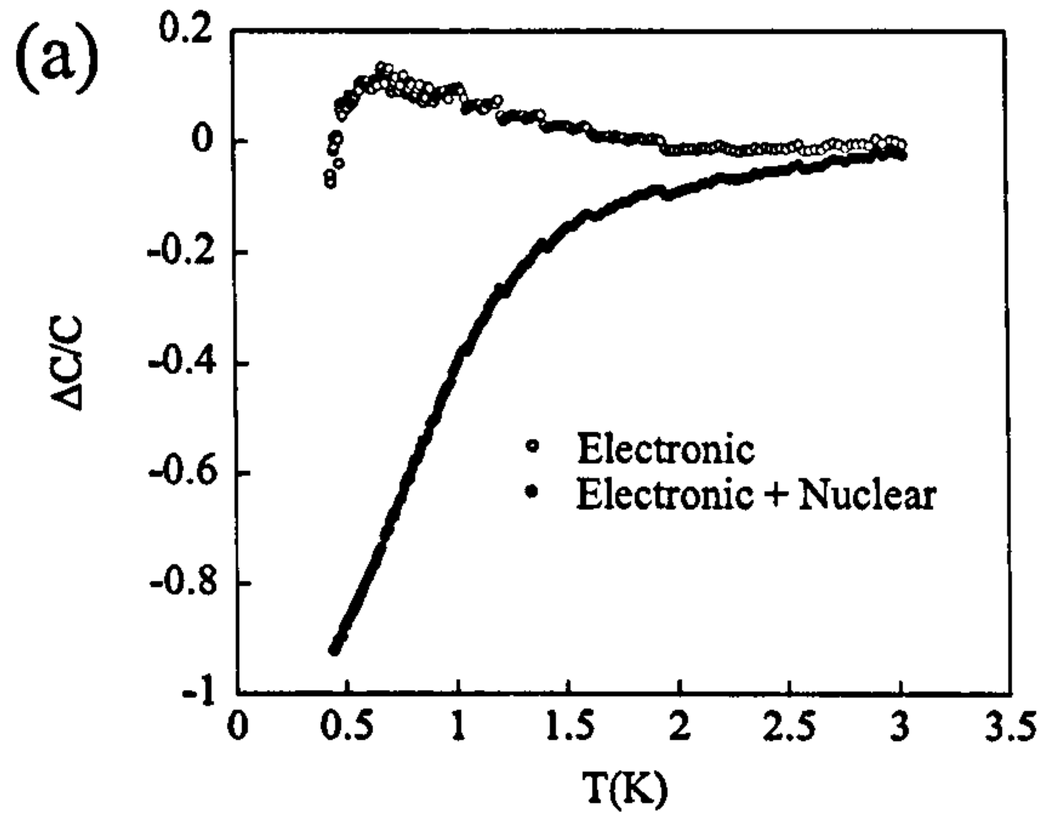

Figure 2.22: (a) Measured heat capacity of copper in 14 T compared to just the electronic contribution and the electronic contribution plus the nuclear contribution. (b) 400 mK temperature relaxation pulse with a fit to the equation found by [68]. The nuclear relaxation time T_1 is found to be 4.2 s, which is in good agreement with [68].

larger temperature range. The heat capacity due to the nuclear moment of silver does not contribute to the measurment due to the large value of T_1. Narath *et al* [67] have measured TT_1 of silver and find it to be 10.4±0.2 sK for ^{107}Ag and 9.1±0.2 sK for ^{109}Ag (the two most common isotopes of silver). At base temperature, where the nuclear heat capacity is largest, the nuclear relaxation time is approximately 40 s. This is far longer than any long relaxation pulse performed at this temperature and consequently the nuclear heat capacity does not contribute in silver. The measurement of copper in a magnetic field is complicated by the nuclear magnetic moment of the copper atoms. The nuclear contribution to heat capacity is coupled to the electronic contribution by the nuclear spin relaxation time T_1. This means that the thermal diagram can be modelled as two heat capacities coupled with a time constant of T_1. If the relaxation occurs with a relaxation time $\tau \ll T_1$ then only the electronic contribution will be measured, however if the relaxation occurs with $\tau \gg T_1$ then both the electronic contribution and the nuclear contribution will be measured. The measurement of copper in 14 T shows poor agreement with both the reference data when considering

just the electronic contribution and the reference data when considering the electronic plus the nuclear contribution, see Figure 2.22. This is because the relaxation time τ is of a similar size to the nuclear relaxation T_1. The consequences of this can be seen when looking at the pulse shape at 400 mK, the temperature does not settle even after several seconds. This pulse can be analysed using a simple model as described by Andraka [68]. This analysis is very similar to that for the case of a τ_2 effect. Instead of one relaxation, there are now two exponentials with two different time constants τ_a and τ_b. A pulse of size $\Delta T(t)$ has a time dependence of

$$\Delta T(t) = \frac{\Delta T(0)}{\tau_a - \tau_b}\left((\tau_a - T_1)e^{-\frac{t}{\tau_a}} - (T_1 - \tau_b)e^{-\frac{t}{\tau_b}}\right). \tag{2.18}$$

Fitting this equation to the pulse produces a value of 4.2 s for T_1 (see figure 2.22). This is in reasonable agreement with the value of T_1T of 1.21 sK [69] obtained from NMR measurements. From this analysis it is clear that the long relaxation model is insufficient to describe the pulse when there is an additional time constant T_1 in the system.

In 14 T, adjusting the temperature points by up to 7 mK can bring the silver heat capacity into good agreement with the zero field data. These adjustments are much larger than the 3 mK ones made in zero field. The error on the vapour pressure calibration is 5 mK in zero field and adjustments of 7 mK in field could be the result of increased noise levels due to the field. This coupled with the reduced thermal conductivities due to the magnetoresistance of the thermal links could lead to an increased error in the vapour pressure calibration in a magnetic field.

Silver was measured in several other fields to check the calibration of the main stage Cernox. As well as 0 T and 14 T, 3 T and 7 T were also measured. The analysis process for each field is the same as described for 14 T. However the adjustments that

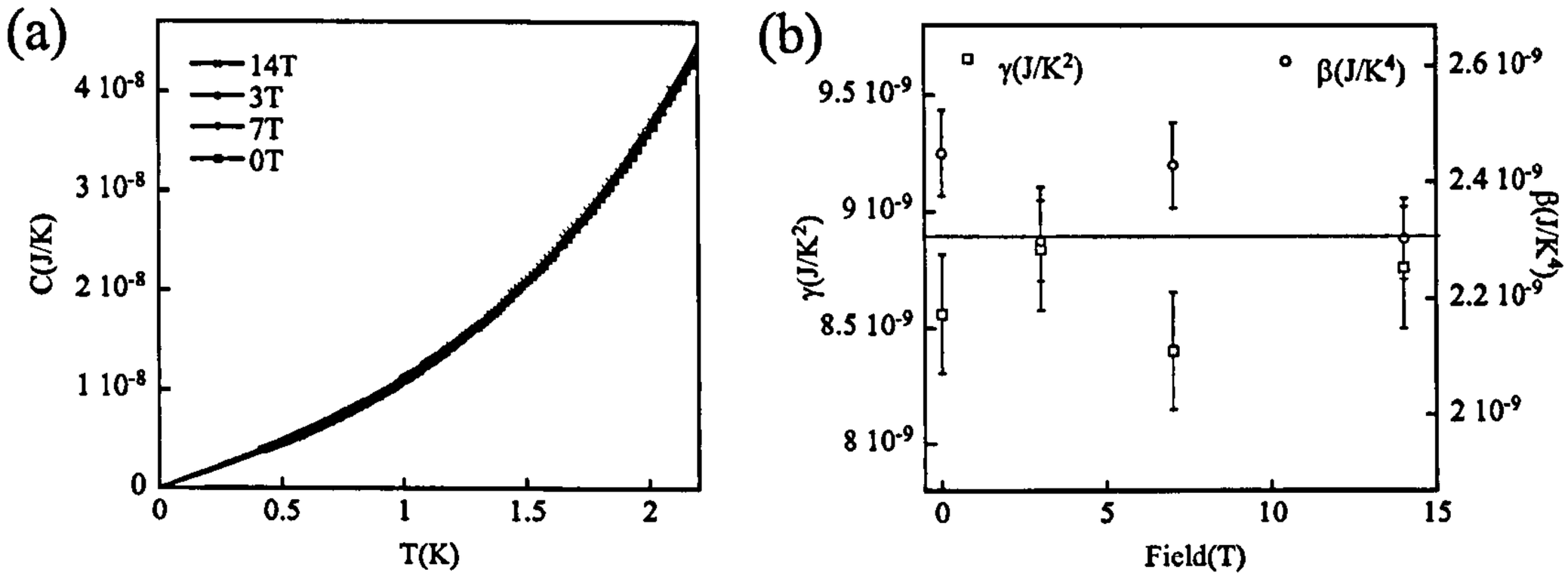

Figure 2.23: (a) Heat Capacity of silver in four fields. (b) Measured γ and β of silver for each field. Solid line represents the values of γ and β obtained from the reference data.

were required were smaller, typically closer to the zero field adjustments of 3 mK. Figure 2.23 shows the heat capacity in each of the four fields and the measured γ and β of silver in each field. The error bars shown in Figure 2.23 are 3 % of the value and represent the extrapolation to zero temperature and the change which occurs when changing the fitting range. After the calibration adjustment the heat capacity is accurate to 2 % in every field over the whole temperature range.

2.4.7 AC Calorimetry Method

To measure the heat capacity using the AC calorimetry method, the same electrical circuit is used as the one used for bare chip calorimetry. Two Stanford 830 lock in amplifiers are used to generate the AC current and measure the first and third harmonic voltages. The measurement of the third harmonic is performed with a 90° phase shift as this is what is expected for an ideal system. A series resistor is placed across the lock in output in order to generate the correct current. Before an AC heat capacity measurement can be made, the frequency dependence of the phase and the signal amplitude must be measured in order to determine the appropriate

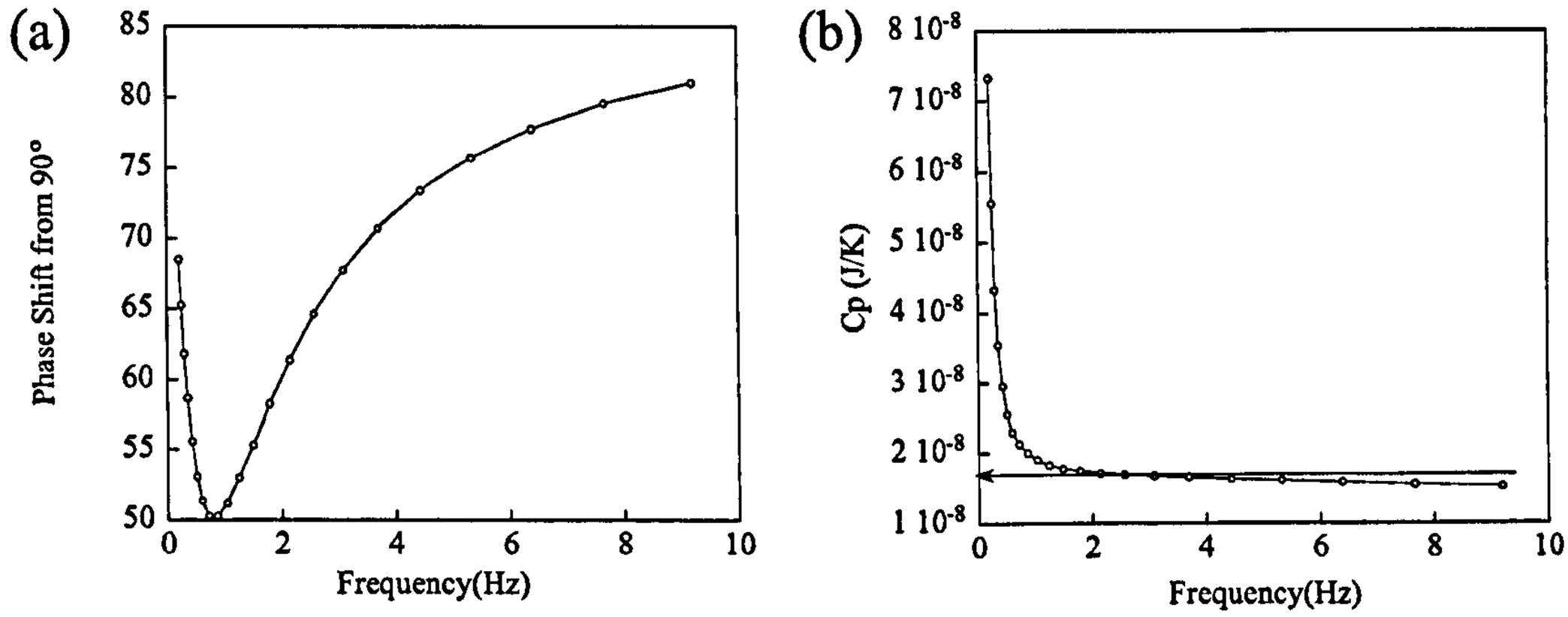

Figure 2.24: (a) Frequency dependence of the phase measured from 90°. (b) The corresponding heat capacity value for each frequency, the arrow is the correct value.

measurement frequency. The ideal frequency is when $\tau_b^{-1} \ll \omega \ll \tau_i^{-1}$ where τ_b is the time constant of the stage to the bath and τ_i is the internal time constant between the sample and the bare chip. In the Sullivan and Seidel model [70] if this criterion is fulfilled then the $f(\omega)$ is $\sim$1 and the phase shift δ is 90° however this model does not apply in this case. This means the phase is shifted from 90° but is still a minimum when closest to the ideal regime. Figure 2.24 shows the frequency dependence of the phase and the heat capacity. The phase shift never falls to zero indicating that it is not possible to be in the desired frequency regime. Consequently when the minimum phase is selected there is a significant error on the heat capacity. In this case the error is 5 %. In general, the lowest temperatures are furthest from the ideal regime and have the biggest error. The example shown was taken at 400 mK and represents the biggest error. The frequency is always selected as the point where the phase shift from 90° is minimum.

2.4.8 Angle Dependent Heat Capacity

Using AC calorimetry on the bare chip leads to better resolution in the heat capacity at the expense of a systematic error of around 5 %. This makes AC calorimetry better suited for use in examining angle dependence or field dependence of heat capacity than examining the precise temperature dependence. Silver was once again measured to test the accuracy of the method. A larger silver sample with a mass of 5802 μg was placed on the rotator. The rotator was controlled with a geared down stepper motor with a ratio of 176 turns to 1. This combined with the low temperature worm drive which has 20 turns to 1 results in a angular resolution of less than 1°. A Toshiba THS118 Hall sensor was attached to the rotator and a 1 T field applied. The Hall voltage of the sensor was measured using a lock in amplifier to test the reproducibility of the rotation, this is shown in figure 2.25. The rotator was found to be very reproducible, as long as a backlash of 1.5° was taken into account. The backlash can be seen in figure 2.25, where rotating clockwise and then anticlockwise shows a phase shift of 1.5°. To test the rotation dependence, the field was set to 14 T as any errors from any angle dependence of the magnetoresistance of the Cernox or misalignment of the Cernox will be maximum in this field. To measure heat capacity as a function of angle, the stage temperature was set, followed by a 2 minute wait to allow the sample to come to thermal equilibrium. Fifty data points were then recorded over the course of a minute and averaged together. The stage was turned causing heating and the process repeated. As the ^{3}He system used is a sorb pumped, one shot system then after multiple rotations the ^{3}He is expended and has to be recondensed. This is not a problem for measuring silver, however when measuring a superconductor this can present a problem when in the vortex state. Figure 2.26 shows the heat capacity of silver as a function of angle at two temperatures in 14 T. The RMS error on the measurement is 0.12 % and only small structure is observed on the 0.1 % scale. This

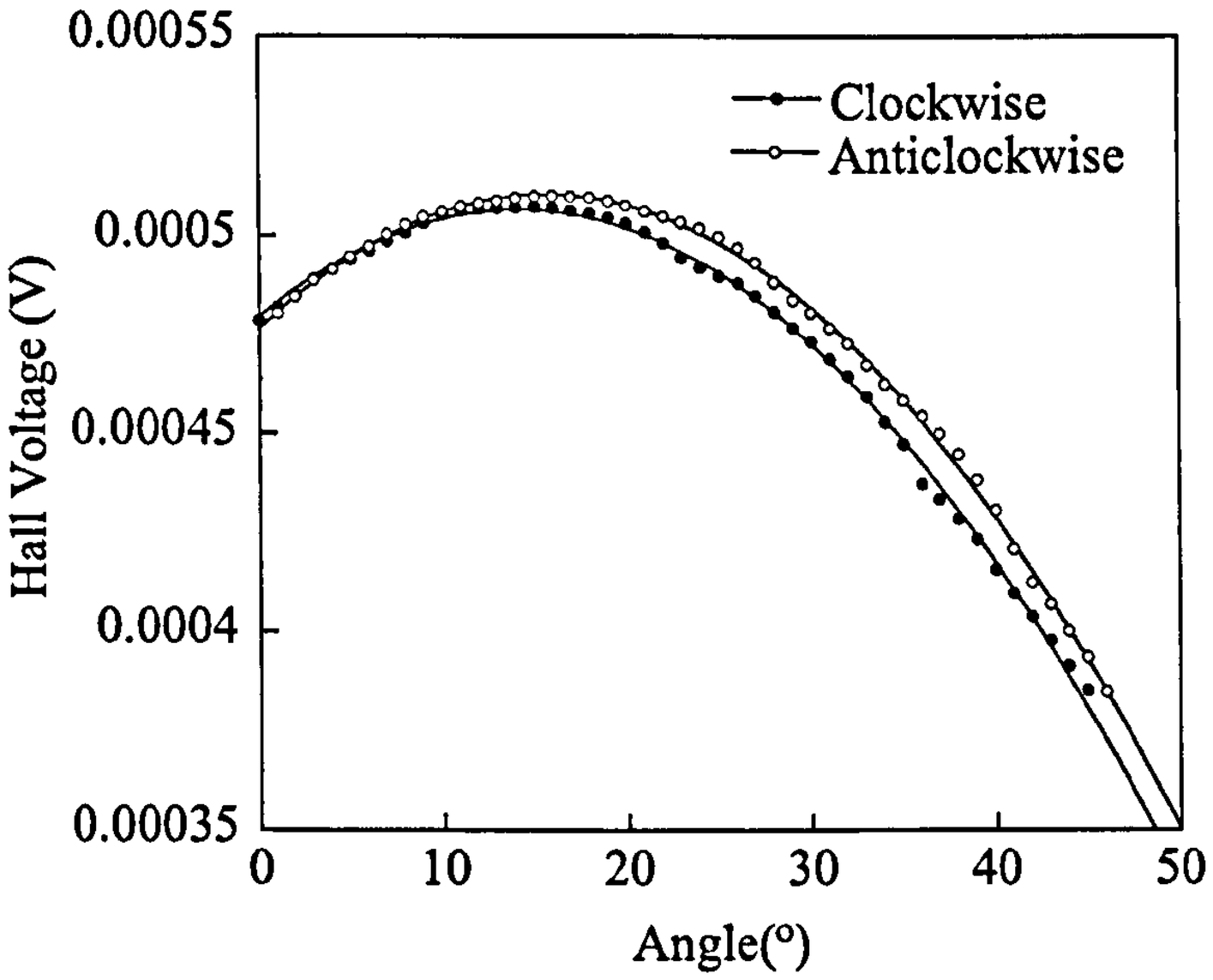

Figure 2.25: The Hall voltage when rotating first clockwise and then anticlockwise. The lines are fit to a sine curve and have a phase difference of 1.5°.

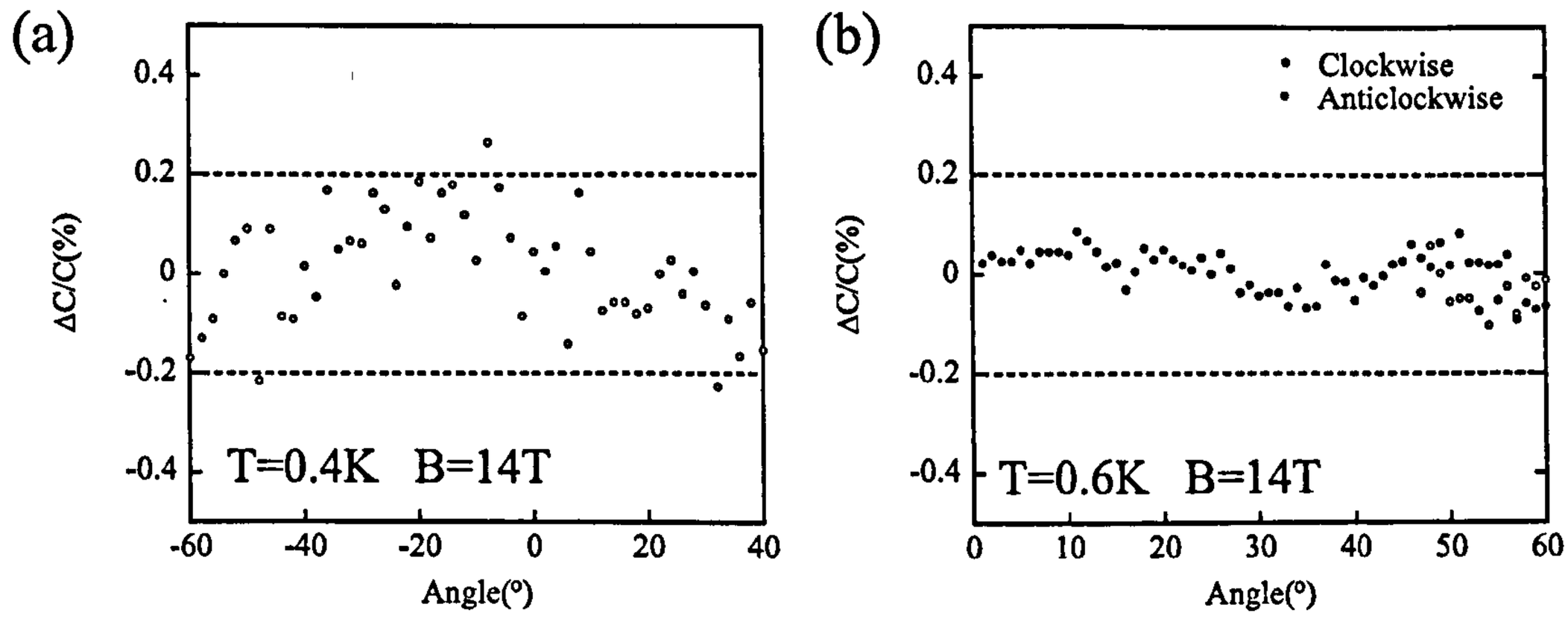

Figure 2.26: (a) Heat Capacity as a function of angle for silver at 0.4 K and 14 T. Plotted as deviations from the mean in percentage. (b) Heat Capacity as function of angle for silver at 0.6 K and 14 T, some points were taken in both anticlockwise and clockwise directions to check reproducibility.

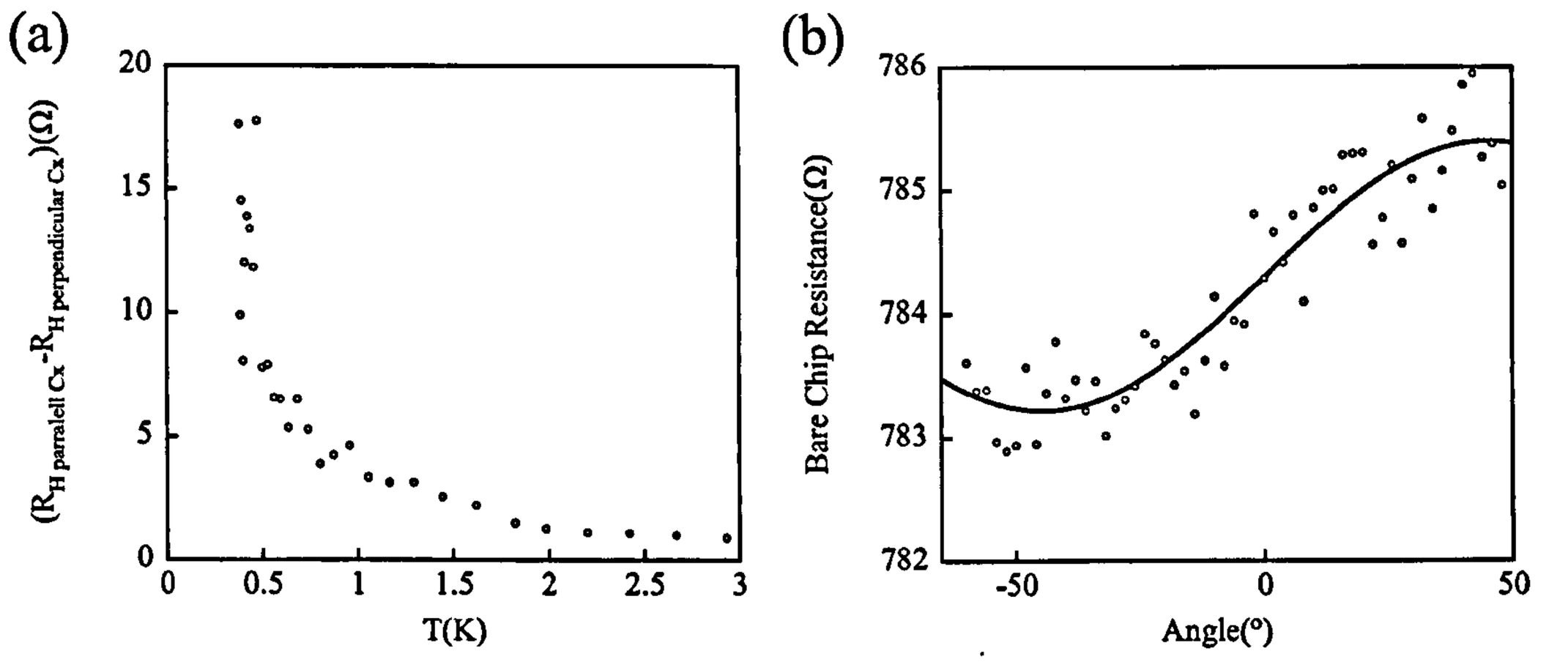

Figure 2.27: (a) Anisotropy of the bare chip Cernox. (b) Variation of resistance with angle

structure mostly likely stems from the anisotropy of the magnetoresistance of the bare chip Cernox. The bare chip Cernox is a thin film thermometer and consequently one might expect small anisotropy in the plane of the film but a reasonable anisotropy between the parallel and perpendicular directions. The difference between calibrating the bare chip perpendicular to the field and parallel to the field is shown in Figure 2.27. At 400 mK this is about 18 Ω, the variation of bare chip resistance with angle is also shown with a two fold anisotropy fit. The magnitude of the two fold term is 1 Ω. A change of 1 in 18 produces a misalignment angle of $\sim 3°$. There are several sources or error associated with this method of finding the misalignment angle. The assumption that the bare chip was perfectly parallel and perpendicular to the field could mean the anisotropy is larger. If there is any in plane variation of the Cernox resistance then this will also reduce the misalignment angle. Consequently, the value 3° should be considered as an upper boundary to the misalignment angle. This misalignment most likely arises from the non-uniformity of the glass fibres used to produce the chip.

2.5 Penetration Depth Techniques

2.5.1 Penetration Depth Measurements

Even though the absolute penetration depth of a superconductor is several thousands of Angstroms, at low temperature it can change by a few Angstroms at most. Therefore an extremely sensitive experimental setup is required in order to obtain accurate results. Hardy et al [14] had particular success measuring the penetration depth in YBCO using a microwave cavity and measuring the surface impedance of the sample. The sample is lowered into a microwave cavity and the change in frequency is measured. From the change in frequency the penetration depth can be extracted. The frequency of the cavity is 900 MHz. In a sample with dimensions of 1.5 mm, changes in the penetration depth of better than 1Å can be resolved.

Susceptibility measurements are able to extract the temperature dependence of the penetration depth but not its absolute value. To measure the absolute value of the penetration depth in the Meissner state is difficult. To extract the absolute penetration depth by measuring the susceptibility requires a good knowledge of the volume of the superconductor and is complicated by de-magnetising factors. Muon spin rotation can be used to measure the penetration depth in the mixed state by measuring the length scale of the vortices, however this length is not always the same as the Meissner state penetration depth due to non-local effects, the field dependence of the penetration depth and pinning effects.

2.5.2 Tunnel Diode Oscillator Technique

This study will employ a radio frequency tunnel diode oscillator technique. This technique involves an ultra stable resonant circuit with the sample placed in the inductor. Changes in the resonant frequency are directly proportional to the changes

in penetration depth (similar to the microwave surface impedance technique). The exact experimental setup has been extensively described in [71] and [72]. I will provide an overview here.

The experiment is mounted on a pumped ^{4}He cryostat with a base temperature of 1.3 K. The oscillator technique was developed by van der Grift [73] for low temperature operation and has a sensitivity of 1 ppb. The oscillator electronics consists of a cold section which is mounted on the cryostat and temperature stabilised to 4.5 K and a room temperature section. The resonant circuit is stabilised with a tunnel diode which has a DC bias applied so as to be in the region of the I-V curve with a negative gradient. In effect this gives the tunnel diode a negative resistance which is used to compensate for losses in the resonant circuit. A circuit diagram of the low temperature section and a schematic of the room temperature processing is shown in Figure 2.28. Of the components shown in the figure, R_1 isolates the circuit from room temperature rf interference while still passing the DC current, R_2 sets the correct DC bias of the tunnel diode, R_3 damps oscillation caused by the tunnel diode's intrinsic capacitance, C_1 allows a small amount of the signal up to room temperature, C_2 is essentially a short circuit at the operating frequency, L_2 is the tap and C_3 and L_1 form the resonant circuit. The values of these components can be calculated following a recipe by van der Grift [73] based on the maximum possible power, the operating frequency and the impedance of the LC combination at resonance. For this experiment the values of the capacitors and resistors have been determined in [71] and are shown in Figure 2.28. For the inductor L_1 a coil of wire is wound to have the maximum Q possible and L_2 is found by trial and error. The room temperature signal is amplified and then mixed with a signal from a local oscillator. The circuit typically oscillates at $\simeq$ 12 Mhz and the local oscillator is offset by 3 kHz lower than the resonant frequency. The mixed signal is then processed through a pre-amplifier with a 3 kHz band pass filter before being

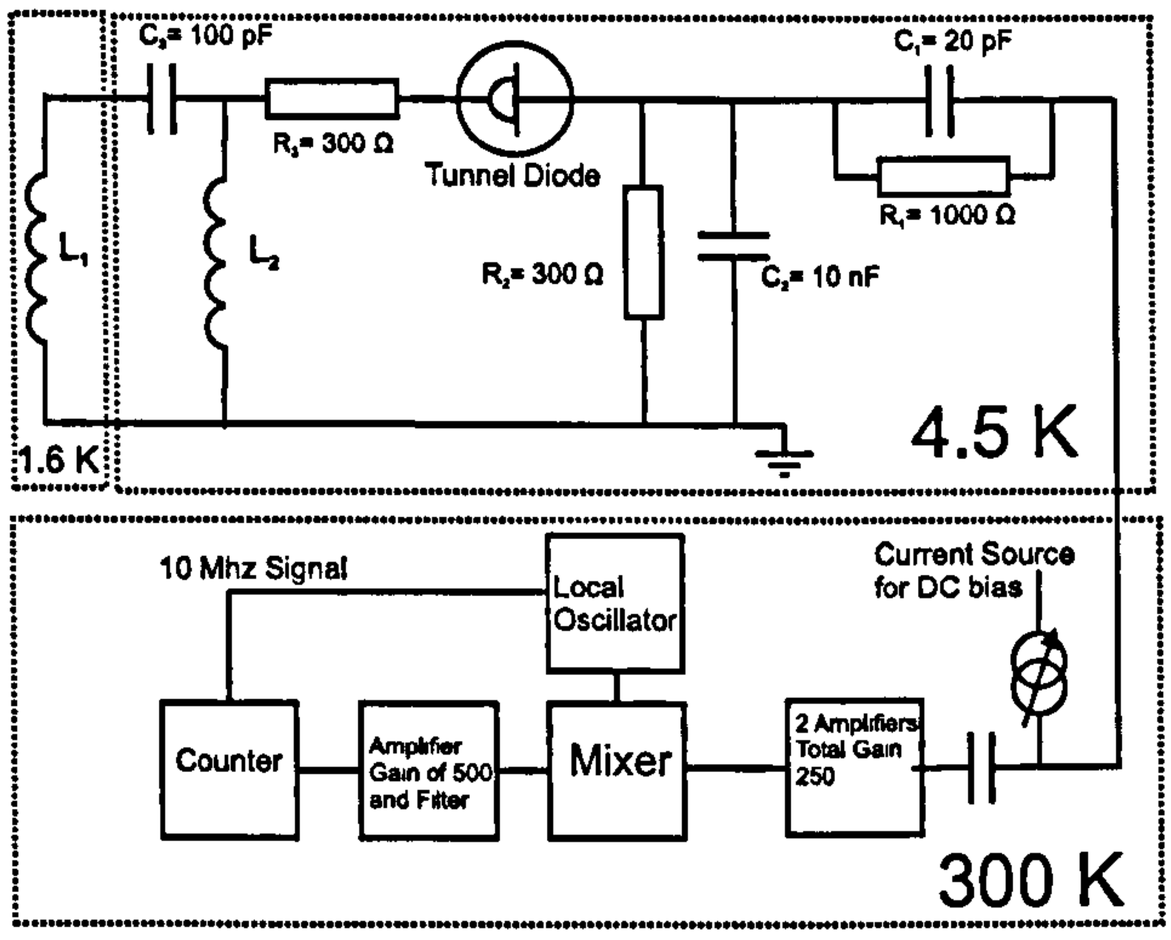

Figure 2.28: Basic diagram of the electronics. The sample is inserted into L_1 (which is stabilised at around 1.6 K) and the temperature of the sample can be varied from 1.5 k to 100 K.

measured by a frequency counter. The frequency counter is tied to the local oscillator by a 10 Mhz signal. The counter records the difference between the local oscillator and the resonant frequency and this is logged by a PC. The sample is mounted on the end of a sapphire rod and is inserted into the coil which serves as inductor L_1 for the resonant circuit. The sapphire rod and sample can be temperature controlled between 1.5 K and 100 K. The field produced by the inductor is $< 10^{-4}$ T which ensures the sample is in the Meissner state and the vacuum can is encased in mu-metal to reduce external fields. The sample can be measured in two different orientations, the field parallel to the c-axis or the field parallel to the ab-plane. The coil is temperature stabilised between 1.3 K and 1.8 K depending on the sample temperature. Ramping the temperature of the sample and stabilising the other parts of the experiment results in a change in resonant frequency directly proportional to the penetration depth. The sample can be extracted from the coil when cold in order to measure Δf_0 (change of frequency between the sample in and out of the coil measured at base temperature)

which is dependent on the superconducting volume and demagnetising effects of the sample.

The constant of proportionality between the measured frequency shift f and the penetration depth λ is impossible to know accurately for a real sample of arbitrary shape. If the dimensions of the sample are known then an approximation can be made as described in [74],

$$\frac{\Delta f}{f_0} = \frac{1}{H^2} \int \mathbf{M_{ac}} \cdot \mathbf{H} dV. \tag{2.19}$$

Equation 2.19 shows the relative frequency shift for a superconducting sample placed in the coil. A cuboid sample placed in the H parallel to c configuration has all the currents flowing in the ab-plane and λ_{ab} is measured. Prozorov *et al* [74] analytically solve the London equations for a square sample. For a square sample there is no simple demagnetising factor like a sphere. They approximate by assuming there is an effective dimension R of a square sample which can be found from the dimensions of the sample (w and l) in the ab-plane and that $\lambda \rightarrow 0$,

$$R \sim \left(\frac{wl}{4}\right)^{\frac{1}{2}} \tag{2.20}$$

$$\frac{\Delta f}{f_0} = \frac{V_s}{2V_0(1-N)}(1 - \frac{\lambda}{R}). \tag{2.21}$$

Equation 2.21 shows the result for $\lambda << R$. V_s is the superconducting volume, V_0 is the total volume and N is the demagnetising factor. The measurement of Δf_0 reveals the effective superconducting volume and Equation 2.21 can be written as equation 2.22,

$$\Delta\lambda(T) = -\frac{R}{\Delta f_0}\Delta f(T). \tag{2.22}$$

Equation 2.22 can then be used to determine the penetration depth from the raw frequency shifts in the H parallel to c configuration.

In the H parallel to ab configuration the currents flow along the c-axis and either the a or b axis (depending on sample orientation). This results in a contribution from both λ_c and λ_a. If the sample has dimensions such that $l_c << l_{a,b}$ then the λ_c contribution will be small. The contribution due to λ_c can be quantified by considering the dimensions of the sample. The volume contribution from the ab side will be $l_a l_b \Delta\lambda_a$ and the volume contribution from the bc side will be $l_b l_c \Delta\lambda_c$. Therefore the frequency shift can be related to the volume change due to λ in equation 2.23.

$$, \frac{\Delta f}{\Delta f_0} = \frac{\Delta V}{V_0} = \frac{2 l_a l_b \Delta\lambda_a + 2 l_b l_c \Delta\lambda_c}{l_a l_b l_c}. \tag{2.23}$$

This can be considered in another way,

$$\Delta f = \frac{2\Delta f_0}{l_c} \Delta\lambda_{eff}, \tag{2.24}$$

where $\Delta\lambda_{eff}$ is $\lambda_a + \frac{l_c}{l_a}\Delta\lambda_c$. In this form it is obvious that the ratio of l_a to l_c defines the contribution of λ_c, for a thin platelet sample this can be as low as 1%. The anisotropy of the superconductor must also be taken into account, if $\lambda_c >> \lambda_a$ then a large contribution of λ_c will still be seen even for platelet samples.

2.5.3 Susceptibility of Superconducting Powders

Susceptibility measurements of superconducting powders can be used to measure both the temperature dependence of λ and provide an estimate of λ_0. The analysis relies on the assumption that the powder grains are spheres with a radius r the same order of magnitude as λ. Following Shoenberg's [75] analysis, the susceptibility of a small sphere will depend on the amount of penetration of the field. If $\lambda >> r$ then the entire sphere will be penetrated and the susceptibility will be small. If $\lambda << r$ then

the sphere will act like a perfect diamagnet and the susceptibility will tend to -3/2 (including demagnetising effect). A powder sample will have a susceptibility χ which is a sum of all the grains,

$$\chi = -\frac{3}{2}\frac{\Sigma_i^N \left(1 - 3\frac{\lambda}{r_i}\coth\left(\frac{r_i}{\lambda}\right) + \frac{3\lambda^2}{r_i^2}\right) r_i^3.n_i}{\Sigma_i^N r_i^3 n_i} \tag{2.25}$$

In equation 2.25, the sum is over all grain sizes i, N is the total number of grain sizes, n is the number of grains of that size and λ is the penetration depth. Therefore if the size distribution of the powder is known then a fit to equation 2.25 can be done and the penetration depth extracted.

2.6 Conclusion

In summary, a precise heat capacity experiment has been built which is capable of measuring the heat capacity of $\sim 100\mu g$ samples to an accuracy of 2 % down to 400 mK and in a magnetic field up to 14 T. The experiment is very sensitive to the thermometer calibration. To solve this problem, a vapour pressure thermometer was constructed which is capable of 1 mK accuracy from 400 mK up to 4.2 K and is field independent. Although the vapour pressure thermometer achieved the required accuracy, the accuracy of the heat capacity was limited by the Chebyshev fit to the thermometer calibration. Finally AC calorimetry was used to measure heat capacity as a function of field angle with a resolution of 0.1 %. The rotator has an angular resolution of 1° and a misalignment angle $\lesssim 3°$.

The tunnel diode oscillator technique has been developed in [72], [71]. The setup is capable of measuring $\Delta\lambda(T)$ to a resolution of 1 Å in a crystal with dimensions ~1 mm. It is not possible to measure the absolute penetration depth using this method and

the accuracy of the calibration is about 20 % due to the difficulties associated with measuring small crystals and demagnetising effects.

Chapter 3

Angle Dependent Heat Capacity Measurements of the Organic Superconductors κ-$(ET)_2Cu(NCS)_2$ and κ-$(ET)_2Cu[N(CN)_2]Br$

3.1 Introduction

The organic superconductors have attracted a considerable amount of interest due to their unconventional properties and similarities with the cuprates [6]. These similarities include a quasi-2D electronic structure, a phase diagram with a Mott insulator in close proximity to a superconducting state and a nodal order parameter. Good quality single crystals are available and comprehensive studies of the Fermiology of these compounds have been performed using quantum oscillations and angle dependent magnetoresistance measurements. The expected quasi-2D Fermi surface is observed and is well characterised. The symmetry of the order parameter has been measured

by thermal conductivity [25] [16], NMR [76] [15], penetration depth [77] and STM [78], all of which show evidence for a d-wave order parameter. Until recently the temperature dependence of the specific heat had shown evidence for a fully gapped superconducting state [13], however the latest evidence [12] supports a nodal gap. Although the majority of the evidence points to a nodal gap, the directions of the nodes is still a controversial subject. STM [78] and angle dependent thermal conductivity [25] report evidence of nodes at 45° to the crystal axis however magneto-optical measurements [79] show evidence for nodes along the crystal axis.

Angle dependent heat capacity measurements have been used on several compounds: Sr_2RuO_4 [9], $CeCoIn_5$ [10] and $CeRhIn_5$ [23] to measure the directions of the nodes. A considerable amount of theoretical work [17], [18] has already been done in order to interpret angle dependent thermodynamic measurements. The aim of this experiment was to measure the angle dependent heat capacity of two organic superconductors κ-$(ET)_2Cu(NCS)_2$ (κ-NCS) and κ-$(ET)_2Cu[N(CN)_2]Br$ (κ-Br) in order to resolve the controversy surrounding the order parameter symmetry of these materials. The temperature dependence of the specific heat will also be examined down to 0.4 K, a lower temperature than is measured in the latest literature. Finally quantum oscillations in the heat capacity of κ-$(ET)_2Cu(NCS)_2$ will be analysed.

3.2 Organic Superconductors

3.2.1 Crystal Structure

The crystal structure of these compounds is formed from large organic molecules which act as electron donors to different anions. The organic molecules consist of rings of atoms whose π-orbitals mix together and donate an electron to the anion, which has led to the name 'charge transfer salts'. Several organic molecules have

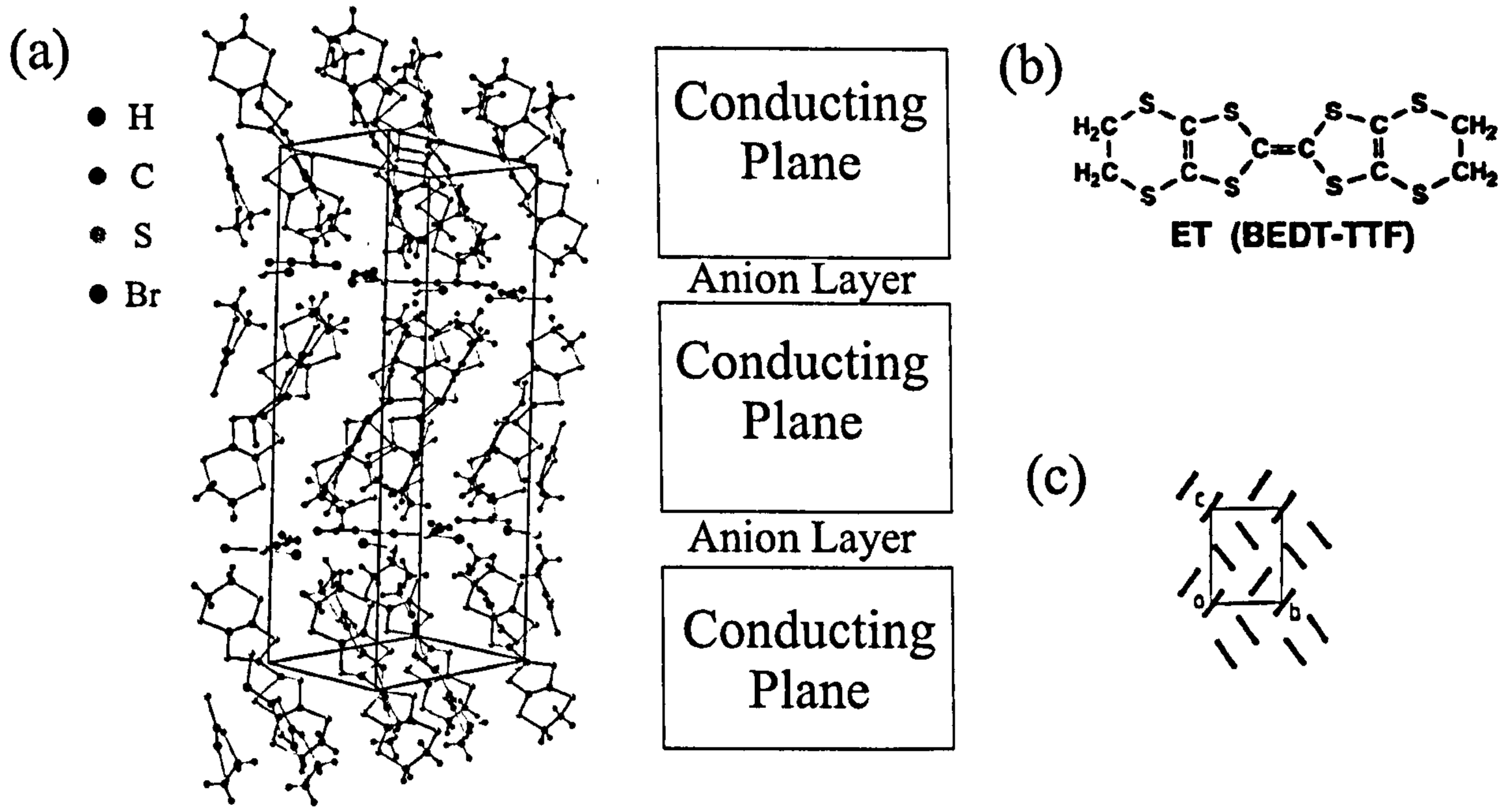

Figure 3.1: (a)The Crytsal structure of κ-Br. The structure is orthorhombic with space group P_{nma}. In this space group the b axis is perpendicular to the conducting planes [80].(b) The ET molecule [81](c) The κ stacking arrangement as viewed along the long axis of the ET molecule. [81]

been used in this process. The first compound produced in this way was TTF-TCNQ [82] which is a quasi-1D conductor. These materials attracted a lot of interest as model 1D systems. In 1982, the ET molecule was used to produce a charge transfer salt [83], this molecule creates quasi-2D systems and when combined with the anion $Cu(NCS)_2$ [84] is an ambient pressure superconductor. The κ in the chemical formula labels the stacking arrangement of the organic molecules, in the κ arrangement they are stacked as shown in figure 3.1. The stacking arrangement of the organic molecule depends on the anion although in some cases the same anion can be used in several stacking arrangements. The crystal structure of κ-$(ET)_2Cu[N(CN)_2]Br$ is shown in figure 3.1. Although the actual crystal structure looks complex, it is a good approximation to think of the structure as layers of conducting planes. The structure of κ-$(ET)_2Cu(NCS)_2$ is slightly different to κ-Br as κ-NCS is orthorhombic and κ-Br is

Compound	Space Group	a(Å)	b(Å)	c(Å)	Symmetry
κ-$(ET)_2Cu(NCS)_2$	$P2_1$	16.248	8.440	13.124	Orthorhombic
κ-$(ET)_2Cu[N(CN)_2]Br$	P_{nma}	12.949	30.016	8.539	Monoclinic

Table 3.1: Table show the lattice parameters of κ-Br and κ-NCS.

monoclinic. The lattice parameters are shown in the table 3.1 (obtained from [81]). Due to the orthorhombic distortion in κ-NCS and the conventions in which crystallographic data are presented, in κ-NCS the conducting planes are in the b-c plane, however in κ-Br the conducting planes are in the a-c plane. Both these conventions are also different to the cuprate superconductors where the conducting planes lie in the a-b plane.

3.2.2 Phase Diagram

A schematic phase diagram is shown in figure 3.2 [85]. The tuning parameter in the phase diagram is either pressure or 'chemical pressure'. The chemical pressure is changing the anion in order to change the interlayer distance. Sometimes this is referred to as U_{eff}/W where U_{eff} is the effective on-site Coulomb repulsion and W is the electron band width. As can be seen from the phase diagram, κ-Br is positioned much closer to the Mott insulator ground state than κ-NCS. In fact a full isotope substitution of deuterium for hydrogen in κ-Br creates a compound which is no longer a superconductor. The compound κ-Cl is also shown on the phase diagram, this compound is an anti-ferromagnetic Mott insulator. In the region close to the superconducting state and the Mott insulator, there can be a co-existence between the superconductor and the insulator in the same sample and consequently the line on the phase diagram is deliberately thickened to indicate this. This is discussed in more detail in relation to the glass transition below.

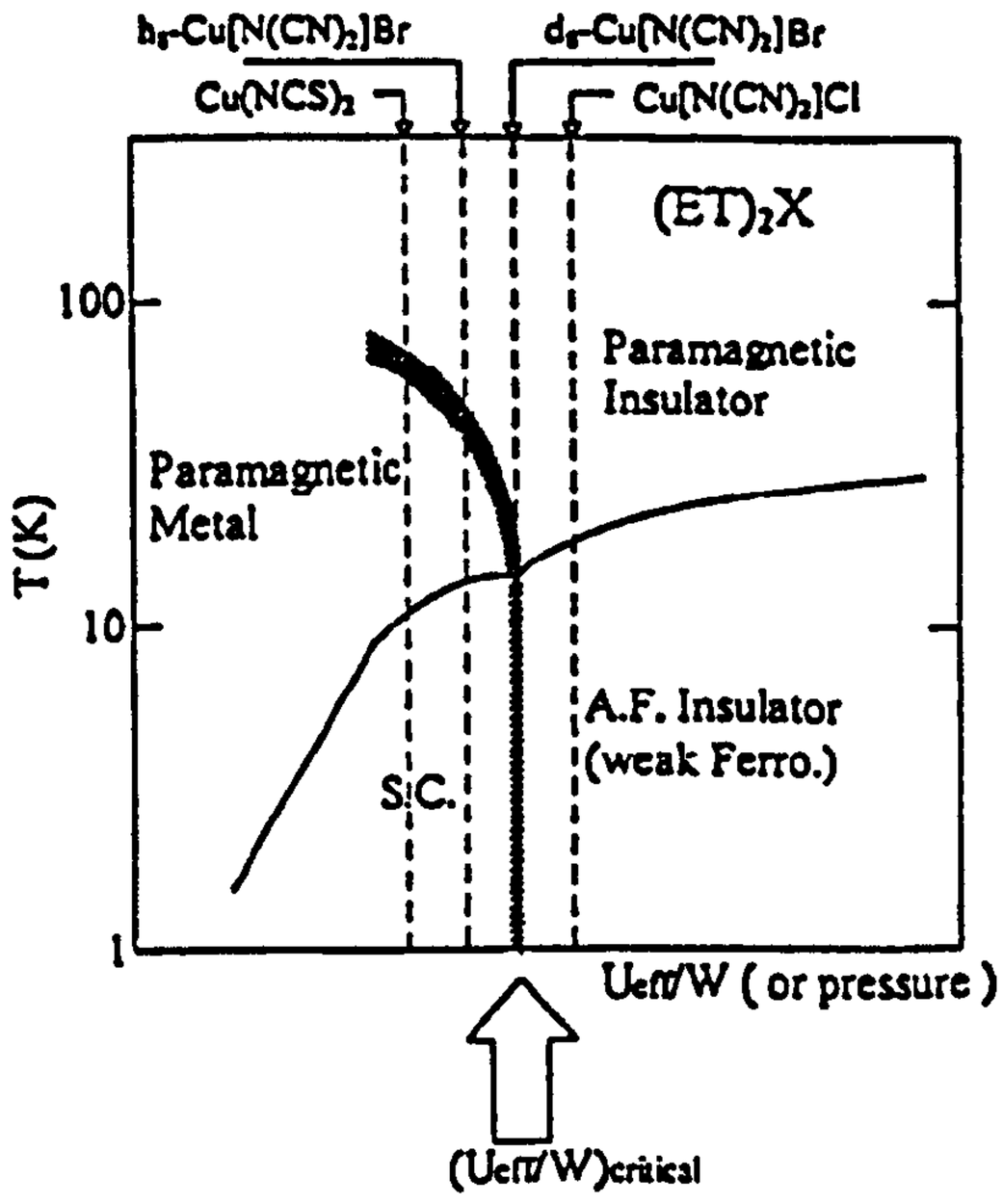

Figure 3.2: The phase diagram of the ET salts and the positions of κ-Br and κ-NCS taken from [85].

3.2.3 Fermi Surface Measurements

Shubnikov-de Haas oscillations [86] were observed almost immediately in κ-NCS. The Fermi surface consists of two small quasi-2D lenses and two quasi-1D sheets. These are the result of back folding one large quasi-2D cylinder (see figure 3.3). Simple molecular orbital calculations accurately reproduce this Fermi Surface. Although initially only the small Fermi surface lenses were observed, at higher magnetic fields a breakdown between the 1D sheets and 2D lenses was observed and the entire Fermi surface was characterised [87], [88]. The gap between the 1D and 2D sheets is small leading to an observable magnetic breakdown at fields greater than 20 T. The small lenses have a quantum oscillation frequency of 625 T (known as the α orbit) which corresponds to 16 % of the Brillouin zone. The magnetic breakdown orbit has a frequency of 3800 T (known as the β orbit) which corresponds to 100 % of the Brillouin zone. The effective mass of the two orbits is 3.5 m_e on the small lenses and 6.9 m_e on

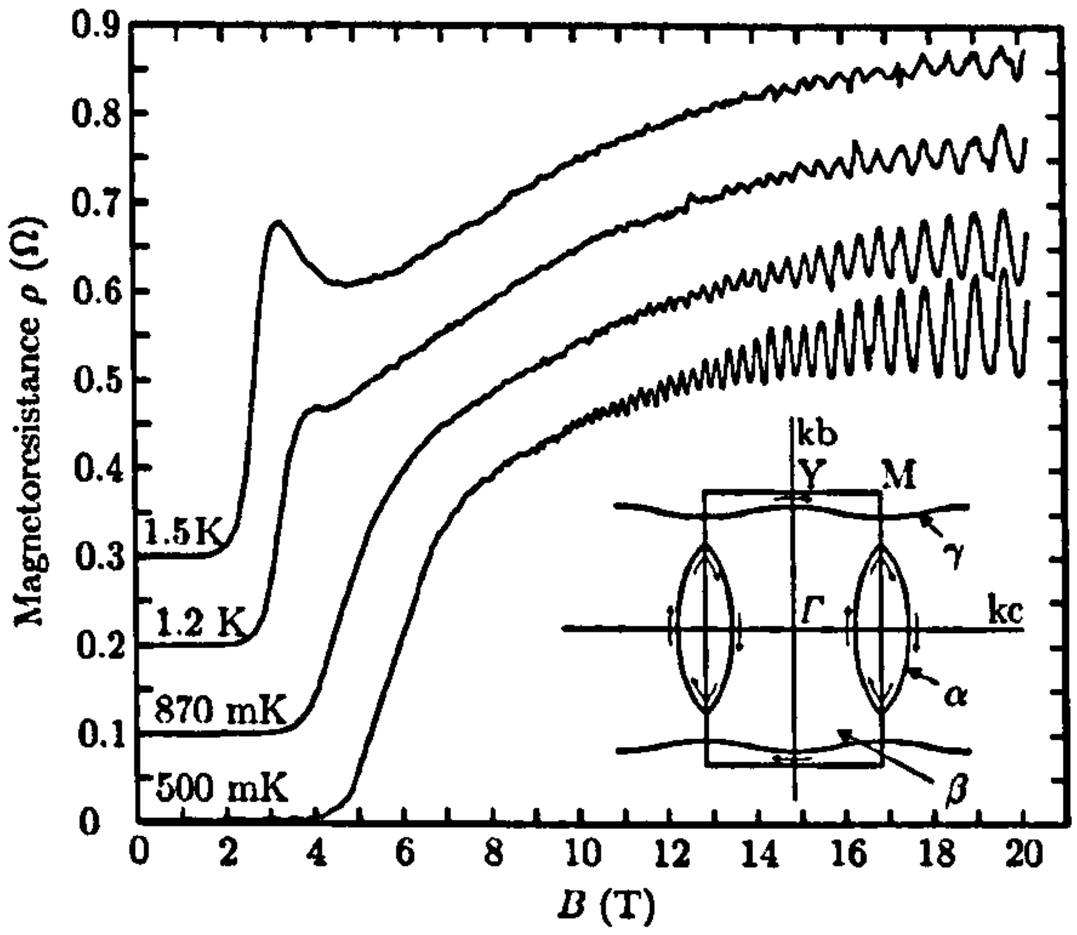

Figure 3.3: Measured SdH oscillations for κ-NCS taken from [89] . The inset shows the Fermi surface with various orbits measured.

the large breakdown orbit.

κ-Br has a very similar Fermi surface to κ-NCS although quantum oscillations are harder to observe in this compound. A comprehensive pressure study [90] [91] observes no small lenses at ambient pressure and only small pockets at higher pressure (frequency of 175 T at 12 kbar with an unexpectedly large 2nd harmonic). The large magnetic breakdown is observed, as in the NCS compound, at fields above 20 T in ambient pressure and with a frequency of 3800 T. The effective mass on the large orbit is 6.9 m_e and around 1.5 m_e on the smaller orbits. Weiss [90] suggests a structural distortion at around 200 K is responsible for the unexpected frequencies obtained for the smaller orbits.

Band structure calculations have been extensively performed on all the organic conductors (see [92] for an overview). In the κ-(ET) superconductors, a good approximation is to ignore the bonding orbitals and just take into account the two antibonding orbitals near the Fermi energy. The problem can then be solved by using three hopping integrals between the dimers in the unit cell [93] [86]. This calculation is in excellent agreement with the results of the quantum oscillation experiments.

3.2.4 The Glass Transition

The organic superconductors based on the ET molecule undergo a glass-like transition at around 80 K. This transition has been observed by AC calorimetry in κ-Br and κ-Cl [94] and thermal expansion measurements on κ-Br and κ-NCS [95]. In AC calorimetry a kink in the specific heat is observed around 80 K in the κ-Br compound, the exact temperature is dependent on the frequency at which the measurement is performed. In the thermal expansion a clear anomaly is observed at around 80 K in the κ-Br but at a lower temperature for the κ-NCS compound.

The rate of cooling through the transition can have a dramatic effect on the properties at low temperature as shown in [96]. This study reports a detailed study of the cooling rate dependence of the normal state electronic heat capacity and superconducting electronic heat capacity in κ-Br. Although only a small decrease in T_c is observed there is a large reduction in the normal state electronic specific heat. This could be explained by a phase separation in the sample of insulating and superconducting regions. This explanation is supported by Scanning Microregion Infrared Reflectance Spectroscopy (SMIRS) [97] which shows insulating and superconducting regions at the surface of fast cooled κ-Br samples. In addition measurements of the magnetic susceptibility in the superconducting state are vastly altered in fast cooled samples. Finally it should be noted that there is some controversy over the values of the absolute penetration depth which have been reported for κ-$(ET)_2Cu[N(CN)_2]Br$ [98], [99], this could be the result of insulating regions in the sample.

3.2.5 Magnetic Phase Diagram

The organic superconductors are highly anisotropic superconductors. The upper critical field H_{c2} has been measured parallel to the plane using resistivity measurements

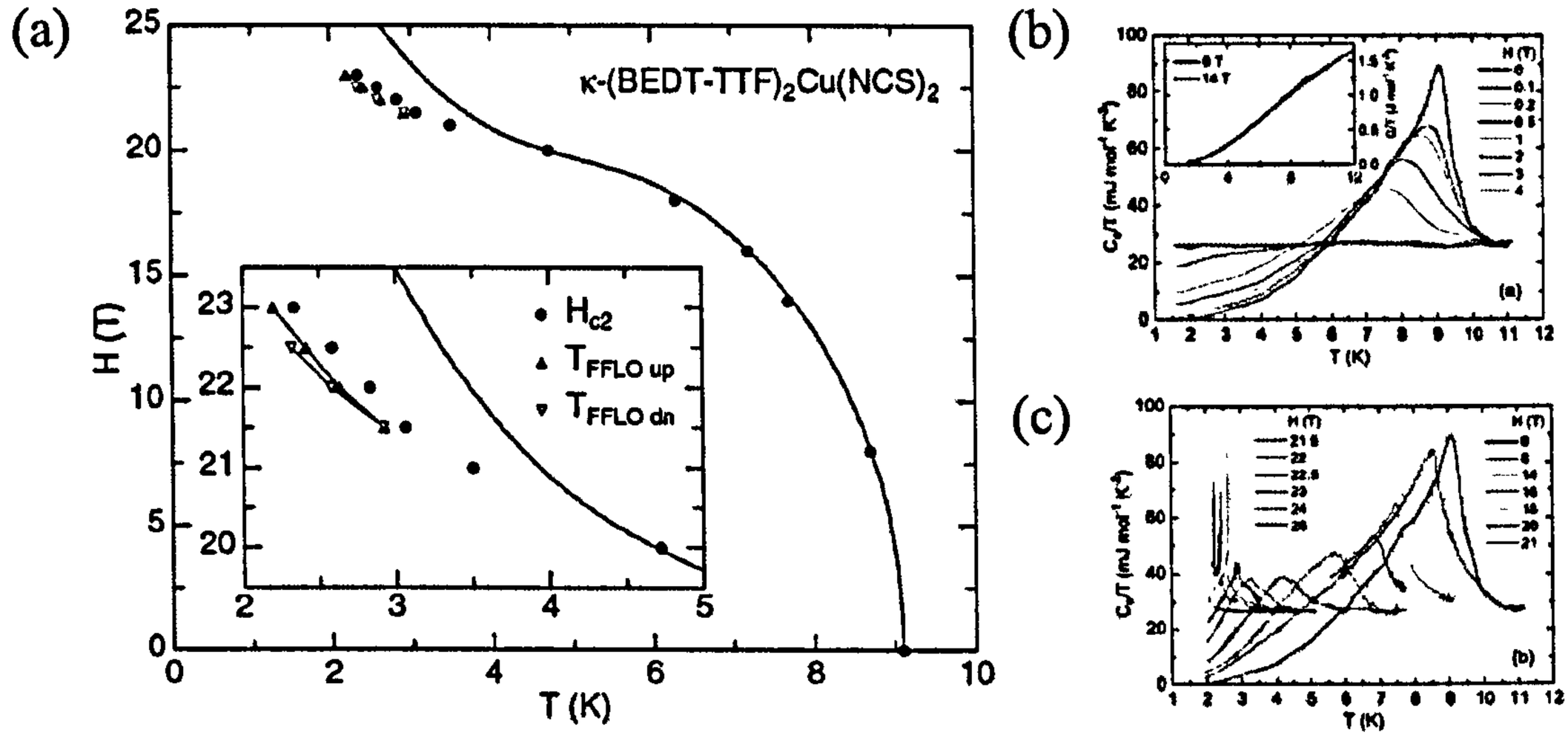

Figure 3.4: Heat Capacity measurements in high field taken from [103] on κ-NCS. (a) Phase diagram when field applied parallel to planes. (b) Heat capacity measurements perpendicular to the plane. (c) Heat capacity measurements parallel to the plane.

on both κ-NCS and κ-Br [100]. The upper critical field parallel to the plane is measured as greater than 30 T in both compounds. The upper critical field is taken as the inflection point in the resistivity curve.. The upper critical field perpendicular to the plane has been measured in κ-Br by NMR as 10 T [101] and by several probes (penetration depth, thermal conductivity and magnetisation) in κ-NCS as 6 T [102]. These results are reinforced by heat capacity studies which show the Sommerfeld coefficient saturates at 6 T for κ-NCS and 10 T for κ-Br [12] implying the sample is in the normal state. A high field heat capacity study has been conducted on κ-NCS [103]. Figure 3.4 shows the results of this study, when the field is parallel to the plane then an anomaly is present at all fields and when the field is perpendicular to the plane the anomaly is unobservable above 4 T. The anisotropy in the upper critical field close to T_c implies a superconducting anisotropy $\gamma = H_{c2||ab}/H_{c2||c}$ of around 18 [81].

3.2.6 The Pairing Mechanism

Although the gap symmetry in the organic superconductors is still a controversial subject, there are several theories suggesting the underlying pairing mechanism. Schmalian [93] suggests that anti-ferromagnetic fluctuations could give rise to a d-wave order parameter. Utilising an analogy to the cuprates, the gap symmetry is predicted to have nodes along the real space crystal axis. When comparing to the cuprates, the Brillouin zone is doubled and rotated by 45°. Consequently the $d_{x^2-y^2}$ paring symmetry observed in the cuprates, is now predicted to be a d_{xy} symmetry in the organics.

An alternative to the AFM spin fluctuations model, is the resonating valence band model [104]. This theory predicts a $d_{x^2-y^2}$ (in the original Brillouin zone). The RVB model was first proposed by Anderson for the cuprate superconductors. Powell [104] shows that the RVB model could by applied to the organic superconductors.

3.2.7 The Gap Symmetry

Many techniques have been employed to measure the gap symmetry of the organic superconductors. The most recent studies all point to a nodal gap symmetry however the directions of the nodes are still under debate.

Penetration Depth Measurements

Low temperature penetration depth measurements in the Meissner state can be a powerful tool in measuring the gap symmetry as described in the next chapter. The low temperature penetration depths of κ-Br and κ-NCS have been measured using a tunnel diode oscillator down to 300 mK [77]. The temperature dependence follows a $T^{1.5}$ power law. This is interpreted in a dirty d-wave scenario and the parameter T^* (see Chapter 1), which measures the impurity bandwidth, is found to be 0.4 K.

It should be noted that these data could also support a highly anisotropic gap (i.e d with a small amount of s), however the s-wave gap size would have to be less than 3 % of the d-wave gap.

NMR Measurements

NMR experiments can be used to measure the spin-lattice relaxation rate T_1 and the Knight shift K_s. In the superconducting state the temperature dependence of $1/T_1T$ can be used to determine the gap symmetry as it is related to the electron electron correlation function, which can be calculated for a conventional BCS superconductor and a d-wave superconductor. ^{13}C NMR measurements on κ-Br have been performed by several groups and all support a nodal gap [15] [105] [106]. The low temperature dependence of $1/T_1T$ shows a T^3 dependence. In addition no Hebel-Slichter coherence peak is observed which is another signature of unconventional pairing. Finally, De Soto [15] observes that there is a striking similarity between the κ-Br NMR data and the NMR data obtained for the cuprate superconductor YBCO.

Thermal Conductivity

Thermal conductivity measurements have been employed in two ways to determine the gap symmetry. The thermal conductivity is sensitive to the density of states of the superconductor. Measuring the temperature dependence of the thermal conductivity will reveal the presence of nodes (similar to penetration depth and heat capacity measurement). Belin [16] measured the temperature dependence of the thermal conductivity of κ-NCS down to 150 mK. A residual linear term (see figure 3.5 (a)) is observed at the lowest temperatures which is indicative of nodes in the order parameter. Another method is to measure the angle dependence of the thermal conductivity

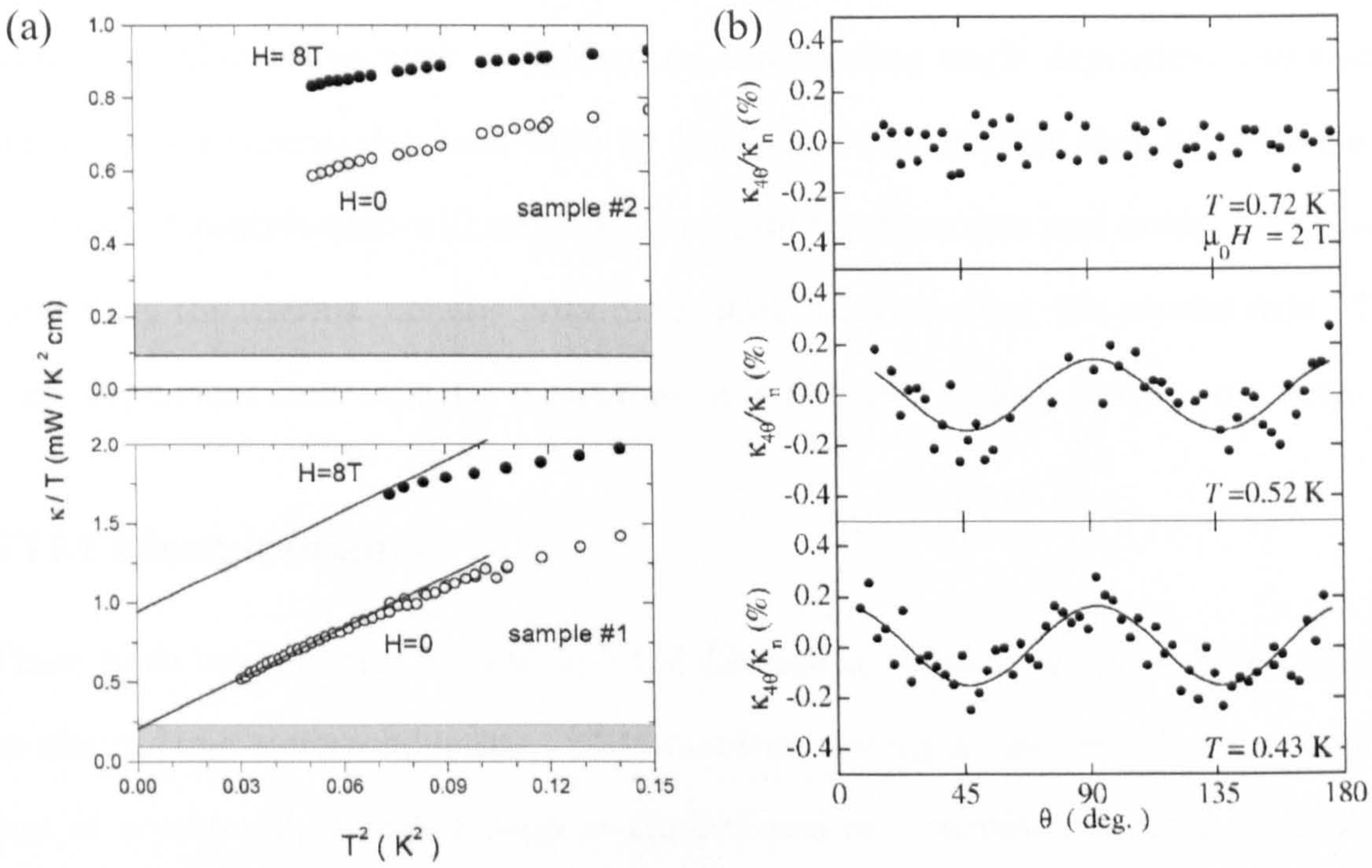

Figure 3.5: (a) Residual linear term in the thermal conductivity of κ-NCS at low temperatures indicating a nodal order parameter [16]. (b) Fourfold oscillations in the thermal conductivity as a function of applied field angle [25].

in a magnetic field. Izawa [25] has measured the thermal conductivity as a function of field angle in κ-NCS (figure 3.5 (b)). A clear fourfold oscillation in the electronic contribution is observed at 2 T and temperatures below 0.6 K. This contribution is interpreted as being from line nodes in the superconducting order parameter. The line nodes lie at 45° to the crystal axis and the data support a d_{xy} order parameter. The d_{xy} notation used in this paper refers to the theoretical work by Schamalian [93] in relation the cuprates and has a Brillouin zone which is rotated by 45°. There has been much theoretical work performed on interpreting angle dependent thermodynamic measurements. A recent work by Vorontsov [20] predicts that an inversion in the fourfold contribution will occur at moderate temperatures and fields. This could mean that the thermal conductivity data implies nodes along the crystal axis. The angle dependent heat capacity measurement is designed to help resolve this issue.

STM Measurements

There have been several reports of STM (Scanning Tunnelling Microscopy) studies on the organic superconductors. STM involves moving a tip very close to the surface of a material, a bias voltage is applied and any current flowing is a result of tunnelling into the material. As the tunnelling is related to the density of states, when a superconductor is measured the gap symmetry can be extracted. The first study on the organics was performed by Arai [78] on κ-NCS. This showed a clearly anisotropic gap as when the sample was rotated the gap magnitude changed. The gap is a maximum when measuring along the crystal axis which indicates nodes at 45° to the crystal axis. This result is in agreement with the angle dependent thermal conductivity experiments. The experiment has also been performed on κ-Br [107] and the same result was obtained. STM measurements are very sensitive to the quality of the surface and as such can sometimes present misleading data.

Magneto-Optical Measurements

Magneto-optical measurements have been taken by Shrama [79] on κ-NCS and imply that the nodal directions are at 45° to the crystal axis. The magneto-optical technique involves placing a sample in a resonant cavity. The measurement frequency is around 70 GHz and the field is applied so the current flows perpendicular to the conducting planes. There has been some debate into the validity of the results obtained by this method [108], [109]. Both these references question the analysis used in [79] to obtain the nodal directions.

3.2.8 Heat Capacity Studies

There have been a number of heat capacity studies performed on the κ-(ET)-X superconductors. The first measurements of specific heat were performed by Andraka [110] and Graebner [111] on κ-NCS and κ-Br [112]. Although no information on the gap symmetry is inferred from the data, the size of the jump at T_c is measured as well as the electronic and phonon terms. Andraka found the Sommerfield constant γ to be $25\pm3\,mJ/K^2mol$ for κ-NCS, however Graebner finds γ to be $34\,mJ/K^2mol$. This difference could be due to the magnetic fields used, Andraka uses 12.5 T to suppress superconductivity and Graebner uses 5 T which may not have completely suppressed superconductivity. In κ-Br Andraka finds γ to be $22\pm3\,mJ/K^2mol$.

Nakazawa [113] first attempted to measure the heat capacity of κ-Br in the superconducting state. Instead of using a magnetic field to subtract the phonon contribution, a non-superconducting deuterated sample of κ-Br was also measured and used as the phonon contribution. The results imply unconventional superconductivity as the slope at low temperatures is several orders of magnitude greater than that predicted by BCS theory. Nakazawa uses a value for γ of $22\,mJ/K^2mol$ which is in

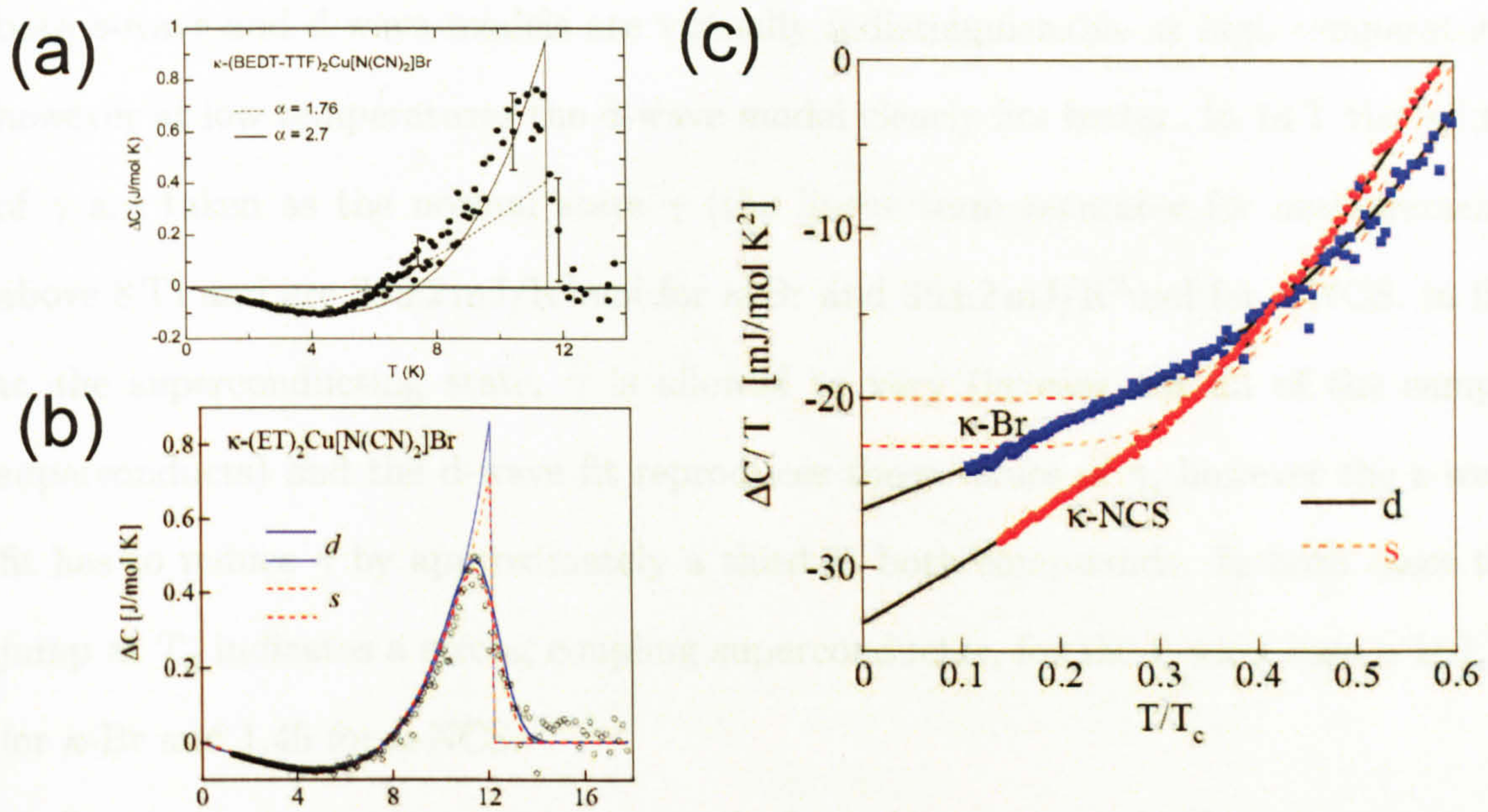

Figure 3.6: Heat Capacity data taken on the ET salts.(a)Data on κ-$(ET)_2Cu[N(CN)_2]Br$ taken from Elsinger [13] with a fit to a strong coupling isotropic gap model. (b) Data on κ-$(ET)_2Cu[N(CN)_2]Br$ taken from Taylor [12] with both an s-wave and d-wave fit. (c) Low temperature data from Taylor, obvious difference between the s-wave and d-wave fit.

agreement with Andraka's work. In addition Nakazawa has also made measurements on non-superconducting ET salts [114] which show no γ and are therefore insulating. Nakazawa has made measurements on κ-NCS [115] which also show unconventional superconductivity.

Elsinger [13] performed measurements on κ-Br in zero field and 14 T down to 1 K. Analysis of the entire curve suggested that a strong coupling conventional model fitted the data well. The size of the jump at T_c corresponds to a gap of $2.7\,k_B T_c$. The size of the normal state γ is $25\,mJ/K^2mol$ and the Debye temperature is measured as 200 K, these values are in reasonable agreement with the previous measurements. Although the conclusion of this paper is that the superconducting gap is isotropic, no attempt is made to fit the data to an unconventional superconducting gap.

The latest data by Taylor [12] supports a strong coupling d-wave superconductor. Both κ-Br and κ-NCS were measured in zero field and 14 T down to 1 K. Fits to

both s-wave and d-wave models are virtually indistinguishable at high temperature, however at low temperatures the d-wave model clearly fits better. In 14 T the values of γ are taken as the normal state γ (the linear term saturates for measurements above 8 T) and are $28\pm2\,\mathrm{mJ/K^2mol}$ for κ-Br and $35\pm2\,\mathrm{mJ/K^2mol}$ for κ-NCS. In fits to the superconducting state, γ is allowed to vary (in case not all of the sample superconducts) and the d-wave fit reproduces these values of γ, however the s-wave fit has to reduce γ by approximately a third in both compounds. In both cases the jump at T_c indicates a strong coupling superconductor, for the d-wave case α is 1.73 for κ-Br and 1.45 for κ-NCS.

In summary, precise measurements in both the superconducting state and the normal state of the low temperature specific heat are needed to accurately determine the gap symmetry of a superconductor. Although there has been controversy in these measurements on the ET salts, the debate seems to have been resolved and supports a d-wave superconductor (or a very highly anisotropic s-wave superconductor).

3.3 Results

3.3.1 Experimental Technique

The samples used in this experiment were grown using a standard electrochemical technique by J. Schlueter in Argonne [116]. The sample of κ-NCS weighed 545 μg and the sample of κ-Br weighed 542 μg. The transitions of both samples were measured by O. Taylor [51]. The T_c of the κ-NCS sample is 9.5 K and the T_c of the κ-Br is 12 K. Transition temperatures quoted are for slow cooled runs (cooling rate $\sim 0.2\,\mathrm{Kmin^{-1}}$). In this experiment the samples were cooled at $0.2\,\mathrm{Kmin^{-1}}$ between 90 K and 65 K to ensure that the sample is superconducting, see Figure 3.7. To cool the sample at this rate, the cryostat was initially cooled to 1 K at the normal rate. The exchange gas

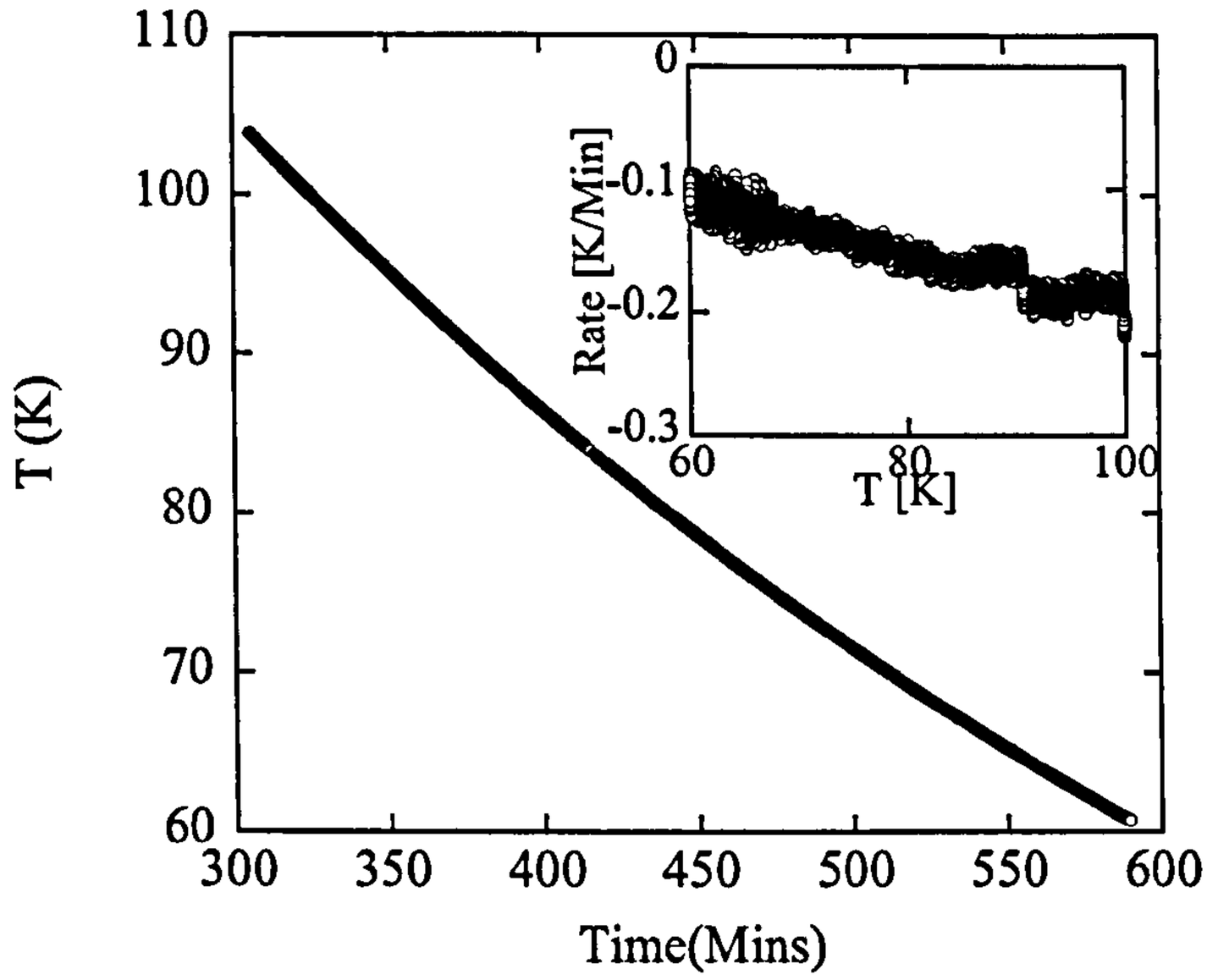

Figure 3.7: Temperature versus time of a typical cool down of an organic sample. Inset: Rate versus temperature.

sorb on the 1 K pot could then pump away the exchange gas. The sample stage was then heated to 100 K while keeping the 1 K pot cold to ensure the exchange gas was still in the sorb. The temperature of the 1 K pot could then be used to determine the cooling rate, a cold 1 K pot meant the sample cooled very slowly as there was no exchange gas and a warm 1 K pot increased the cooling rate. Once the sample had cooled below 60 K, the exchange gas was released from the sorb and the experiment cooled to base temperature at a faster rate.

To determine the crystal orientations the samples were measured on an x-ray diffractometer with Mo source in the University of Bristol Chemistry department (see figure 3.8). The x-ray diffraction showed the expected crystal structure for each sample and that both crystals are good quality single crystals. Figure 3.8 shows both samples on the calorimeter with the crystal directions shown.

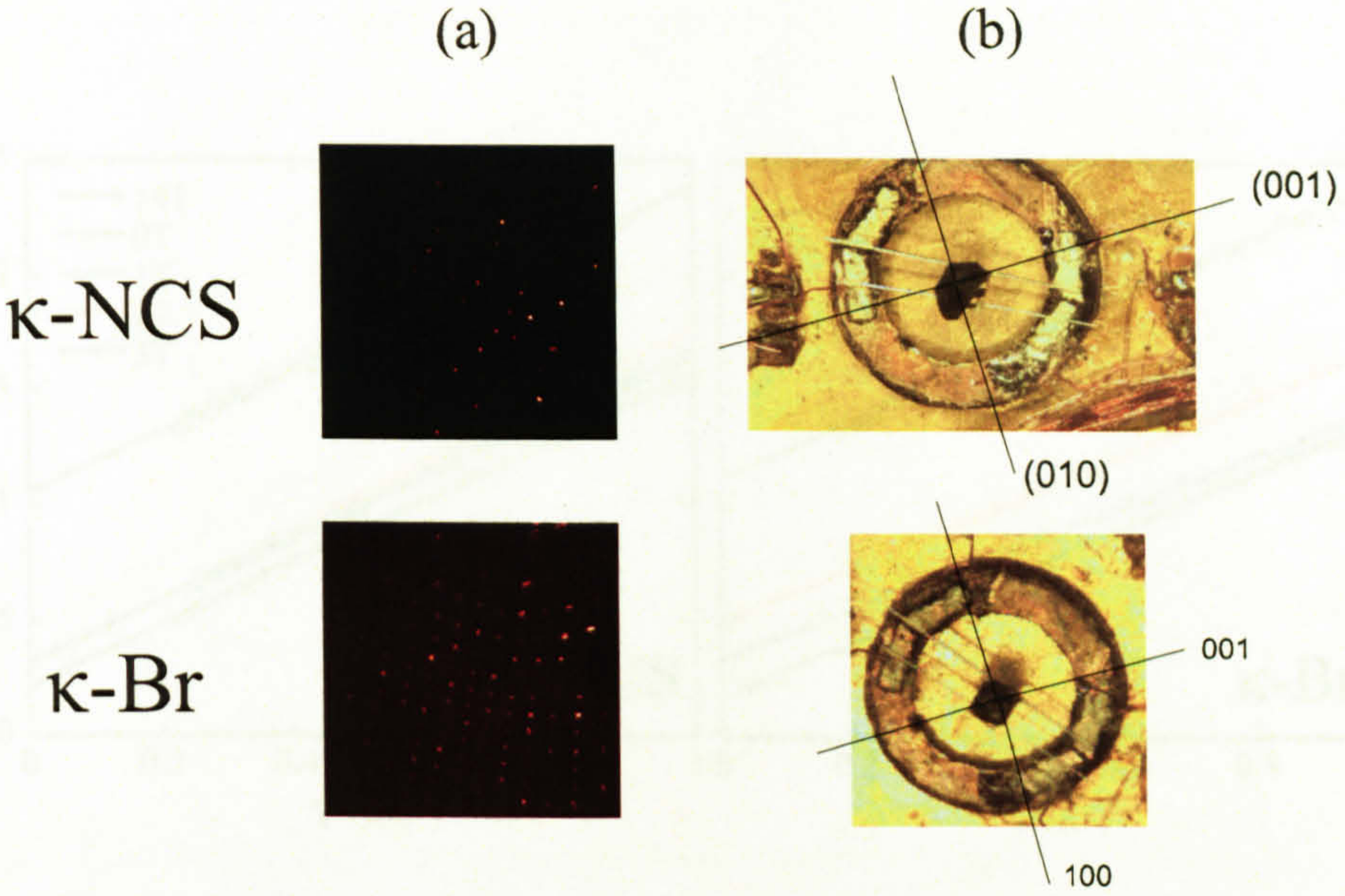

Figure 3.8: (a) X-ray diffaction patterns for both crystals. (b) The samples mounted on the calorimeter with the crystal directions shown.

3.3.2 Temperature Dependence of the Heat Capacity

Field parallel to the conducting planes

The temperature dependence of the heat capacity was measured using long relaxation calorimetry in several fields. The field was applied parallel to the conducting planes. This meant that the upper critical field was around 30 T. Figure 3.9 shows the heat capacity in different fields. Increasing the field increases the Sommerfeld coefficient γ but at the maximum field of 14 T, the Sommerfeld value is still less than half that of the normal state. In a d-wave superconductor the Sommerfeld contribution is expected to have a field dependence of $\gamma_n \sim (H/H_{c2})^{\frac{1}{2}}$, compared with an s-wave superconductor which has a linear field dependence. In this orientation, less than 3 T should constitute a low field however the errors on the value of γ are too high and there are too few points to make an accurate statement about the field dependence of γ.

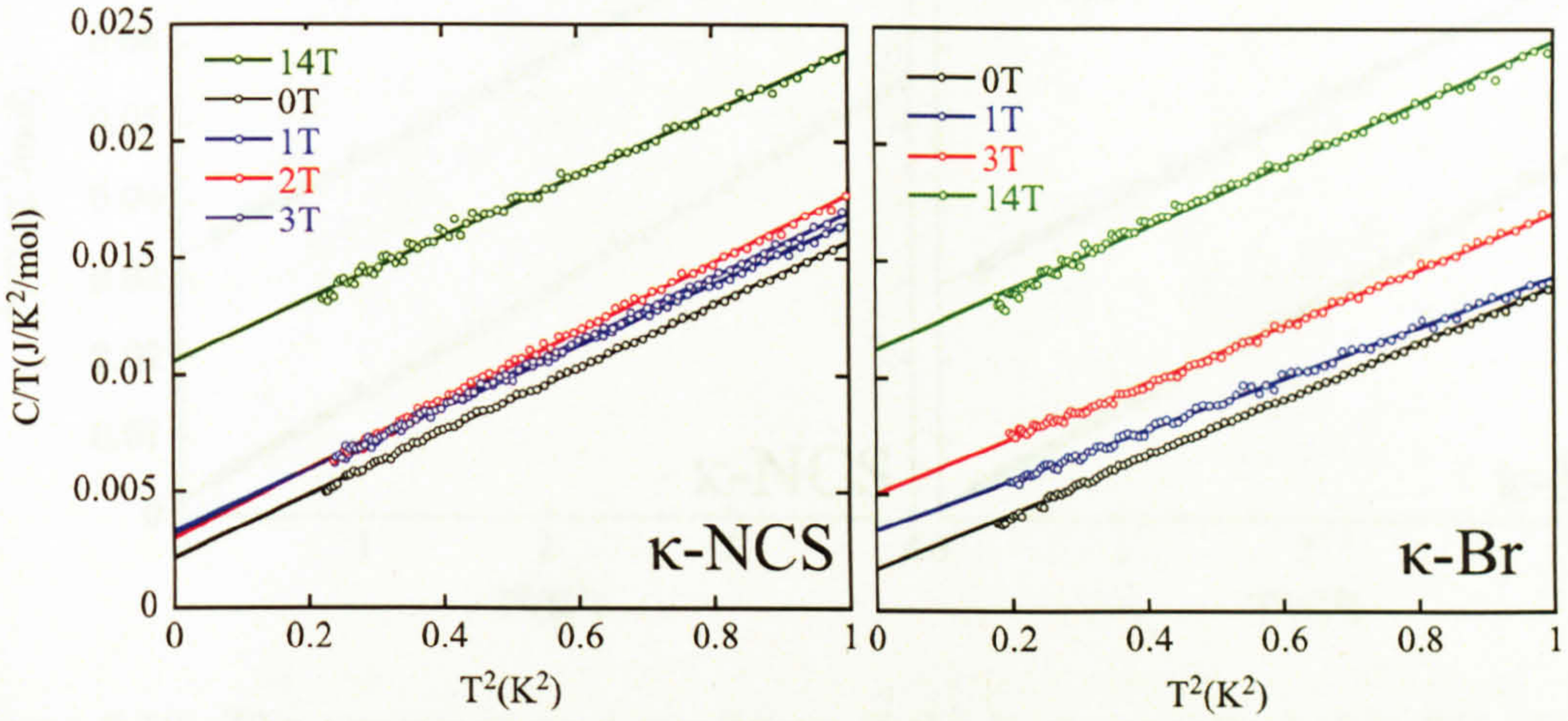

Figure 3.9: The temperature dependence of the heat capacity below 1 K plotted as C/T versus T^2 for κ-NCS (left) and κ-Br (right). The Sommerfeld coefficient increases as a function of field but never saturates as H_{c2} is $\sim$30 T

Field perpendicular to the conducting planes

When the field is applied perpendicular to the conducting planes, then it is possible to suppress superconductivity by applying a 14 T field. The value of γ saturates above $\sim$3 T for κ-NCS and above 8 T for κ-Br [96], indicating that the sample is in the normal state above these fields. Applying a 14 T field ensures that the sample is in the normal state and the field data can be used to subtract the phonon contribution to the heat capacity. Figure 3.10 shows the heat capacity of κ-Br and κ-NCS in 0 T and 14 T with the field applied perpendicular to the conducting planes. In 14 T, the normal state Sommerfeld coefficient γ_n is recovered. To extract this value, a linear fit is applied to the data and the y-intercept is taken as γ_n. For κ-NCS, γ_n is $33.0\pm0.5\,\mathrm{mJK^{-2}mol^{-1}}$ and for κ-Br, γ_n is $29.6\pm0.5\,\mathrm{mJK^{-2}mol^{-1}}$. The error encompasses changing the fitting range for the extrapolation to zero and the error in the measurement. These values are in excellent agreement with those found by Taylor *et al* [12].

To examine the low temperature electronic specific heat the phonon contribution

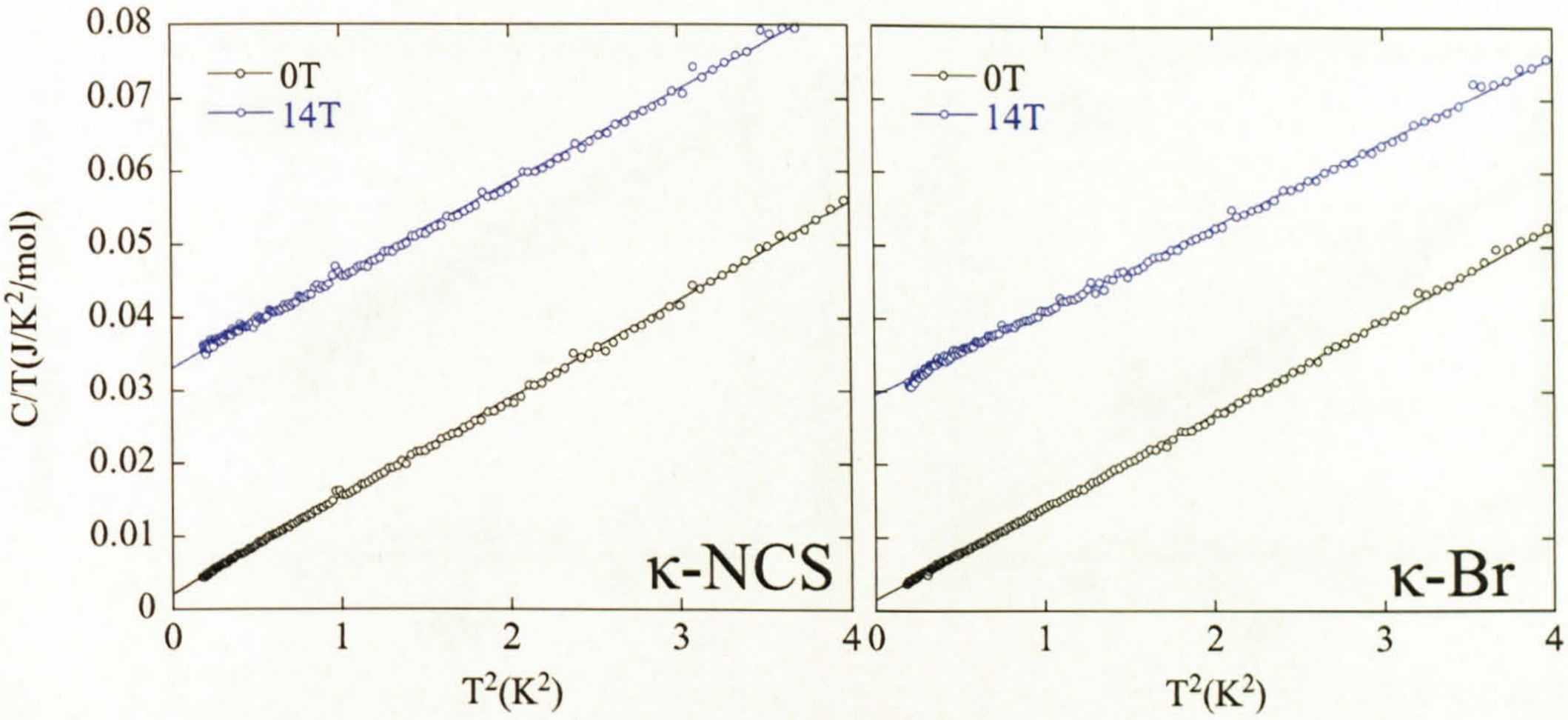

Figure 3.10: The temperature dependence of the heat capacity below 2 K plotted as C/T versus T^2 for κ-NCS (left) and κ-Br (right) in 0 T and 14 T with the field applied perpendicular to the conducting planes.

has to be subtracted from the zero field data. This is done using the 14 T data, which means there is an additional γ_n included in the subtraction. For a simple d-wave superconductor the low temperature specific heat has a T^2 temperature dependence

$$C \simeq \frac{27\zeta(3)}{\pi^2}\frac{k_B\gamma_n}{\Delta_0}T^2, \tag{3.1}$$

where $\zeta(3)$ is the Riemann zeta function (approximately equal to 1.202) and Δ_0 is the gap maximum. The plot of (C(0T)-C(14T))/T will therefore be linear in temperature with an offset of γ_n and a gradient dependent on the gap magnitude. For a BCS weak coupling superconductor the heat capacity will be exponentially activated. The data are shown in Figure 3.11, with a linear fit and the exponential s-wave heat capacity with a BCS weak coupling gap of $1.76\,k_BT_c$. The data are plotted from the normal state γ_n measured in 14 T. The data are clearly linear with the exponential providing a very poor fit. There is an offset in the linear fit for κ-NCS which is outside the error of the experiment and is most likely the result of impurities creating a finite

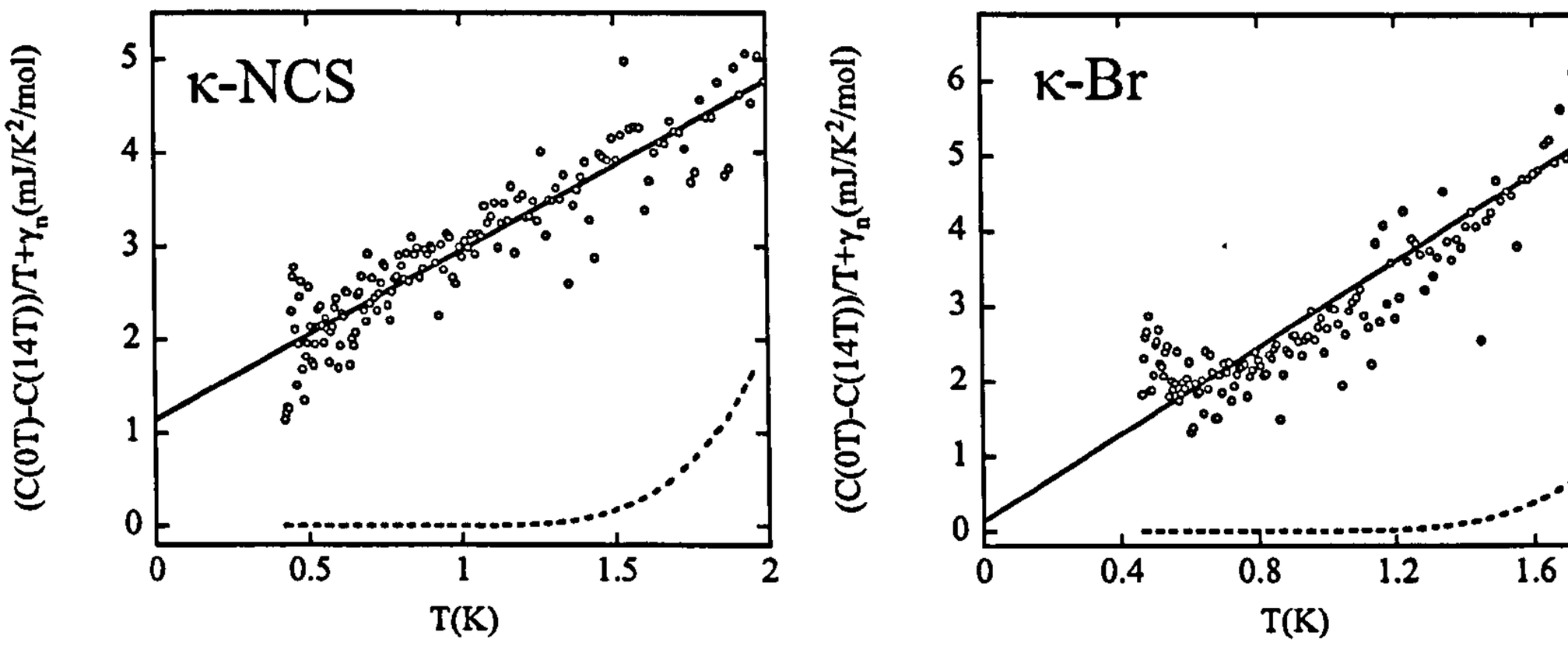

Figure 3.11: The difference between the zero field heat capacity and 14 T heat capacity for κ-NCS (left) and κ-Br (right) plotted from the measured 14 T normal state γ. Solid Lines are fit to a d-wave model (linear) and the dashed lines are the s-wave prediction.

zero energy density of states. The offset for κ-Br is within the experimental error however the lowest temperature data appear to curve up which, as discussed below, could be the result of impurities. It is also possible to conceive a d+s gap structure which explains the data, but the s-wave gap component has to be less than 4% of the d-wave gap component. The gradient of the d-wave fit provides a measure of Δ_0, in the κ-NCS data the gap is extracted as $4.2\pm0.5\,k_B T_c$ and for κ-Br the gap is extracted as $3.6\pm0.5\,k_B T_c$. These expressions are based on a gap which varies as $|\cos(2\theta)|$, however the data could also be explained by a gap with a larger $\frac{d\Delta}{d\theta}$ around the nodes. This scenario seems unlikely based on the angle dependent heat capacity measurements. The value for κ-NCS is slightly higher compared with the value of $3.1\,k_B T_c$ measured in [12]. The value for κ-Br is close to the previous measurement of $3.7\,k_B T_c$ [12]. The data in this study are taken over a lower temperature range and the reason for these slight discrepancies could be impurities. This is especially evident in the κ-Br data as there is a slight upturn at the lowest temperatures. In penetration depth measurements [77], there is a T^* observed which is indicative of the impurity bandwidth. The penetration depth measurements reveal a T^* of around

0.6 K. Following the discussion in chapter 1, this corresponds to a Γ of about 0.15. Numerical calculations have been used to determine the density of states of a dirty d-wave superconductor (see chapter 1). The impurities create a residual DOS around zero energy which would appear in the heat capacity as a flattening or possibly a slight upturn. In general the heat capacity goes flat 3 to 4 times lower than T^*. However this effect would begin reducing the gradient of the heat capacity at higher temperatures and lead to an overestimate of the gap magnitude.

In summary, the temperature dependence of the low temperature specific heat reveals a d-wave gap which is consistent with previous heat capacity and penetration depth experiments. The data show these superconductors to be strongly coupled with gap magnitudes 2 and 1.73 times the weak coupling values for κ-NCS and κ-Br respectively.

3.3.3 Angle Dependent Heat Capacity Measurements

The angle dependent measurements were performed on the rotating calorimeter as described in Chapter 2. As the stage is misaligned by up to 3° the largest contribution to the angle dependence of the heat capacity was a two fold misalignment contribution. The data was then fitted to an equation of the form

$$C(\phi) = C_0 + C_2|\cos(\phi + \delta_2)| + C_4\cos(4\phi), \tag{3.2}$$

where ϕ is the angle away from the b axis. This equation fitted well for the κ-Br data but not for the κ-NCS sample. For the κ-NCS a large $\cos(\phi)$ was required which is probably related to the misalignment, and a $\cos(2\phi)$ term

$$C(\phi) = C_0 + C_1\cos(\phi + \delta_1) + C_2\cos(2\phi + \delta_2) + C_4\cos(4\phi). \tag{3.3}$$

Compound	C_0(nJ/K)	C_1(nJ/K)	δ_1	C_2(nJ/K)	δ_2	C_4(nJ/K)
κ-Br	1.19	-	-	0.30	12.8	0.022
κ-NCS	1.08	0.11	13.8	0.04	0	0.020

Table 3.2: Fit coefficients for the two samples at 0.4 K. κ-NCS requires an additional $\cos(\phi)$ term to describe the data.

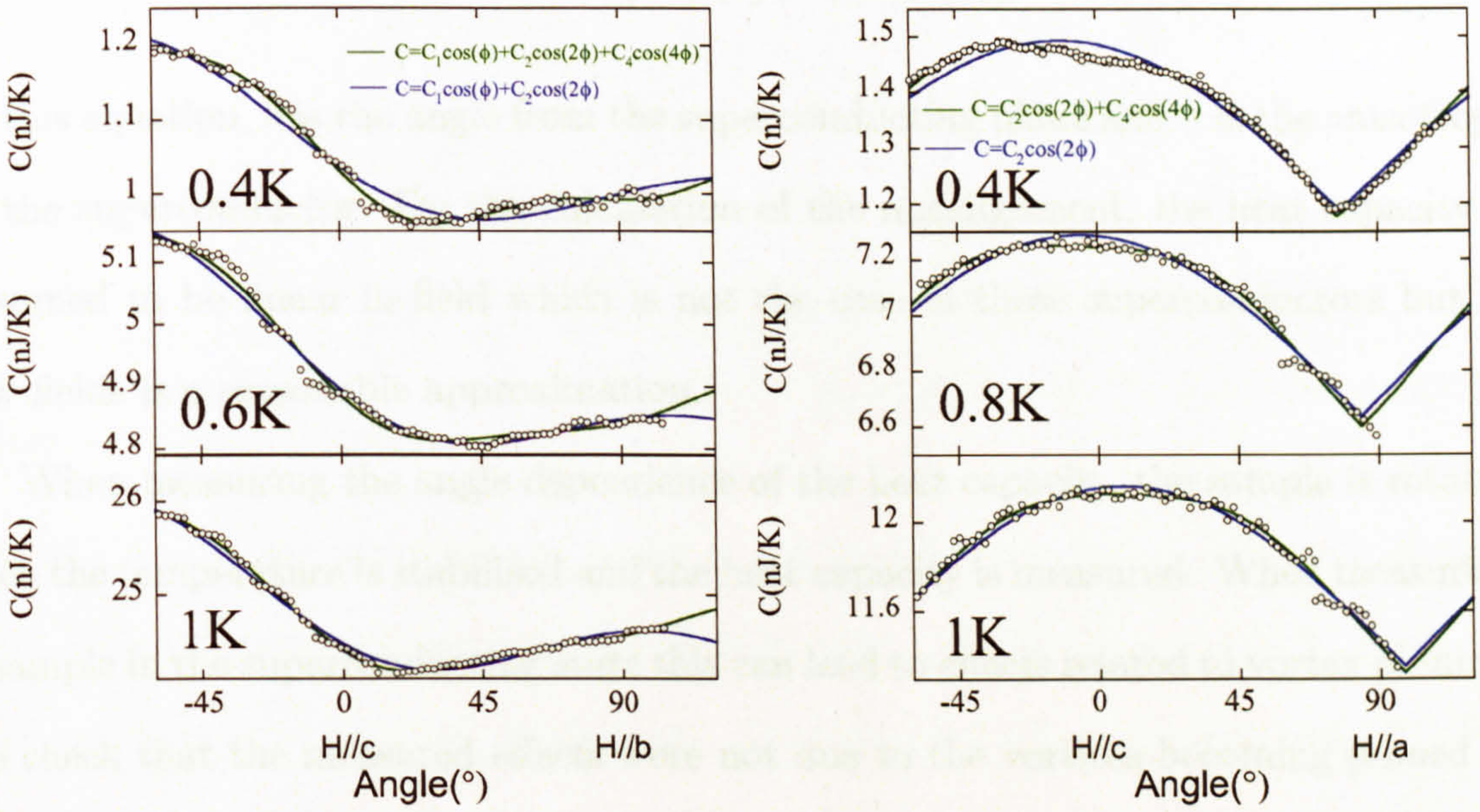

Figure 3.12: Raw angular heat capacity data for κ-NCS (left) and κ-Br (right) at multiple temperatures in 3 T. For both samples, the green line is a fit including a fourfold term and the blue line is a fit without the fourfold term.

This additional term was small and could be related to the orthorhombic distortion in κ-NCS as it is in phase with the fourfold component. At the lowest temperature a fourfold term had to be included in any fit to accurately represent the data. Table 3.2 shows the fitting parameters for the low temperature raw data of both compounds. The amplitude of the fourfold term is similar for both compounds and is about 2 % of the total measured heat capacity (including phonon and addenda contributions). Figure 3.12 shows the raw heat capacity data with fits including and not including the fourfold term for the both samples. The fits which include the fourfold term are considerably better than the one without it at 0.4 K, whilst at higher temperatures

there is little difference between the two. The amplitude of the two fold component is consistent with a misalignment of about 1.5°, based on equation 3.4 for H_{c2} of an anisotropic superconductor [32]

$$H_{c2}(\theta) = \frac{H_{c2}(0)}{\left(\cos^2(\theta) + \gamma^2 \sin^2(\theta)\right)}. \tag{3.4}$$

In this equation, θ is the angle from the superconducting plane and γ is the anisotropy of the superconductor. For the calculation of the misalignment, the heat capacity is assumed to be linear in field which is not the case in these superconductors but at low fields is a reasonable approximation.

When measuring the angle dependence of the heat capacity, the sample is rotated then the temperature is stabilised and the heat capacity is measured. When measuring a sample in the superconducting state this can lead to effects related to vortex pinning. To check that the measured effects were not due to the vortices becoming pinned or unpinned, the samples were heated above T_c between each point for several runs. In general a small difference in background was seen between these two runs. This was attributed to the vortex motion in the sample as it is turned. The fourfold component is constant regardless of how the vortices are treated as is shown in figure 3.13.

To further analyse the fourfold component, the additional contributions to the heat capacity from the phonons and addenda and the misalignment are subtracted. The fourfold component at several different temperatures for both the κ-Br sample and the κ-NCS sample is shown in figure 3.14. Similar behaviour is observed for both samples, the κ-Br exhibits a slightly larger effect. If there is an orthorhombic distortion present, which is the case in κ-NCS but not κ-Br, then the fourfold component should be shifted out of phase with the crystal axis and the maxima of peaks should be different. The phase shift is small and is unobservable in this experiment. The

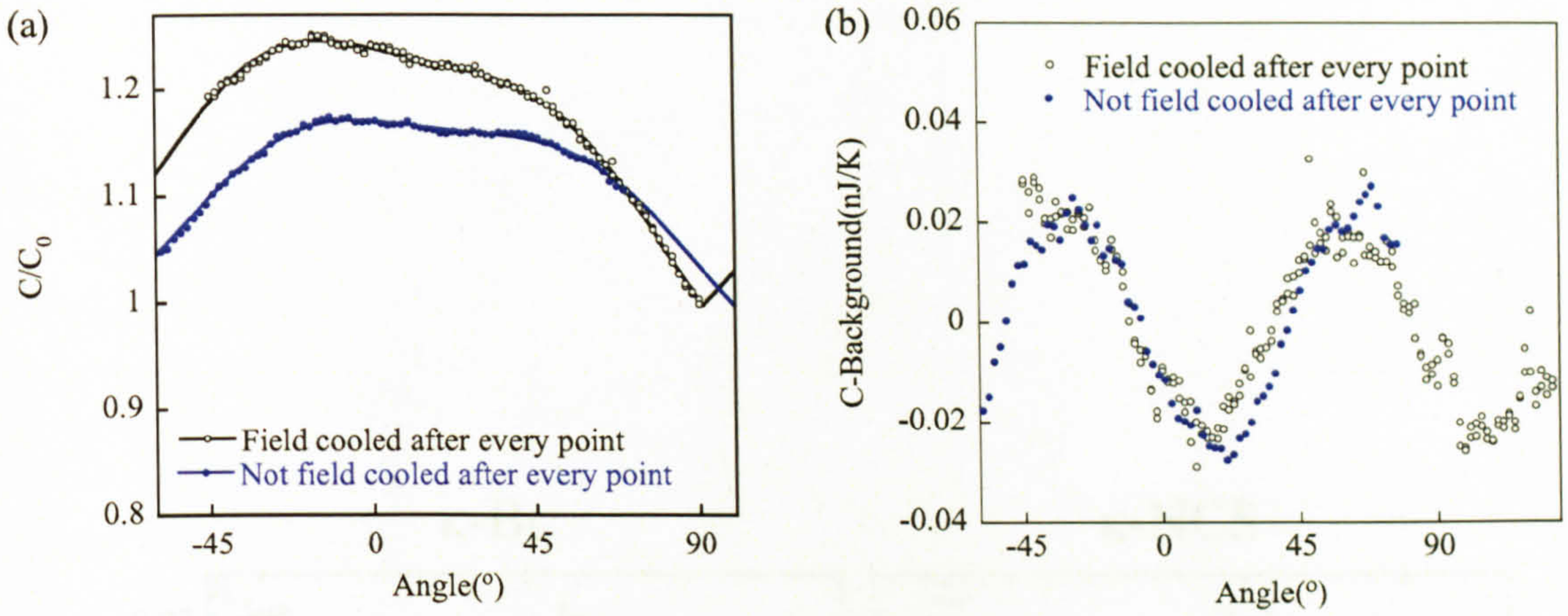

Figure 3.13: Data taken at 0.4 K and 3 T for κ-Br. (a) Two runs, one without field cooling between each point and one with field cooling between each point. Lines are fits to $C = 1 + C_2|\cos(2\phi + \delta)| + C_4\cos(4\phi)$. (b) Fourfold component measured from these two runs is the same.

difference in amplitudes between peaks is not included in the fits but could explain the additional term needed to fit the κ-NCS data. At 1 K there is a very small, almost unobservable fourfold component. However at 0.4 K there is a clear fourfold component which is ~8 % of the electronic heat capacity. This strong temperature dependence can only be explained by considering the nodes in the superconducting gap. Any fourfold component arising from the anisotropy of the Fermi velocity would not be unobservable at high temperatures. The upper critical field is dependent on the Fermi velocity and consequently any fourfold components arising from the Fermi velocity would be present at all temperatures. In addition the Fermi surface is almost elliptical in these materials and any fourfold components would be very small. It is very difficult to conceive of a fourfold contribution to the heat capacity arising from magnetic effects as no evidence for magnetism is observed in the temperature dependence of the heat capacity.

To interpret the data, a simple quasi-classical Doppler shift model is employed as proposed in [18]. As described in Chapter 1, this is a simple model which considers the

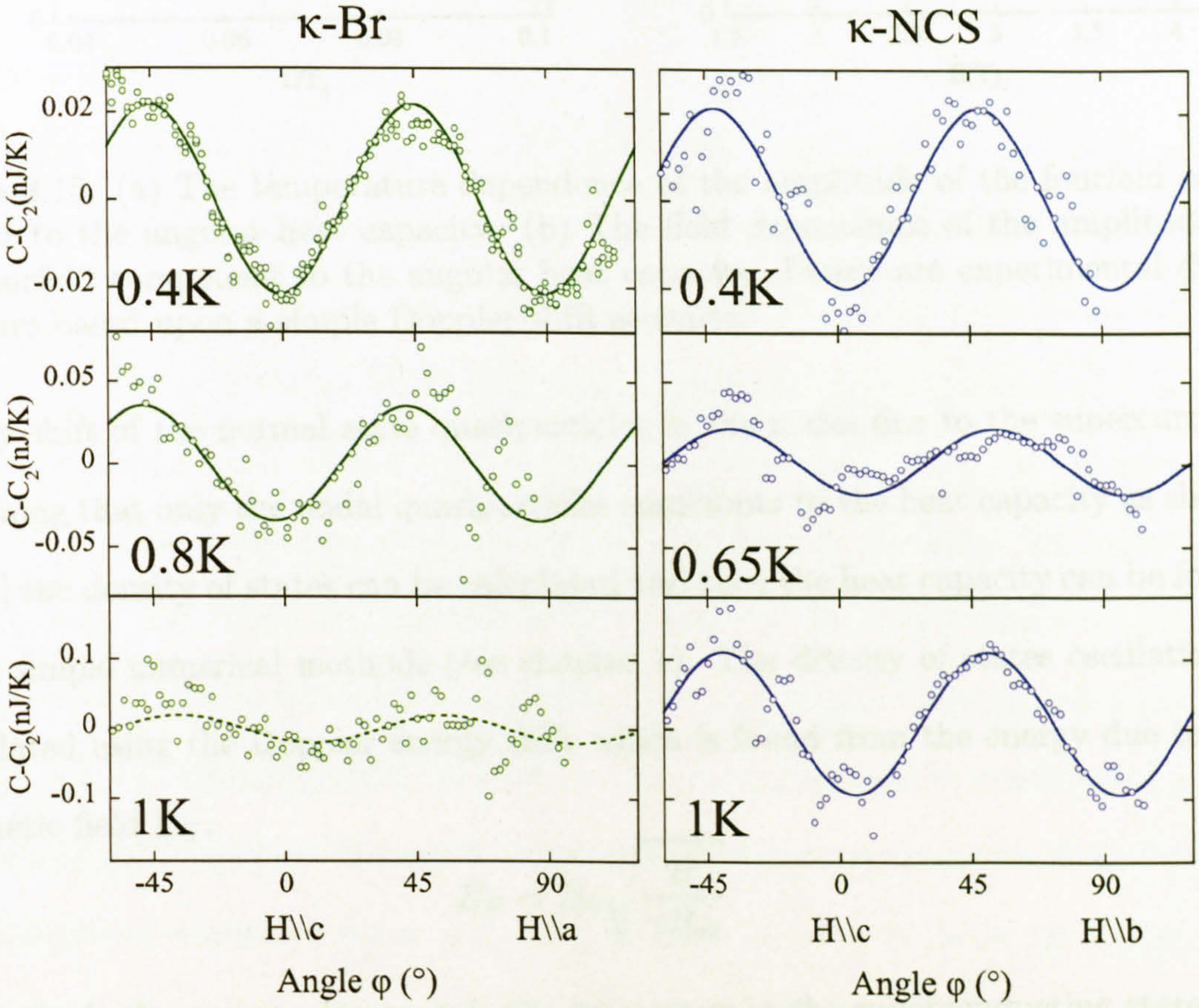

Figure 3.14: Foufold component of the angle dependent heat capacity at various temperatures for κ-Br (left) and κ-NCS (right). The fit is to the equation $C=C_0+C_4\cos(4\phi)$

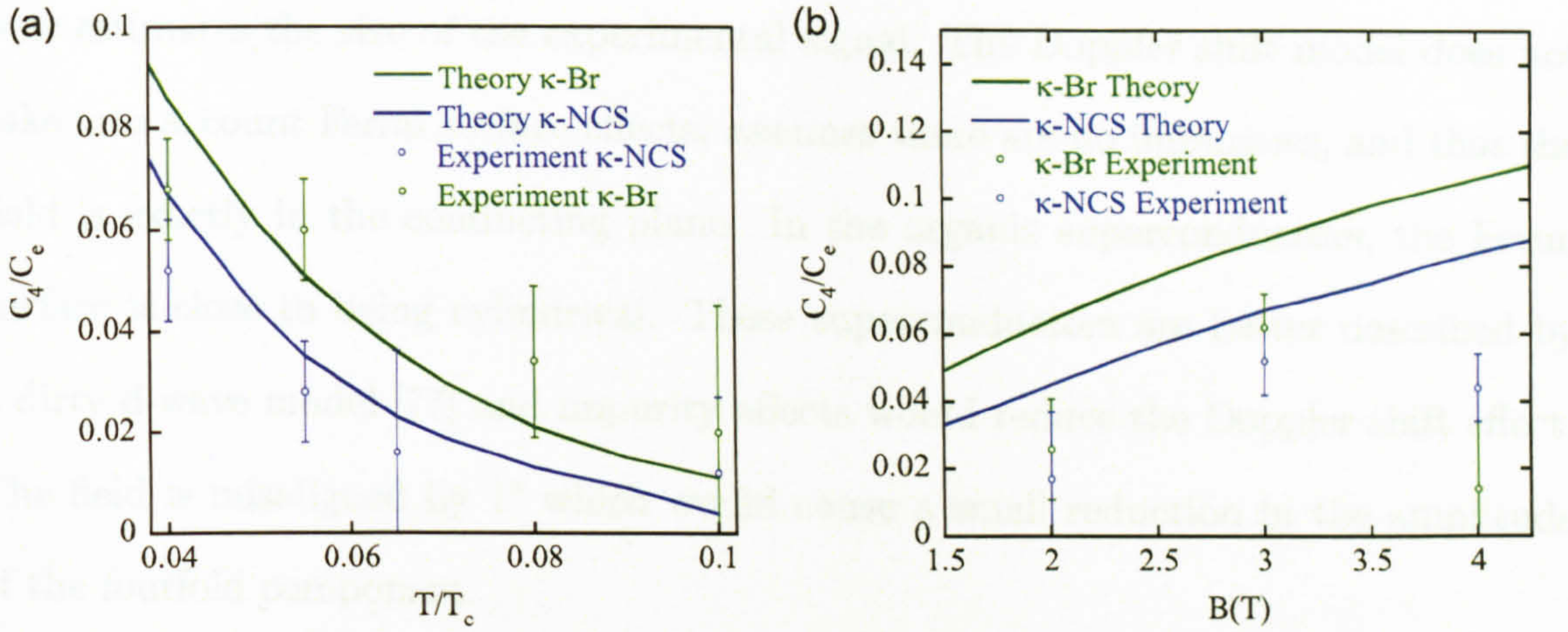

Figure 3.15: (a) The temperature dependence of the amplitude of the fourfold component to the angular heat capacity. (b) The field dependence of the amplitude of the fourfold component to the angular heat capacity. Points are experimental data, lines are based upon a simple Doppler shift scenario.

energy shift of the normal state quasiparticles in the nodes due to the supercurrent. Assuming that only the nodal quasiparticles contribute to the heat capacity as shown in [21] the density of states can be calculated and then the heat capacity can be found using simple numerical methods (see chapter 1). The density of states oscillation is calculated using the Doppler energy shift which is found from the energy due to the magnetic field E_H,

$$E_H \sim \Delta_0 \sqrt{\frac{H}{\gamma H_{c2}}}, \tag{3.5}$$

where Δ_0 is the gap maximum, γ is the anisotropy in the superconducting state and H_{c2} is the upper critical field. To perform the calculation, the size of Δ_0 is taken from the previous heat capacity study [12] and is $3.7\,k_B T_c$ for κ-Br and $3.1\,k_B T_c$ for κ-NCS. The anisotropy factor is taken as 18 [117] and the upper critical field is taken as 30 T [103]. Figure 3.15 shows the amplitude C_4 taken from the sine fits to the fourfold data compared with the results of a simple numerical calculation based on the Doppler shift method. There is good agreement between a simple Doppler shift model and the experimental data. Although at the lowest temperatures the theory

over estimates the size of the experimental signal. The Doppler shift model does not take into account Fermi surface effects, assumes there are no impurities, and that the field is exactly in the conducting plane. In the organic superconductors, the Fermi surface is close to being cylindrical. These superconductors are better described by a dirty d-wave model [77] and impurity effects would reduce the Doppler shift effect. The field is misaligned by 1° which would cause a small reduction in the amplitude of the fourfold component.

The field dependence of the oscillations is also close to what is expected in a simple quasi-classical picture and is shown in Figure 3.16 for data taken at 0.4 K. The fourfold contribution is present at low fields, similar in size for both samples at 2 T and 3 T. It is becoming unobservable in 4 T in κ-Br and in higher fields it is unobservable in both samples. Figure 3.15 shows the experimental results compared with the Doppler shift model. The theory underestimates the size of the signal at all fields. The signal goes to zero between 4 T and 5 T and this is not accounted for in the simple model used in this work. This cut-off field is lower than predicted in more sophisticated theories [20] but the slight misalignment, impurities and increased two-fold contribution could be washing out the signal. Recent theories have predicted an inversion of the fourfold contribution at moderate fields and temperatures [45], no evidence of this is seen although at temperatures above 2 K the phonon contribution has become very large.

These data contradict the angle dependent thermal conductivity data [25] and the STM measurements [78], [118]. The angle dependent thermal conductivity is sensitive to the same effects as the angle dependent heat capacity but in different ways. The thermal conductivity is a non-equilibrium measurement and is therefore sensitive to scattering processes as well as the density of states. Using a full numerical calculation, Vorontsov [20], [46] calculates the angle dependent thermal conductivity and this seems to imply that a 45° phase shift in the fourfold component of the

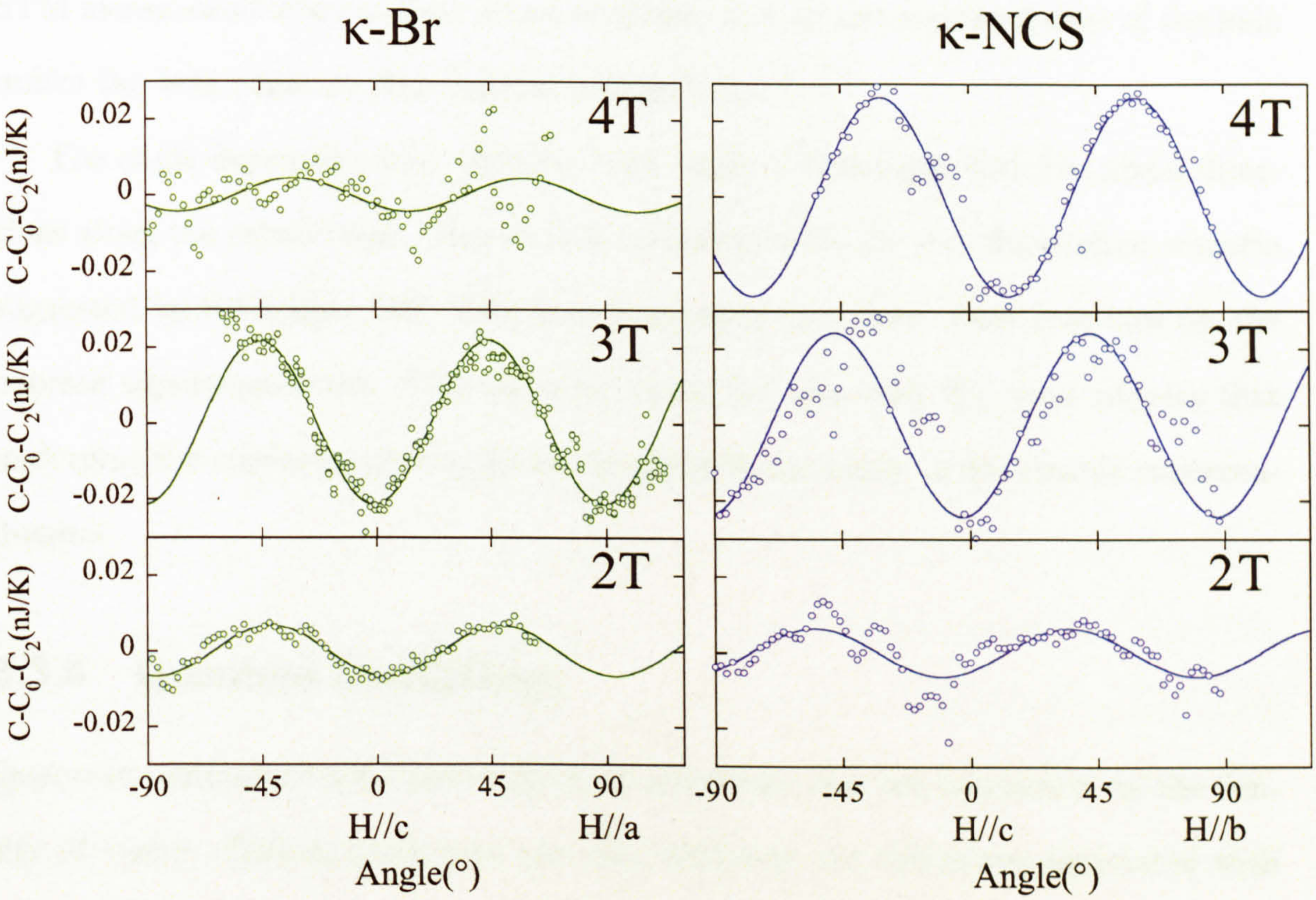

Figure 3.16: Foufold component to the angle dependent heat capacity at various fields for κ-Br (left) and κ-NCS (right) at 0.4 K. The fit is to the equation $C=C_4\cos(4\phi)$

thermal conductivity can occur due to quasiparticle scattering off vortices. In [46], the data on κ-$(ET)_2Cu(NCS)_2$ are examined and it is concluded that the data are taken at a low enough field and temperature that this phase shift will not occur. However the authors also admit that it is not clear exactly where this phase shift may occur and the presence of impurities could alter the results. More theoretical work is needed to compare the thermal conductivity data with the heat capacity data. The STM measurements are surface sensitive probes and are not representative of the bulk unlike the heat capacity and thermal conductivity.

The angle dependent heat capacity data imply a nodal gap with the nodal directions along the crystal axis. This data is consistent with the spin fluctuation scenario suggested by Schmalian [93]. This theory is based on similar ideas proposed for the cuprate superconductors. This data reinforces the idea that the same physics that underpins the cuprate superconductors is also playing a role in the organic superconductors.

3.3.4 Quantum Oscillations

Quantum oscillations are observable in all quantities that are dependent on the density of states. This includes heat capacity, although the difficulties associated with measuring heat capacity mean it is not generally a preferred method. It is possible to measure quantum oscillations in heat capacity using AC calorimetry as shown by Sullivan and Seidel in beryllium [70]. In the case of the organic superconductors it is possible to observe quantum oscillations in κ-NCS at fields accessible in the current experiment but not in κ-Br. The oscillation in the density of states in a metal is derived in [119] and is given by

$$N \sim R_T R_D \sin\left(\frac{2\pi F}{B} + \phi\right), \tag{3.6}$$

where R_T is a reduction factor due to temperature smearing, R_D is the Dingle factor, F is the area of the orbit and B is the applied field. The reduction factor due to temperature depends on the effective mass of the orbit and is given by

$$R_T = \left(\frac{X}{\sinh(X)}\right), X = 14.69\left(\frac{m^* T}{B}\right), \tag{3.7}$$

where T is the temperature and m^* is the effective mass. The Dingle factor is a reduction factor which is derived from the scattering rate related to the orbit being measured. If there is large scattering, then more quasiparticles will not complete an orbit and the signal will be reduced. The Dingle factor is given by

$$R_D = \exp\left(\frac{1140\sqrt{F}}{lB}\right), \tag{3.8}$$

where 1140 is derived from constants and l is the mean free path.

The heat capacity of κ-NCS was measured as a function of field using AC calorimetry. Corrections were made for the magnetoresistance of the thermometer and the power applied to the sample was kept constant. In the superconducting state, the heat capacity increases until the upper critical field is reached and then remains constant. In the measurement of κ-NCS, the heat capacity rapidly rose until 5 T and then slowly rose up to 14 T. This slow rise is due to the changing thermal time constants with magnetic field and is difficult to account for. Therefore the absolute values of the heat capacity have a large error associated with them (around 10 %). Figure 3.17 shows the heat capacity as a function of field for both up and down field sweeps above 9 T. Oscillations are observed above ~8 T and the up and down sweeps are slightly out of phase due to the magnet lag. A fast fourier transform shows a single large peak at a frequency of 625 T which is the same frequency as observed in [86] and ascribed to the lens orbit. No other frequencies are observed as magnetic breakdown does not

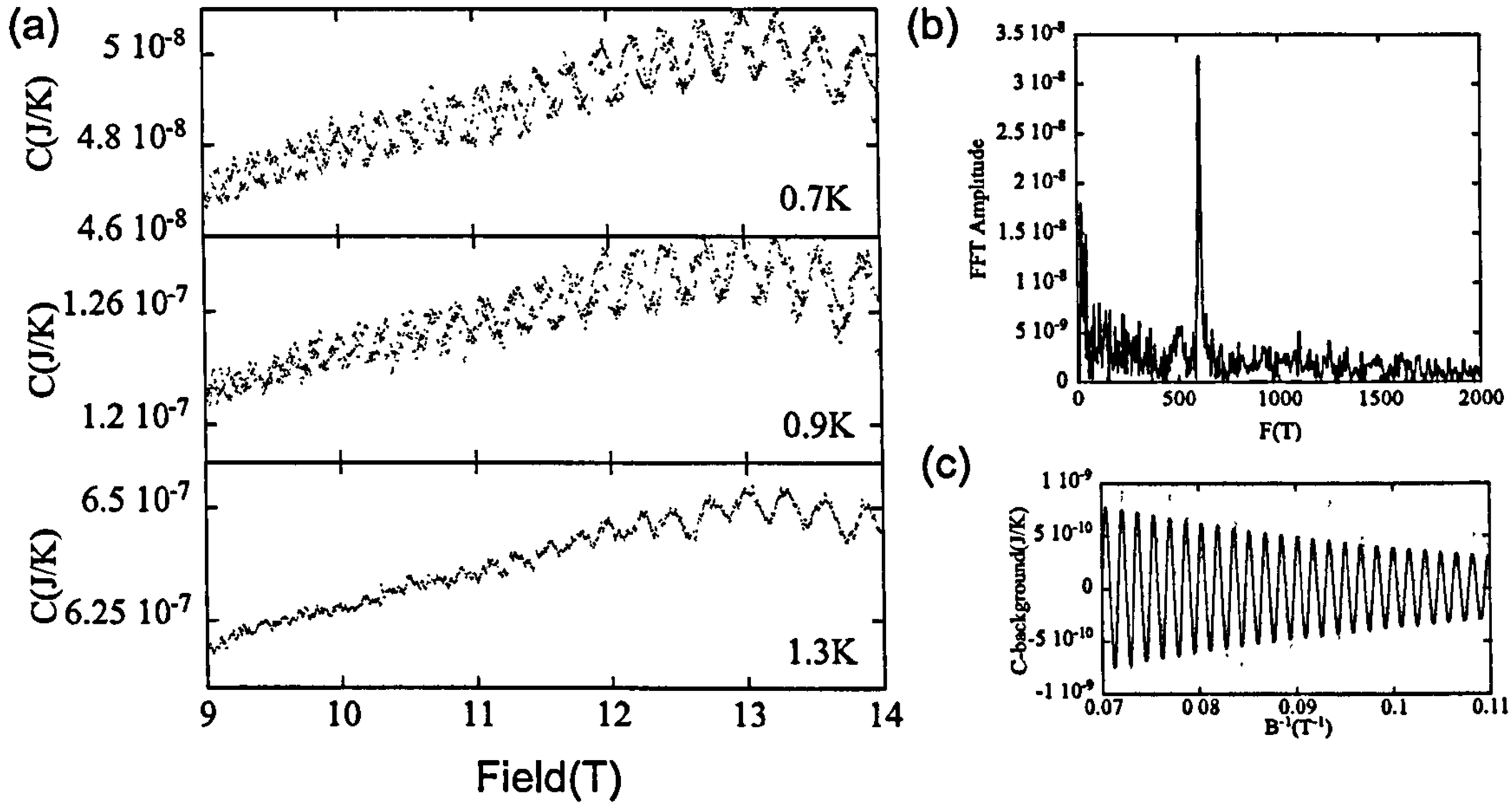

Figure 3.17: (a) Heat capacity of κ-NCS as a function of field for several different temperatures. Oscillations are observable up to 1.5 K. (b) Fast Fourier transform of the 0.7 K data. The frequency of oscillation is 625 T. (c) Fit to the 0.7 K data including the Dingle factor.

occur until the field is above 20 T. To extract the mean free path of the sample, a fit to the 0.7 K data is also shown (a polynomial is subtracted from the data). The size of the exponential envelope implies that the sample has a mean free path of 1200 Å. Although these measurements reveal no new information about the Fermi surface, they do confirm the sample quality and orientation.

3.4 Conclusions

The first measurements of the angle dependent heat capacity of the organic superconductors κ-$(ET)_2Cu(NCS)_2$ and κ-$(ET)_2Cu[N(CN)_2]Br$ have been performed. A clear fourfold oscillation is observed, which is largest at the lowest temperature and is unobservable above 1 K. The minima in the fourfold oscillation are oriented along the crystal axis. The amplitude of the fourfold oscillation is consistent with a quasi-

classical Doppler shift model for a simple d-wave superconductor. This indicates that the nodes are situated along the crystal axis and is consistent with the spin fluctuation scenario proposed by Schmalian [93]. These results are in contrast to angle dependent thermal conductivity measurements [25] and more theoretical work is needed to explain this discrepancy.

The temperature dependence of the heat capacity is analysed in 14 T and 0 T. In 14 T the Sommerfeld coefficient is found to be $33.0 \pm 0.5\,\mathrm{mJK^{-2}mol^{-1}}$ for κ-$(ET)_2Cu(NCS)_2$ and $29.6 \pm 0.5\,\mathrm{mJK^{-2}mol^{-1}}$ for κ-$(ET)_2Cu[N(CN)_2]Br$, which is in agreement with the results in [12]. Subtracting the phonon contribution from the 0 T data reveals a linear term down to the lowest temperatures. This constrains the gap symmetry to be d-wave, or at least d-wave with a small amount of s-wave. The gradient of the linear term implies that these superconductors are strongly coupled. Penetration depth measurements [77] show an impurity bandwidth of 0.6 K, which could affect the heat capacity data. There is a slight upturn in the κ-$(ET)_2Cu[N(CN)_2]Br$ but the κ-$(ET)_2Cu(NCS)_2$ is linear. Finally, quantum oscillations in the heat capacity were observed in the κ-$(ET)_2Cu(NCS)_2$ sample, these measurements reveal the lens orbit of 625 T and imply a mean free path of 1200 Å.

Chapter 4

Magnetic Penetration Depth of $SmFeAsO_{0.8}F_{0.2}$ and $Ba(Fe_{0.93}Co_{0.07})_2As_2$

4.1 Introduction

The pnictide superconductors are the first non-cuprate superconductors discovered to have a T_c in excess of 50 K. The system was first discovered in $LaFeAsO_xF_{1-x}$ [7] with a T_c of 26 K. Since then La has been replaced with Sm, Nd, Pr, Gd, or Ce [120], [121], [122], [123] with the highest T_c being $\simeq$ 55 K (in SmFeAsO). As well as these '(1111)' pnictides, there are several pnictides of the '(122)' type, such as $BaFe_2As_2$ with a maximum T_c of 38 K [124]. The (1111) pnictides are electron doped to produce superconductivity and (122) type are either hole doped or electron doped. The parent compounds of these superconductors are semi-metals with strong spin fluctuations [125]. This has led to speculation that the mechanism behind the superconductivity is unconventional [126], [127], [128]. There are also apparent similarities between the

pnictide superconductors and the cuprate superconductors as both have a quasi 2-D band structure and a proximity to an antiferromagnetic parent compound (although in the cuprates the parent compound is an insulator and in the pnictides it is a metal). Therefore one might expect the pnictide superconductors to have a superconducting gap symmetry the same as the cuprates (d-wave). In the pnictide superconductors, the superconducting gap has been measured by point contact Andreev spectroscopy [129] [130], NMR [131] and photoemission [132] but no agreement has been reached, with some experiments showing evidence of nodes and others a fully gapped Fermi surface. An approach which has been successful for the cuprates [14] and MgB_2 [133] is taking precise low temperature measurements of the magnetic penetration depth λ. The low temperature behaviour of the penetration depth can be calculated from the BCS gap equation and is exponential for a fully gapped superconductor and a power law for a nodal superconductor. In this study, measurements of the penetration depth down to 1.5 K of newly synthesised [134] $SmFeAsO_{0.8}F_{0.2}$ crystals with a T_c of $\simeq 50$ K and $Ba(Fe_{0.93}Co_{0.07})_2As_2$ crystals with a T_c of 22 K are performed in order to determine the superconducting gap symmetry.

4.2 Background to Pnictide Superconductors

4.2.1 (1111)-type Pnictides

The (1111) pnictide superconductors have the chemical formula ReFeAsO. They only have one FeAs layer per unit cell and have a tetragonal P4/nmm structure. Doping the oxygen sites with fluorine introduces electrons and the compound becomes superconducting. The structure of SmFeAsO is shown in figure 4.1. The parent compounds undergo a structural transition from a tetragonal space group to a monoclinic space group [135]. The structural transition occurs at 155 K and precedes a magnetic

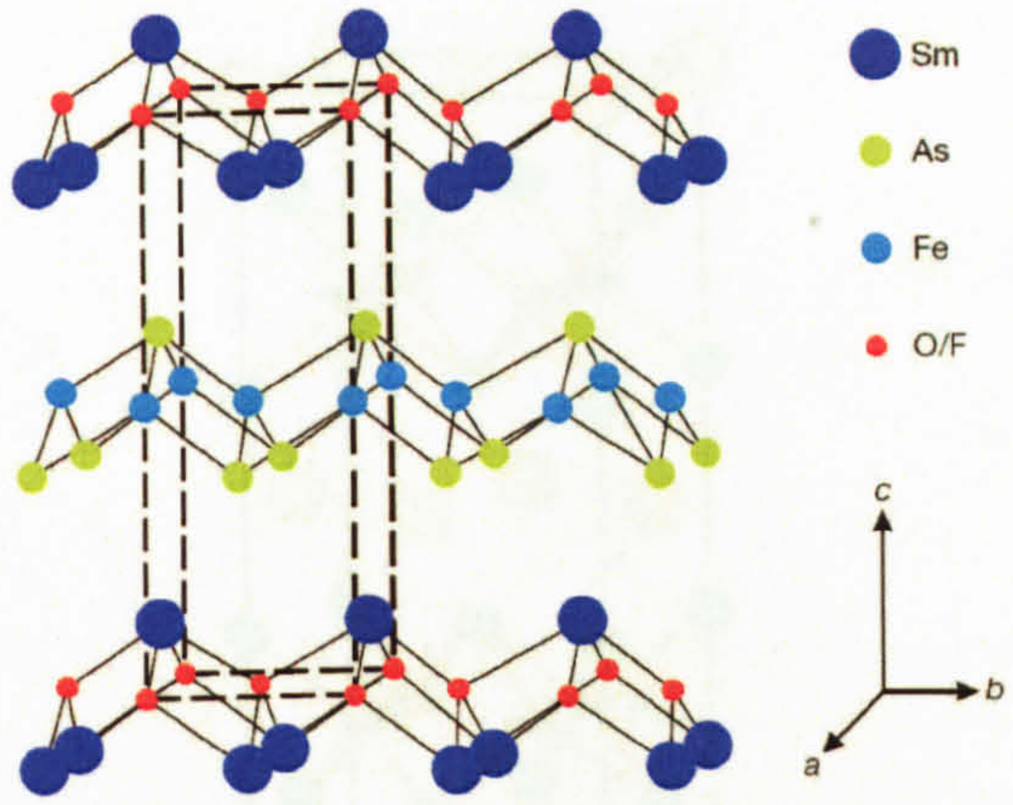

Figure 4.1: Structure of SmFeAsO taken from [123]

transition into a spin density wave state at 137 K. As the compound is doped, these transitions are suppressed and superconductivity emerges. It is unclear whether the SDW state is suppressed before superconductivity occurs or if there is a coexistence in a region of the phase diagram.

4.2.2 (122)-type Pnictides

The (122)-type pnictide superconductors have the chemical formula XFe_2As_2 (X=Ba, Sr, Eu). The (122)-type have two FeAs layers per unit cell. Hole or electron doping the FeAs layers or the X layer with another metal results in superconductivity. These compounds have a body centred tetragonal structure. The first (122) superconductor discovered was $Ba_xK_{1-x}Fe_2As_2$ with a maximum T_c of 38 K [124]. Since then superconductors with Eu [136] and Sr [137] replacing Ba have been discovered. The spin density wave transition is present in the parent compounds. It is possible to dope these compounds with different metals, for example $BaFe_2As_2$ has been doped with K, Ni and Co. The metals can be doped into the FeAs layer unlike the (1111) pnictides which are doped in the rare earth metal layer. The crystal structure of these compounds is shown in figure 4.2. This diagram is taken from [138] which is a neutron

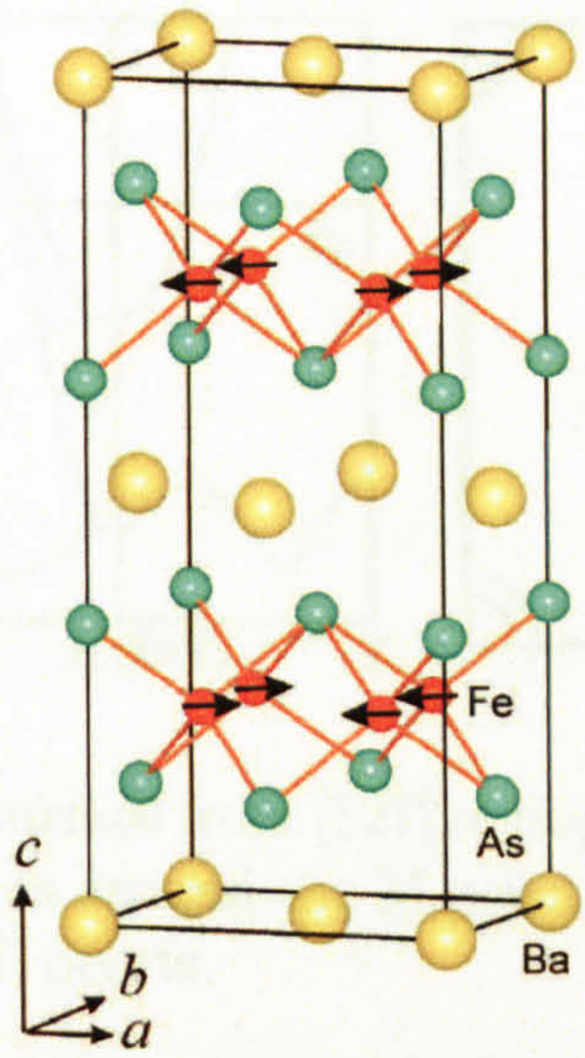

Figure 4.2: Structure of $BaFe_2As_2$ taken from [138]

study of the magnetic and structural properties of the parent compounds $BaFe_2As_2$. This reveals that the parent compound also undergoes a structural transition from a tetragonal space group to an orthorhombic space group at 142 K. At the same temperature, there is also a magnetic transition into an ordered spin density wave state. This is similar behaviour to that observed for the (1111) pnictides, however the magnetic and structural transitions occur at the same temperature.

4.2.3 Fermi Surface of Pnictide Superconductors

Local Density Approximation (LDA) calculations [127] have shown that the electronic conduction occurs in the FeAs plane of the pnictide superconductors meaning they have a quasi-2D electronic structure. There are two electron cylinders at the M point of the Brillouin zone and hole cylinders at the Γ point. To date, only one study has reported quantum oscillations in a pnictide superconductor, de Haas-van Alphen (dHvA) measurements have been performed on the superconductor LaFePO [139]. This compound is isostructural with LaFeAsO and has a T_c of 6 K. No magnetic tran-

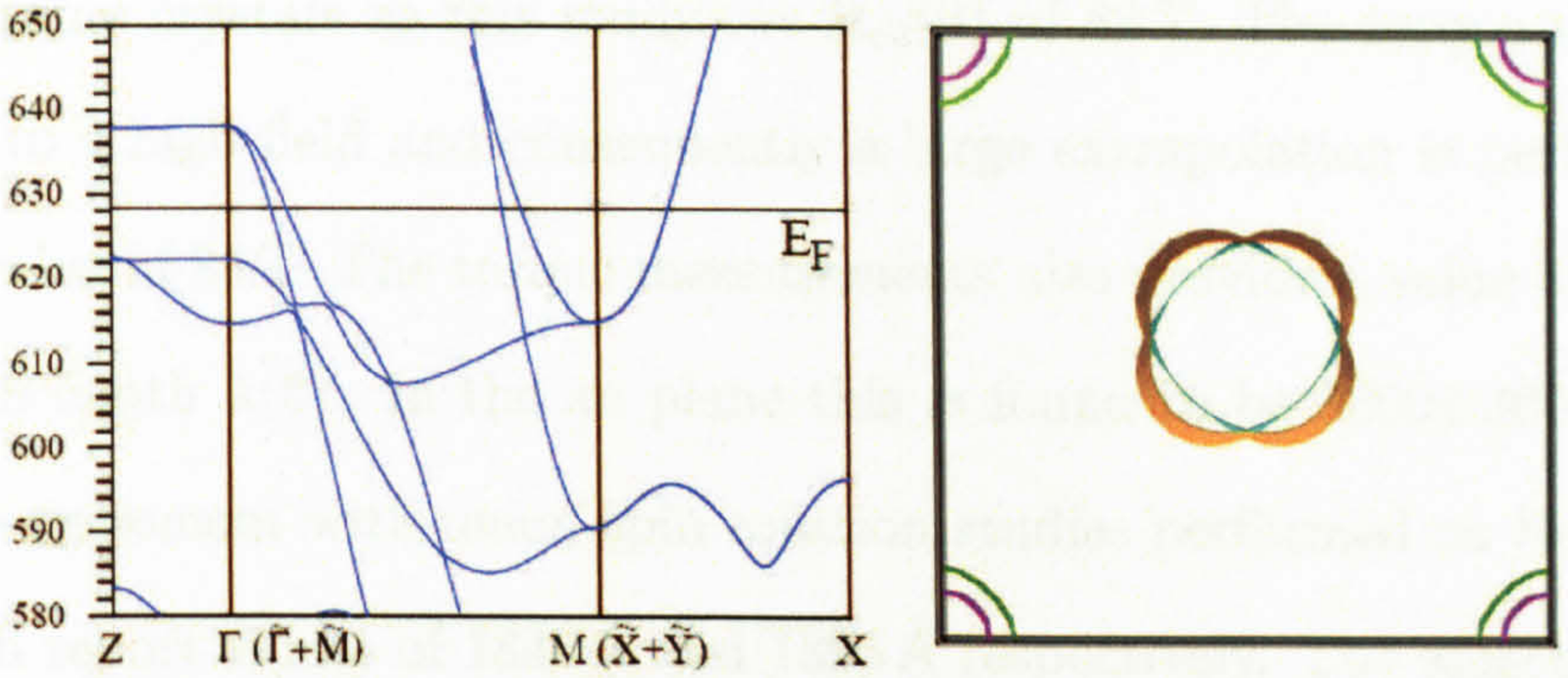

Figure 4.3: Calculated Fermi Surface from [127] of doped LaFeAsO. The Fermi Surface consists of two electron cylinders around the M point (centre of the diagram) and hole cylinders centred around the Γ points.

sition has been observed in LaFePO and no doping is required for superconductivity. The same Fermi surface is observed with electron cylinders in the zone centre and hole cylinders at the corners. This Fermi surface has a strong nesting vector between the electron cylinders and the hole cylinders along the (π,π) direction. This nesting vector implies that this compound is close to a spin density wave instability.

Angle resolved photo emission spectoscopy(ARPES) measurements have been performed on $NdFeAsO_xF_{1-x}$ [140] and $Ba_xK_{1-x}Fe_2As_2$ [141]. The major features of the LDA calculations are reproduced in the ARPES data (i.e there are electron and hole cylinders as expected). The evolution with doping is also measured in $Ba_xK_{1-x}Fe_2As_2$. The electron cylinder shrinks in size and the hole pocket increase in size as expected.

4.2.4 Properties of SmFeAsO Superconductors

The upper critical field of SmFeAsO has been investigated by torque measurements [142] and heat capacity measurements [143]. The heat capacity measurements are performed on polycrystalline samples in fields up to 20 T. A clear specific heat anomaly is seen at all fields and $H_{c2}(0)$ is extrapolated to above 100 T. The torque measurements are carried out using a small cantilever in fields up to 1.4 T. The torque measurements

using the same crystals as this study see $H_{c2}(0)$ of 88 T. The torque measurements do not go to a high field and consequently a large extrapolation is performed to extract the value of 88 T. The torque measurements also provide a value of the absolute penetration depth $\lambda(0)$. In the ab plane this is found to be 2000±300 Å. This is in reasonable agreement with muon spin rotation studies performed on SmFeAsO [144] [145] which report values of 1840 Å and 1895 Å respectively. The anisotropy γ in the superconducting state is measured to be 8 at T_c with a strong temperature dependence. A temperature dependence of γ is also seen in two gap superconductors such as MgB_2 [146]. In contrast the anisotropy of SmFeAsO was measured to be over 30 by infrared ellipsometry [147]. They deduce this value by measuring the c-axis penetration depth λ_c to be 6 μm and comparing this value to the λ_{ab} obtained from muon spin rotation.

4.2.5 Properties of $Ba(Fe_xCo_{1-x})_2As_2$ Superconductors

The discovery of superconductivity in the $Ba(Fe_xCo_{1-x})_2As_2$ system was reported in [148]. This compound is interesting as it might not be expected that doping Co directly into the FeAs layers would create superconductivity, especially when considering the example of the cuprates where doping Zn into the CuO planes destroys superconductivity. The maximum T_c is found to be 22 K which is lower than the maximum of 38 K found in potassium doped $BaFe_2As_2$. In this compound the upper critical field and anisotropy has been measured in several studies. A high field resistivity study [149] reveals an in plane upper critical field in the region of 60 T. The resistive transitions in field are sharp which is in contrast to the cuprates. A small anisotropy is observed in the upper critical field, around 2 over the entire temperature range is measured. This anisotropy represents the anisotropy in the effective mass of the quasi-particles. A similar study [150] also reports a small anisotropy in

the upper critical field. The latest work [151], is a comprehensive study measuring the anisotropy of the upper critical field, the penetration depth and the resistivity. All these techniques suggest a small anisotropy of around 2 which has only a small temperature dependence. This small anisotropy is unexpected as the quasi-2D nature of the Fermi surface seems to imply highly anisotropic properties.

4.2.6 Pairing Mechanism

Calculations have been performed on the pnictide superconductors and they indicate that the electron phonon interaction is too small to produce such a high T_c [126]. Predictions of the T_c based on the electron phonon interaction are around 0.5 K. Neutron scattering experiments on the parent compound LaFeAsO and superconducting $LaFeAsO_{0.89}F_{0.11}$ [152] have measured the phonon density of states $F(\omega)$ in both compounds. This agrees qualitatively with Boeri's calculations [126] when including a 10% shift of the frequencies. $F(\omega)$ is not the relevant quantity in determining T_c, it is the function $\alpha^2F(\omega)$ which includes the coupling strength to the electrons. No high frequency phonons are observed, which are required for a high T_c. In addition the phonon density of states is very similar in both the parent compound and the superconducting compound indicating that the phonons are not inducing superconductivity. If phonons are not responsible for superconductivity then many theories exist for spin fluctuations to be the cause. Mazin [127] predicts an exotic, fully gapped gap symmetry. Based on the proximity to spin fluctuations and taking into account the small Fermi surface an exotic s+/s- state (see Figure 4.4) has the lowest energy state. The s+/s- state has two s-wave gaps on the different Fermi sheets with a π phase shift between them. There are also theories which show that the exotic s+/s- state is close in energy to a d-wave state [154].

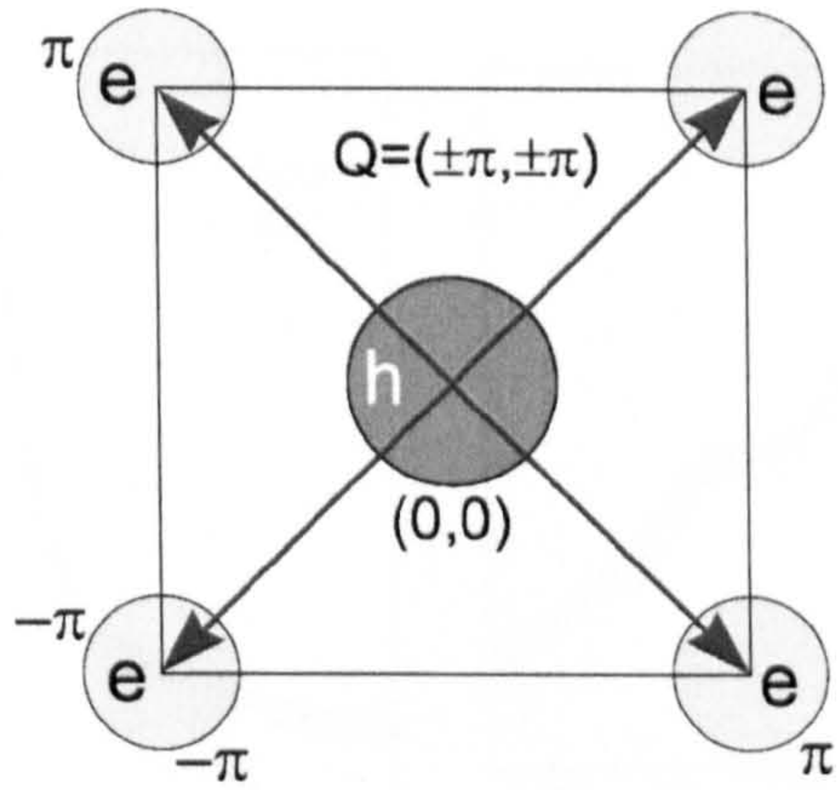

Figure 4.4: The exotic s+/s- state taken from [153]. Different gaps exist on the hole and electron sheets, Q is the antiferromagnetic wave vector.

4.2.7 Gap Symmetry of Pnictides

Point Contact Andreev Spectroscopy

Point Contact Andreev Spectroscopy (PCAS) has been used to measure the superconducting gap in $SmFeAsO_xF_{1-x}$ by two groups [129], [130]. PCAS involves driving a conducting tip into the sample and measuring the conductance. The results are analysed by the BTK method which takes into account contact resistance and the gap value can be extracted. Chen *et al* [130] report PCAS measurements on polycrystalline samples of $SmFeAsO_{0.8}F_{0.2}$. A single s-wave gap is measured with maximum Δ_0 close to the BCS value of $1.76\,k_BT_c$. In contrast Wang *et al* [129] perform the same experiment and see two gaps and a zero bias conductance peak (ZBCP). This ZBCP is interpreted as evidence for a nodal gap symmetry. PCAS is a surface sensitive technique and consequently results can be dependent on the surface quality.

NMR

NMR measurements can be used to determine the gap symmetry of superconductors. The nuclear spin relaxation time T_1 is related to the correlation function of

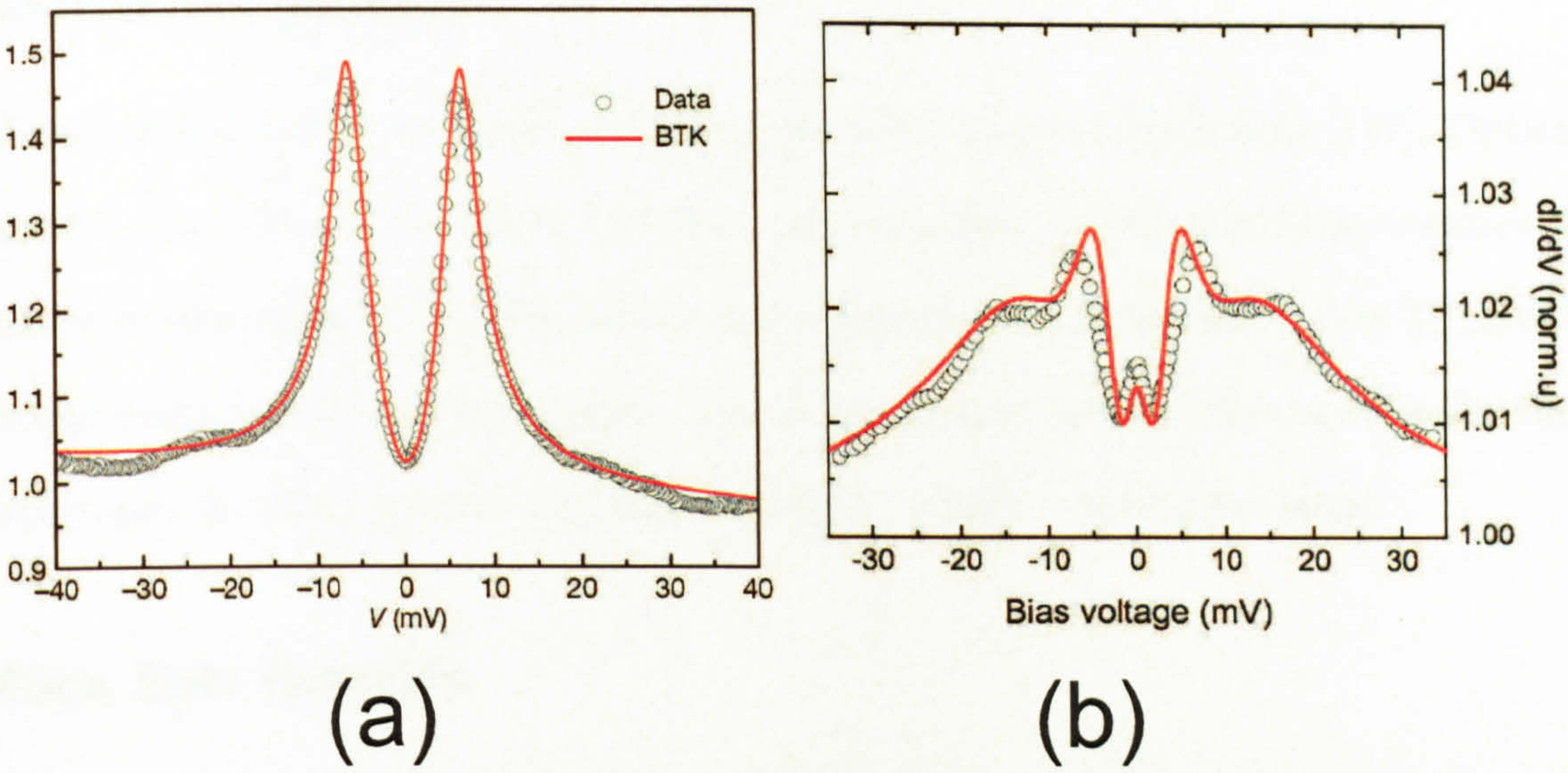

Figure 4.5: PCAS data from (a)[130] and (b) [129].(a) Chen sees one gap of 6.8 meV and (b) Wang clearly see two gaps of 11 meV and 4.5 meV .

the electrons. For a simple s-wave superconductor this can be simplified using the BCS gap equation to show an exponential temperature dependence of the quantity $1/T_1T$ and a Hebel-Slichter coherence peak around T_c. In a d-wave superconductor $1/T_1T$ follows a T^3 temperature dependence. Using ^{75}As, NMR has been performed on $LaFeAsO_{0.9}F_{0.1}$ by Grafe *et al* [155] and by Nakai *at al* [131] on several compositions of $LaFeAsO_{1-x}F_x$. Both see a T^3 dependence of $1/T_1T$ and the absence of a coherence peak at T_c. This is interpreted as evidence for line nodes on the Fermi surface.

NMR has also been performed on $Ba(Fe_xCo_{1-x})_2As_2$ using both ^{59}Co and ^{75}As [156] and $Ba_{1-x}K_xFe_2As_2$ using ^{75}As [157]. The data for $Ba_{1-x}K_xFe_2As_2$ show T^3 dependence in the superconducting state and no coherence peak, which implies an unconventional gap symmetry. For $Ba(Fe_xCo_{1-x})_2As_2$, there is little data in the superconducting state and therefore no comment is made on the gap symmetry. However the results do rule out spin triplet pairing.

Infrared Ellipsometry

Infrared Ellipsometry has been performed on NdFeAsO and SmFeAsO [147]. Optical conductivity and the dielectric function are measured at different temperatures in polycrystalline samples. A subtraction of the conductivity above and below T_c reveals a suppression below a certain energy. This is interpreted as twice the superconducting energy gap Δ. The reported gap value is $4k_BT_c$, which is extremely large.

Muon Spin Rotation

Muon spin rotation has been used to measure the superfluid density of $Ba_{1-x}K_xFe_2As_2$ in the mixed state [158]. The superfluid density follows a BCS like dependence with a gap of $2.5\,k_BT_c$, indicating strong coupling fully gapped superconductivity. It should be noted that specific gap symmetries are distinguished by the superfluid density at low temperatures and this study analyses the whole range and concedes that the data could be explained by more than one gap.

4.3 $SmFeAsO_{0.8}F_{0.2}$ Single Crystals

4.3.1 Low Temperature Penetration Depth

Single crystals of $SmFeAsO_{0.8}F_{0.2}$ were grown using a NaCl/KCl flux method [134] by the group of J Karpinski in Zurich. Two batches of crystals were used, Batch 1 was the first produced and is described in [134] and Batch 2 were grown later and were of a better quality [159]. Crystals from each batch were characterised in Zurich using susceptibility measurements and x-ray diffraction [134]. Two samples were measured from Batch 1 (#1 and #2) and one sample from Batch 2 (#3). All samples were approximately $(80 \times 80 \times 20)\mu$m. Figure 4.6 shows pictures of samples #1 and #2.

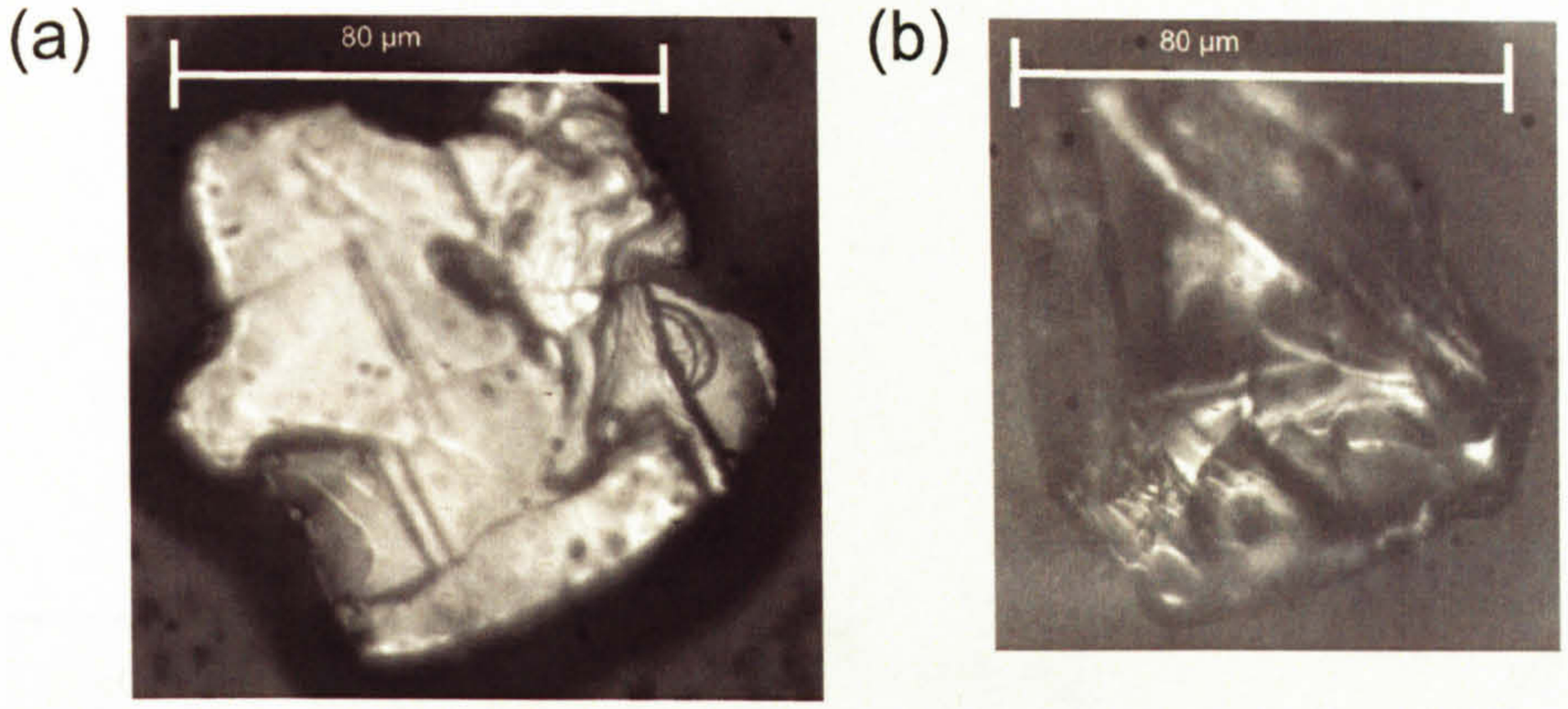

Figure 4.6: Pictures of (a) Sample #1 (b) Sample #2

An SEM in the university of Bristol geology department was used to measure the width of the samples. The samples are irregular shapes and were measured with the field parallel to c, therefore λ_{ab} was measured. The raw frequency shifts are shown in Figure 4.7. The total frequency shift is only 50 Hz for sample #1, 40 Hz for sample #2 and 60 Hz for sample #3. This is consistent with the sensitivity of the coil which is 219 kHz/mm^3 [71]. A sample of $(80 \times 80 \times 20)\mu$m should have a total frequency shift of about 30 Hz which is within the errors of the dimensions. To measure Δf_0 it is necessary to extract the sample from the coil. This because the total frequency shift obtained from the temperature sweep may be affected by normal state properties. For example, the skin depth may result in the sample not being fully penetrated. The extraction values are 46 Hz for sample #1, 38 Hz for sample #2 and 58 Hz for sample #3 which implies that the samples are fully penetrated in the normal state. The calibration factors are calculated by finding R for each sample from equation 2.20 and then using equation 2.22. For sample #1 the calibration factor is 1466 Å/Hz, for sample #2 it is 2160 Å/Hz and for sample #3 it is 1289 Å/Hz. These calibration factors are dependent on the approximation used in R and the error in the sample dimensions. The transitions of samples #1 and #2 show some structure but the low temperature behaviour of both samples is very similar, both having a

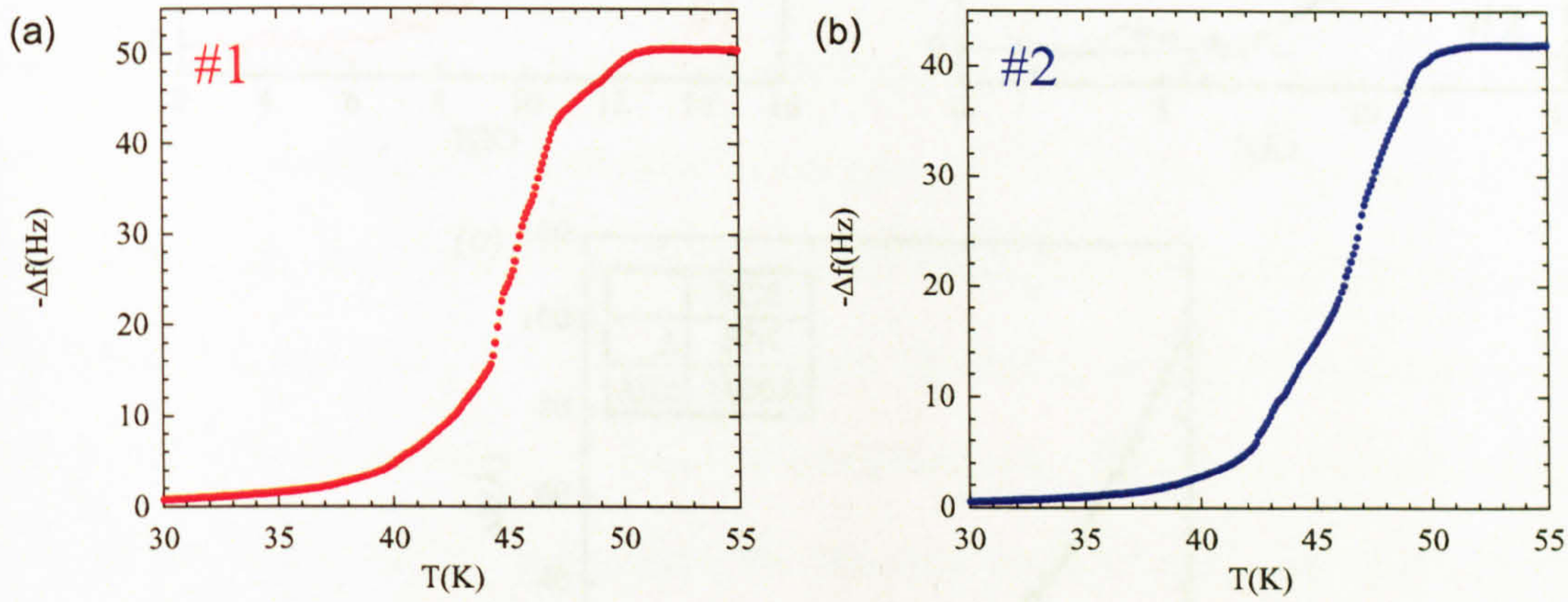

Figure 4.7: The raw frequency shifts for each sample. (a) Sample #1. (b) Sample #2. (c) Sample #3

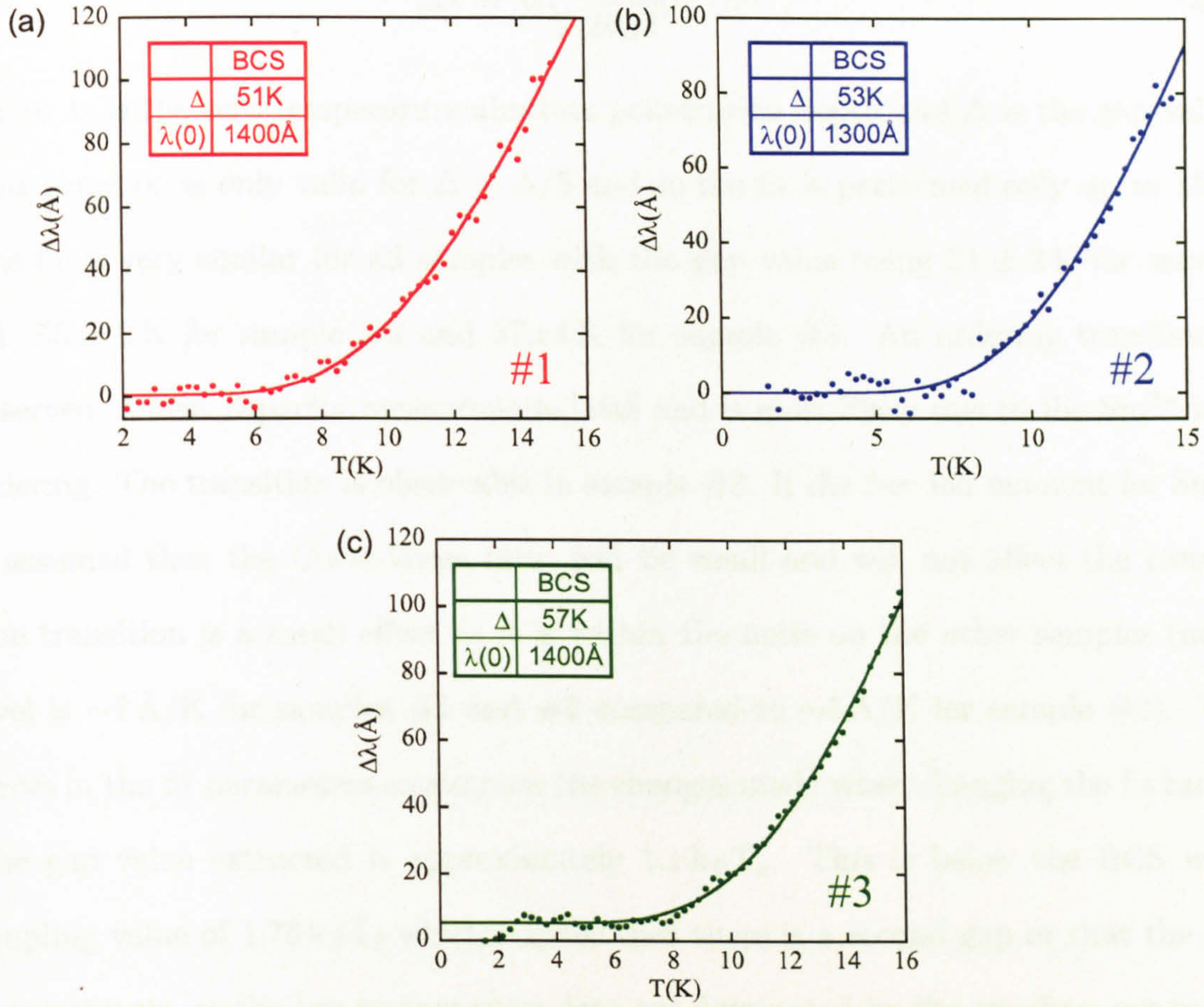

Figure 4.8: Low temperature penetration depth for all the samples. (a) Sample #1 data and fit to the BCS equation. Fit parameters are Δ=51 K and $\lambda(0)$=1400 Å. (b) Sample #2 data and fit to the BCS equation. Fit parameters are Δ=53 K and $\lambda(0)$=1300 Å. (c) Sample #3 data and fit to the BCS equation. Fit parameters are Δ=57 K and $\lambda(0)$=1400 Å.

$\Delta\lambda(T) \sim 100$ Å at 15 K. Sample #3 has a sharper transition with no structure and demonstrates similar low temperature behaviour, but as there is a lower noise level in this measurement an ordering transition is observed at 3 K. The low temperature data for the three samples measured is shown in Figure 4.8. The low temperature behaviour of the penetration depth shows clear exponential behaviour. A fit to the low temperature expansion of the BCS s-wave gap equation 4.1 is in excellent agreement with the data,

$$\Delta\lambda = \lambda_0 \sqrt{\frac{\pi\Delta_0}{2k_BT}} e^{(-\frac{\Delta}{k_BT})}, \tag{4.1}$$

where λ_0 is the zero temperature absolute penetration depth and Δ is the gap value. This equation is only valid for $\Delta \leq \Delta/5$ and so the fit is performed only up to 15 K. The fit is very similar for all samples with the gap value being 51 ± 2 K for sample #1, 53 ± 2 K for sample #2 and 57 ± 4 K for sample #3. An ordering transtion is observed in heat capacity measurments [160] and is most likely due to the Sm^{3+} ions ordering. The transition is observable in sample #3. If the free ion moment for Sm^{3+} is assumed then the Curie-Weiss term will be small and will not affect the results. The transition is a small effect as it is within the noise on the other samples (noise level is $\sim$7 Å/K for samples #1 and #2 compared to $\sim$5 Å/K for sample #3). The errors in the fit parameters encompass the changes made when changing the fit range. The gap value extracted is approximately $1.1\,k_BT_c$. This is below the BCS weak coupling value of $1.76\,k_BT_c$ which implies that there is a second gap or that the gap is anisotropic, as the low temperature data are dominated by the smallest gap in the system. The λ_0 in the fit is an effective penetration depth, which is dependent on the gap structure of the system. The fit to the exponential equation is excellent, however some superconductors with line nodes have been shown to appear to have fully gapped behaviour in the penetration depth due to paramagnetic impurities [161]. This manifests itself as an upturn in the low temperature penetration depth due to susceptibility of paramagnetic ions. For a d-wave superconductor a linear term arising from the nodal quasiparticles is predicted by the BCS gap equation,

$$\Delta\lambda = \ln(2)\lambda_0 \frac{k_BT}{\Delta_0}. \tag{4.2}$$

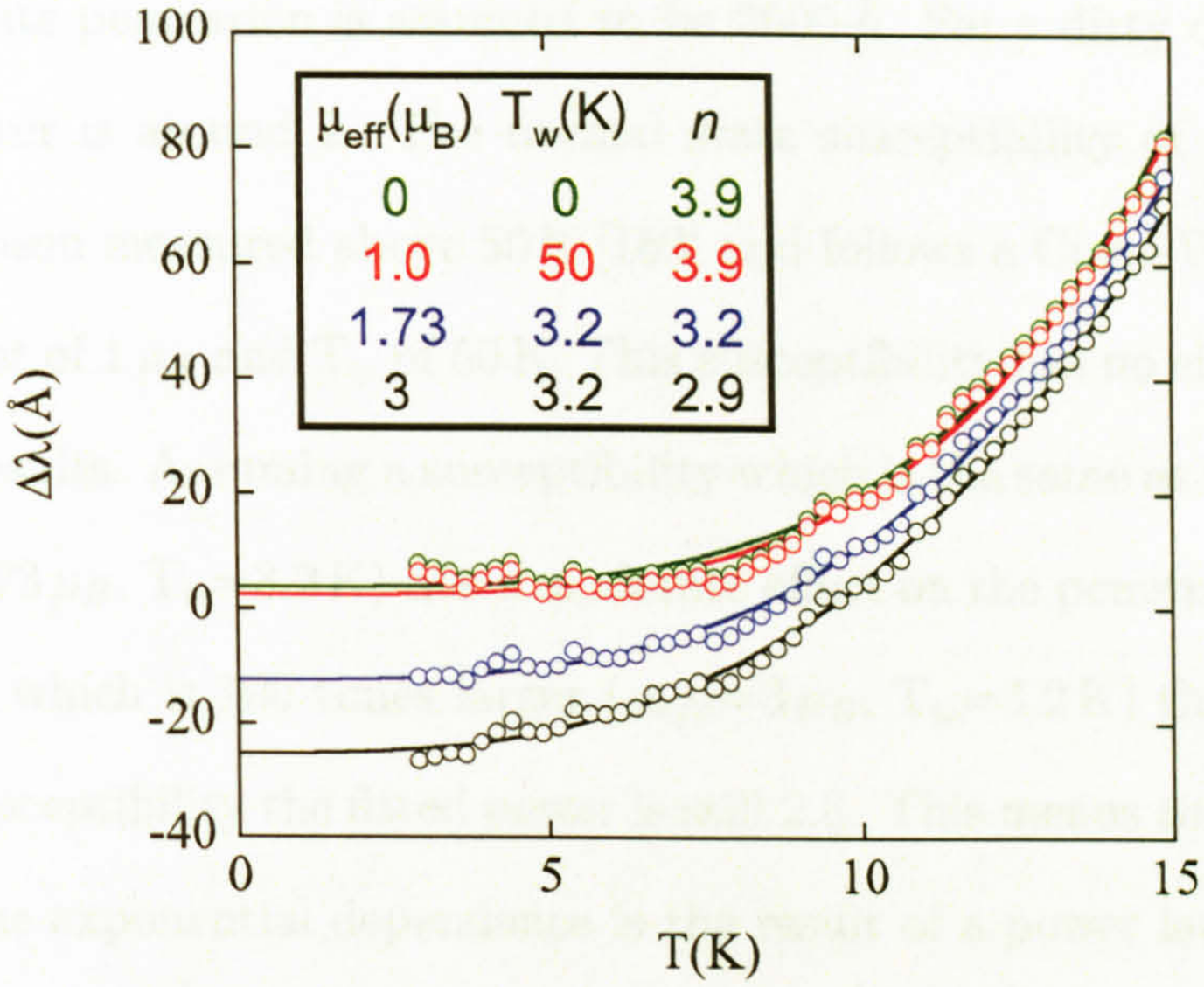

Figure 4.9: The effect of a significant normal state susceptibility on the measured penetration depth. The lines are fits to $\Delta\lambda$=aT^n. The table shows the parameters used for the susceptibility subtraction and the fitted power. The transition is excluded from this analysis.

Equation 4.2 shows the BCS prediction for a d-wave superconductor. Δ_0 is the gap maximum in this case. Taking $\lambda_0 = 2000$Å and a BCS gap maximum of $2.1\,k_BT_c$ gives a linear term of 14 Å/K. In the data there are clearly no linear term of this magnitude below 6 K. If the susceptibility is of a Curie-Weiss form:

$$\chi = \frac{n\mu_0\mu_{eff}^2}{3k_B(T+T_w)}. \tag{4.3}$$

Here μ_{eff} is the effective magnetic moment, T_w is the ordering temperature and the number of atoms n is found using the volume of the unit cell. Following J. Cooper [161], the measured penetration depth is modified as shown in equation 4.4.

$$\Delta\lambda_{meas} = \Delta\lambda\sqrt{1+\chi} \simeq \ln(2)\lambda_0\frac{k_BT}{\Delta_0} + \frac{\lambda(0)C}{2(T+T_w)} + \dots . \tag{4.4}$$

Figure 4.9 shows the data after subtracting various susceptibilites, fitted with a power

law. The absolute pentration is assumed to be 2000 Å. For a dirty d-wave superconductor this power is around 2. The normal state susceptibility of powdered doped SmFeAsO has been measured above 50 K [162] and follows a Curie-Weiss law with an effective moment of 1 μ_B and T_w of 50 K. This susceptibility has no effect on the penetration depth results. Assuming a susceptibility which is the same as the free ion value of Sm (μ_{eff}=1.73 μ_B, T_w=3.2 K) has a moderate effect on the penetration. Even with a susceptibility which is 100 times larger (μ_{eff}=3 μ_B, T_w=3.2 K) than the measured normal state susceptibility the fitted power is still 2.8. This means that it is extremely unlikely that the exponential dependence is the result of a power law combined with a paramagnetic upturn. Since these measurements were performed, two groups have measured the low temperature penetration depth of pnictide samples. Martin *et al* [163] have measured NdFeAsO using a tunnel diode oscillator technique. Hashimoto *et al* [164] have measured PrFeAsO using microwave surface impedance. Both see an exponential temperature dependence with a small gap ($\sim 1.3\, k_B T_c$) consistent with the results presented here.

4.3.2 Superfluid Density

The low temperature behaviour reveals the smallest gap in the system. To find the larger gap or quantify the anisotropy it is possible to do a fit to the superfluid density. The model assumes there are two gaps which both follow a BCS temperature dependence. The combined superfluid density is given in the equation

$$\rho = x\rho_1[\Delta_1, T] + (1-x)\rho_2[\Delta_2, T]. \tag{4.5}$$

The parameters of the fit are the gaps Δ_1 and Δ_2, x the fraction of superfluid density attributed to each gap, T_c and the absolute penetration depth λ_0. These can all be

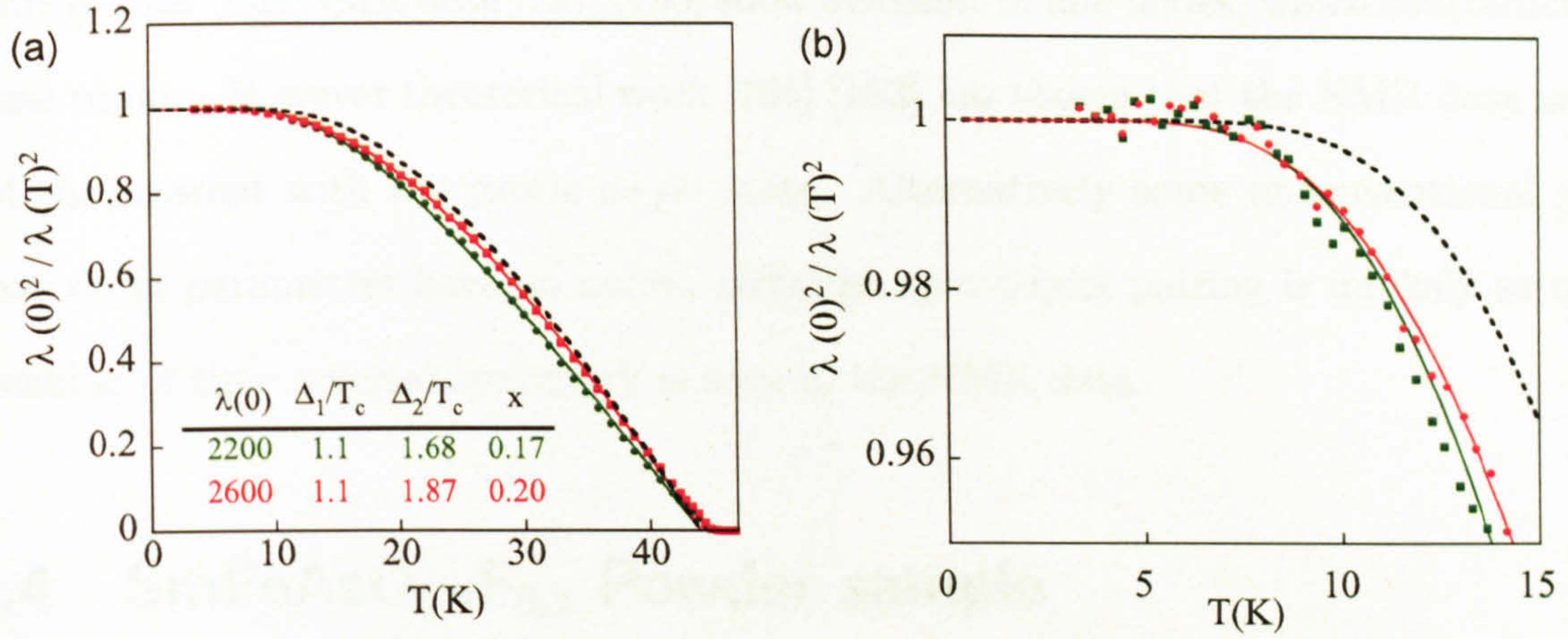

Figure 4.10: Fit to the superfluid density of Sample #3. Two values of λ_0 are used, 2200 Å and 2600 Å to encompass the range of values. The black dashed line is the BCS weak coupling result. Fit parameters are shown in the table. (a) Over the whole temperature range. (b) Close up of the low temperature behaviour.

varied, however, Δ_1 is known from the low temperature behaviour, T_c is set to 41.5 K as extrapolated from the superfluid density and λ_0 is known to be 2000±300 Å as measured by torque [142]. Two values for λ_0 are used to take into account the error in λ_0 from the torque measurements and the error in the calibration factors. The fits are shown in figure 4.10. The two values of $\lambda(0)$ show a second gap around the BCS gap value of $1.8\,k_B T_c$ with appoximately 20% of the superfluid density being associated with the small gap Δ_1. The large gap is the same size as the one seen by Chen *et al* [130] in the PCAS data and the smaller gap has only a small percentage of the superfluid density, which may explain why it is not observed in their PCAS data. The smaller gap is the same size as the small gap seen by Wang *et al* [129] in their PCAS data. This fully gapped two gap system is similar to that seen in MgB_2 and $NbSe_2$. Both of these are electron-phonon superconductors. As discussed above, electron-phonon interactions appear too small to be responsible for superconductivity in the pnictides. The exotic two gapped state s+/s- predicted by Mazin [127] is also consistent with this result, but a phase sensitive technique will be required to

confirm this. The NMR data [131] [155] show evidence of line nodes, which contradicts these results. However theoretical work [165] [153] has shown that the NMR data are not inconsistent with the exotic s+/s- state. Alternatively some unconventional p-wave order parameters have no nodes, although spin-triplet pairing is unlikely as no breaking of time reversal symmetry is seen in the NMR data.

4.4 $SmFeAsO_{0.8}F_{0.2}$ Powder sample

To confirm the results on the single crystal samples, a powder sample of $SmFeAsO_{0.8}F_{0.2}$ was measured. The powder sample was prepared by grinding up polycrystalline $SmFeAsO_{0.8}F_{0.2}$ and then setting the powder in some 5 minute epoxy. The powder was ground for 20 mins before 0.4 mg of powder was mixed with 2.9 mg of epoxy. The mixture was then allowed to set in a $(1 \times 0.8 \times 0.2)$ mm indent in some wax. The indent was created using a piece of aluminum machined flat apart from an upwards square the same size as the indent. This was then pushed firmly into some partially melted wax to create the indent. Some of the powder was saved and photographed in the SEM as shown in figure 4.11. The average grain size was 3.6 μm (see figure 4.11). Once the epoxy was dry the sample was placed on the H parallel to ab rod and measured in the tunnel diode apparatus. The raw frequency shifts are shown in Figure 4.12. The grains are not aligned so a mixture of λ_c and λ_{ab} will be measured. The superconducting volume in the powder sample is 0.1 mm^3 (calculated from the volume of the unit cell and the formula mass). From the sensitivity of the coil this should result in a total frequency shift of 22 kHz, but a total frequency shift of only 46 Hz is observed. This means the grains are fully penetrated and that $\lambda >> r$. Assuming the grain size distribution measured and shown in figure 4.11, the low temperature behaviour of λ is shown in figure 4.13. The low temperature behaviour of

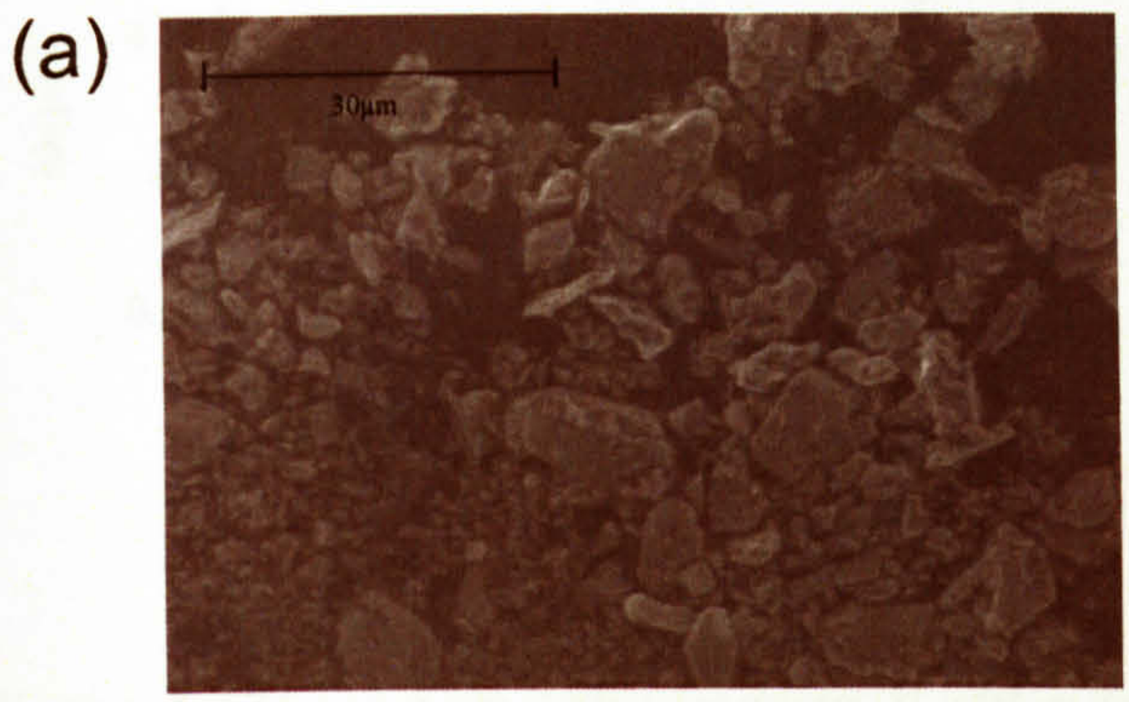

Figure 4.11: (a) SEM picture of the powder. (b) Histogram of measured grain size, mean is 3.6 μm and standard deviation is 2 μm.

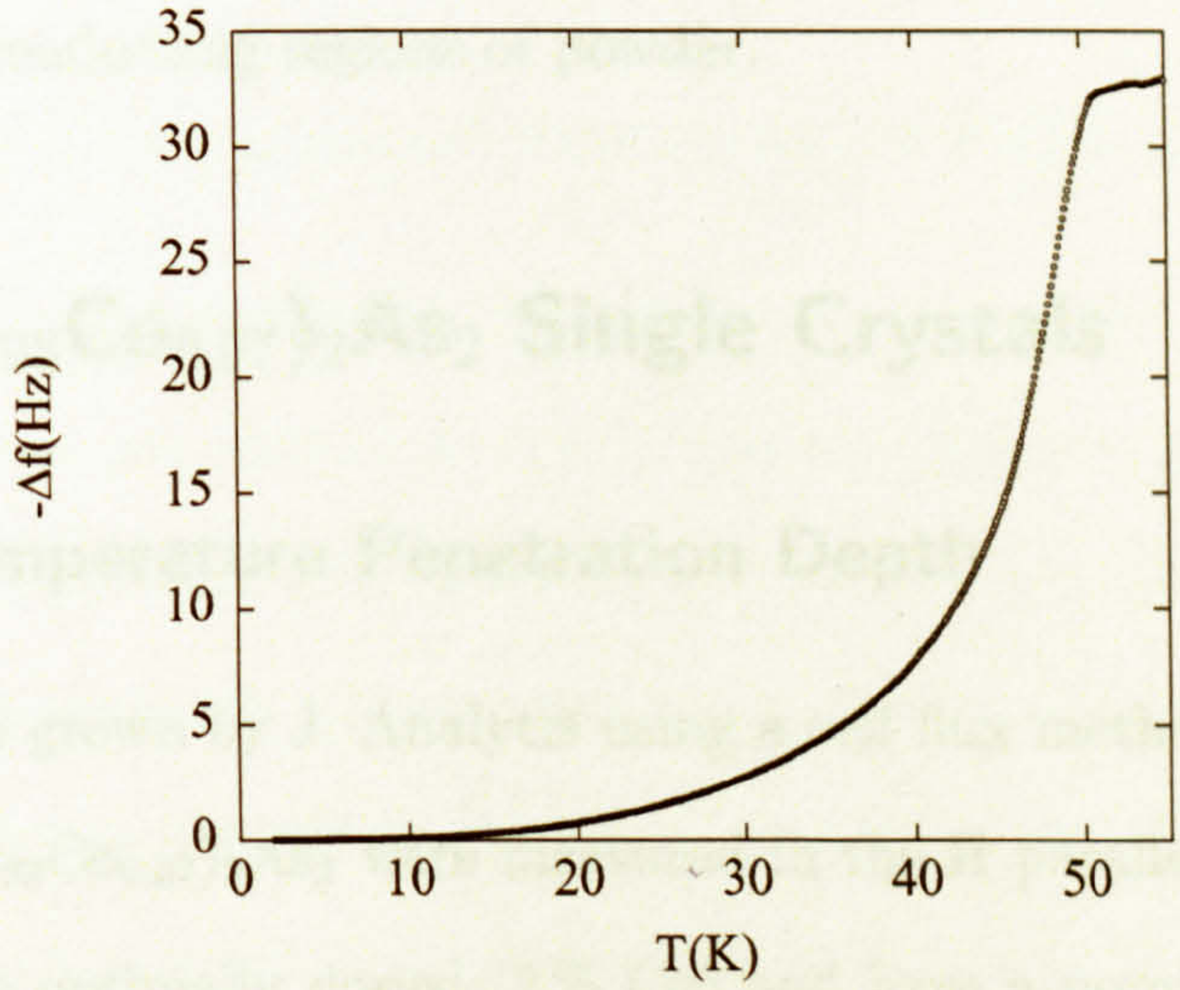

Figure 4.12: Raw frequency shifts of the powder sample.

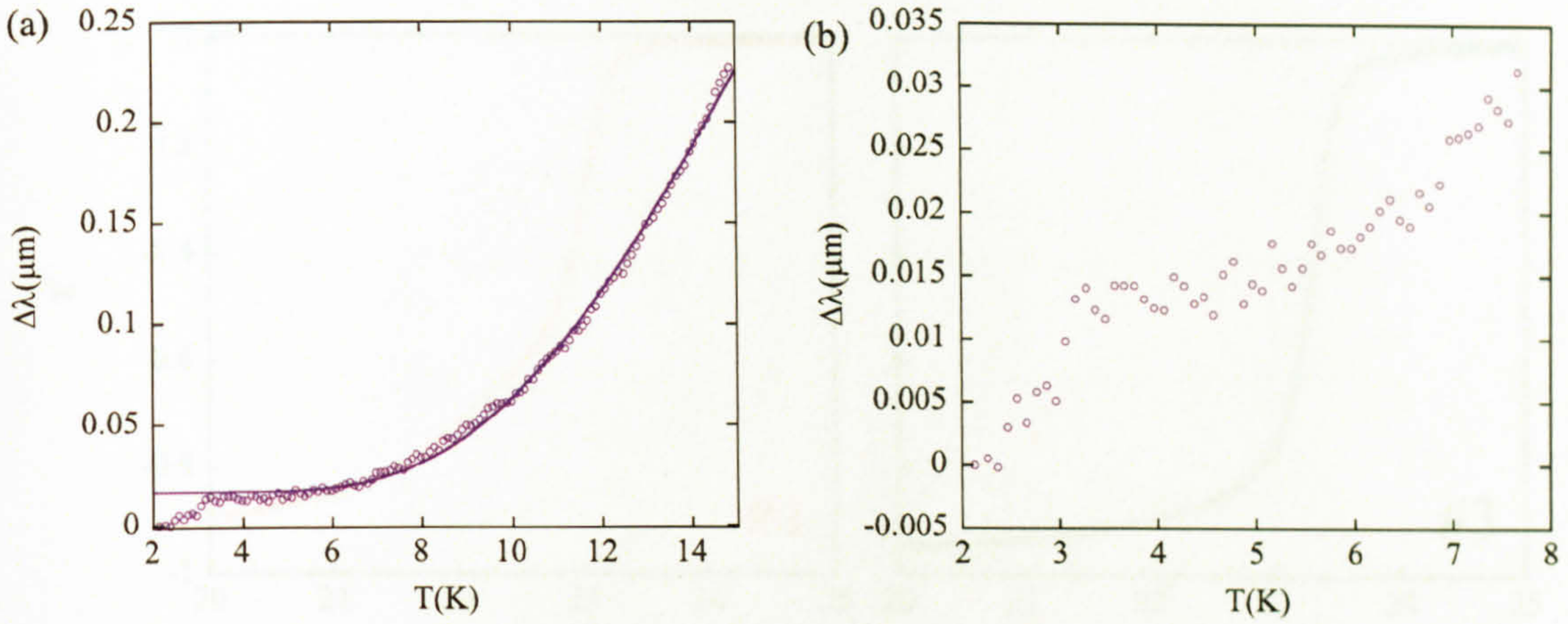

Figure 4.13: (a) Low temperature λ, extracted from a fit to equation 2.25. The solid line is a fit to equation 4.1 with parameters Δ=51±5 K and $\lambda(0)$=50 μm (b) Close up of the Sm ordering transition observed in one crystal and confirmed here.

λ is similar to the single crystal samples. There is a clear ordering transition at 3 K as observed in the single crystal sample #3. The gap Δ from the fit is 51±5 K which is $1.1\pm0.1 k_B T_c$. The zero temperature penetration depth λ_0 is much longer. In a randomly oriented powder sample with λ_c much larger than λ_{ab} then λ_{ab} dominates the susceptibility contribution [166]. The large measured λ in this case could be the result of non-superconducting regions of powder.

4.5 $Ba(Fe_{0.93}Co_{0.07})_2As_2$ Single Crystals

4.5.1 Low Temperature Penetration Depth

Single crystals were grown by J. Analytis using a self flux method [167]. Four single crystals of $Ba_2(Fe_{0.93}Co_{0.07})_2As_2$ were measured in the H parallel to c configuration. These crystals were optimally doped (7 % Co) and have a nominal T_c of 22 K. The samples are larger and not as flat as the SmFeAsO samples and are around 0.2 mm by 0.2 mm by 0.1 mm. The largest sample is #4 which has a 0.45 mm by 0.45 mm cross section. Sample #2 showed two superconducting transitions and is excluded

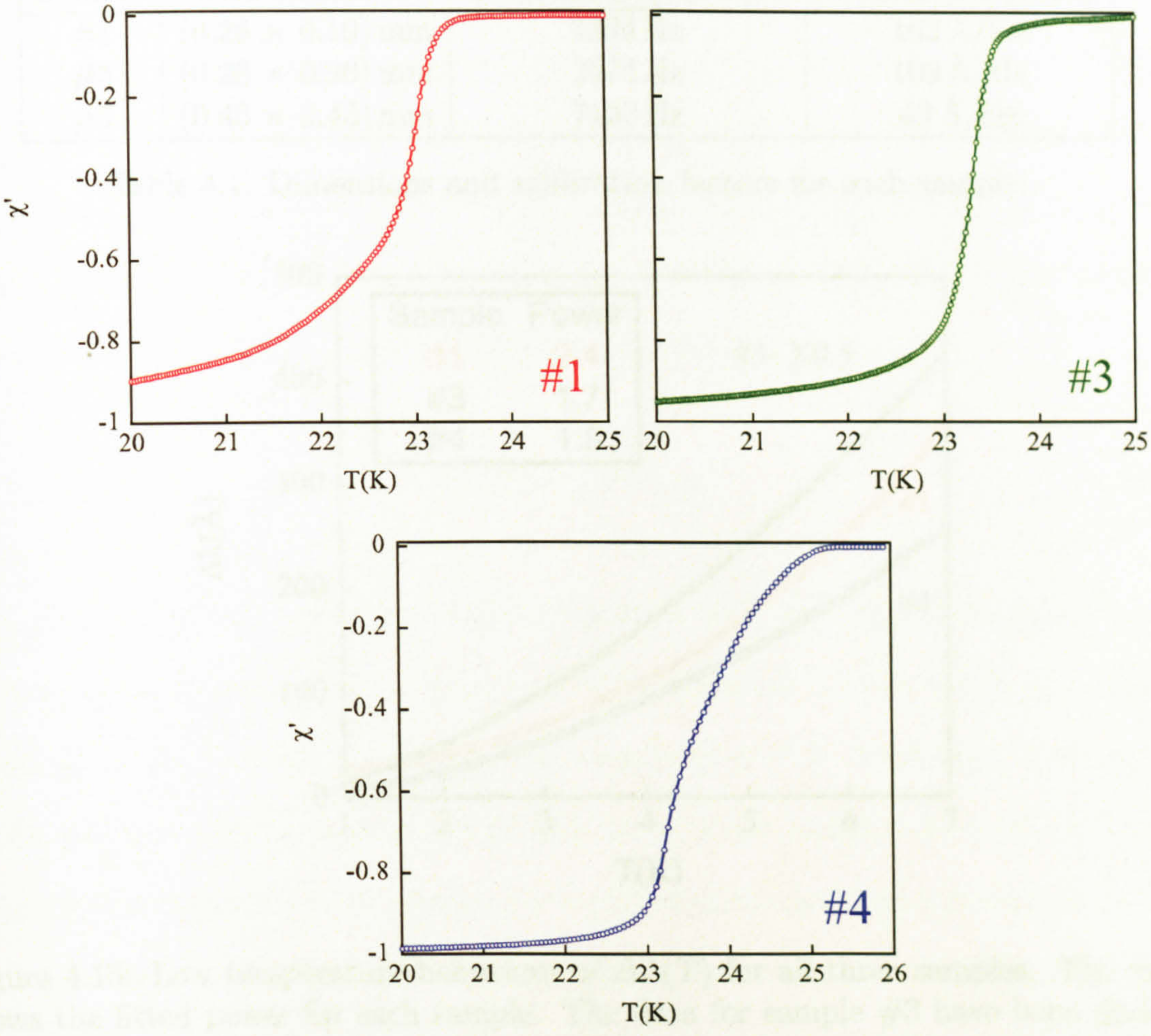

Figure 4.14: The transitions of three crystals of $Ba(Fe_{0.93}Co_{0.07})_2As_2$.

from this discussion. The transitions of samples #1, #3 and #4 are shown in Figure 4.14. The transitions are slightly varied in quality. Sample #1 has the broadest transition with a little structure. Sample #3 has a sharp transition and is very smooth. Sample #4 is slightly broader and not as smooth. The calibration factors of the three samples are calculated as described previously and are shown in table 4.1 along with the sample size and total frequency shift. These samples are reasonably big and therefore the resolution is much better than the SmFeAsO samples, up to $\sim$1 Å. The low temperature behaviour is similar for samples #1 and #4 but different for sample #3. Samples #1 and #4 follow a power law with a power between 1.7

Sample	ab Dimensions	Total Frequency Shift	Calibration Factor
#1	(0.26×0.19) mm	1394 Hz	162 Å/Hz
#3	(0.28×0.26) mm	2474 Hz	109 Å/Hz
#4	(0.45×0.45) mm	7138 Hz	63 Å/Hz

Table 4.1: Dimensions and calibration factors for each sample.

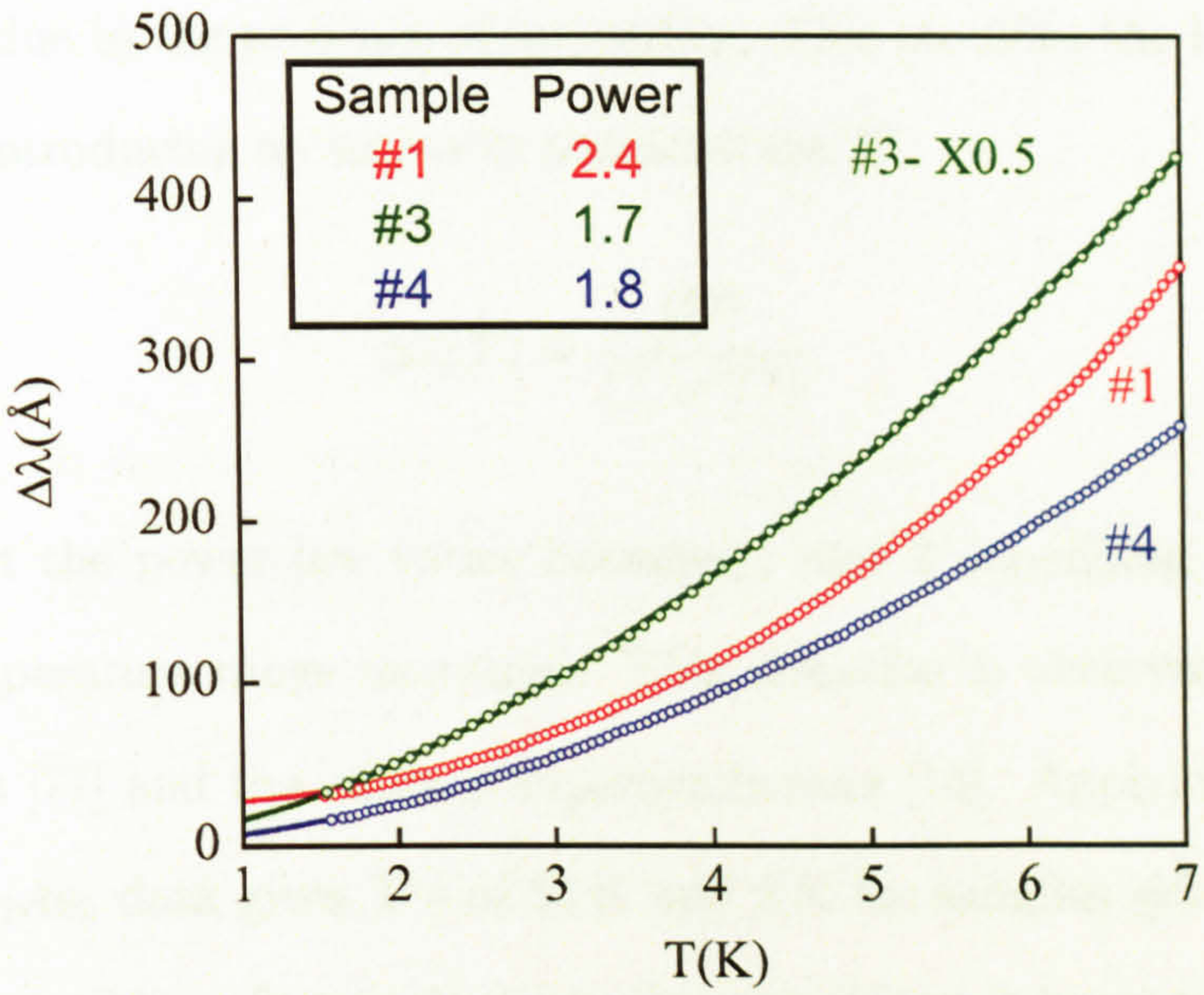

Figure 4.15: Low temperature behaviour of $\Delta\lambda$(T) for all three samples. The table shows the fitted power for each sample. The data for sample #3 have been divided by two for clarity.

and 2.4 and at 7 K $\Delta\lambda$ is about 300 Å. Sample #3 also follows a power law with the power around 1.7 however at 7 K $\Delta\lambda$ is 800 Å. The calibration factors are accurate to around 20 % which is not enough to explain this difference in values. An obvious explanation could be a difference in λ_0 between samples. This could be the result of surface roughness in sample #3. It should also be noted that sample #3 has the sharpest transition and therefore it might be expected that this sample has the highest quality and reveals the true dependence in this material. Figure 4.15 shows the low temperature behaviour of the penetration in each sample with a fit to

$$\Delta\lambda(T) = aT^n. \tag{4.6}$$

This equation fits the data well below 7 K with n varying between 1.7 and 2.4 between samples. This behaviour is indicative of an unconventional order parameter. For a clean simple d-wave superconductor the low temperature penetration depth is linear as shown in equation 4.2. A perfect linear T dependence is rarely observed in a d-wave superconductor due to the presence of impurities. This modifies the low temperature dependence by introducing an impurity temperature T*

$$\Delta\lambda(T) = \frac{bT^2}{(T+T^*)}. \tag{4.7}$$

This means that the power law varies between 1 and 2 depending on the value of T* and the temperature range measured. This situation is observed in the organic superconductors [77] and the cuprate superconductors [14]. Applying this fit to the $Ba(Fe_{0.93}Co_{0.07})_2As_2$ data gives T*s of 15 K and 8 K for samples #3 and #4 respectively. It is not possible to fit sample #1 in this scenario as it has a power law greater than 2. If the gap symmetry is not a simple d-wave case then the power law can change. It is possible that impurities are modifying the properties especially as these are newly synthesised materials and the crystal growth is not optimised yet. Another possible reason for the measured power law is if the slope of the gap at the nodes $\frac{d\Delta}{d\theta}$ is larger than a conventional d-wave superconductor. A more exotic gap symmetry, for example point nodes can give a power law greater than 2. Finally, it has been suggested that an s+/s- state would be sensitive to impurities in a similar way to a d-wave superconductor and this could create an unconventional power law in a fully gapped superconductor which is discussed below.

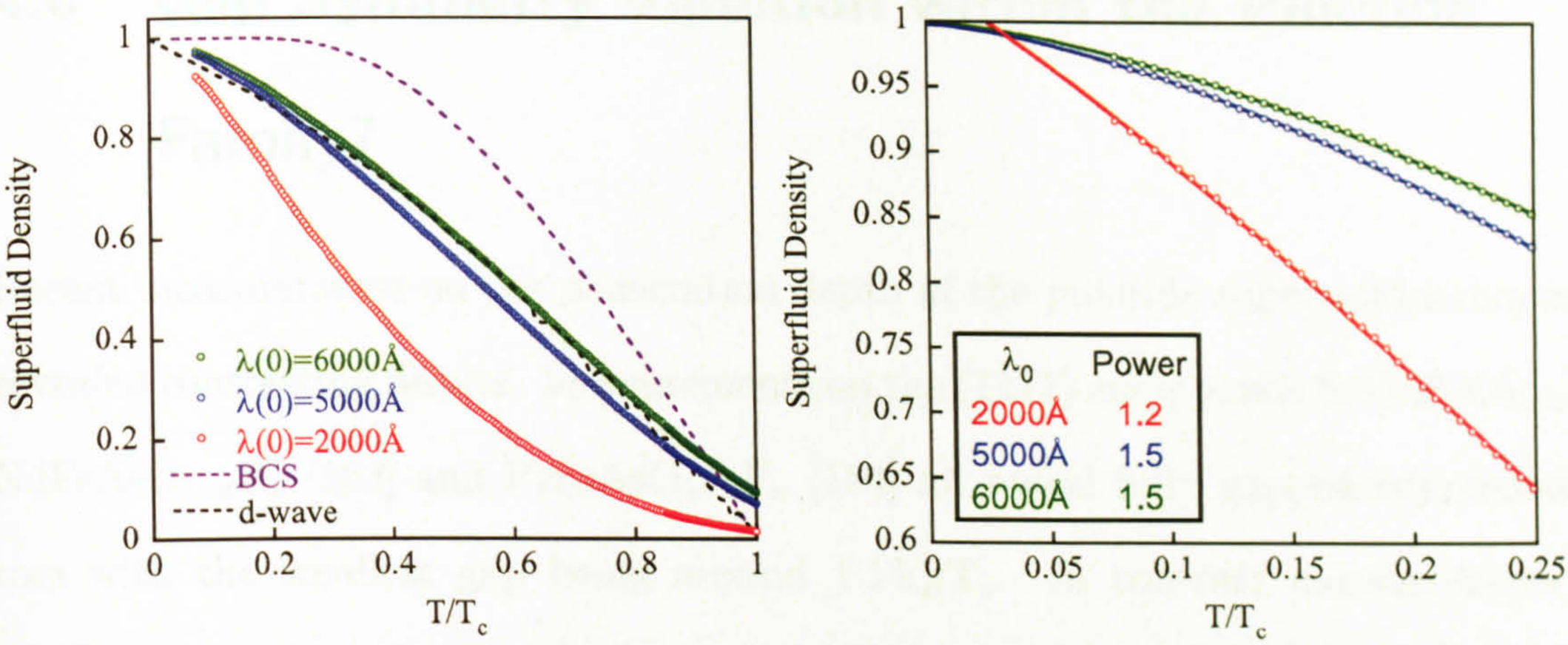

Figure 4.16: Left: Superfluid density of Sample #3 plotted with different values of λ_0 and compared with the predictions for s-wave and d-wave weak coupling superconductors. Right: Low temperature behaviour with fits to a simple power law.

4.5.2 Superfluid Density

Figure 4.16 shows the behaviour of the superfluid density of sample #3. Three values of λ_0 are chosen to show the variation of the curve with λ_0. No experiments have been reported that have measured λ_0 in this superconductor. The values used to get a reasonable superfluid density are slightly large, especially when compared to the values of the (1111) pnictides. A λ_0 of 2000 Å is included as this is the value measured in the (1111) pnictides but this does not give a reasonable superfluid density. λ_0 is dependent on the Fermi surface, impurities and surface roughness, all of which can increase the value. The simple power law fits show a $T^{1.5}$ dependence at the lowest temperature. If a λ_0 of 2000 Å is used then the low temperature power law is 1.2. This is consistent with a dirty d-wave superconductor, but not with an unconventional s+/s- state with impurities.

4.6 Gap Symmetry Variation within the Pnictide Family?

Recent measurements on the penetration depth of the pnictide superconductors have revealed contrasting results. Measurements on the (1111) compounds $SmFeAsO_{1-x}F_x$, $NdFeAsO_{1-x}F_x$ [163] and $PrFeAsO_{1-x}F_x$ [164] all reveal fully gapped superconductors with the smallest gap being around $1.1\,k_BT_c$. In contrast measurements on $Ba(Fe_xCo_{1-x})_2As_2$ reveal a low temperature power law dependence of $\Delta\lambda(T)$ (measured in this study and in a similar study [168]). Another group have measured $Ba_xNi_{1-x}Fe_2As_2$ [169] and found a power law in some samples and an exponential in other samples. Finally measurements on LaFePO [170] show the best evidence for a d-wave superconductor as they have a linear temperature dependence (see figure 4.17). These different results suggest that there could be different gap symmetries in different members of the pnictide family. Alternatively poor sample quality could be disrupting measurements, similar to measurements after the discovery of the cuprates. One proposed theory [171] analyses the experimental data for each compound and suggests that the power law exhibited in some samples is actually the result of impurities in the unconventional s+/s- state. Non-magnetic impurities in this state create a constant DOS at low energies, in a similar fashion to a d-wave superconductor. These impurities can create a low temperature power law down to a power of about 1.6 (see figure 4.17). Therefore this theory can explain all the results apart from the measurements on LaFePO. It should also be noted that two $Ba(Fe_{0.93}Co_{0.07})_2As_2$ crystals described above follow a power of 1.5 which is also not consistent with this theory. An alternative theory [172] suggests that a d-wave pairing symmetry and an s+/s- pairing symmetry are very close in energy. This means it would only take small variations in some parameters to change from an s+/s- state to a d-wave state. More measure-

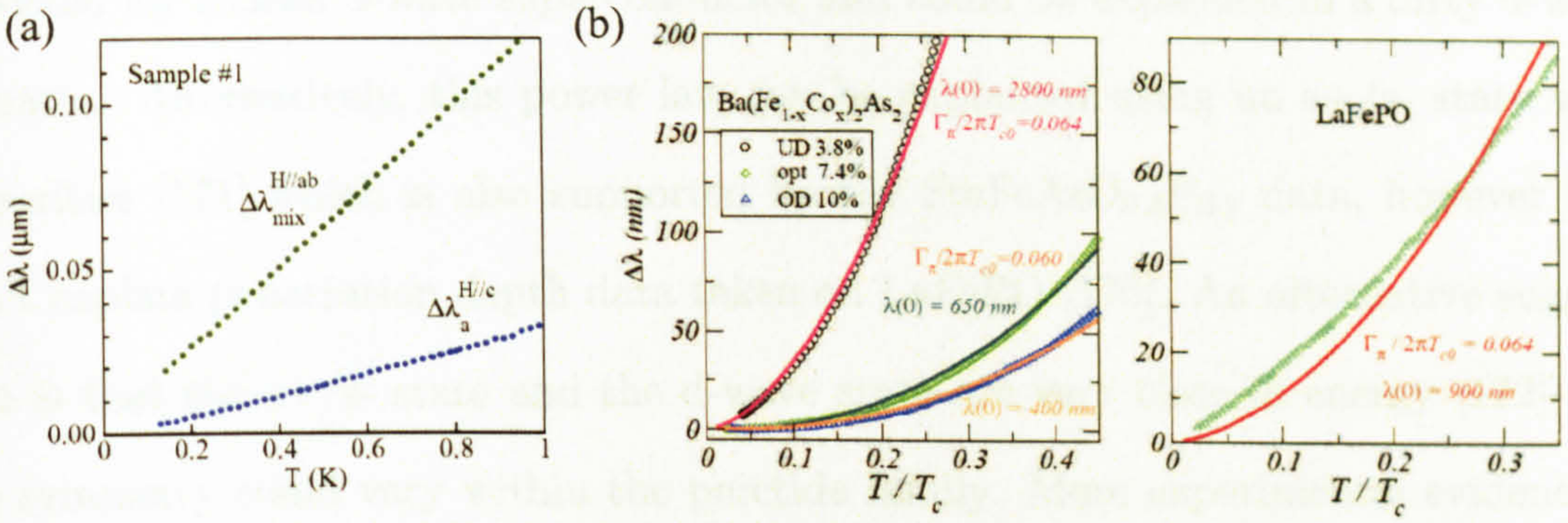

Figure 4.17: (a) Measured penetration depth of LaFePO showing linear dependence at low temperature [170]. (b) Fits to the penetration depth of $Ba(Fe_xCo_{1-x})_2As_2$ and LaFePO assuming an s+/s- state with impurities [171].

ments, particularly phase sensitive measurements like those suggested in [173], [174] or angle dependent thermodynamic probes, of the order parameter are required to establish the pairing symmetry (symmetries) in the pnictides.

4.7 Conclusions

The newly discovered pnictide superconductors are interesting compounds due to their high transition temperatures in combination with a magnetic parent compound. Magnetic penetration depth measurements using a tunnel diode oscillator on single crystal and powder $SmFeAsO_{0.8}F_{0.2}$ support a fully gapped superconducting state. The single crystal data supports a two gap superconductor with a small gap of $1.1\,k_BT_c$ and a larger gap of around $1.8\,k_BT_c$, or a single anisotropic gap with a minimum of $1.1\,k_BT_c$. These results are in agreement with similar studies on $NdFeAsO_{1-x}F_x$ [163] and $PrFeAsO_{1-x}F_x$ [164] which show similar fully gapped superconducting states. In contrast, magnetic penetration depth measurements on single crystal $Ba(Fe_{0.93}Co_{0.07})_2As_2$ support an unconventional order parameter. The low temperature penetration depth follows a power law with a power between 1.7 and 2.4. This power is higher than

expected for a clean d-wave superconductor and could be explained in a dirty d-wave scenario. Alternatively, this power law can be explained using an s+/s- state with impurities [171] which is also supported by the $SmFeAsO_{0.8}F_{0.2}$ data, however this can't explain penetration depth data taken on LaFePO [170]. An alternative suggestion is that the s+/s- state and the d-wave state are very close in energy [172] and the symmetry could vary within the pnictide family. More experimental evidence is needed before either scenario can be confirmed.

Chapter 5

The Phase diagram of $AgNiO_2$: Heat Capacity in Very High Magnetic Fields

5.1 Introduction

Frustrated magnetism has attracted a lot of research interest [175] due to the possibility of unconventional phases of matter. The frustrated magnet silver nickel oxide $AgNiO_2$ is a newly synthesised metal [176]. Neutron diffraction has been performed on this material and reveals magnetic nickel ions on a triangular lattice [177]. Measurements of the resistivity show metallic behaviour down to low temperatures [178]. In zero field, heat capacity and susceptibility measurements reveal an antiferromagnetic transition at 20 K [179]. In high magnetic fields, resistivity and torque measurements by A. Coldea show quantum oscillations and kinks at several fields [180]. These kinks were postulated to be a cascade of magnetic phase transitions and measurements of heat capacity can show if this is the case. In collaboration with A. Coldea a heat ca-

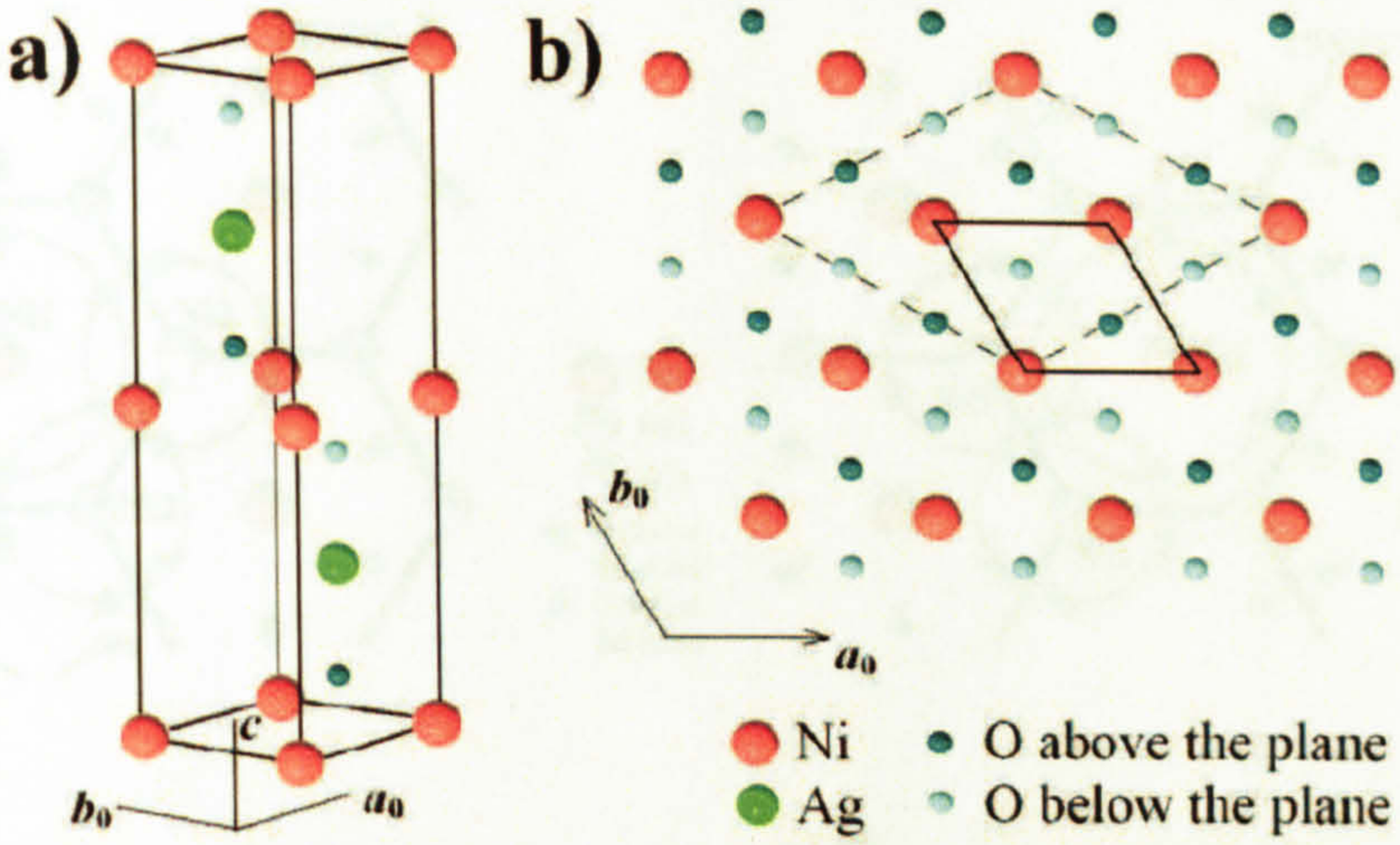

Figure 5.1: The crystal structure of $AgNiO_2$ taken from [179]. (a) The unit cell. (b) The layers of NiO showing unit cell above the transition (solid line) and below the transition (dashed line).

pacity probe was designed and built which was capable of measuring the heat capacity of small single crystals of $AgNiO_2$ in fields up to 33 T. In addition, long relaxation calorimetry measurements on powdered $AgNiO_2$ were performed to measure the Sommerfeld coefficient.

5.2 Silver Nickel Oxide

5.2.1 Structure

Neutron and X-ray diffraction studies were performed on powder samples of $AgNiO_2$ [179]. The material consists of layers of Ni and O in a hexagonal arrangement separated by Ag layers. At 365 K a resistance anomaly is observed, which is associated with a structural transition involving the oxygen ions [178]. This transition effectively triples the unit cell and produces charge order on the nickel ions. Using simple chemical arguments it could be expected that all Ni ions carry a charge of 3+, the Ag

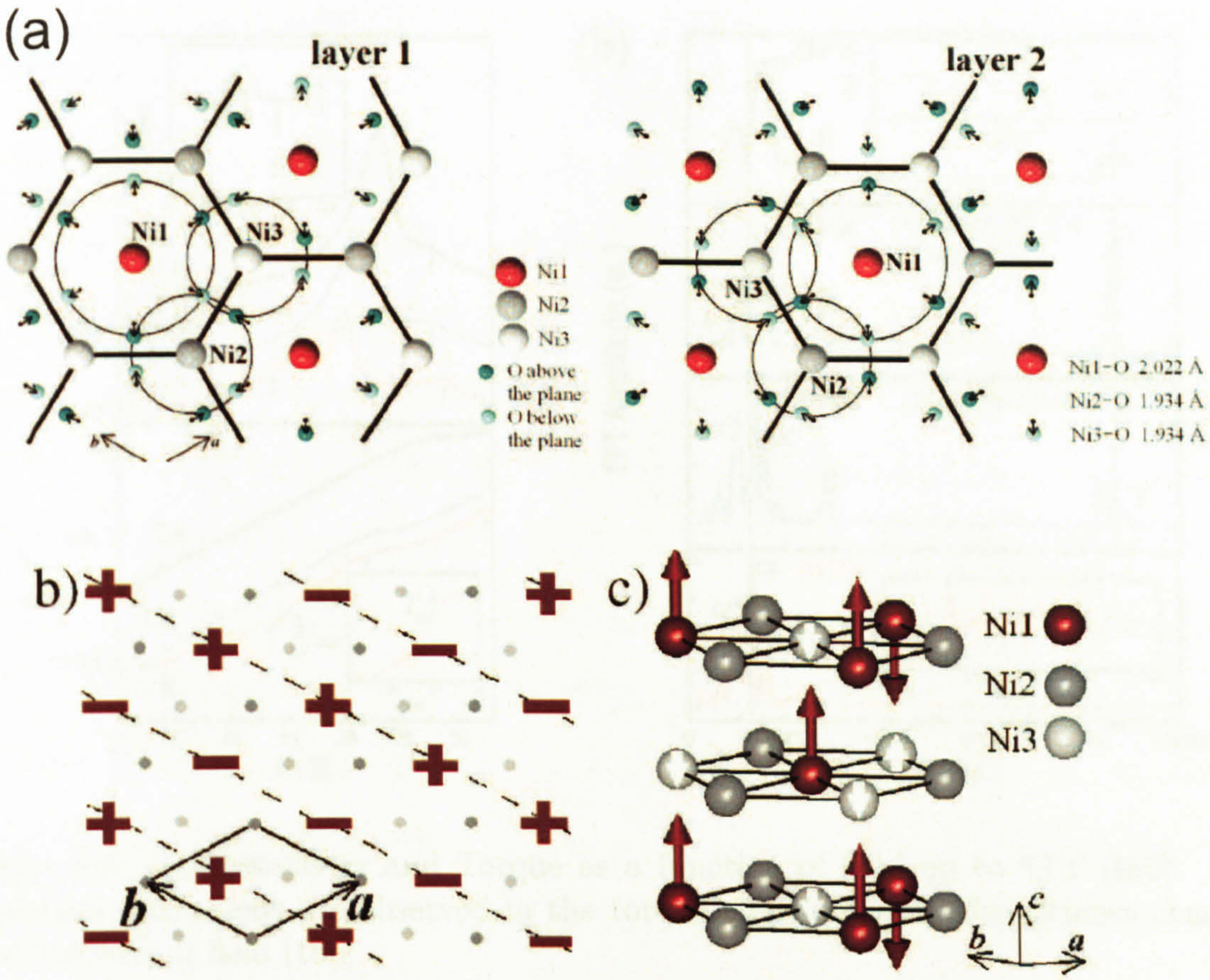

Figure 5.2: (a) The Ni sublattice taken from [179]. The arrows on the oxygens indicate their movement in the structural distortion and red Ni ions are the 2+ positions (b) and (c) The antiferromagnetic arrangement of the Ni ions taken from [177]

1+ and the O 2-. The bond lengths between the Ni and O atoms indicate that one third of the Ni atoms carry a charge of around 2+ while two thirds carry a charge of around 3.5+. These numbers are for complete charge order but the actual charges are probably some fraction of this. This charge order is similar to what is proposed to occur in $YNiO_3$ [181], which has two Ni sublattices.

5.2.2 Magnetic Structure

The Ni 2+ ions form a triangular sublattice as shown in Figure 5.2. Susceptibility measurements [179] above the antiferromagnetic transition indicate a Curie-Weiss law

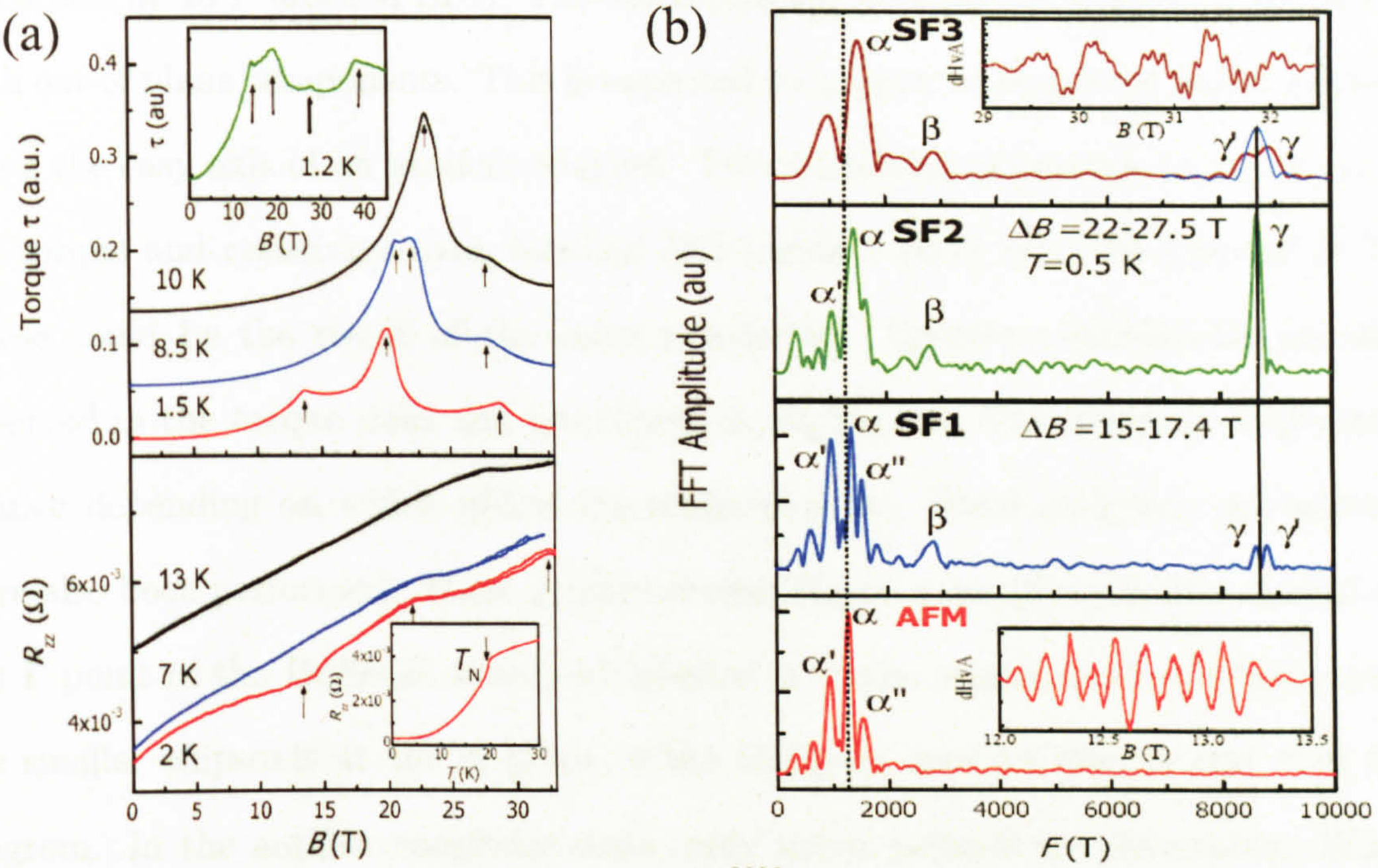

Figure 5.3: (a) Resistivity and Torque as a function of field up to 33 T [180]. (b) Quantum oscillations are observed in the torque. The measured frequencies change as a function of field [180].

with an effective moment of 1.63 μ_B. This value is within 6 % of the value of S=1/2 on each Ni ion. For a full Ni 2+ then the electronic configuration has 6 electrons in the t_{2g} levels and 2 in the e_g band which has a spin of 1. This indicates that full charge disproportionation is not occurring. Below the Neél temperature of 20 K, the Ni ions form ferromagnetic rows in an antiferromagnetic arrangement as shown in Figure 5.2. There are two layers per unit cell and these are arranged differently.

5.2.3 Resistivity and Torque Measurements

Coldea *et al* [180] have measured the resistivity and torque of $AgNiO_2$ in fields up to 33 T. The torque data show several kinks and maxima as shown in Figure 5.3. The resistivity also shows several anomalies as a function of field. This implies that there are multiple phase transitions as a function of field. There is an expected spin flop

transition at 15 T labelled SF1. The spins reorient so they are mostly in the plane with out of plane components. This is expected to happen when a large field is applied along the easy axis of an antiferromagnet. Two additional anomalies are observed in the torque and resistivity data, labelled SF2 (around 20 T) and SF3 (around 30 T). These could be the result of the spins reordering. Quantum oscillations are also observed in the torque data and are shown in Figure 5.3. The observed frequencies change depending on which phase the material is in. Band structure calculations have also been performed. These predict several larger quasi-2D cylinders centred on the Γ point of the Brillouin zone and labelled γ in the diagram. In addition, there are smaller ellipsoids at the K point of the Brillouin zone labelled α and β in the diagram. In the antiferromagnetic state, only the α pockets are observable. When the field is increased above SF1 then the γ and β orbits are observable. The Fermi surface is expected to change as the spins change due to changes in the local moment. It is possible that impurities in the sample are preventing the observation of all the frequencies in the antiferromagnetic phase.

The cascade of magnetic anomalies observed in the torque and resistivity data could imply several phase transitions as the spins reorient. If this was the case then measurements of the heat capacity could reveal anomalies as the field is increased and allow distinct phases to be identified. If no anomalies in heat capacity are observed then the kinks in in the torque may not be phase transitions or could represent some spin reordering with a very small free energy change.

5.3 Heat Capacity Probe for High Fields

5.3.1 Design of the Probe

The probe used to measure the heat capacity in high fields was designed to use AC calorimetry with a thermocouple and optic fibre. This technique is described in [51] and is based on the AC calorimetry technique by Sullivan and Seidel [70] described in Chapter 2. In brief, the sample is glued to a constantan- chromel thermocouple using GE varnish. The thermocouple is made of wire 12 μm thick and is stretched across a Mylar ring stuck to the copper stage. The sample is therefore thermally isolated from the bath as only the thermocouple provides thermal contact. The modulated heating is provided by a room temperature LED shining on the sample through a length of optic fibre running the length of the probe. Sample temperature deviations from the bath temperature can be measured using the thermopower of the thermocouple. This technique is extremely useful for measuring very small samples. As it is impossible to measure the power applied to the sample, this technique does not extract absolute numbers for the heat capacity therefore it is very useful for measuring phase transitions. In a high field magnet the bore is very narrow meaning there is a small amount of space for the experiment. In resistivity and torque measurements the sample can be immersed in the Helium without the need for a vacuum seal. In heat capacity measurements, this is not possible and a cone seal was used to create a vacuum seal. Figure 5.4 shows the low temperature arrangement of the AC calorimetry probe in high field. There are two copper stages attached to the brass cone, the first holds the optic fibre in place above the sample and the second holds the sample on the thermocouple. A 100 Ω constantan wire is wrapped around the second stage to act as a heater. A Cernox 1050 is attached to the bottom of the second stage to measure the bath temperature. Using brass standoffs means it is possible to heat the second

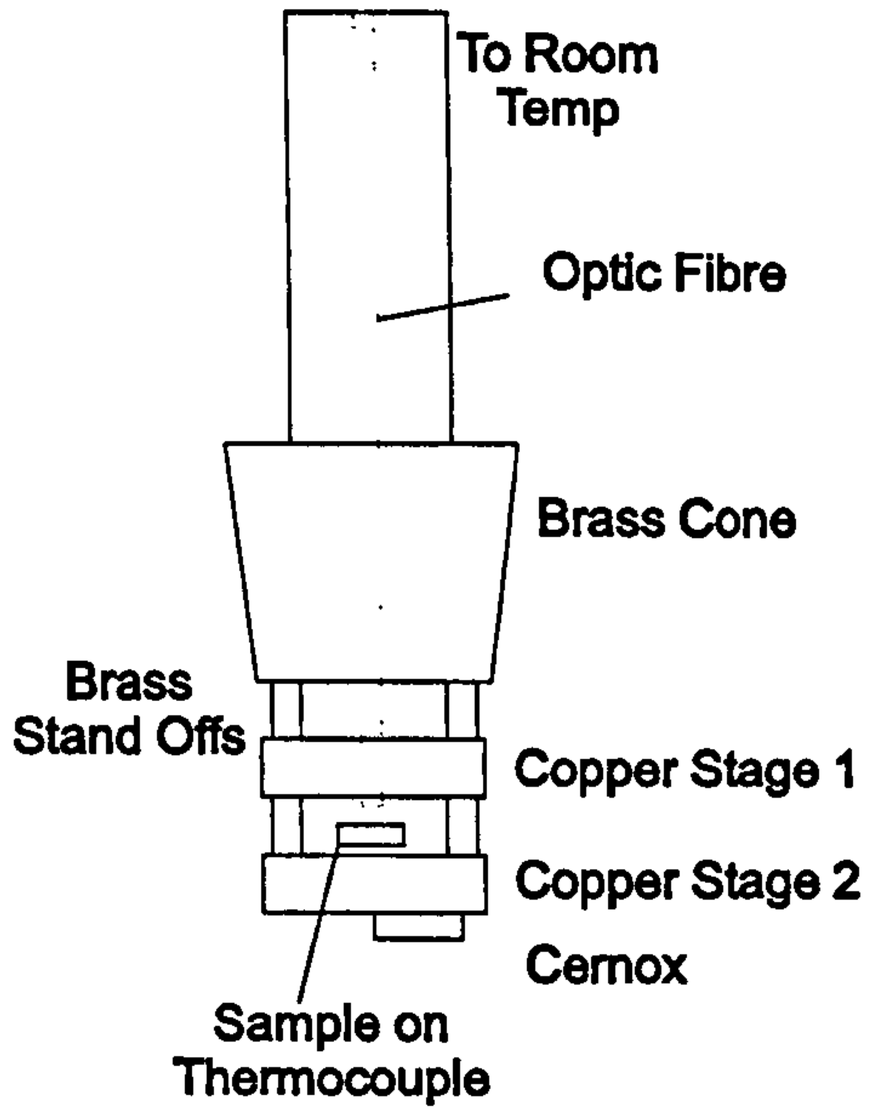

Figure 5.4: Schematic showing the probe design for AC calorimetry in the high field magnet.

stage to 25 K with a moderate heater power. The probe can be used at 2.2 K by pumping on the helium bath. At the room temperature end, the LED is mounted on a small temperature controlled stage inside the vacuum space. This stage is held at a constant temperature to ensure a constant power is emitted by the LED.

5.3.2 Measurements in High Field

A Lakeshore 340 is used to stabilise the temperature of the stage. A Stanford 830 lock-in amplifier is used to provide the oscillating power for the LED and measure the oscillating part of the temperature deviations. A Keithley nano voltmeter is used to measure the constant temperature offset. The measurements of the heat capacity require a circuit capable of measuring small signals (typically microvolt levels). The voltage signal measured is related to the temperature deviations by the thermopower of the thermocouple. At 4.2 K this is approximately $2\,\mu$V/K for a type E thermal couple. The temperature deviations consist of a constant T_{dc} and an oscillating T_{ac}

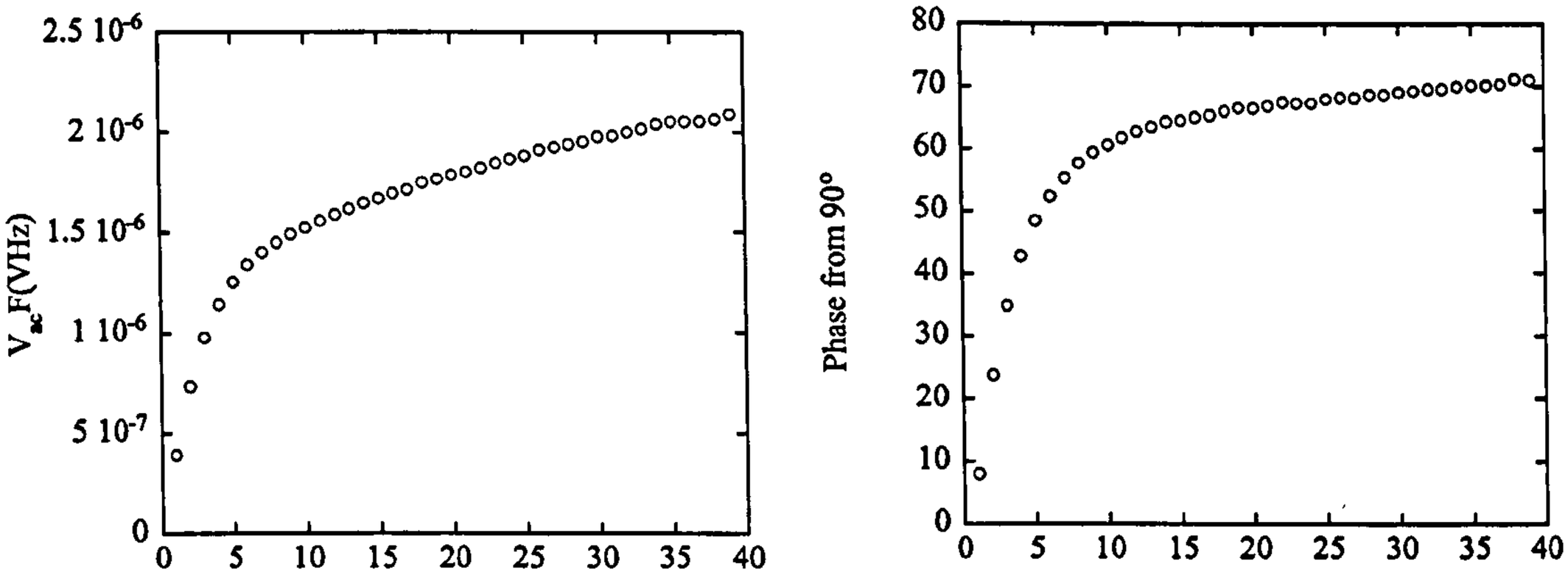

Figure 5.5: The quantities VF and the phase shift are used to determine the measurement frequency. The frequency used for this sample is 20 Hz.

and, as described previously, the temperature of the sample is

$$T = T_{bath} + T_{dc} + \frac{P}{2\omega C}\cos(\omega t + \delta) f(\omega). \tag{5.1}$$

T_{ac} is inversely proportional to the heat capacity of the sample. Typically T_{ac} is of the order of 10 mK and T_{dc} is about 0.5 K. The oscillating voltage signal V_{ac} used to measure the heat capacity is of the order of 0.1 μV. This is a small signal and care must be taken to reduce the noise level. The wires to the thermocouple are placed in a separate stainless tube in the cryostat to shield them from interference from the temperature control wires. The output signal is analysed through a low noise transformer with coils of 10:1000 and then a pre-amplifier with a 12 dB filter above 30 Hz and a gain of 1000 before the lock-in amplifier. The measurement frequency for the sample used in the Niemegen high field magnet lab was 20 Hz. The frequency is dependent on the heat capacity and thermal conductivity of the sample and the thermocouple. For the single crystal measured in the magnet lab the frequency was determined in Bristol in a test run (see Figure 5.5). In all the measurements below, there is a slight error on the temperature quoted due to the magnetoresistance of the

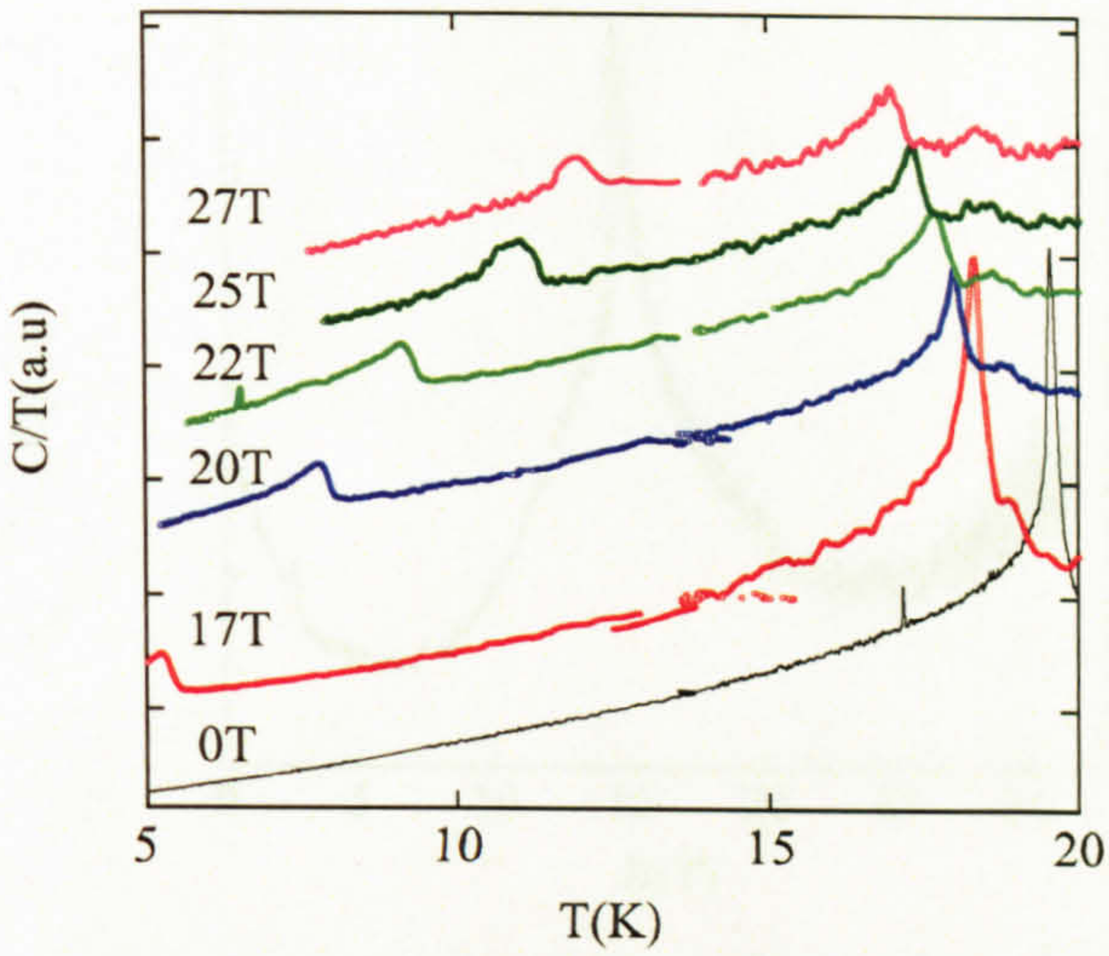

Figure 5.6: Temperature sweeps at fields up to 27 T with a 0 T sweep shown for comparison.

Cernox thermometer. At worst this is 5 % at base temperature of 2.2 K.

5.4 Results

5.4.1 High Field, Single Crystal Data

The high field data was taken at the high magnetic field lab in Nijmegen. The field was applied along the c axis of the crystal and the water cooled copper magnet was capable of a maximum field of 33 T. As the field increased, the noise on the measurement increased. Temperature sweeps were taken at fixed fields up to 20 K. These are shown in Figure 5.6. Data taken in 0 T are shown for comparison. As the field is increased the antiferromagnetic transition decreases in temperature to around 17 K at 27 T. At 17 T, a second transition becomes visible which increases in temperature as the field is increased. This transition is most likely the spin flop transition (SF1) and is first order. The spins reorder at this transition as the field approaches the spin gap of the spin fluctuations in the antiferromagnetic phase. To confirm this a field sweep was

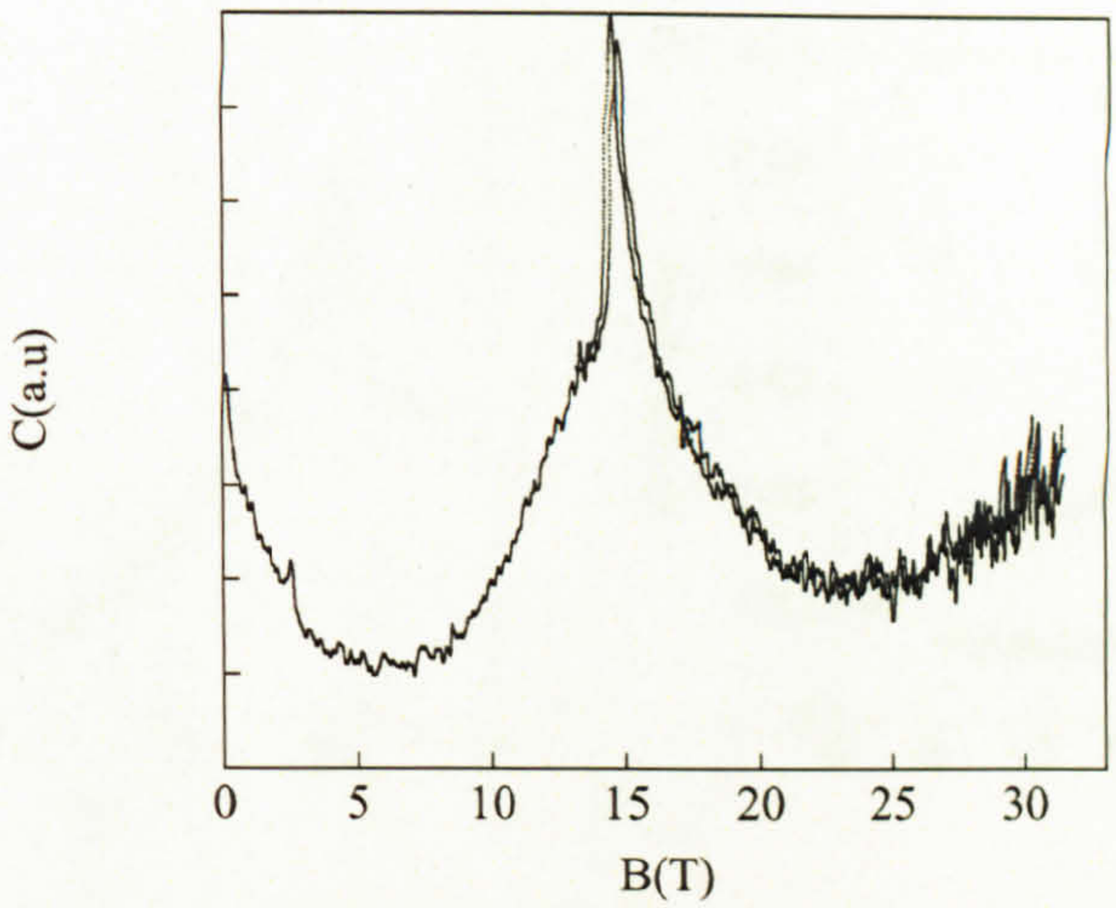

Figure 5.7: Field sweep at 2.2 K, the spin flop transition is clearly visible at 15 T but no other transitions are observed outside the noise of the experiment.

performed at 2.2 K up to 33 T. One large transition was observed at 15 T. The up and down sweeps are shown in Figure 5.7. A very large peak is observed in the field sweep, centred on the SF1 transition at 15 T but extending up to 20 T. The resistance and torque data appear to show evidence of multiple transitions, but only one is observed in the heat capacity data. The one observed in the heat capacity data is associated with SF1 in the torque data but no evidence for SF2 and SF3 are observed in the heat capacity. The transitions observed in the resistance and torque could be due to spin reordering which have small energy changes and therefore will not be observed in the heat capacity outside of the noise levels.

5.4.2 Powder Data

High precision heat capacity measurements were performed on powdered $AgNiO_2$ to determine the Sommerfeld coefficient γ. The long relaxation calorimetry technique was used as described in Chapter 2 and [51]. The calorimeter used was purpose built for measuring small samples between 1.5 K and 25 K. 1.24 mg of $AgNiO_2$ pellet was greased to the bare chip calorimeter. The addenda, consisting of the bare chip and

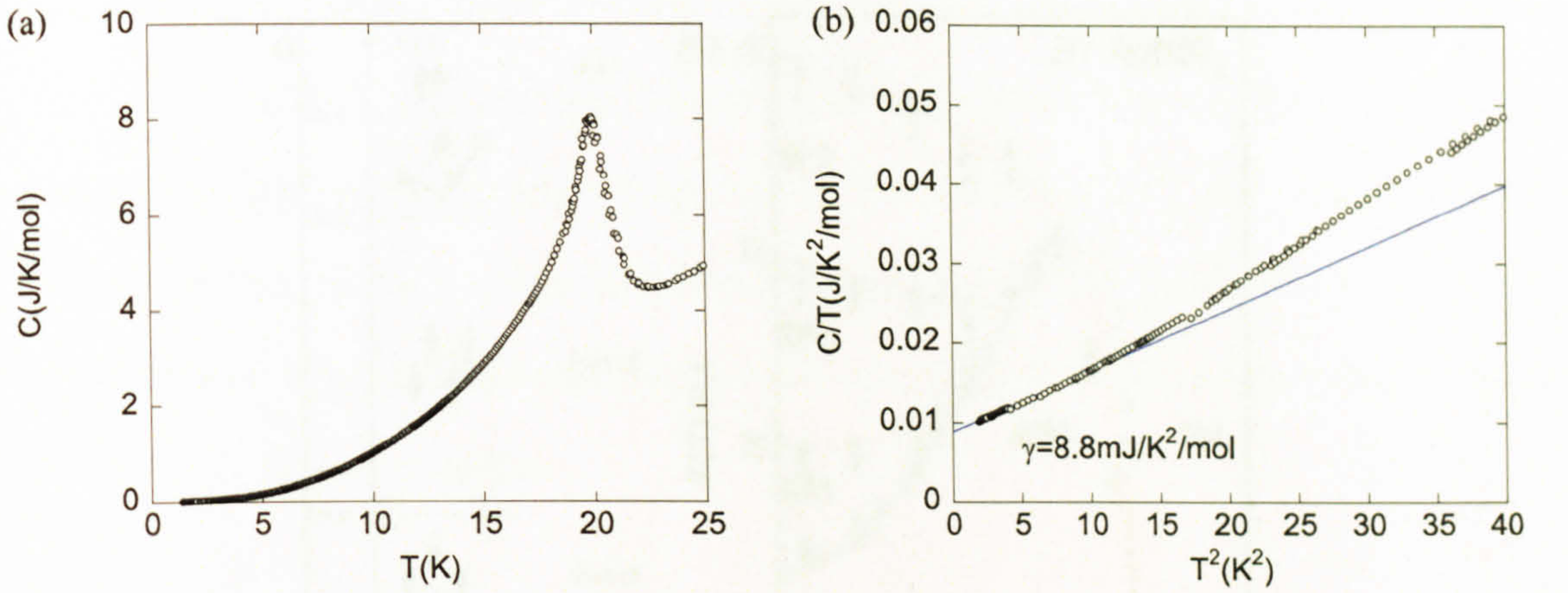

Figure 5.8: (a) Zero field heat capacity measured by the Bare Chip from 1.5 K to 25 K. The antiferromagnetic transition is clearly visible. (b) C/T versus T^2 used to determine γ. The solid line is a fit to the data below 3 K.

the grease, was measured beforehand and subtracted. The low temperature heat capacity in zero field will have three contributions: an electronic contribution, a phonon contribution and a spin wave contribution due to the magnetism of the state. This can be expressed as

$$C = \gamma T + \beta T^3 + Ce^{-\frac{\Delta}{T}}, \tag{5.2}$$

where γ is the Sommerfeld coefficient, β is related to the phonon structure and the third term is derived from spin waves with a spin gap of Δ. Neutron scattering [177] measures this spin gap as 18 K. At low temperature ($T \ll 3\,K$) then the exponential will be very small (less than 3×10^{-3}). The fit used to extract γ is therefore performed below 3 K. The data are shown in Figure 5.8. The C versus T curve shows the large peak associated with the antiferromagnetic transition at 20 K. A plot of C/T versus T^2 does not show a linear behaviour over a large temperature range. The contribution from the spin waves will change the linear behaviour and higher order terms in the phonon contribution can have an effect in some materials. The linear fit below 3 K extrapolates to a value of $8.8\pm0.3\,mJ/K^2/mol$. The error in this value includes uncertainty derived from the fitting range and the extrapolation. Band structure cal-

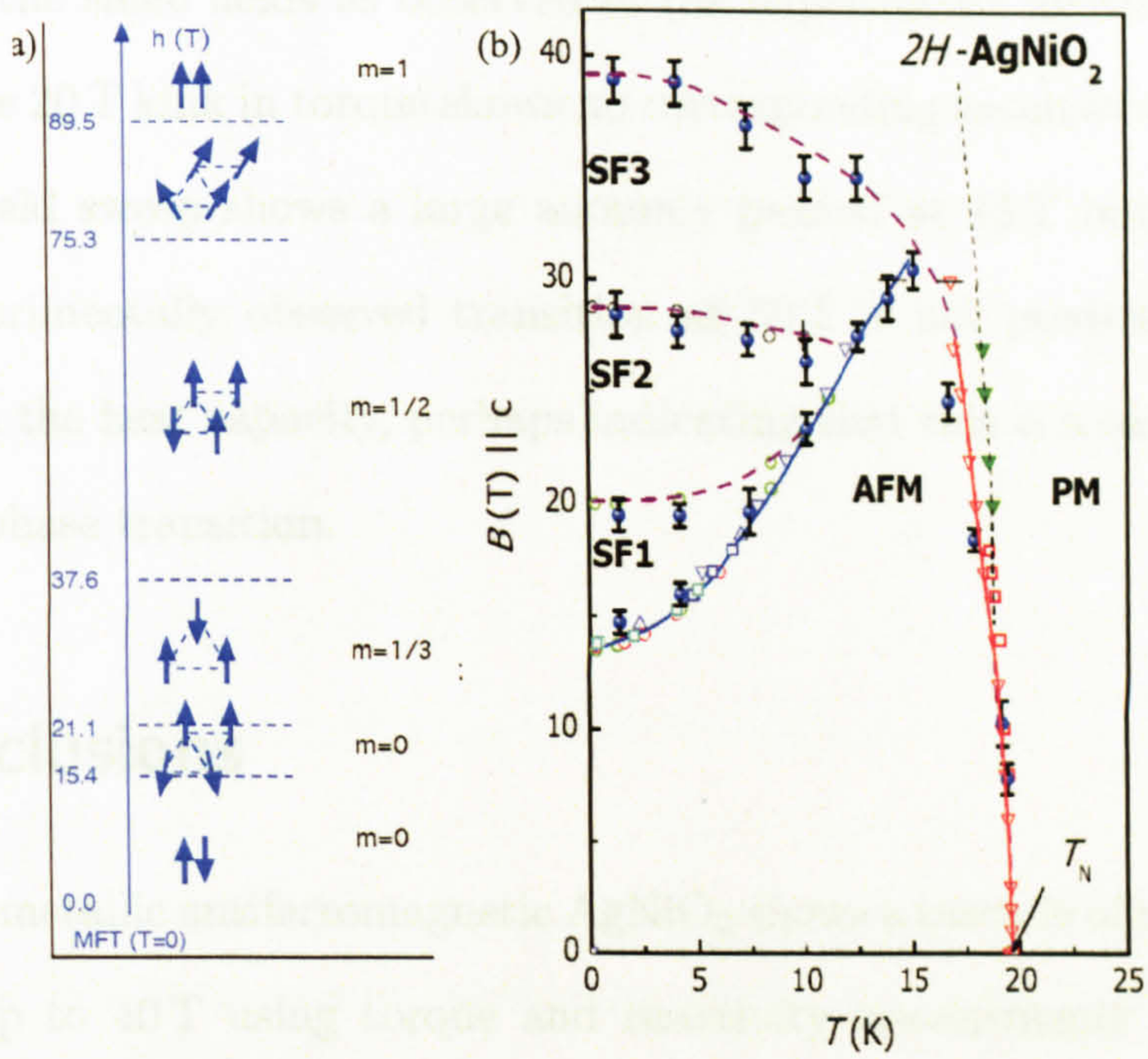

Figure 5.9: (a) Theoretical spin alignments as a function of field calculated from Monte Carlo simulations [183]. (b) The experimental phase diagram based on torque, resistivity and heat capacity measurements [180]. Circles represent anomalies in torque magnetometery, squares represent resistivity measurements and triangles represent heat capacity. The solid lines are phase transitions observed in all measurements and the dashed lines from anomalies only seen in resistivity and torque.

culations show a value of $3.5\,\mathrm{mJ/K^2/mol}$ which implies a mass enhancement of $2.5\,\mathrm{m}_e$. This number is similar to that calculated for Ag_2NiO_2 [182] which is due to magnetic fluctuations.

5.4.3 Phase Diagram of $AgNiO_2$

The measured phase diagram of $AgNiO_2$ shows complex structure. Monte Carlo calculations based on appropriate parameters of $AgNiO_2$ have been performed using a classical Heisenberg model [183]. The experimental phase diagram is shown in Figure 5.9 along with a diagram showing the spin orientations predicted from the Monte Carlo calculations at each field. The theoretical spin reorientations occur at

approximately the same fields as observed in the experiments for the 15 T and 20 T transitions. The 20 T kink in torque shows no corresponding anomaly in heat capacity, although the field sweep shows a large anomaly peaked at 15 T but reaching up to 20 T. The experimentally observed transition at 30 T is not predicted theoretically nor observed in the heat capacity, perhaps indicating that this is a reordering of spins rather than a phase transition.

5.5 Conclusions

The frustrated metallic antiferromagnetic $AgNiO_2$ shows a cascade of magnetic anomalies in fields up to 40 T using torque and resistivity measurments [180]. AC heat capacity studies in high fields on single crystal $AgNiO_2$ show evidence for one large spin flop transition at 15 T but no other evidence for transitions at higher fields is observed. The magnetic anomalies at higher fields could have small energy changes which are within the noise of the heat capacity experiment at those fields. Long relaxation calorimetry measurements of powder $AgNiO_2$ reveal a Sommerfeld coefficient of $8.8 \pm 0.3\,mJ/K^2/mol$, which implies a mass enhancement of $2.5\,m_e$ in this material.

Chapter 6

Conclusions

The majority of this thesis was on performing precision measurements on two classes of unconventional superconductor, the organic superconductors and the pnictide superconductors, to determine the gap symmetry of these novel superconductors.

A low temperature heat capacity experiment capable of measuring the heat capacity of small single crystal samples down to 400 mK in fields up to 14 T with an accuracy of 2 % was developed. Initial results were favourable in zero field but difficulty was encountered when calibrating the thermometer in fields. To overcome this a helium vapour pressure thermometer was developed which was essentially field independent and had a resolution better than 3 mK between 4.2 K and 0.4 K. Measurements of the heat capacity using this calibration had errors up to around 8 % in field which could be reduced by adjusting the Chebyshev polynomial used to fit the thermometer calibration curve. The calorimeter was mounted on a rotating platform with an angular resolution of 1°. Using AC calorimetry, the heat capacity could be measured as a function of applied field angle with a precision of 0.1 %. This experiment is a powerful tool for probing quasiparticle excitations in unconventional superconductivity and this is demonstrated through measurements on the organic superconductors.

The organic superconductors show similarities to the cuprates [6] and it might be expected that the same physics that drives the cuprates is also dominant in the organic superconductors. The cuprates have a $d_{x^2-y^2}$ order parameter [8] but the gap symmetry of the organic superconductors is a controversial subject. Measurements of the thermal conductivity [25], [16], penetration depth [77] and microwave conductance [79] all show evidence of nodes. The temperature dependence of the heat capacity has shown evidence for both a nodal [12] and a fully gapped [13] superconducting state. The directions of the nodes is also under debate, with STM [78] and angle dependent thermal conductivity measurements [25] revealing nodes at 45° to the crystal axis and microwave conductance [79] showing nodes along the crystal axis. Angle dependent heat capacity measurements have measured the nodal directions in Sr_2RuO_4 [9], $CeCoIn_5$ [10] and $CeRhIn_5$ [23] and were used in this study to resolve the controversy surrounding the organic superconductors.

Precise measurements of the temperature dependence of κ-$(ET)_2Cu(NCS)_2$ and κ-$(ET)_2Cu[N(CN)_2]Br$ down to 0.4 K support a nodal gap in agreement with the previous study [12] down to 1.3 K. The low temperature behaviour indicates that these are strong coupling superconductors with gap magnitudes of $4.2\pm0.5\,k_BT_c$ for κ-$(ET)_2Cu(NCS)_2$ and $3.6\pm0.5\,k_BT_c$ for κ-$(ET)_2Cu[N(CN)_2]Br$. The angle dependent heat capacity measurements below 1 K on κ-$(ET)_2Cu(NCS)_2$ and κ-$(ET)_2Cu[N(CN)_2]Br$ in fields less than 4 T show a clear fourfold oscillation which derives from the superconducting order parameter. There is good agreement between the data and a quasi-classical Doppler shift model [18]. These results indicate that the order parameter of these compounds has nodes along the crystal axis in agreement with microwave conductance measurements but not angle dependent thermal conductivity measurements. This order parameter symmetry is consistent with a spin fluctuation mediated superconducting mechanism [93] and is the same as observed in the cuprate super-

conductors, which underlines the similarities between the two classes of compounds. It seems that a consensus is being reached that the order parameter of the organic superconductors has nodes and this work implies that they are along the crystal axis.

The newly discovered pnictide superconductors [7] have attracted a large amount of interest due to their high transition temperatures (up to 55 K in SmFeAsO [123]). Low temperature measurements of the magnetic penetration of $SmFeAsO_{0.8}F_{0.2}$ and $Ba(Fe_{0.93}Co_{0.07})_2As_2$ show contrasting results. The measurements on $SmFeAsO_{0.8}F_{0.2}$ show an exponential activation of the penetration depth with temperature indicating a fully gapped superconductor state. Analysis of the low temperature penetration depth shows a minimum gap in the system of $1.1 \pm 0.1\, k_b T_c$. The superfluid density can be explained in a two gap model with the second gap close to the BCS weak coupling value or an anisotropic gap model. These results could also be explained by an unconventional extended s+/s- state [127]. The measurements on $Ba(Fe_{0.93}Co_{0.07})_2As_2$ show a power law temperature dependence of the penetration depth which indicates a nodal superconductor. This power law varies between samples and is between 1.7 and 2.4. This variation could be the result of impurities in a d-wave superconductor, or impurities in an s+/s- state [171].

Low temperature penetration depth measurements on the pnictide family have shown some contradictory results. Measurements on the (1111) family show exponential behaviour (NdFeAsO [163], PrFeAsO [164] and SmFeAsO in this study). Measurements on the (122) family show a power law behaviour with a power around 2 ($Ba(Fe_xCo_{1-x})_2As_2$ in this study and [168]) and exponential behaviour ($Ba_xNi_{1-x}Fe_2As_2$ in [169]). The compound LaFePO, which is like the (1111) family but has P as the pnictogen rather than As, shows the best evidence for a nodal gap symmetry with a linear temperature dependence. One interpretation is that a d-wave order parameter and s+/s- state are very close in energy and small variations in Fermi surface pa-

rameters mean there are different order parameters across the pnictide family [172]. An alternative interpretation is that all the pnictides have an s+/s- gap symmetry and the contrasting results are caused by impurities creating a zero energy density of states and therefore a power law in the penetration depth [171]. However this does not explain the LaFePO data. It is clear that more experimental measurements are required to differentiate between these two scenarios. Phase sensitive techniques such as those suggested in [173], [174] could achieve this. Angle dependent heat capacity experiments as performed on the organic superconductors in this thesis could also determine the position of any nodes in the system. The pnictides are the first superconductors to have transition temperatures above 50 K apart from the cuprates and they could in time provide a theoretical insight into high T_c superconductivity that could lead to advances in the cuprate superconductors.

Appendix A

Calculating the Density of States of a Dirty d-wave Superconductor

The program written to calculate the density of states was written in the Delphi programming language. As Delphi does not support complex numbers an extra unit was included which handled the complex algebra. Initially the parameter Γ (impurity scattering rate) was selected (typical value of 0.05) and the associated self energy Σ_0 is derived from Γ as

$$\Sigma_0 = \Gamma + 1 \times 10^{-6} i \tag{A.1}$$

This Σ_0 is also saved as Σ_{old}. The particle energy is initialised as ω in units of the gap maximum Δ_0. The renormalised particle energy can then by calculated as

$$\widetilde{\omega} = \omega - i\Sigma_0 \tag{A.2}$$

The propagator $g_0(\theta)$ for that energy can then be calculated as

$$g_0(\theta) = \frac{-i\widetilde{\omega}}{\sqrt{\widetilde{\omega}^2 - (\Delta_0 \cos(2\theta))^2}} \tag{A.3}$$

It is important when calculating the complex square root in the denominator to handle the branch cut correctly [43]. For the complex square root in equation A.3, when $\omega > 0$ then

$$\sqrt{\widetilde{\omega}^2 - \Delta(\theta)^2} = \eta|\sqrt{\widetilde{\omega}^2 - \Delta(\theta)^2}|e^{\frac{i\phi}{2}} \tag{A.4}$$

Where η=1 if $\Re(\widetilde{\omega}) > |\Delta(\theta)|$ and $\eta = i$ if $\Re(\widetilde{\omega}) < |\Delta(\theta)|$. The angle ϕ is given by

$$\phi = \tan^{-1}\left(\frac{\Im(\widetilde{\omega})}{\Re(\widetilde{\omega}) - \Delta(\theta)}\right) + \tan^{-1}\left(\frac{\Im(\widetilde{\omega})}{\Re(\widetilde{\omega}) + \Delta(\theta)}\right) \tag{A.5}$$

The propagator $g_0(\theta)$ is then numerically integrated over all angles. To perform the integration the real and imaginary parts are integrated separately.

$$g_0 = \int_0^{\frac{\pi}{4}} g_0(\theta) d\theta \tag{A.6}$$

Once g_0 has been found then the self energy can be recalculated using

$$\Sigma_0 = \frac{\Gamma g_0}{c^2 - g_0^2} \tag{A.7}$$

Where c is the scattering strength parameter and is always set to 0 for strong scattering. This value for Σ_0 is then compared to the previous value calculated in equation A.1. This process is then iterated from equation A.2 until Σ_0 converges on a value. The criterion for converge is that the difference in Σ_0 is less than 1×10^{-6}. Once the loop has converged the density of states can be calculated using

$$N(\omega) = -\Im(g_0) \tag{A.8}$$

This process is repeated at all energies ω.

Publications

Magnetic penetration depth of single crystal $SmFeAsO_{1-x}F_y$: a fully gapped superconducting state ,

L.Malone, J.D. Fletcher, A. Serafin, A. Carrington, N.D. Zhigadlo, Z. Bukowski, S. Katrych and J. Karpinski, Phys. Rev. B, **79**, R140501 (2009).

Evidence for nodal superconductivity in LaFePO ,

J.D. Fletcher, A. Serafin, L. Malone, J. Analytis, J-H Chu, A.S. Erickson, I.R. Fisher and A. Carrington, Phys. Rev. Lett, **102** 147001 (2009)

Bibliography

[1] J. Nagamatsu, N. Nakagawa, T. Muranaka, Y. Zenitani, and J. Akimitsu, Nature **410**, 63 (2001).

[2] J. F. Annett, *Superconductivity, Superfluids and Condensates* (Oxford University Press, 2004).

[3] J. G. Bednorz and K. A. Muller, Z. Phys **B64**, 189 (1986).

[4] G. R. Stewart, Rev. Mod. Phys **56**, 755 (1984).

[5] A. P. Mackenzie and Y. Maeno, Rev. Mod. Phys. **75**, 657 (2003).

[6] R. H. McKenzie, Science **278**, 820 (1997).

[7] Y. Kamihara, T. Watanabe, M. Hirano, and H. Hosono, J. Am. Chem. Soc. **130**, 3296 (2008).

[8] C. C. Tsuei and J. R. Kirtley, Rev. Mod. Phys **72**, 969 (2000).

[9] K. Deguchi, Z. Mao, H. Yaguchi, and Y. Maeno, Phys. Rev. Lett. **92**, 047002 (2004).

[10] H. Aoki, T. Sakakibara, H. Shishido, R. Settai, Y. Onuki, P. Miranovic, and K. Machida, J. Phys.-Condes. Matter **16**, L13 (2004).

[11] Y. Kasahara, T. Iwasawa, Y. Shimizu, H. Shishido, T. Shibauchi, I. Vekhter, and Y. Matsuda, Phys. Rev. Lett. **100**, 207003 (2008).

[12] O. Taylor, A. Carrington, and J. Schlueter, Phys. Rev. Lett. **99**, 057001 (2007).

[13] H. Elsinger, J. Wosnitza, S. Wanka, J. Hagel, D. Schweitzer, and W. Strunz, Phys. Rev. Lett. **84**, 6098 (2000).

[14] W. Hardy, D. Bonn, D. Morgan, R. Liang, and K. Zhang, Phys. Rev. Lett **70**, 3999 (1993).

[15] S. Desoto, C. Slichter, A. Kini, H. Wang, U. Geiser, and J. Williams, Phys. Rev. B **52**, 10364 (1995).

[16] S. Belin, K. Behnia, and A. Deluzet, Phys. Rev. Lett **81**, 4728 (1998).

[17] G. E. Volovik, JETP **58**, 469 (1993).

[18] I. Vekhter, P. Hirschfeld, J. Carbotte, and E. Nicol, Phys. Rev. B **59**, R9023 (1999).

[19] I. Vekhter, P. Hirschfeld, and E. Nicol, Phys. Rev. B **6406**, 064513 (2001).

[20] A. Vorontsov and I. Vekhter, Phys. Rev. Lett. **96**, 237001 (2006).

[21] G.R.Boyd, P.J.Hirschfeld, I.Vekhter, and A.B.Vorontsov, arxiv/0810.2772 (2008).

[22] T. Park, M. Salamon, E. Choi, H. Kim, and S. Lee, Phys. Rev. Lett. **90**, 177001 (2003).

[23] T. Park, E. Bauer, and J. Thompson, Phys. Rev. Lett. **101**, 177002 (2008).

[24] H. Aoki, T. Sakakibara, H. Shishido, R. Settai, Y. Onuki, P. Miranovic, and K. Machida, Physica B **359**, 410 (2005).

[25] K. Izawa, H. Yamaguchi, T. Sasaki, and Y. Matsuda, Phys. Rev. Lett. **88**, 027002 (2002).

[26] T. Watanabe, K. Izawa, Y. Kasahara, Y. Haga, Y. Onuki, P. Thalmeier, K. Maki, and Y. Matsuda, Phys. Rev. B **70**, 184502 (2004).

[27] O. Fischer, M. Kugler, I. Maggio-Aprile, and C. Berthod, Rev. Mod. Phys **79**, 353 (2007).

[28] R. D. Parks, *Superconductivity vol 1* (Marcel Dekker, New York, 1969).

[29] J. Bardeen, L. Cooper, and J. Schrieffer, Phys. Rev **108**, 1175 (1957).

[30] L. Cooper, Phys. Rev **104**, 1189 (1956).

[31] H. Frohlich, Phys. Rev **79**, 845 (1950).

[32] M. Tinkham, *Introduction to Superconductivity 2nd Edition* (Dover Publications, 1996).

[33] I. Giaever, K. Megerle, and H. Hart, Phys. Rev **126**, 941 (1962).

[34] J. R. Schrieffer, D. J. Scalapino, and J. W. Wilkins, Phys. Rev. Lett **10**, 336 (1963).

[35] G. Eliashberg, Soviet Physics JETP **11**, 696 (1960).

[36] W. Mcmillan and J. Rowell, Phys. Rev. Lett. **14**, 108 (1965).

[37] R. Stedman, L. Almqvist, and G. Nilsson, Phys. Rev **162**, 549 (1967).

[38] M. K. Wu, J. R. Ashburn, C. J. Torng, P. H. Hor, R. L. Meng, L. Gao, Z. J. H. Y. Q., Wang, and C. W. Chu, Phys. Rev. Lett **58**, 908 (1987).

[39] A. S. Alexandrov, V. V. Kabanov, and N. F. Mott, Phys. Rev. Lett **77**, 4796 (1996).

[40] H. Padamsee, J. E. Neighbor, and C. A. Shiffman, J. Low. Temp. Phys. **12**, 387 (1973).

[41] T. Hotta, J. Phys. Soc. Japan **62**, 274 (1993).

[42] P. J. Hirschfeld, P. Wlfle, and D. Einzel, Phys. Rev. B **37**, 83 (1988).

[43] P. J. Hirschfeld and N. Goldenfeld, Phys. Rev. B **48**, 4219 (1993).

[44] C. Kubert and P. Hirschfeld, Solid. State. Commun **105**, 459 (1998).

[45] A. Vorontsov and I. Vekhter, Phys. Rev. B **75**, 224501 (2007).

[46] A. Vorontsov and I. Vekhter, Phys. Rev. B **75**, 224502 (2007).

[47] Y. Nagai and N. Hayashi, Phys. Rev. Lett. **101**, 097001 (2008).

[48] W. Meissner and R. Ochsenfeld, Naturwissenschaften **21**, 787 (1933).

[49] F. London and H. London, Proc. Roy. Soc **A149**, 71 (1935).

[50] B. S. Chandrasekar and D. Einzel, Annalen Der Physik **2**, 535 (1993).

[51] O. Taylor, Ph.D. thesis, University of Bristol (2007).

[52] A.Junod, *Studies of High Temperature Superconductors, edited by A. Narlikar*, vol. 19 (Nova Science, Commack, New York,, 1996).

[53] Y. Wang, B. Revaz, A. Erb, and A. Junod, Phys. Rev. B **63**, 094508 (2001).

[54] http://www.lakeshore.com/.

[55] K. Kiefer, R. Haueisen, and G. Weiss, J. Low Temp Phys **147**, 517 (2007).

[56] B. Magnum, J. Res. Nat. Inst. Stand. Technol **95**, 69 (1990).

[57] F. Pobell, *Matter and Methods at Low Temperatures* (Springer, 1995), 2nd ed.

[58] D. S. Betts, *Refrigeration and Thermometry below One Kelvin* (Sussex University Press, 1975).

[59] O. V. Lounasmaa, *Experimental Principles and Methods Below 1K* (Academic Press: London and New York, 1974).

[60] S. Weber and G. Schmidt, Leiden Commun p. 246 (1936).

[61] A. Vanitterbeek and E. Degrande, Physica **13**, 289 (1947).

[62] J. Hobson, J. Vac Sci Tech **6**, 257 (1969).

[63] A. Freddi and I. Modena, Cryogenics **8**, 18 (1968).

[64] T. Bernat and H. Cohen, J. Low Temp. Phys. **14**, 597 (1974).

[65] R. Watkins, W. Taylor, and W. Haubach, J. Chem. Phys. **46**, 1007 (1967).

[66] B. L. Brandt, D. W. Liu, and L. G. Rubin, Rev. Sci. Instrum. **70** (1999).

[67] A. Narath, A. T. Fromhold, and E. Jones, Phys. Rev. **144**, 428 (1966).

[68] B. Andraka and Y. Takano, Rev. Sci. Instrum. **67**, 4256 (1996).

[69] G. C. Carter, L. H. Bennett, and D. J. Kahan, *Metallic Shifts in NMR* (Pergamon, Oxford, published as Vol. 20 of Prog. Mater. Sci., 1977).

[70] P. Sullivan and G. Seidel, Phys. Lett. A **25**, 229 (1967).

[71] F. Manzano, Ph.D. thesis, University of Bristol (2001).

[72] J. Fletcher, Ph.D. thesis, University of Bristol (2005).

[73] C. van der Grift, Rev. Sci. Instrums **46**, 599 (1974).

[74] R. Prozorov, R. W. Giannetta, A. Carrington, and F. M. Araujo-Moreira, Phys. Rev. B **62**, 115 (1999).

[75] D. Shoenberg, *Superconductivity* (Cambridge University Press, 1952), 2nd ed.

[76] K. Kanoda, K. Miyagawa, A. Kawamoto, and Y. Nakazawa, Phys. Rev. B **54**, 76 (1996).

[77] A. Carrington, I. Bonalde, R. Prozorov, R. Giannetta, A. Kini, J. Schlueter, H. Wang, U. Geiser, and J. Williams, Phys. Rev. Lett. **83**, 4172 (1999).

[78] T. Arai, K. Ichimura, K. Nomura, S. Takasaki, J. Yamada, S. Nakatsuji, and H. Anzai, Phys. Rev. B **6310**, 104518 (2001).

[79] J. Schrama, E. Rzepniewski, R. Edwards, J. Singleton, A. Ardavan, M. Kurmoo, and P. Day, Phys. Rev. Lett. **83**, 3041 (1999).

[80] J. D. Fletcher, compiled the Crystallographic data and produced the Figure.

[81] M. Lang and J. Muller, *The Physics of Superconductors - Vol.2* (Springer-Verlag, 2003).

[82] L. Coleman, M. Cohen, D. Sandman, A. Yamagish.fggarito, and A. Heeger, Solid State Commun. **12**, 1125 (1973).

[83] G. Saito, T. Enoki, K. Toriumi, and H. Inokuchi, Solid State Commun. **42**, 557 (1982).

[84] H. Urayama, H. Yamochi, G. Saito, K. Nozawa, T. Sugano, M. Kinoshita, S. Sato, K. Oshima, A. Kawamoto, and J. Tanaka, Chem. Lett. p. 55 (1988).

[85] K. Kanoda, Physica C **282**, 299 (1997).

[86] K. Oshima, T. Mori, H. Inokuchi, H. Urayama, H. Yamochi, and G. Saito, Phys. Rev. B **38**, 938 (1988).

[87] T. Sasaki, H. Sato, and N. Toyota, Physica C **185**, 2687 (1991).

[88] T. Sasaki, H. Sato, and N. Toyota, Solid. State. Comm **76**, 507 (1990).

[89] J. Singleton, Rep. Prog. Phys. **63**, 1111 (2000).

[90] H. Weiss, M. Kartsovnik, W. Biberacher, E. Steep, E. Balthes, A. Jansen, K. Andres, and N. Kushch, Phys. Rev. B **59**, 12370 (1999).

[91] H. Weiss, M. Kartsovnik, W. Biberacher, E. Balthes, A. Jansen, and N. Kushch, Phys. Rev. B **60**, R16259 (1999).

[92] T. Ishiguro, K. Yamaji, and G. Saito, *Organic Superconductors, 2nd edition* (Springer, 1998).

[93] J. Schmalian, Phys. Rev. Lett. **81**, 4232 (1998).

[94] H. Akutsu, K. Saito, and M. Sorai, Phys. Rev. B **61**, 4346 (2000).

[95] J. Muller, M. Lang, F. Steglich, J. Schlueter, A. Kini, and T. Sasaki, Phys. Rev. B **65**, 144521 (2002).

[96] O. Taylor, A. Carrington, and J. Schlueter, Phys. Rev. B **77**, 060503 (2008).

[97] N. Yoneyama, T. Sasaki, N. Kobayashi, Y. Ikemoto, and H. Kimura, Phys. Rev. B **72**, 214519 (2005).

[98] M. Pinteric, S. Tomic, M. Prester, D. Drobac, O. Milat, K. Maki, D. Schweitzer, I. Heinen, and W. Strunz, Phys. Rev. B **61**, 7033 (2000).

[99] M. Lang, N. Toyota, T. Sasaki, and H. Sato, Phys. Rev. B **46**, 5822 (1992).

[100] Y. Shimojo, S. Kamiya, M. Tanatar, E. Ohmichi, A. Kovalev, T. Ishiguro, H. Yamochi, G. Saito, J. Yamada, H. Anzai, et al., Synth. Met. **133**, 197 (2003).

[101] H. Mayaffre, P. Wzietek, D. Jrome, C. Lenoir, and P. Batail, Phys. Rev. Lett. **75**, 4122 (1995).

[102] C. Mielke, J. Singleton, M.-S. Nam, N. Harrison, C. C. Agosta, B. Fravel, and L. K. Montgomery, J. Phys. Cond. Mat. **13**, 8325 (2001).

[103] R. Lortz, Y. Wang, A. Demuer, P. H. M. Bttger, B. Bergk, G. Zwicknagl, Y. Nakazawa, and J. Wosnitza, Phys. Rev. Lett **99**, 187002 (2007).

[104] B. J. Powell and R. H. McKenzie, Phys. Rev. Lett **94**, 047004 (2005).

[105] A. Kawamoto, K. Miyagawa, Y. Nakazawa, and K. Kanoda, Phys. Rev. Lett **74**, 3455 (1995).

[106] H. Mayaffre, P. Wzietek, C. Lenoir, D. Jerome, and P. Batail, EuroPhys. Lett **28**, 205 (1994).

[107] K. Ichimura, M. Takami, and K. Nomura, J. Phys. Soc. Jpn. **77**, 114707 (2008).

[108] S. Hill, N. Harrison, M. Mola, and J. Wosnitza, Phys. Rev. Lett **36**, 3451 (2001).

[109] T. Shibauchi, Y. Matsuda, M. B. Gaifullin, , and T. Tamegai, Phys. Rev. Lett **36**, 3452 (2001).

[110] B. Andraka, J. Kim, G. Stewart, K. Carlson, H. Wang, and J. Williams, Phys. Rev. B **40**, 11345 (1989).

[111] J. Graebner, R. Haddon, S. Chichester, and S. Glarum, Phys. Rev. B **41**, 4808 (1990).

[112] B. Andraka, C. Jee, J. Kim, G. Stewart, K. Carlson, H. Wang, A. Crouch, A. Kini, and J. Williams, Solid State Commun. **79**, 57 (1991).

[113] Y. Nakazawa and K. Kanoda, Phys. Rev. B **55**, R8670 (1997).

[114] Y. Nakazawa and K. Kanoda, Phys. Rev. B **53**, R8875 (1996).

[115] Y. Nakazawa and K. Kanoda, Physica C **282**, 1897 (1997).

[116] A. Kini, U. Geiser, H. Wang, K. Carlson, J. Williams, W. Kwok, K. Vandervoort, J. Thompson, D. Stupka, and D. Jung, Inorg. Chem. **29**, 2555 (1990).

[117] D. E. Farrell, C. J. Allen, R. C. Haddon, and S. V. Chichester, Phys. Rev. B. **42**, 8694 (1990).

[118] K. Ichimura, K. Nomura, and A. Kawamoto, AIP Conf Proc **850**, 607 (2006).

[119] D. Shoenburg, *Magnetic Oscillations in Metals* (Cambridge University Press, 1984).

[120] Z. A. Ren, J. Yang, W. Lu, W. Yi, G. C. Che, X. L. Dong, L. L. Sun, and Z. X. Zhao, arxiv/08034283 (2008).

[121] Z. A. Ren, J. Yang, W. Lu, W. Yi, X. L. Shen, Z. C. Li, G. C. Che, X. L. Dong, L. L. Sun, F. Zhou, et al., arxiv/08034234 (2008).

[122] P. Cheng, L. Fang, H. Yang, X. Zhu, G. Mu, H. Luo, Z. Wang, and H.-H. Wen, arxiv/08040835 (2008).

[123] X. H. Chen, T. Wu, G. Wu, R. H. Liu, H. Chen, and D. F. Fang, Nature **453**, 761 (2008).

[124] M. Rotter, M. Tegel, and D. Johrendt, Phys. Rev. Lett **101**, 107006 (2008).

[125] C. de la Cruz, Q. Huang, J. W. Lynn, J. Li, W. Ratcliff, J. L. Zarestky, H. A. Mook, G. F. Chen, J. L. Luo, N. L. Wang, et al., arxiv/08040795 (2008).

[126] L. Boeri, O. Dolgov, and A. A. Golubov, Phys. Rev. Lett **101**, 026403 (2008).

[127] I. Mazin, D. Singh, M. Johannes, and M. Du, arxiv/0803.2740 (2008).

[128] K. Haule, J. H. Shim, and G. Kotliar, Phys. Rev. Lett. **100**, 226402 (2008).

[129] Y. Wang, L. Shan, L. Fang, P. Cheng, C. Ren, and H.-H.Wen., arxiv/0806.1986 (2008).

[130] T. Y. Chen, Z. Tesanovic, R. H. Liu, X. H. Chen, and C. L. Chien, Nature (2008).

[131] Y. Nakai, K. Ishida, Y. Kamihara, M. Hirano, and H. Hosono, arxiv/08044765 (2008).

[132] H. Liu, X. Jia, W. Zhang, L. Zhao, J. Meng, G. Liu, X. Dong, G. Wu, R. H. Liu, X. H. Chen, et al., arxiv/08053821 (2008).

[133] F. Manzano, A. Carrington, N. Hussey, S. Lee, A. Yamamoto, and S. Tajima, Phys. Rev. Lett 88 (2002).

[134] N. D. Zhigadlo, S. Katrych, Z. Bukowski, and J. Karpinski, J. Phys. Cond. Mat **20**, 342202 (2008).

[135] C. de la Cruz, Q. Huang, J. W. Lynn, J. Li, W. Ratcliff, J. L. Zarestky, H. A. Mook, G. F. Chen, J. L. Luo, and N. L. Wang, Nature **453**, 899 (2008).

[136] Y. Qi, Z. Gao, L. Wang, D. Wang, X. Zhang, and Y. Ma, arxiv/0807.3293 (2008).

[137] G. F. Chen, Z. Li, D. Wu, G. Li, W. Z. Hu, J. Dong, P. Zheng, J. L. Luo, and N. L. Wang, arxiv/08033790 (2008).

[138] Q. Huang, Y. Qiu, W. Bao, M. A. Green, J. Lynn, Y. C. Gasparovic, T. Wu, G. Wu, and X. H. Chen, Phys. Rev. Lett **101**, 257003 (2008).

[139] A. I. Coldea, J. D. Fletcher, A. Carrington, J. G. Analytis, A. F. Bangura, J.-H. Chu, A. S. Erickson, I. R. Fisher, N. E. Hussey, and R. D. McDonald, Phys. Rev. Lett **101**, 216402 (2008).

[140] C. Liu, T. Kondo, M. E. Tillman, R. Gordon, G. D. Samolyuk, Y. Lee, C. Martin, J. L. McChesney, S. Bud'ko, M. A. Tanatar, et al., arxiv/0806.2147 (2008).

[141] M. Yi, D. H. Lu, J. G. Analytis, J.-H. Chu, S.-K. Mo, R.-H. He, X. J. Zhou, G. F. Chen, J. L. Luo, N. L. Wang, et al., arxiv/0902.2628 (2009).

[142] S. Weyeneth, U. Mosele, S. Kohout, J. Roos, H. Keller, N. Zhigadlo, S. Katrych, Z. Bukowski, and J. Karpinski, arxiv/0806.1024 (2008).

[143] C. Senatore, M. Cantoni, G. Wu, R. Liu, X. Chen, and R. Flukiger, arxiv/08052389 (2008).

[144] A. J. Drew, F. L. Pratt, T. Lancaster, S. J. Blundell, P. J. Baker, R. H. Liu, G. Wu, X. H. Chen, I. Watanabe, V. K. Malik, et al., arxiv/08051042 (2008).

[145] R. Khasanov, H. Luetkens, A. Amato, H.-H. Klauss, Z.-A. Ren, J. Yang, W. Lu, and Z.-X. Zhao, arxiv/0805.1923 (2008).

[146] J. Fletcher, A. Carrington, O. Taylor, S. Kazakov, and J. Karpinski, Phys. Rev. Lett **95** (2005).

[147] A. Dubroka, K. W. Kim, M. Roessle, V. Malik, R. H. Liu, G. Wu, X. H. Chen, and C. Bernhard, arxiv/08052415 (2008).

[148] A. S. Sefat, R. Jin, M. A. McGuire, B. C. Sales, D. J. Singh, and D. Mandrus, Phys. Rev. Lett **101**, 117004 (2008).

[149] A. Yamamoto, J. Jaroszynski, C. Tarantini, L. Balicas, J. Jiang, A. Gurevich, D. Larbalestier, R. Jin, A. Sefat, M. McGuire, et al., arxiv/0810.0699 (2008).

[150] N. Ni, M. E. Tillman, J.-Q. Yan, A. Kracher, S. T. Hannahs, S. L. Bud'ko, and P. C. Canfield, Phys. Rev. B **78**, 214515 (2008).

[151] M. A. Tanatar, N. Ni, C. Martin, R. T. Gordon, H. Kim, V. G. Kogan, G. D. Samolyuk, S. L. Bud'ko, P. C. Canfield, and R. Prozorov, arxiv/0812.0343 (2008).

[152] A. D. Christianson, M. D. Lumsden, O. Delaire, M. B. Stone, D. L. Abernathy, M. A. McGuire, A. S. Sefat, R. Jin, B. C. Sales, D. Mandrus, et al., arxiv/0807.3370 (2008).

[153] D. Parker, O. Dolgov, M. Korshunov, A. Golubov, and I. Mazin6, arxiv/0807.3729 (2008).

[154] S. Graser, T. A. Maier, P. J. Hirschfeld, and D. J. Scalapino, arxiv/0812.4991 (2008).

[155] H.-J. Grafe, D. Paar, G. Lang, N. J. Curro, G. Behr, J. Werner, J. Hamann-Borrero, C. Hess, N. Leps, and R. K. B. Buchner, Phys. Rev. Lett **101**, 047003 (2008).

[156] F. Ning, K. Ahilan, T. Imai, A. S. Sefat, R. Jin, M. A. McGuire, B. C. Sales, and D. Mandrus, J. Phys. Soc. Jpn **77**, 103705 (2008).

[157] H. Fukazawa, T. Yamazaki, K. Kondo, Y. Kohori, N. Takeshita, P. M. Shirage, K. Kihou, K. Miyazawa, H. Kito, H. Eisaki, et al., arxiv/0901.0177 (2008).

[158] M. Hiraishi, R. Kadono, S. Takeshita, M. Miyazaki, A. Koda, H. Okabe, and J. Akimitsu, arxiv/0812.2069 (2008).

[159] J. Karpinski, N. Zhigadlo, S. Katrych, Z. Bukowski, P. Moll, S. Weyeneth, H. Keller, R. Puzniak, M. Tortello, D. Daghero, et al., arxiv/0902.0224 (2009).

[160] L. Ding, C. He, J. K. Dong, T. Wu, R. H. Liu, X. H. Chen, and S. Y. Li, Phys. Rev. B **77**, 180510 (2008).

[161] J. Cooper, Phys. Rev. B **54**, R3753 (1996).

[162] R. Cimberle, C. Ferdeghini, F. Canepa, M. Ferretti, A. Martinelli, A. Palenzona, A. Siri, and M. Tropeano, arxiv/0807.1688 (2008).

[163] C. Martin, R. T. Gordon, M. A. Tanatar, M. D. Vannette, M. E. Tillman, E. D. Mun, P. C. Canfield, V. G. Kogan, G. D. Samolyuk, J. Schmalian, et al., arxiv/0807.0876 (2008).

[164] K. Hashimoto, T. Shibauchi, T. Kato, K. Ikada, R. Okazaki, H. Shishido, M. Ishikado, H. Kito, A. Iyo, H. Eisaki, et al., Phys. Rev. Lett **102**, 017002 (2009).

[165] A. Chubukov, D. Efremov, and I. Eremin, arxiv/0807.3735 (2008).

[166] W. Anukool, S. Barakat, C. Panagopoulos, and J. R. Cooper.

[167] J.-H. Chu, J. G. Analytis, C. Kucharczyk, and I. R. Fisher, arxiv/0811.2463 (2008).

[168] R. T. Gordon, N. Ni, C. Martin, M. A. Tanatar, M. D. Vannette, H. Kim, G. Samolyuk, J. Schmalian, S. Nandi, A. Kreyssig, et al., arxiv/0810.2295 (2008).

[169] K. Hashimoto, T. Shibauchi, S. Kasahara, K. Ikada, T. Kato, R. Okazaki, C. J. van der Beek, M. Konczykowski, H. Takeya, K. Hirata, et al., arxiv/0810.3506 (2008).

[170] J. Fletcher, A. Serafin, L. Malone, J. Analytis, J.-H. Chu, A. Erickson, I. Fisher, and A. Carrington, arxiv/0812.3858 (2008).

[171] A. Vorontsov, M. Vavilov, and A. Chubukov, arxiv/0901.0719 (2008).

[172] S. Graser, T. A. Maier, P. J. Hirschfeld, and D. J. Scalapino, arxiv/0812.0343 (2008).

[173] J. Wu and P. Phillips, arxiv/0901.0038 (2008).

[174] D. Parker and I. Mazin, arxiv/0812.4416 (2008).

[175] A. Harrison, J. Phys. Cond. Mat **16**, S553 (2004).

[176] T. Sorgel and M. Jansen, Z. Anorg. Allg. Chem. **631**, 2970 (2005).

[177] E. Wawrzynska, R. Coldea, E. Wheeler, I. Mazin, M. Johannes, T. Sorgel, M. Jansen, R. Ibberson, and P. Radaelli, Phys. Rev. Lett. **99**, 157204 (2007).

[178] T. Sorgel and M. Jansen, J. Solid State Chem. **180**, 8 (2007).

[179] E. Wawrzynska, R. Coldea, E. Wheeler, T. Sorgel, M. Jansen, R. Ibberson, P. Radaelli, and M. Koza, Phys. Rev. B **77**, 094439 (2008).

[180] A. I. Coldea, A. Carrington, R. Coldea, L. Malone, E. Yelland, A. Bangura, J. G. Analytis, I. I. Mazin, M. D. Johannes, T. Sorgel, et al.

[181] J. A. Alonso, J. L. Garca-Muoz, M. T. Fernndez-Daz, M. A. G. Aranda, M. J. Martnez-Lope, and M. T. Casais, Phys. Rev. Lett **82**, 3871 (1999).

[182] M. D. Johannes, S. Streltsov, I. I. Mazin, and D. I. Khomskii, Phys. Rev. B **75**, 180404 (2007).

[183] L. Seabra, unpublished.